

Properties of small $3d$ -metal based clusters: A journey from wave function to density functional methods

Le Nhan Pham

Supervisor:

Prof. dr. Minh Tho Nguyen

Dissertation presented in partial
fulfillment of the requirements for the

degree of Doctor of Science (PhD):

Chemistry

September 2019

Properties of small $3d$ -metal based clusters: A journey from wave function to density functional methods

LE NHAN PHAM

Examination committee:

Prof. dr. Tatjana Parac-Vogt, chair
Prof. dr. Minh Tho Nguyen, supervisor
Prof. dr. Ewald Janssens
Prof. dr. Jeremy Harvey
Prof. dr. Daniel Escudero
Prof. dr. Andrei Kirilyuk
(Radboud University Nijmegen)

Dissertation presented in partial fulfillment of the requirements for the degree of Doctor of Science (PhD): Chemistry

September 2019

© 2019 KU Leuven – Faculty of Science
Uitgegeven in eigen beheer, Le Nhan Pham, Celestijnenlaan 200F box 2402, B-3001 Leuven (Belgium)

Alle rechten voorbehouden. Niets uit deze uitgave mag worden vermenigvuldigd en/of openbaar gemaakt worden door middel van druk, fotokopie, microfilm, elektronisch of op welke andere wijze ook zonder voorafgaande schriftelijke toestemming van de uitgever.

All rights reserved. No part of the publication may be reproduced in any form by print, photoprint, microfilm, electronic or any other means without written permission from the publisher.

Preface

My journey to the end of PhD student life is done after nearly five years of living and studying in Leuven. This is a long run with several different experiences, emotions, memories, and learning. All things harvested during my PhD program were tremendous and super meaningful to me. I would like to express my deep gratitude towards all the individuals making up my PhD journey a success.

First and foremost, I would like to give special thanks to my supervisor Prof. Minh Tho Nguyen for his excellent support, guidance, patience, and motivation throughout my PhD program in Belgium. Without his invaluable support and efforts, I would not have had the chance to experience scientific life and study at KU Leuven. I will bring every single piece of knowledge learned from my supervisor and his merits of being a professor back to Vietnam and disseminate them to my future students.

I want to show my great thanks to Prof. Ewald Janssens for the fruitful discussions and enthusiastic support over the collaborative projects. I have gained huge experience throughout preparation of manuscripts under his guidance and revisions. These are all highly valuable to me during the PhD program here at KU Leuven.

I am grateful to Prof. Marc Hendrickx for his supervision during my pre-doctoral program. After more than one year of working with him, I have learned many skills and techniques related to computational and quantum chemical research. The skills and knowledge obtained from my pre-doctoral research were helpful for all research projects in my PhD program.

I truly appreciate Dr. Alex Domingo for his very kind technical support. I have learned

from him all basic skills to do computational chemistry, especially how to use the Molcas program. Under Alex's help, I have become more familiar with linux systems, and confident of doing computations and analyzing computational data. I would say that he was a scientific mentor during my first years at KU Leuven. I also want to thank Tzvetan for his help in dealing with technical problems at the beginning of my pre-doctoral program.

My thanks go to all friends in the Division of Quantum Chemistry and Physical Chemistry who have been creating an amazing atmosphere both on- and off-office: Dragan, Andrea, Carlos, Ana, Tolga, Tuan Anh, Simon, Quan, Xiaoyong, Ewa, Athanasios, Milica, Eliot, Prashant, Jason, May Mee, Hung Hang, Trang, Berna, Cansu, Maike, Zhen, Pierre-Louis, Damiano, Carlo, and some others. I also want to give my sincere thanks to Mrs. Rita Jungbluth and Dr. Hans Vansweevelt for their support and time.

Thank you Dr. Lars Goerigk for hosting me during the time I was doing my exchange at the University of Melbourne. There I got more opportunities to learn more about computational chemistry, especially double-hybrid density functional theory. At the University of Melbourne I also have more friends such as Nisha and Marcos.

I am indebted to the KU Leuven research Council for a doctoral scholarship within a GOA program on "Quantum Rule on Clusters".

I thank the University of Dalat for making me totally free of any teaching duty, so that I could fully invest my time into doing research at KU Leuven.

I also want to thank all jury members for their time and energy in evaluation and correction of this thesis.

Con xin cảm ơn Ba Má ở nhà rất nhiều vì đã luôn động viên và khuyên bảo con trong suốt quá trình học tập tại Bỉ. Cảm ơn Bố Mẹ đã quan tâm chăm sóc gia đình nhỏ của con trong suốt thời gian con đi học xa nhà.

Last but not least, I have to say that I owe my wife and my daughter the greatest thanks ever for supporting me unconditionally. I have been staying away from my little family for almost 5 years, and my wife has been taking care of our daughter alone for such long time, even though my wife is still doing her PhD research. There are not enough words to show my deep gratitude to her. I love you - my wife - and our family so much. All the time here in Leuven, I just wanted to finish the PhD research as soon as possible and go back to my little family.

Abstract

This dissertation is dedicated to study of small clusters containing 3d-block metals. Although these clusters can be synthesized and probed by experimental techniques, they are geometrically and electronically unknown. Data on clusters obtained from the experiment supply initial information about synthesized clusters like stoichiometry, and such primary information can be used as very reliable reference for identification of atomic arrangements and electronic structures of clusters. Additional secondary properties of the studied clusters can also be drawn once electronic and geometric structures of clusters are determined. To identify geometry of atomic combination and electronic structures, quantum chemical methods such as wave function based approaches and density functional theory can be used for reproduction of and interpretation on experimental outcomes. In this doctoral study, two categories of experimental data measured are ionization energy or detachment energy of electrons removed from clusters under irradiation of photon laser beams, and the unique fingerprint vibrations of atomic components within clusters. Detachment energies of electrons removed from anionic clusters are measured and recorded in anion photoelectron spectra. The vibrations of atoms in this dissertation are mainly measured by using the infrared multiphoton dissociation spectroscopic technique; and therefore, obtained vibrations are recorded in so-called infrared multiphoton dissociation spectra.

The first part of this thesis including Chapter 3 to Chapter 6 focuses on the small clusters that have been studied with highly accurate methods (CASSCF/CASPT2, NEVPT2, MRCI, DMRG-CASPT2, and CCSD(T)). By applying these methods and comparing calculated results with experimental ones, geometries, ground and excited states of the studied clusters can be determined correctly. From the electronic structures and calculated detachment energies of outer electrons, all possible electronic transitions within a limit of theoretical methods can be also predicted and all observed experimental bands (corresponding to

specific detachment processes) can be understood and assigned. To further support band assignments made on the basis of theoretical calculations, we used simulations of detachment bands by calculating multidimensional Franck-Condon factors. The simulated bands can provide more detailed insights into each experimental band. In parallel with highly accurate methods mentioned above, DFT-based methods were used thoroughly for all studied systems.

It is worth noting that all clusters studied in each chapter from Chapter 3 to Chapter 6 were arranged in an order of increasing multireference features indicated by the coefficients of dominant configurations. The more the studied systems are multiconfigurational, the more they are challenging to single reference methods. With the increasing multiconfigurational features and the testing use of DFT methods, we would like to find out suitable density functionals for study of similar systems in terms of magnitude of multireference. Indeed, for single reference systems like $\text{ScSi}_2^{-/0}$, all tested functionals and the RCCSD(T) method could well reproduce the experimental ionization energies of all electronic transitions in comparison to values obtained from the experiment and multireference methods. More importantly, we always find out relevant functionals which can relatively reproduce the experimental results, even though the system studied has strong multireference features like $\text{Cr}_2\text{O}_2^{-/0}$. Overall, there are no general rules for selection of functionals to deal with specific levels of multireference. Such a selection becomes an empirical exercise.

The second part (Chapters 7 and 8) of this dissertation concentrates on a bit larger clusters containing multiple transition metal atoms. To be more specific, all clusters studied in this part are transition metal oxides in the gas phase (M_mO_n^+). Owing to possession of multiple transition metal atoms, correct wave functions of clusters studied in this part are believed to be multiconfigurational. But due to the large sizes of these clusters, they cannot be studied with high-accuracy methods mentioned above. The only possible choice here is to use density functional theory barely. As we have no general rules for choosing good functionals, a set of several functionals collected from all studies in the first part and some additional popular functionals were utilized to study Cr_mO_n^+ clusters. Geometric arrangements of atoms were discovered by comparing the simulated IR spectra with the experimental ones. Magnetic interplay, evolution, and insights of these chromium oxide clusters were revealed. For the mixed $\text{Cr}_x\text{Mn}_y\text{O}_z^+$ clusters, three functionals selected from the previous study were used for geometric identification. Geometrical and magnetic evolution of these clusters was also studied following addition of oxygen atoms and by changing the ratio of the different metals.

Beknopte samenvatting

Dit proefschrift is gewijd aan de studie van kleine clusters die 3d-block metalen bevatten. Deze clusters kunnen worden gesynthetiseerd en gekarakteriseerd door middel van experimentele technieken, maar hun geometrische en elektronische kenmerken zijn onbekend. Gegevens over de clusters verkregen uit experiment en leveren initiële informatie zoals stoichiometrie, en dergelijke primaire informatie kan als zeer betrouwbare referentie voor identificatie van geometrische en elektronische structuren van clusters worden gebruikt. Andere secundaire eigenschappen van de bestudeerde clusters kunnen ook worden bepaald zodra hun elektronische en geometrische structuren zijn gekend. Om de geometrie van atoomcombinaties en elektronische structuren te identificeren, kunnen kwantumchemische methoden zoals golffunctiegebaseerde methoden en dichtheidsfunctionaaltheorieën worden gebruikt voor de reproductie en interpretatie van experimentele resultaten.

Twee categorieën van de gemeten experimentele gegevens in dit proefschrift zijn ionisatie-energie of verwijderingsenergie van elektronen uit clusters onder bestraling met laserlicht, en vibratiemodes die een unieke vingerafdruk zijn van atomaire componenten binnen clusters. Verwijderingsenergieën van elektronen die uit anionische clusters worden gemeten en geregistreerd in een anion-fotoelektronspectrum. De vibraties van atomen in dit proefschrift worden voornamelijk gemeten met behulp van de infrarood fotodissociatie spectroscopische techniek, en daarom worden de verkregen trillingen opgenomen in infraroodfotodissociatiespectra.

Het eerste deel van dit proefschrift, met inbegrip van hoofdstukken 3 t/m 6, richt zich op de kleine clusters die met zeer nauwkeurige methoden kunnen worden bestudeerd (CASSCF/CASPT2, NEVPT2, MRCI, DMRG-CASPT2, en CCSD(T)). Door deze methoden

toe te passen en de berekende resultaten te vergelijken met de experimentele, kunnen geometrieën, grond- en aangeslagen toestanden van de bestudeerde clusters correct worden bepaald. Uit de elektronische structuren en berekende verwijderingsenergieën van buitenste elektronen kunnen ook alle mogelijke elektronische overgangen binnen de theoretische grenzen van de methoden worden voorspeld en kunnen alle waargenomen experimentele banden (die overeenkomen met specifieke verwijderingsenergieën) worden begrepen en toegewezen. Om de bandtoewijzing op basis van theoretische berekeningen verder te ondersteunen, gebruiken we simulaties van verwijderingsenergieën door multidimensionale Franck-Condon factoren te berekenen. De gesimuleerde banden kunnen meer gedetailleerd inzicht verschaffen in elke experimentele band. Parallel met de zeer nauwkeurige hierboven vermelde methoden, worden DFT methoden ook uitgebreid gebruikt in alle bestudeerde systemen.

Het is vermeldenswaard dat alle bestudeerde clusters in elk hoofdstuk van hoofdstuk 3 tot hoofdstuk 6 werden gerangschikt in een volgorde van toenemende multireferentie-eigenschappen, aangegeven door de coëfficiënten van de dominante configuraties. Hoe meer de bestudeerde systemen multiconfigurationeel zijn, hoe meer uitdagend ze zijn voor mono-referentiemethoden. Met de toenemende volgorde van multiconfigurationele kenmerken en het testen van het gebruik van DFT-methoden, willen we graag weten welke dichtheidsfunctionalen geschikt zijn voor het bestuderen van gelijkaardige systemen in termen van de omvang van multireferentie. Inderdaad, voor enkelvoudige referentiesystemen zoals $\text{ScSi}_2^{-/0}$, kunnen alle geteste functionalen en de coupled-cluster RCCSD(T)-methode, de experimentele ionisatieenergieën van alle elektronische overgangen goed reproduceren in vergelijking met de waarden verkregen uit het experiment en multireferentiemethoden. Belangrijker is dat we altijd relevante functionalen vinden die de experimentele resultaten relatief kunnen weerspiegelen, ook al heeft het bestudeerde systeem sterke multireferentie eigenschappen zoals $\text{Cr}_2\text{O}_2^{-/0}$. Er zijn geen algemene regels voor het gebruik van functionalen met specifieke niveaus van multireferentie.

Het tweede deel (hoofdstukken 7 en 8) van dit proefschrift concentreert zich op een paar grotere clusters met meerdere overgangsmetaalatomen. Om specifieker te zijn, zijn alle onderzochte clusters in dit deel overgangsmetaloxide in de gasfase (Cr_mO_n^+ en $\text{Cr}_x\text{Mn}_y\text{O}_z^+$). Door het bezit van meerdere transitiemetaalatomen zijn de correcte golffuncties van de in dit deel bestudeerde clusters multiconfigurationeel. Als deze clusters groot zijn kunnen zij niet bestudeerd worden met zeer nauwkeurige methoden zoals hierboven vermeld. De enig mogelijke keuze hier is om gebruik te maken van de

dichtheidsfunctionaaltheorie. Omdat we geen algemene regels hebben voor de selectie van goede functionalen, hebben we dus een set van verschillende functionalen verzameld uit alle studies in het eerste deel en ook een aantal extra populaire functionalen werden gebruikt om $M_mO_n^+$ clusters te bestuderen. Geometrieën van de clusters worden ontdekt door een vergelijking van de gesimuleerde IR-spectra met experiment. Magnetische interactie, evolutie en inzichten van deze chroomoxideclusters worden onthuld. Voor $Cr_xMn_yO_z^+$ clusters, werden drie geselecteerde functionalen uit de vorige studie gebruikt voor geometrische identificatie. Geometrische en magnetische evolutie van deze clusters werden ook bestudeerd onder toevoeging van zuurstofatomen en wijziging van de metaal-metaal verhoudingen.

List of Abbreviations

ADE Adiabatic Detachment Energy.

AIM Atoms In Molecules.

ANO Atomic Natural Orbital.

AO Atomic Orbital.

CASPT2 Complete Active-Space Second-Order Perturbation Theory.

CASSCF Complete Active Space Self-Consistent Field.

CC Coupled-Cluster.

CCD Coupled-Cluster Doubles.

CCSD Coupled-Cluster Singles and Doubles.

CI Configuration Interaction.

CSF Configuration State Function.

DE Detachment Energy.

DFT Density Functional Theory.

DMRG Density Matrix Renormalization Group.

FCF Franck-Condon Factor.

FCI Full Configuration Interaction.

FELIX Free Electron Laser for Infrared eXperiments.

GGA Generalized Gradient Approximation.

GTO Gaussian Type Orbital.

HF Hartree Fock.

HOMO Highest Occupied Molecular Orbital.

IE Ionization Energy.

IR Infrared.

IRMPD Infrared Multiphoton Dissociation.

IRPD Infrared Photodissociation.

LDA Local-Density Approximation.

LUMO Lowest Unoccupied Molecular Orbital.

MCSCF Multiconfiguration Self-Consistent Field.

MO Molecular Orbital.

MPS Matrix Product State.

MRCI Multireference Configuration Interaction.

NEVPT2 N-Electron Valence State Perturbation Theory.

PDOS Partial Density of States.

PE Photoelectron.

RASPT2 Restricted Active Space Second-Order Perturbation.

RASSCF Restricted Active Space Self-Consistent Field.

RCCSD Restricted Coupled-Cluster Singles and Doubles.

RHF Restricted Hartree-Fock.

ROHF Restricted Open-shell Hartree-Fock.

SCF Self-Consistent Field.

SD Stater Determinant.

STO Slater Type Orbital.

TDDFT Time Dependent Density Functional Theory.

TDOS Total Density of States.

TM Transition Metal.

UHF Unrestricted Hartree-Fock.

UPS Ultraviolet Photoelectron Spectroscopy.

VDE Vertical Detachment Energy.

XPS X-ray Photoelectron Spectroscopy.

ZPE Zero-Point Energy.

Contents

Abstract	iii
Beknopte samenvatting	v
List of Abbreviations	ix
List of Symbols	xiii
Contents	xiii
List of Figures	xvii
List of Tables	xxiii
1 Introduction	1
References	6
2 Experimental and Theoretical Methods	8
2.1 Experimental Methods	8
2.1.1 Anion photoelectron spectroscopy	8
2.1.2 Infrared Multiphoton Dissociation Spectroscopy	13

2.2	Computational methods	15
2.2.1	Schrödinger Equation	15
2.2.2	Wave functions	17
2.2.3	Hartree-Fock Method	18
2.2.4	Restricted, Restricted Open-shell and Unrestricted wave functions	19
2.2.5	Basis Sets	20
2.2.6	Post Hartree-Fock Methods	21
2.2.7	Density matrix renormalization group	28
2.2.8	Density Functional Methods	29
	References	32
3	Scandium Disilicon	36
3.1	Introduction	37
3.2	Computational Details	39
3.3	Results and Discussion	41
3.3.1	Ground States and Low-Lying States of $\text{ScSi}_2^{-/0}$	41
3.3.2	Electronic Structures and Possible One-Electron Detachments .	44
3.3.3	Anion photoelectron Spectrum and Band Assignments	48
3.3.4	Franck-Condon Factor Simulations	53
3.4	Concluding Remarks	55
	References	56
4	Titanium Digermanium TiGe_2	59
4.1	Introduction	59
4.2	Computational Details	61
4.3	Results and Discussion	63
4.3.1	Ground and Low-Lying States of $\text{TiGe}_2^{-/0}$	63

4.3.2	Electronic Structures and One-Electron Electronic Transitions	65
4.3.3	Anion PE Spectrum and Band Assignments	72
4.3.4	Franck-Condon Factor Simulations	76
4.4	Concluding Remarks	78
	References	79
5	Vanadium Trigermanium VGe₃	83
5.1	Introduction	83
5.2	Computational Details	86
5.3	Results and Discussion	88
5.3.1	The Most Stable Isomer and Ground States	88
5.3.2	Electronic Structures and One-Electron Electronic Transitions	90
5.3.3	Anion Photoelectron Spectrum and Band Assignments	96
5.3.4	Franck-Condon Factor Simulations	98
5.4	Concluding Remarks	100
	References	100
6	Dichromium oxide Cr₂O₂	103
6.1	Introduction	103
6.2	Computational Methods	106
6.3	Results and Discussion	108
6.3.1	Ground-State Identification	108
6.3.2	Electronic Structures and One-Electron Removals	112
6.3.3	Anion Photoelectron Spectra	116
6.3.4	Franck-Condon Factor Simulations	121
6.4	Concluding Remarks	123
	References	123

7 Small chromium oxide clusters	127
7.1 Introduction	128
7.2 Experimental Methods	129
7.3 Computational Methods	130
7.4 Results and Discussion	131
7.4.1 Structural Assignments	131
7.4.2 Magnetic Properties	136
7.5 Conclusion	140
References	141
8 Bimetallic Cr-Mn Oxide Clusters	144
8.1 Introduction	145
8.2 Methodology	146
8.3 Results and discussion	148
8.3.1 Structural assignments	148
8.3.2 Structural evolution	156
8.3.3 Magnetic interactions	157
8.3.4 Conclusion	159
References	160
9 Conclusions and Outlook	164
9.1 Conclusions	164
9.2 Outlook	168
References	170
List of publications	173

List of Figures

2.1	The anion photoelectron spectrum of Cr_2O_2^- at 266 nm (reproduced with permission from ref 5, Copyright 2006, AIP Publisher).	9
2.2	Relative intensity of peaks within progressions. This is redrawn on the basis of Figure 7.2 from ref 9.	13
2.3	Experimental set-up used for IRMPD measurements. This figure is taken from ref 10 with permission from Springer Publishing.	14
2.4	IRMPD spectrum of the Cr_4O_4^+ measured on the $\text{Cr}_4\text{O}_4^+\cdot\text{Ne}$ complex (reproduced with permission from ref 11, Copyright 2018, ACS Publisher).	15
2.5	Schematic representation of the electronic structure obtained with RHF for a singlet state and ROHF and UHF for a doublet state	20
2.6	Possible configurations of first three excited states generated from a Hartree-Fock single configuration.	23
2.7	The schemes for electron distribution in the CASSCF and RASSCF methods	27
3.1	Two isomers of $\text{ScSi}_2^{-/0}$ clusters and the coordinate systems used.	39
3.2	Occupied CASSCF pseudonatural active orbitals of ${}^3\text{B}_2$ and corresponding active orbitals of ${}^2\text{B}_2$. Average occupation numbers are given in parentheses. Scandium atoms are on the right-hand side of each cluster. .	45

3.3 Anion photoelectron spectrum of ScSi_2^- recorded at the photon energy of 266 nm (reproduced with permission from ref 14. Copyright 2011, CPS). Five bands in the spectrum are labeled as the traditional nomenclature of anion photoelectron bands (X – D).	49
3.4 Franck-Condon factor simulations for the four bands X, A, B, and D of the photoelectron spectrum of ScSi_2^-	54
4.1 Two low-lying isomers of $\text{TiGe}_2^{-/0}$ and the Cartesian coordinate axes.	61
4.2 Occupied pseudonatural orbitals in the active spaces of states $^4\text{B}_1$ and $^3\text{B}_1$ (CASSCF wave functions). The average occupation numbers are given in parentheses. The metal atom Ti is located on the right-hand side.	66
4.3 Experimental anion PE spectrum of TiGe_2^- (reproduced with permission from ref 22, Copyright 2014, RSC Publisher).	73
4.4 Franck-Condon factor simulations of two bands X and A making use of CASPT2 vibrational frequencies given in Table 4.5 and of related equilibrium geometries in Table 4.1. Each band is simulated with two simultaneous electronic transitions.	78
5.1 Anion photoelectron spectrum of VGe_3^- with five distinguishable bands denoted as X, A, B, C, and D is taken from ref 6. Reproduced with permission from ref 6. Copyright 2015 American Chemical Society.	85
5.2 Three possible geometries of $\text{VGe}_3^{-/0}$ and the coordinate systems employed.	85
5.3 Occupied pseudonatural orbitals in the active space of $^1\text{A}'$ (C_s) and corresponding active orbitals of $^2\text{A}'$. Orbitals are obtained from CASSCF wave functions. The average occupation numbers are given in parentheses. The metal atom V is on the top of the tetrahedral $\eta^3\text{-}(\text{Ge}_3)\text{V}$ isomer.	91
5.4 MO diagram of the anionic ground state $^1\text{A}'$ ($^1\text{A}_1$) within the treated active space. Orbital labels with respect to a C_{3v} spatial symmetry are placed in parentheses. The energy ordering is figured out on the basis of the corresponding single-reference wave functions.	95

5.5	Two distortion directions under a Jahn–Teller effect upon one-electron photodetachments at the degenerate HOMO. The blue atom is vanadium.	95
5.6	Franck–Condon factor simulations of two transitions underlying the PE band X.	99
6.1	Anion photoelectron spectra of Cr_2O_2^- at two different photon energies of 266 and 193 nm (reproduced with permission from ref 11, Copyright 2006, AIP Publisher).	105
6.2	Coordinate systems used for RASSCF/RASPT2 calculations of four different Cr_2O_2 isomers in both neutral and anionic states.	106
6.3	Potential energy curves for the ground and first excited states of $\text{Cr}_2\text{O}_2^{-/0}$ along the Cr–Cr distance at the RASPT2 level.	109
6.4	Pseudonatural orbitals within the active spaces of the ground and first excited states of Cr_2O_2^- . In parentheses are the occupation numbers.	113
6.5	Franck–Condon factor simulations of the first two bands X' and X in the anion photoelectron spectra of Cr_2O_2^- . Vibrational modes obtained from DFT computations giving rise to significant integrals can be seen in the insets.	122
7.1	(a) Experimental IRPD spectra and (b) simulated harmonic IR spectra of Cr_2O_2^+ . The simulated spectrum of the ${}^8\text{B}_{1g}$ ground state is presented by the blue line, the spectrum of the ${}^8\text{B}_{1u}$ excited state by the red line. The geometries of the lowest-lying states are shown as insets.	132
7.2	Experimental IRPD spectra and simulated harmonic IR spectra of Cr_3O^+ , Cr_3O_2^+ , and Cr_3O_3^+ . The geometries of lowest-lying states for each cluster are shown as insets.	133
7.3	Experimental IRPD spectra and simulated harmonic IR spectra of Cr_4O_4^+ . The geometries of the two most stable isomers are shown as insets.	134

7.4 Simulated harmonic IR spectra of structural isomer A of Cr_4O_4^+ in four different spin states.	135
7.5 Structures of Cr_2O_2^+ , Cr_3O^+ , Cr_3O_2^+ , Cr_3O_3^+ , and Cr_4O_4^+ as assigned by comparison of simulated IR spectra with the experimental IRPD spectra. In addition, the structures of Cr_3^+ , Cr_3O_4^+ and Cr_3O_5^+ , for which no IRPD data is available, are added to the figure. Spin magnetic moments of Cr_3^+ , Cr_3O_4^+ and Cr_3O_5^+ were calculated from their energetically lowest geometry and electronic states. Chromium and oxygen atoms are represented by blue and red balls, respectively. Green (red) arrows indicate the orientation of the local spin magnetic moments ($> 0.05 \mu_B$) on the chromium (oxygen) atoms.	136
7.6 Total density of states (TDOS) and partial density of states (PDOS) of Cr_3O_3^+ (left part) and Cr_3O^+ (right part). For each part the left (right) side corresponds to alpha or up (beta or down) orbitals as indicated by the black arrows: (a) TDOS of Cr_3O_3^+ , (b) TDOS of Cr_3O^+ , (c) PDOS of Cr_3O_3^+ , and (d) PDOS of Cr_3O^+ . For PDOS, the projections in oxygen-2p (chromium-3d) orbitals are shown in red (blue). Atoms are numbered according to the structures shown in the insets. Vertical short dashed lines indicate the highest occupied alpha and beta orbitals.	139
7.7 Evolution of the total spin magnetic moment for Cr_3O_n^+ ($n = 0 - 5$) clusters.	140
8.1 Experimental IRMPD and simulated (at the TPSS level) harmonic IR spectra of low-energy isomers of CrMnO_4^+ . The geometrical structures of selected low-lying states are given as inset with chromium (manganese) atoms represented by blue (black) balls.	149
8.2 Experimental IRMPD and simulated (at the TPSS level) harmonic IR spectra of low-energy isomers of (left panel) $\text{CrMn}_2\text{O}_5^+$ and (right panel) $\text{CrMn}_2\text{O}_6^+$. The geometrical structures of selected low-lying states are given as insets with chromium (manganese) atoms represented by blue (black) balls.	149

8.3 Experimental IRMPD and simulated (at the TPSS level) harmonic IR spectra of low-energy isomers of (a) $\text{Cr}_2\text{MnO}_6^+$ and (b) $\text{Cr}_2\text{MnO}_7^+$. The geometrical structures of selected low-lying states are given as insets with chromium (manganese) atoms represented by blue (black) balls.	151
8.4 Experimental IRMPD and simulated harmonic IR spectra of $\text{CrMn}_3\text{O}_6^+$ at the TPSS level. The geometrical structures of selected low-lying states are given as insets with chromium (manganese) atoms represented by blue (black) balls.	152
8.5 Experimental IRMPD and simulated harmonic IR spectra of $\text{Cr}_2\text{Mn}_2\text{O}_z^+$ ($z = 7, 8$) at the TPSS level. The geometrical structures of selected low-lying states are given as insets with chromium (manganese) atoms represented by blue (black) balls.	154
8.6 Experimental IRMPD and simulated harmonic IR spectra of $\text{Cr}_3\text{Mn}_z\text{O}_z^+$ ($z = 8, 9$) at the TPSS level. The geometrical structures of selected low-lying states are given as insets with chromium (manganese) atoms represented by blue (black) balls.	155
8.7 Structural evolution of $\text{Cr}_x\text{Mn}_y\text{O}_z^+$ ($x + y = 2 - 4, z = 2 - 10$). The numbers of chromium and manganese atoms are on the left-hand column, and the number of oxygen atoms is arranged horizontally below oxide structures. Chromium (manganese) balls are blue (black) balls.	156
8.8 Total magnetic moments of $\text{Cr}_x\text{Mn}_y\text{O}_z^+$ ($x + y = 2 - 4, z = 2 - 10$)	158
8.9 Total magnetic moments and the orientation of the local spin magnetic moments on the metallic sites (chromium and manganese) withdrawn from natural bond orbital (NBO) analysis using the TPSS electron density. Chromium (manganese) atoms are represented by blue (black) balls.	159
8.10 Averaged absolute local magnetic moments of Cr and Mn in $\text{Cr}_x\text{Mn}_y\text{O}_z^+$ ($x + y = 2 - 4, z = 2 - 10$). All values were calculated from natural bond orbital (NBO) analysis using the TPSS electron density.	160

List of Tables

3.1	Relative Energies and Structural Parameters of the Ground and Low-Lying States	43
3.2	CASSCF Leading Configurations and Possible Ionization Processes Starting from the Anionic Ground State $^3\text{B}_2$, and from the Nearly Degenerate State $^1\text{B}_2$	44
3.3	Atomic Net Charges of Sc and Si (CASSCF)	48
3.4	Adiabatic Detachment Energies and Vertical Detachment Energies Calculated at CASPT2 Geometries in Table 3.2	50
3.5	Equilibrium geometries and harmonic vibrational frequencies (B3LYP/aug-cc-pVTZ-DK) for the initial anionic state $^3\text{B}_2$ and four neutral final states corresponding to the bands X, A, B and D in the PE spectrum	53
4.1	Determination of Ground States of Both Anionic and Neutral TiGe_2 at Different Levels	65
4.2	Leading Configurations of the Two Most Stable Anionic Ground States and of Neutral Ones	67
4.3	Mulliken Atomic Charges of Ti and Ge Analyzed from CASSCF Wave Functions	72

4.4	Calculated VDE of TiGe_2^-	74
4.5	Vibrational frequencies of involving states underlying two X and A bands in the PE spectrum calculated at the CASPT2 level of theory	77
5.1	Determination of the Ground States at BP86, RCCSD(T), and CASPT2 Levels	89
5.2	CASSCF Leading Configurations of Anionic and Neutral Ground States, and Electronic Transitions Allowed by Selection Rules	93
5.3	VDEs of Electronic Transitions Originating from the Anionic Ground State ${}^1\text{A}_1$	97
6.1	Relative Energies (eV) of All Electronic States with Spin Multiplicities of 8, 9, 10, and 11 Determined Using Different Methods	110
6.2	Insignificant Effects of ZPEs on Energetic Ordering of the Two Lowest Anionic States	111
6.3	Leading Configurations of the Two Most Stable Anionic Ground States and of Neutral Ones. Continuous bands are noted as con.	114
6.4	RASPT2 ADE and VDE Values of Electronic Transitions Starting from the Nearly Degenerate Anionic States	118
6.5	Comparison of Band Assignments from This Work and Two References 11 and 6	121
7.1	Total Spin Magnetic Moments of Clusters and Local Spin Magnetic Moments of Chromium and Oxygen Atoms	137
9.1	Summary of all studied systems and general results	169

Chapter 1

Introduction

3d-block metals are elements whose electronic structures are characterized by the ongoing filling-up of the *3d* orbitals along the series. In the Periodic Table, *3d*-block metals, except for scandium and zinc, are known as the first-row transition metals, bridging two sides of *s*- and *p*-block elements. As mentioned above, five *3d* orbitals of the *3d*-block atoms are gradually filled with electrons in order of increasing atomic number. Due to these *3d* electrons, transition metals expose several different properties in comparison to main group elements, for example, multiple oxidation states and magnetic field manifestation found in bulk iron, cobalt, and nickel. Different oxidation states of transition metals can readily interconvert owing to incomplete *3d*-filled orbitals, which facilitates catalytic capability of transition metals and their complexes.^{1–4} Interestingly, in forms of clusters, transition metals can chemically and physically behave in such a way that they are totally unique and unexpected when compared to corresponding bulk materials. With unique and unexpected properties of transition metals, clusters of materials doped with or containing transition metals are also expected to have new features and/or their existing properties will be tuned. Adding one or more *3d*-block metallic atoms to pristine clusters is a popular procedure that is experimentally and theoretically employed to investigate novel materials.

Several methods can be used to synthesize and characterize clusters that contain transition metals. In this work, clusters were generated (partially by our experimental coworkers) on the basis of laser vaporization processes, and then probed by two different spectroscopic

techniques. The first technique is called anion photoelectron spectroscopy. Anionic clusters generated and mass-selected are irradiated with high-energy photon beams. Under such high-energy photon beams, electrons in anionic clusters are detached, and their kinetic energies are, in turn, measured. All signals obtained under the form of ionization energy are recorded in anion photoelectron spectra. Through ionization energies, one can indirectly identify geometric and electronic structures of synthesized clusters in combination with relevant quantum chemical theories. The second technique is infrared multiphoton dissociation spectroscopy. In this technique, energy of photons which are resonantly absorbed by clusters is recorded by tracing any dissociation happening in the clusters.⁵ This technique is also called action spectroscopy and was designed to circumvent all difficulties that prevented applying direct IR spectroscopy to gas phase clusters. Vibrational spectra obtained from this technique provide vibrational details that are directly related to geometric structures of the clusters studied. Again, quantum chemical calculations are used to understand properties of the clusters.

As can be understood from above, quantum chemical calculations are essential to fully understand synthesized clusters. Due to the incomplete $3d$ -filled orbitals, quantum chemical methods employed must be able to recover enough correlation energy to describe clusters containing transition metals. Conveniently, the correlation energy can be divided into two types: static and dynamic correlation energy. For clusters doped with transition metals, electronic structures are not always correctly described by single-reference wave functions. In most cases, multiconfigurational wave functions methods are needed to treat these systems. Multiconfigurational wave functions can recover static correlation energy which cannot be obtained by using single-reference wave functions. Dynamic correlation energy, understood as instantaneous interaction among electrons, can be considered by many popular methods such as DFT, coupled clusters, and perturbation theory. A method that can recover enough both static and dynamic correlation energy can give reliable energy of the studied systems. A popular method is complete active space self-consistent field in combination with second order perturbation theory (CASSCF/CASPT2). However, multireference methods like CASSCF/CASPT2 and MRCI cannot be used for large systems.

Multireference methods, that can provide reliable results on clusters containing transition metals, can only treat systems with a limited number of orbitals in the active space. This makes multiconfigurational methods applicable to clusters containing one or two transition metal atoms. To study larger clusters containing more transition metal atoms, the possible

option is to use DFT methods. The point for using DFT methods to treat systems containing transition metals is about to find appropriate functionals. Therefore, in this work, we used multiconfigurational methods to investigate energetic and electronic properties of small clusters containing one and two 3d-block metal atoms. Simultaneously, numerous density functionals were also employed to study these clusters. The results obtained from DFT methods were compared to those obtained from experiments and multireference methods. Good functionals were then selected for larger clusters for which multireference methods cannot be used. To identify good functionals, the complexity of studied systems was increased by choosing clusters doped with more complex metallic atoms (more electrons in the 3d subshell). Because large clusters with more transition metal atoms are believed to have strong multireference features, increase of the complexity of small systems allows us to determine suitable functionals that can handle strong multireference systems.

Briefly, this dissertation can be divided into two main parts: i) study of ground and excited states of small clusters containing one and two 3d-block metallic atoms in order of increasing multiconfigurational features and ii) probe of larger clusters with more than two 3d-block metallic atoms. All results are included in six out of the nine chapters (Chapter 3 to Chapter 8). Results of each chapter are summarized concisely in the following paragraphs.

In Chapter 3, scandium, the simplest 3d-block metal in the Periodic Table, with 1 electron in the 3d subshell, is the first object. This metal can form clusters with different main group elements.⁶⁻⁹ Various scandium doped clusters have been synthesized and studied. Among them, $\text{ScSi}_2^{-/0}$ is the simplest one synthesized and experimentally probed with anion photoelectron spectroscopy. Experimental data on ionization energies of the anionic cluster ScSi_2^- were precisely measured and reported. Various theoretical studies using single-reference methods (DFT) gave inconsistent conclusions on its ground and excited states. Therefore, to shed light on this cluster, multireference methods are definitely needed. Geometrical structures of several possible low-lying states of both neutral and anion were optimized using the CASPT2 method. In addition, the MRCI method was also utilized to confirm the ground and low-lying states on the potential surface. Several single-reference methods, such as RCCSD(T) and DFT, were also used to reinforce our obtained results and test how DFT methods work with clusters containing the simple 3d-block metal Sc.

The next 3d-block transition metal in the Periodic Table is titanium. This transition

metal has two electrons in its $3d$ orbitals, which is one electron more than Sc in the $3d$ subshell; therefore, clusters containing titanium are believed to be more complex in terms of multireference features. Similar to scandium, several types of clusters containing this transition metal were synthesized and characterized.^{10–15} In Chapter 4, the titanium digermanium clusters $\text{TiGe}_2^{-/0}$ were selected as the next object of this work. There are also several reports that used DFT methods to identify geometry and electronic structures of $\text{TiGe}_2^{-/0}$. Two multireference methods CASPT2 and NEVPT2 were used to ensure reliable results on ground and low-lying states. This type of systems was found to be more multiconfigurational than $\text{ScSi}_2^{-/0}$, and therefore, it is worth employing single-reference methods to see how DFT functionals are able to reproduce experimental ionization energy. All results calculated with single-reference methods were also used to assist the assignment of all ionization processes observed in the experiments.

In the next chapter (Chapter 5), a species of clusters containing vanadium was selected to evaluate if DFT methods can be used to study stronger multireference systems. From experimentally available clusters containing vanadium, the $\text{VGe}_3^{-/0}$ clusters are the smallest experimentally reported ones. A quick review over previous computational works shows that the use of DFT methods led to different geometry and electronic ground states. No clear-cut conclusions on the most stable geometry, electronic structures, and energetic ionization processes were withdrawn by using only single-reference methods. Therefore, a better way to proceed with the $\text{VGe}_3^{-/0}$ clusters is to use multireference methods. Indeed, the CASPT2 method was used to optimize geometry of the clusters, and relative energies of several electronic states were also calculated at this level. All results from CASPT2 calculations were then used as reliable references for evaluation of DFT results. In this work, several DFT functionals were employed to calculate relative energies and compared with results from CASPT2 calculations. Besides the explanation for all experimental observations, specific density functionals were also found to be good for treatment of systems with more multiconfigurational characters.

The following transition metal considered in this dissertation is chromium. The $\text{Cr}_2\text{O}_2^{-/0}$ clusters are the central object in Chapter 6. The complexity of the studied system is increased not only by adding more electrons into the $3d$ subshell but also by including more metallic atoms in the cluster. Two groups independently synthesized and probed clusters of $\text{Cr}_2\text{O}_2^{-/0}$ with the anion photoelectron spectroscopy technique.^{16,17} As expected, the dichromium dioxide clusters $\text{Cr}_2\text{O}_2^{-/0}$ are very computationally challenging due to strong multiconfigurational insights of this kind of clusters. For studying $\text{Cr}_2\text{O}_2^{-/0}$,

CASSCF/CASPT2 cannot be employed because the number of orbitals in the active space is too large for CASSCF calculations. Hence, the geometry of $\text{Cr}_2\text{O}_2^{-/0}$ was optimized at the RASPT2 level of theory. The Cr_2O_2^- cluster was determined to have close-lying states competing for the ground state. The DMRG-CASPT2 method with a larger active space was employed to clarify the correct ground state and other low-lying states. DFT functionals were also used to locate energetic positions of several close-lying states. Similar to other clusters mentioned above, specific density functionals are expected to give a good description to such strong multireference systems like $\text{Cr}_2\text{O}_2^{-/0}$.

From all of the above results, we can observe that there are always suitable functionals for the treatment of strong multireference systems. Therefore, DFT methods can be used to study clusters containing more transition metal atoms with strong multireference characters. The conclusion here is that we do not know which functionals can correctly describe geometrical and energetic properties of these clusters. However, on the basis of previous studies, some popular functionals were empirically opted for our next studies on larger clusters containing more transition metal atoms.

In the next chapter (Chapter 7), we studied a series of unsaturated chromium oxide clusters Cr_mO_n^+ ($m = 2 - 4$, $n \leq m$). This series of oxide clusters was synthesized and spectroscopically characterized. Infrared multiphoton dissociation spectra measured on the synthesized clusters were then used as reliable references for identification of their geometric and electronic structures. Clearly, we can see that the number of chromium atoms in most unsaturated oxide clusters is larger than 2 except for Cr_2O_2^+ . Multiconfigurational methods cannot be used for all cluster sizes but Cr_2O_2^+ . Therefore, in this series of oxide clusters, various prevalent functionals were employed to simulate IR spectra of these clusters, and additionally, RASSCF/RASPT2 was used for Cr_2O_2^+ as an energetic benchmark for several single-reference methods. The experimentally populated isomers and their electronic structures obtained from DFT calculations, in turn, provided details of magnetic interaction between metallic sites within each cluster and magnetic evolution under addition of oxygen atoms. Insights into magnetic interplay and evolution were also revealed. As mentioned previously, seven functionals were used for two main purposes, which are to confirm DFT results and to choose some of good functionals for other strong multireference oxide clusters of transition metals.

Another series of oxide clusters containing chromium atoms is our final object of this dissertation. The difference of this series from the above chromium oxide clusters is

that new synthesized clusters are bimetallic. Aside from chromium, manganese is the second transition metal incorporated into these clusters. The main purpose of Chapter 8 is to investigate the simultaneous effects of two transition metals on the geometrical structures of chromium-manganese oxide clusters and the roles of metallic types in controlling magnetic properties. To accomplish this, vibrational spectra, that are obtained from infrared multiphoton dissociation spectroscopy, were applied as the basis for DFT geometric assignments of all synthesized clusters. Three good functionals selected from the previous chapter were utilized to simulate IR spectra. From all results obtained, geometrical and magnetic evolution of this series of bimetallic clusters were figured out.

In Chapter 9, the conclusions will briefly summarize all results obtained in this dissertation. On the basis of current works, we propose an outlook for our future research. All chapters from 3 to 8 are main works of this doctoral study and they provide all important data. For all remaining data, each chapter from 3 to 8 has relevant supporting information available online. It should be stressed that this is a study using quantum chemical computations. Experimental results were either taken from literature (PE spectra) or provided by our experimental coworkers, mainly by the group of Prof. Ewald Janssens, Department of Physics KU Leuven, and Prof. Andrei Kirilyuk, Institute of Molecules and Materials, Radboud University Nijmegen, The Netherlands.

References

- (1) Gandeepan, P.; Müller, T.; Zell, D.; Cera, G.; Warratz, S.; Ackermann, L. *Chem. Rev.* **2018**, *119*, 2192–2452.
- (2) Zweig, J. E.; Kim, D. E.; Newhouse, T. R. *Chem. Rev.* **2017**, *117*, 11680–11752.
- (3) Li, X.-W.; Nay, B. *Nat. Prod. Rep.* **2014**, *31*, 533–549.
- (4) Chirik, P.; Morris, R. *Acc. Chem. Res.* **2015**, *48*, 2495–2495.
- (5) Fielicke, A.; Von Helden, G.; Meijer, G. *Eur. Phys. J. D* **2005**, *34*, 83–88.
- (6) Xu, H.-G.; Zhang, Z.-G.; Feng, Y.; Zheng, W. *Chem. Phys. Lett.* **2010**, *498*, 22–26.
- (7) Gong, Y.; Ding, C.; Zhou, M. *J. Phys. Chem. A* **2007**, *111*, 11572–11578.
- (8) Hong-Guang, X.; Miao-Miao, W.; Zeng-Guang, Z.; Qiang, S.; Wei-Jun, Z. *Chin. Phys. B* **2011**, *20*, 043102.

- (9) Wu, H.; Wang, L.-S. *J. Phys. Chem. A* **1998**, *102*, 9129–9135.
- (10) Zhai, H.-J.; Wang, L.-S. *J. Am. Chem. Soc.* **2007**, *129*, 3022–3026.
- (11) Kim, J. B.; Weichman, M. L.; Neumark, D. M. *J. Am. Chem. Soc.* **2014**, *136*, 7159–7168.
- (12) Wang, L.-S.; Wang, X.-B.; Wu, H.; Cheng, H. *J. Am. Chem. Soc.* **1998**, *120*, 6556–6562.
- (13) Atobe, J.; Koyasu, K.; Furuse, S.; Nakajima, A. *Phys. Chem. Chem. Phys.* **2012**, *14*, 9403–9410.
- (14) Wang, X.-B.; Ding, C.-F.; Wang, L.-S. *J. Phys. Chem. A* **1997**, *101*, 7699–7701.
- (15) Deng, X.-J.; Kong, X.-Y.; Xu, X.-L.; Xu, H.-G.; Zheng, W.-J. *RSC Adv.* **2014**, *4*, 25963–25968.
- (16) Tono, K.; Terasaki, A.; Ohta, T.; Kondow, T. *J. Chem. Phys.* **2003**, *119*, 11221–11227.
- (17) Zhai, H.-J.; Wang, L.-S. *J. Chem. Phys.* **2006**, *125*, 164315.

Chapter 2

Experimental and Theoretical Methods

2.1 Experimental Methods

Experimental data on gas phase clusters in this dissertation were obtained from two techniques which are anion photoelectron spectroscopy and infrared multiphoton dissociation spectroscopy. The first technique, anion photoelectron spectroscopy, provides energy needed to remove one electron (usually valence electrons) from gas phase anionic clusters, while the second one probes the infrared active vibration modes of atoms in clusters. The basic ideas behind these techniques are presented in the following subsections.

2.1.1 Anion photoelectron spectroscopy

Photoelectron spectroscopy, historically known as Photoemission spectroscopy, is one of the most important methods used to investigate the electronic structure of molecules, clusters, surfaces, and solids.¹ The earliest experiment, which showed the effect of light on solids, was observed in 1887.¹ This is considered as the starting point of photoemission spectroscopy. Less than two decades later, in 1905, the concepts of photon and its energy

were presented by Einstein. These theories set the ground for experiments in the early 1960s, that led to the modern photoelectron spectroscopy.²⁻⁴ Nowadays, photoelectron spectroscopy is categorized in two main types, X-ray photoelectron spectroscopy (XPS) and ultraviolet photoelectron spectroscopy (UPS). The division is made based on the different wavelengths used in these two methods and their application scope. UPS uses far-ultraviolet radiation with an energy large enough to remove valence electrons, while the higher energy X-ray employed on XPS, which is X-ray with higher energy, can ionize the core.

Since the spectroscopic data referred to in this thesis were measured by UPS, we will briefly introduce this technique. As mentioned above, the energy source of UPS can remove electrons from the valence states of the samples, and hence this method is used to determine the detachment energy of atomic and molecular systems. In a UPS spectrum, there are, normally, several peaks or bands corresponding to specific levels of detachment energies. Those bands are denoted by capital letters such as X, A, B, and C in order of increasing energy levels. Figure 2.1 shows the photoelectron spectrum of Cr_2O_2^- , in which there are five bands noted as X to D and a very low-intensity band X'. Any single band allows for determination of the corresponding energy of ionization or electron detachment.

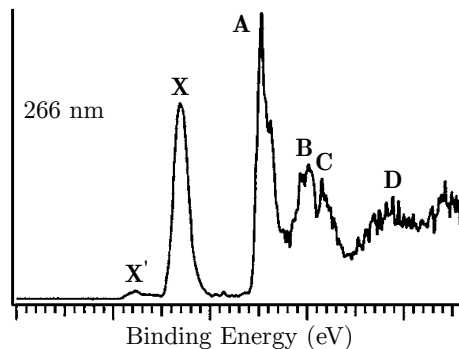


Figure 2.1: The anion photoelectron spectrum of Cr_2O_2^- at 266 nm (reproduced with permission from ref 5, Copyright 2006, AIP Publisher).

The detachment energy (DE) withdrawn from photoelectron spectra, adiabatic detachment energy (ADE) and vertical detachment energy (VDE), is defined as:

$$DE = E_{in} - E_{fi} \quad (2.1)$$

where E_{in} and E_{fi} are the energies of the initial and final states, respectively. From the theoretical aspect, to calculate ADE the geometric structure of the initial state and the final state are both optimized before calculating the energies. In case of VDE, energy of the final state is computed on the basis of the optimized geometry of the initial state. From the experimental perspective, DE can be calculated from the energy difference of laser source and kinetic energy of removed electrons.

$$DE = E_{photon} - E_{kinetic} = h\nu - \frac{1}{2}mv^2 \quad (2.2)$$

where E_{photon} is the energy of laser photons defined as $h\nu$ and $E_{kinetic}$ is the kinetic energy of detachment electrons expanded as $\frac{1}{2}mv^2$. In some situations, the vibrational frequencies of the system in its final state can be extracted from the photoelectron spectra.

The visible bands in photoelectron spectra correspond to transitions with a non-zero transition dipole moment. Equation 2.3 defines the transition dipole moment for a molecule or cluster absorbing a photon

$$\mu = \langle \Psi'' | \hat{\mu} | \Psi' \rangle \quad (2.3)$$

where $\hat{\mu}$ is the dipole operator including the electronic and nuclear dipole operators $\hat{\mu} = \hat{\mu}_{elec} + \hat{\mu}_{nuc}$, and Ψ' and Ψ'' are the total wave functions of the initial and final states, respectively. The total wave function of the initial and final states can be factorized into electronic, vibrational, and rotational parts.

$$\Psi = \psi_e(\mathbf{r}, \mathbf{R}_e) \cdot \psi_v(\mathbf{R}) \cdot \psi_r(\mathbf{R}) \quad (2.4)$$

The vibrational $\psi_v(\mathbf{R})$ and rotational $\psi_r(\mathbf{R})$ parts of Equation 2.4 depend on the coordinates of nuclei (\mathbf{R}), while the electronic part $\psi_e(\mathbf{r}, \mathbf{R}_e)$ depends on electron coordinates (\mathbf{r}) and equilibrium coordinates of nuclei (\mathbf{R}_e) by application of the Born-Oppenheimer approximation.⁶ By placing Equation 2.4 into Equation 2.3, one obtains

$$\begin{aligned}
\mu &= \langle \psi_e''(\mathbf{r}, \mathbf{R}_e) \cdot \psi_v''(\mathbf{R}) \cdot \psi_r''(\mathbf{R}) | \hat{\mu}_{elec} + \hat{\mu}_{nuc} | \psi_e'(\mathbf{r}, \mathbf{R}_e) \cdot \psi_v'(\mathbf{R}) \cdot \psi_r'(\mathbf{R}) \rangle \\
&= \langle \psi_e''(\mathbf{r}, \mathbf{R}_e) | \hat{\mu}_{elec} | \psi_e'(\mathbf{r}, \mathbf{R}_e) \rangle \langle \psi_v''(\mathbf{R}) | \psi_v'(\mathbf{R}) \rangle \langle \psi_r''(\mathbf{R}) | \psi_r'(\mathbf{R}) \rangle \quad (2.5) \\
&\quad + \langle \psi_e''(\mathbf{r}, \mathbf{R}_e) | \psi_e'(\mathbf{r}, \mathbf{R}_e) \rangle \langle \psi_v''(\mathbf{R}) | \hat{\mu}_{nuc} | \psi_v'(\mathbf{R}) \rangle \langle \psi_r''(\mathbf{R}) | \hat{\mu}_{nuc} | \psi_r'(\mathbf{R}) \rangle
\end{aligned}$$

Due to the orthogonality of the electronic wave functions on the initial and final states ($\langle \psi_e''(\mathbf{r}, \mathbf{R}_e) | \psi_e'(\mathbf{r}, \mathbf{R}_e) \rangle = 0$) the transition dipole moment μ becomes

$$\mu = \langle \psi_e''(\mathbf{r}, \mathbf{R}_e) | \hat{\mu}_{elec} | \psi_e'(\mathbf{r}, \mathbf{R}_e) \rangle \langle \psi_v''(\mathbf{R}) | \psi_v'(\mathbf{R}) \rangle \langle \psi_r''(\mathbf{R}) | \psi_r'(\mathbf{R}) \rangle \quad (2.6)$$

Since the rotational part has a negligible effect on UPS spectra, it will not be considered. Therefore, the two remaining parts of Equation 2.6 define electronic and vibrational selection rules for electronic transitions. The transition probability can be written as

$$\mu^2 = |\langle \psi_e''(\mathbf{r}, \mathbf{R}_e) | \hat{\mu}_{elec} | \psi_e'(\mathbf{r}, \mathbf{R}_e) \rangle|^2 |\langle \psi_v''(\mathbf{R}) | \psi_v'(\mathbf{R}) \rangle \langle \psi_r''(\mathbf{R}) | \psi_r'(\mathbf{R}) \rangle|^2 \quad (2.7)$$

From Equation 2.7, the electronic integral (I_e) and the Franck-Condon Factor (FCF) can be defined as

$$I_e = |\langle \psi_e''(\mathbf{r}, \mathbf{R}_e) | \hat{\mu}_{elec} | \psi_e'(\mathbf{r}, \mathbf{R}_e) \rangle|^2 \quad (2.8)$$

$$FCF = |\langle \psi_v''(\mathbf{R}) | \psi_v'(\mathbf{R}) \rangle|^2 \quad (2.9)$$

The $\hat{\mu}_{elec}$ operator in Equation 2.8 is a one-electron operator for photoelectron transitions, and by applying the Slater-Condon rule,⁷ we can prove that I_e is non-zero when the photoionizations involve only one electron, and I_e is not always the same for all electronic transitions. Since one electron is removed in the photoelectron process, the spin-multiplicity difference between the initial and final states is one ($\Delta S \pm 1/2$). For example, if

an electron is removed from a quartet state, the final state will be a triplet or a quintet. In the one-electron detachment process, the arrangement of remaining electrons of the final state is the same as that of the initial state.

Since Equation 2.9 does not include the one-electron operator $\hat{\mu}$, the Franck-Condon Factor can be qualitatively predicted by employing symmetrical properties of the initial and final states' vibrational modes following the Franck-Condon principle. In general, the FCF is zero if a non-totally symmetric integrand is obtained from Equation 2.9. For polyatomic molecules, vibrational modes can be totally symmetric and non-totally symmetric. Concerning the former case, vibrational wave functions are always totally symmetric for all values of the vibrational quantum number v , and therefore the FCF, theoretically, can be non-zero for any transitions between two vibrational wave functions ($\Delta v = 0, \pm 1, \pm 2, \dots$). In contrast, for the case of non-totally symmetric vibrational modes, the vibrational wave function alternates from totally symmetric to non-totally symmetric as the vibrational number v changes from even to odd. Hence, the FCF will be non-zero for $\Delta v = 0, \pm 2, \pm 4, \dots$. In both cases, it is possible to correlate the relative intensities of the peaks within a progression with the overlap (Equation 2.9) between the vibrational wave functions of the involved states (Figure 2.2). Therefore, the transitions responsible for the most intense and sharp peaks of the spectra can be considered as vertical excitations where the motion of nuclei is negligible. The progression or band in photoelectron spectra will be very narrow, or even only one sharp peak if the normal coordinates of the initial and final states are not too much different. On the other hand, photoelectron bands will be broader when normal coordinate displacements between the initial and the final are large. In the cases of transitions involving large changes in normal coordinates, photoelectron bands will vanish from the spectra. In this dissertation, the MolFC program⁸ was used to calculate FCF defined in Equation 2.9.

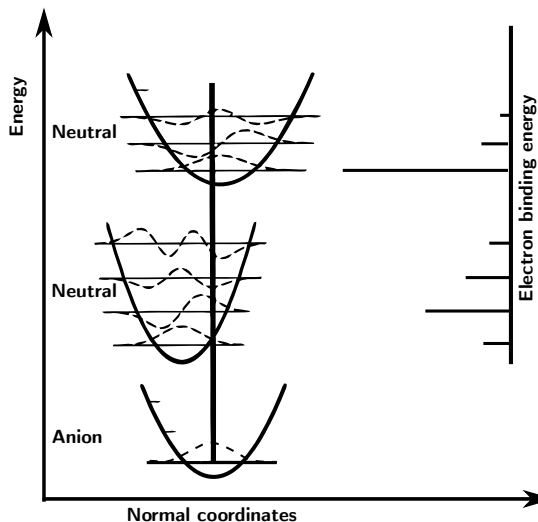


Figure 2.2: Relative intensity of peaks within progressions. This is redrawn on the basis of Figure 7.2 from ref 9.

2.1.2 Infrared Multiphoton Dissociation Spectroscopy

A molecule can be characterized by some primary properties such as molecular masses and chemical bonding (strength, angle, and length). All of these primary features can govern other related chemical and physical properties of a molecule. Vibration of molecules is one of related features governed by abovementioned primary properties. Under resonant absorption of photons, molecules will undergo vibrations and these vibrations are unique for a specific molecular structure. Such vibrations provide a unique fingerprint to identify geometric structures of specific molecules. The signals of these vibrations are recorded in vibrational spectra. Conventionally, vibrational spectra of molecules are measured by direct absorption of photons, and therefore this method is called direct IR spectroscopy. Direct IR spectroscopy has several shortcomings, and one of them is that this technique of IR spectroscopy requires sufficient density of samples. As a result, this technique is usually used for liquid samples. For molecules and clusters in the gas phase, density of samples is much lower than that of samples in the liquid phase. Such low intensity of samples prevents direct IR spectroscopy from application to gas phase clusters. Instead of that, IR action spectroscopy was designed to overcome shortcomings of direct IR spectroscopy.

Infrared multiphoton dissociation (IRMPD) spectroscopy is one of the popular techniques in the family of IR action spectroscopy. This method is size selective and sensitive. This is due to IRMPD spectroscopy combines both mass spectrometry and IR excitation. This is why IRMPD spectroscopy can be used for probing solid-state clusters at low density in the gas phase. Clusters are produced through the vaporization process of target solid samples under irradiation of a vaporization cluster source. After being cooled and expanded into vacuum, the distribution of formed clusters is analyzed by using a time-of-flight (TOF) mass spectrometer. The ion packet is, then, irradiated with the IR laser pulse. When a cluster, so-called the mother cluster, absorbs photons with relevant levels of energy, this cluster or complex of clusters with messenger gases will be fragmented to form the product, namely the daughter cluster. Any change of masses (in the mother and daughter ones) in the cluster beam under IR irradiation is traced to produce the depletion value which is then used to extract the absorption cross section, known as IRMPD signals. An experimental set-up coupled to "Free Electron Laser for Infrared eXperiments" (FELIX) is visualized in Figure 2.3. IRMPD spectra are obtained by scanning the wavelength of the intense IR laser beam. An example of IRMPD spectra is given in Figure 2.4. More details of the IRMPD measurement and technique for specific kinds of clusters are provided in related chapters and ref 10.

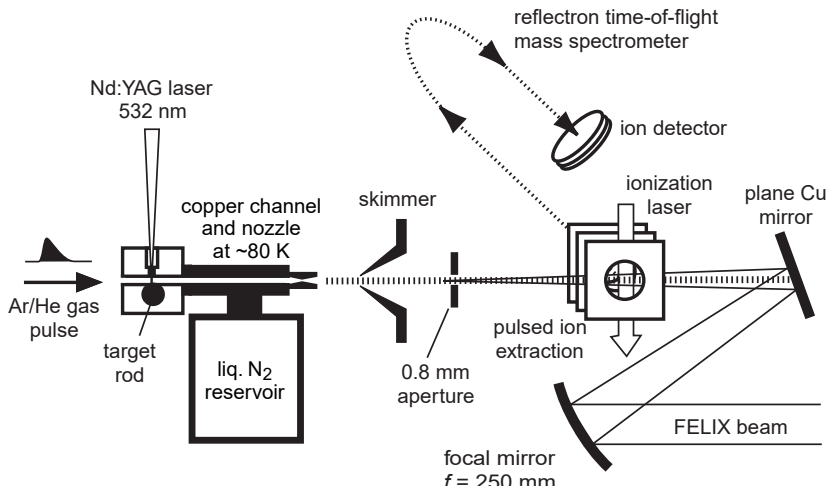


Figure 2.3: Experimental set-up used for IRMPD measurements. This figure is taken from ref 10 with permission from Springer Publishing.

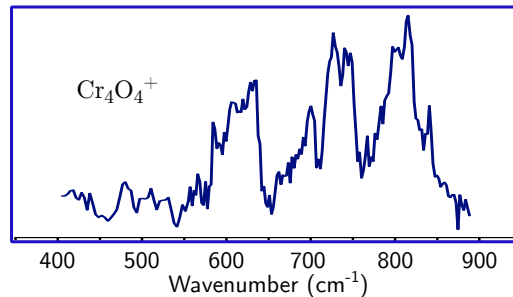


Figure 2.4: IRMPD spectrum of the Cr_4O_4^+ measured on the $\text{Cr}_4\text{O}_4^+\cdot\text{Ne}$ complex (reproduced with permission from ref 11, Copyright 2018, ACS Publisher).

2.2 Computational methods

2.2.1 Schrödinger Equation

In 1926, with motivation from the de Broglie hypothesis about wave-like behaviors of matter, Erwin Schrödinger invented a partial differential equation derived from quantum mechanics describing the state of a physical system changing in time,¹² the so-called Schrödinger equation. For stationary states, systems can be considered to be independent of time; and hence the Schrödinger equation is written as the time-independent form:

$$\hat{H}\Psi(\mathbf{r}, \mathbf{R}) = E\Psi(\mathbf{r}, \mathbf{R}) \quad (2.10)$$

where \hat{H} is the Hamiltonian operator including electronic and nuclear parts of the physical system and E is an eigenvalue of Equation 2.10 corresponding to the energy of the system. \hat{H} is a differential operator acting on $\Psi(r, R)$, that can be formulated as Equation 2.11 in atomic units for a system of M nuclei and N electrons without magnetic or electric fields.

$$\hat{H} = -\frac{1}{2} \sum_{i=1}^N \nabla_i^2 - \frac{1}{2} \sum_{A=1}^M \frac{1}{M_A} \nabla_A^2 - \sum_{i=1}^N \sum_{A=1}^M \frac{Z_A}{r_{iA}} + \sum_{i=1}^N \sum_{j>i}^N \frac{1}{r_{ij}} + \sum_{A=1}^M \sum_{B>A}^M \frac{Z_A Z_B}{R_{AB}} \quad (2.11)$$

Here, i and j run over the electrons, and A and B run over the nuclei. The first two terms in Equation 2.11 describe the kinetic energy of electrons and nuclei, and the Laplace operator $\nabla^2_{..}$ is a sum of differential operators with regard to Cartesian coordinates

$$\nabla^2_{..} = \frac{\partial^2}{\partial x_{..}^2} + \frac{\partial^2}{\partial y_{..}^2} + \frac{\partial^2}{\partial z_{..}^2} \quad (2.12)$$

The three remaining terms in Equation 2.11 define the electron-nuclei attractive interaction, electron-electron potential and repulsive nuclei-nuclei interaction in the quantum system, respectively.

Since electrons are very light and move very fast in comparison to nuclei, the nuclei can be considered as fixed centers following the Born-Oppenheimer approximation.⁶ As a result, the kinetic energy of the nuclei is zero and the repulsive potential due to nuclei-nuclei interaction is constant. Therefore, the only part that needs to be dealt with is the electronic one, so-called electronic Hamiltonian, instead of treating both nuclear and electronic parts in the Hamiltonian.

$$\hat{H}_{elec} = -\frac{1}{2} \sum_{i=1}^N \nabla_i^2 - \sum_{i=1}^N \sum_{A=1}^M \frac{Z_A}{r_{iA}} + \sum_{i=1}^N \sum_{j>i}^N \frac{1}{r_{ij}} = \hat{T}_e + \hat{V}_{Ne} + \hat{V}_{ee} \quad (2.13)$$

Thus, the Schrödinger equation becomes

$$\hat{H}_{elec} \Psi_{elec} = E_{elec} \Psi_{elec} \quad (2.14)$$

The solution of the Schrödinger equation in the Born-Oppenheimer approximation involves the electronic wave function Ψ_{elec} and electronic energy E_{elec} . The total energy of the quantum system is therefore the sum of E_{elec} and the nuclear repulsion term E_{NN} .

$$E_{tot} = E_{elec} + E_{NN} \quad (2.15)$$

2.2.2 Wave functions

The electronic part (shortly noted as $\Psi(\mathbf{r})$) of the wave function in Equation 2.14 is an abstract function. This abstract wave function has no universal form and itself has no physical meaning. However a physical attribute comes from the square modulus of the wave function $|\Psi(\vec{r}_1, \vec{r}_2, \dots, \vec{r}_n)|^2$, which is the probability density of all electrons in positions $\vec{r}_1, \vec{r}_2, \dots, \vec{r}_n$.

To make the Schrödinger equation become practical, one must construct the electronic wave function in a specific form. Obviously, the wave function of a multi-electron system depends on all electrons of the system. Therefore, building up the wave function from all electrons of the system is meaningful. In an attempt to solve the Schrödinger equation, an approach for construction of the wave function was proposed by Hartree with the idea that the wave function could be factorized as a product of one-electron functions,¹³ which means that the motion of an electron is independent of that of other electrons.

$$\Psi(\vec{r}_1, \vec{r}_2, \dots, \vec{r}_n) = \chi_1(\vec{r}_1)\chi_2(\vec{r}_2)\cdots\chi_n(\vec{r}_n) \quad (2.16)$$

The wave function given in Equation 2.16 is known as the Hartree product. However, this factorized wave function does not satisfy the antisymmetry principle. To surmount this issue, Fock introduced a new way to derive the many-particle wave function $\Psi(\vec{r}_1, \vec{r}_2, \dots, \vec{r}_n)$ using a Slater determinant. For a simple closed-shell electronic system, the wave function can be written as

$$\Psi(\vec{r}_1, \vec{r}_2, \dots, \vec{r}_n) = \Phi_{SD} = \frac{1}{\sqrt{N!}} \begin{vmatrix} \chi_1(\vec{r}_1) & \chi_2(\vec{r}_1) & \cdots & \chi_N(\vec{r}_1) \\ \chi_1(\vec{r}_2) & \chi_2(\vec{r}_2) & \cdots & \chi_N(\vec{r}_2) \\ \vdots & \vdots & \ddots & \vdots \\ \chi_1(\vec{r}_N) & \chi_2(\vec{r}_N) & \cdots & \chi_N(\vec{r}_N) \end{vmatrix} \quad (2.17)$$

or in a compact notation where only the diagonal elements are presented

$$\Phi_{SD} = |\chi_1(\vec{r}_1)\chi_2(\vec{r}_2)\cdots\chi_N(\vec{r}_N)| \quad (2.18)$$

The one-electron functions $\chi_i(\vec{r}_i)$ are called *spin orbitals* and are composed of two parts including a spatial orbital ϕ_i and a spin function $\sigma(s)$ ($\alpha(s)$ or $\beta(s)$), where s is the spin coordinate taking two values of $\frac{1}{2}$ and $-\frac{1}{2}$.

$$\chi_i = \phi_i \sigma(s) \quad (2.19)$$

Describing the wave function of an open-shell electronic system is more demanding, as usually they require a linear combination of more than one Slater determinant. Other states of the electronic system, for example excited states, need more sophisticated approaches to reach accurate results.

2.2.3 Hartree-Fock Method

As mentioned above, the Hartree-Fock method considers the electrons to be independent of one another. To be clearer, electrons approximately move in an average electrostatic field arising from all other electrons. By using the Slater determinant for a closed-shell electronic system and applying the variational principle to the Schrödinger equation, the Hartree-Fock equations are obtained as

$$\hat{f}\chi_i = \epsilon_i \chi_i, i = 1, 2, \dots, N \quad (2.20)$$

where ϵ_i are the eigenvalues of the operator \hat{f} . The ϵ_i are related to orbital energies and \hat{f} is the Fock operator defined as

$$\hat{f}_i = -\frac{1}{2} \nabla_i^2 - \sum_A^M \frac{Z_A}{r_{iA}} + \hat{V}_{HF}. \quad (2.21)$$

where V_{HF} can be written in terms of the Coulomb and exchange operators as

$$V_{HF} = \sum_{j=1}^N (2\hat{J}_j - \hat{K}_j) \quad (2.22)$$

where \hat{J}_j and \hat{K}_j are conveniently defined by application to a one-electron wave function

$$\hat{J}_j(1)\chi_i(1) = \left[\int \chi_i^*(2) \frac{1}{r_{12}} \chi_i(2) d\tau_2 \right] \chi_i(1) \quad (2.23)$$

$$\hat{K}_j(1)\chi_i(1) = \left[\int \chi_j^*(2) \frac{1}{r_{12}} \chi_i(2) d\tau_2 \right] \chi_j(1) \quad (2.24)$$

The Hartree-Fock equations 2.20 are solved iteratively. First, a set of guessed functions $(\chi_1, \chi_2, \dots, \chi_n)$ is used to calculate the set of effective potentials V_{HF} . The Hartree-Fock equations are solved to produce a set of improved functions χ_i . These new functions serve to update the effective potentials, which in turn are used to calculate a new improved set of functions χ_i by solving the Hartree-Fock equations again. The cycles of calculations continued until the changes on functions χ_i are negligible. This is the so-called self-consistent field (SCF) method.

2.2.4 Restricted, Restricted Open-shell and Unrestricted wave functions

As mentioned above, electrons have two options of spin functions $\alpha(s)$ or $\beta(s)$. For closed-shell systems, each pair of electrons is treated with the same spatial orbital. This is called the *restricted Hartree-Fock* method (RHF). Most organic compounds and small molecules, for instance water or carbon dioxide, are closed-shell systems. Open-shell electronic states (radicals for example) can be described with an orbital set in which both doubly (by forcing electrons of opposite spin functions in the same spatial orbital) and singly occupied orbitals are used. This is the so-called *restricted open-shell Hartree-Fock* method (ROHF). Finally, the unrestricted Hartree-Fock (UHF) formalism describes each electron with its own spin and spatial function. These differences are illustrated in Figure 2.5.

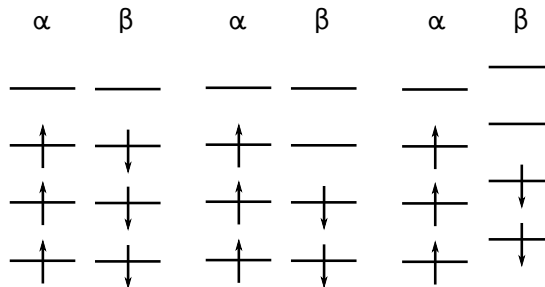


Figure 2.5: Schematic representation of the electronic structure obtained with RHF for a singlet state and ROHF and UHF for a doublet state

2.2.5 Basis Sets

In order to solve the Schrödinger equation by the Hartree-Fock method with Roothan's procedure,¹⁴ a set of basis atomic functions must be employed. Ideally, this set of basis functions should be infinite to obtain the lowest energy of the system for the corresponding wave function. Since it is not possible to work with an infinite set of basis functions, we work with finite basis sets.

Slater introduced in 1930 the so-called Slater type orbitals (STO),¹⁵ which are defined as Equation 2.25 in atom-centered polar coordinates

$$S_{\zeta,n,m,l}(r, \theta, \phi) = N Y_{l,m}(\theta, \phi) r^{n-1} e^{-\zeta r} \quad (2.25)$$

in which N is a normalization constant and $Y_{l,m}$ are spherical harmonic functions that depend on the angular momentum and magnetic quantum numbers l and m . $Y_{l,m}$ functions are quite analogous to angular parts of the hydrogen atom's wave functions gathered from the solution of Schrödinger equation for the hydrogen atom.

Because Slater type atomic orbitals are similar to wave functions of the hydrogen atom, they are a very advantageous basis type to construct molecular orbitals. The STOs have correct exponential change when r (the distance of the electron from the atomic nucleus) increases in comparison to the exact hydrogenic orbitals, and the 1s orbital has a cusp at the nucleus. However, STOs are just suitable for single atoms or relatively small molecules because two-electron integrals with three and four different functions and three- and

four-center cannot be performed analytically but numerically, which negatively affects its evaluation.

In 1960, Boys¹⁶ introduced Gaussian functions in the so-called Gaussian type orbitals (GTOs) for the first time, which can be written in polar coordinates as

$$G_{\zeta,n,m,l}(r,\theta,\phi) = NY_{l,m}(\theta,\phi)r^{2n-2-l}e^{-\zeta r^2}. \quad (2.26)$$

Basis functions G_s can be primitive Gaussian functions or linear combination of primitive Gaussian functions to mimic STOs, namely *contracted* Gaussian functions.

$$\varphi = \sum_1^u c_u G_u \quad (2.27)$$

where c_u are contraction coefficients. The set of primitive or contracted functions forms a Gaussian basis set. Combinations of Gaussian primitives are able to approximate correct nodal properties of atomic orbitals and to describe the orbitals for atoms and molecules. However, contracted Gaussian functions have a zero slope at the nucleus, which is, consequently, a drawback of GTOs in representing the proper behaviour near the nucleus vis-à-vis STOs.

Nowadays, an abundance of basis sets composed of GTOs are widely used in modern quantum packages. Each type of basis sets was designed for a specific element or computational method. Typical basis sets widely used are those of Pople (3-21G, 6-31G, 6-311G,...), Ahlrichs (def2-SVP, def2-TZVP, and def2-QZVP), Dunning (cc-PVnZ), and atomic natural orbitals (ANO) basis sets.

2.2.6 Post Hartree-Fock Methods

Correlation Energy

Since the Hartree-Fock method uses one Slater determinant, it lacks electron correlation, which is an effect that stems from electron-electron interaction. It is only about 1% of the system total energy, but this amount is crucial for explaining or estimating properties

of correlated quantum systems. The electron correlation energy (E_{corr}) can be defined as the difference between the exact energy (E_{exact}) and the energy calculated by the HF methods (E_{HF}).

$$E_{corr} = E_{exact} - E_{HF} \quad (2.28)$$

Correlation energy E_{corr} can be abstractly divided into two types, namely static and dynamic correlation. Static energy is known as the difference in energy between wave functions represented by a single Slater determinant (SD) and a linear combination of SDs. In many situations, a single SD cannot be used to represent the wave function of a system such as bond dissociation, excited states, and transition-metal compounds. Dynamic correlation energy is caused by instantaneous interaction among electrons. Recovering the E_{corr} contribution is a difficult task that led to the development of sophisticated wave function based methods, or the so-called post Hartree-Fock methods.

Configuration Interaction (CI)

The CI method¹⁷ expands the Hartree-Fock wave function, which uses a single Slater determinant, with an arbitrary number of determinants that form a linear combination of n-electron wave function configurations.

$$\Psi_{CI} = a_0\Phi_{HF} + \sum a_S\Phi_S + \sum a_D\Phi_D + \sum a_T\Phi_T + \dots = \sum a_i\Phi_i \quad (2.29)$$

The Hartree-Fock wave function is expanded with Slater determinants for electronic configurations arising from excitations of one, two or more electron(s) from occupied orbital(s) to unoccupied one(s). These excited electronic configurations are often referred to as *Singles* (S), *Doubles* (D), *Triples* (T), *Quadruples* (Q), etc. and visualized in Figure 2.6.

Replacing CI wave functions described by Equation 2.29 into Equation 2.14 and solving the resulting equation will recover some amount of E_{corr} . Nonetheless, the number of excited configurations becomes very high very fast, and it is infinite with a complete set of basis functions. Therefore, its solution becomes practically impossible when the linear

MO				
8	—	— —	— — — +	— — + +
7	—	— —	— + —	— + + —
6	+ —	— —	— + + —	— + + + +
5	— +	+ + —	— + + +	+ + — + +
4	+ +	+ + —	— + + + +	— + + + +
3	+ +	+ + +	+ + — + +	+ — + + +
2	+ +	+ + +	+ + + + +	+ + + + +
1	+ +	+ + +	+ + + + +	+ + + + +
ψ_{HF}	Singles	Doubles	Doubles	Triples

Figure 2.6: Possible configurations of first three excited states generated from a Hartree-Fock single configuration.

combination Equation 2.29 involves numerous excited determinants. Hence, in practice CI methods are implemented at limited amount of excitations. For instance, a common approach is the so-called CISD method that only includes single and double excitations.

$$\Psi_{CI} = a_0 \Phi_{HF} + a_S \Phi_S + a_D \Phi_D \quad (2.30)$$

Other levels of accuracy can be considered and added to Equation 2.30 to meet the demand if it is necessary.

Perturbation Theory

In perturbation theory, a reference Hamiltonian \hat{H}^0 is improved by applying a perturbation operator $\lambda \hat{H}'$ as in Equation 2.31.

$$\hat{H} = \hat{H}^0 + \lambda \hat{H}' \quad (2.31)$$

where λ varies from 0 to 1. If eigenvectors and eigenvalues of the reference operator \hat{H}^0 are known and the contribution of \hat{H}' is small in comparison to \hat{H}^0 , we can find the eigenvectors of the full operator as an expansion of the eigenvectors of \hat{H}^0 and the corrected eigenvalues of the system. To be more specific, the first-order and second-order

corrections to the energy are given by Equation 2.32 and 2.33.

$$E_n^{(1)} = \left\langle \Psi_n^{(0)} | H' | \Psi_n^{(0)} \right\rangle \quad (2.32)$$

$$E_n^{(2)} = \sum_{m \neq n} \frac{\left| \left\langle \Psi_m^{(0)} | H' | \Psi_n^{(0)} \right\rangle \right|^2}{E_n^{(0)} - E_m^{(0)}} \quad (2.33)$$

Møller and Plesset applied perturbation theory to quantum systems by adding the perturbation operator to the Hartree-Fock Hamiltonian.¹⁸ As a result, this will generate n-order corrections to the HF wave function and energy. The levels of Møller-Plesset (MP) perturbation theory are denoted as MPn (n = 0, 1, 2, · · ·). MP0 corresponds to the sum of all the Hartree-Fock one-electron energies, and MP1 is the HF level of energy (MP0 plus coulomb and exchange integral energy). We can write $E_{MP1} = E_{total}^{HF} = E_{MP0} + E^{(1)}$. MP2 is the first corrected level beyond the Hartree-Fock method:

$$E_{MP2} = E_{total}^{HF} + E^{(2)} \quad (2.34)$$

Coupled-Cluster Theory

Coupled-cluster theory was developed in 1966¹⁹ and this is, notably, one of the most accurate methods for electron correlation energies of quantum systems. CC theory describes the wave function as

$$\Psi = e^{\hat{T}} \Psi_{HF} \quad (2.35)$$

where $e^{\hat{T}}$ is the exponential cluster operator defined as

$$e^{\hat{T}} = 1 + \hat{T} + \frac{\hat{T}^2}{2!} + \frac{\hat{T}^3}{3!} + \dots + \frac{\hat{T}^k}{k!} \quad (k = \infty) \quad (2.36)$$

and \hat{T} is the summation of operators $\hat{T}_1, \hat{T}_2, \dots, \hat{T}_N$

$$\hat{T} = \hat{T}_1 + \hat{T}_2 + \dots + \hat{T}_N \quad (2.37)$$

Each \hat{T}_i acts on the HF wave function to create all possible i-electron excited states from the ground-state wave function, for example

$$\hat{T}_2 \Psi_{HF} = \sum_{ij}^{\text{occ}} \sum_{ab}^{\text{vir}} t_{ij}^{ab} \psi_{ij}^{ab} \quad (2.38)$$

in which ij and ab are the numbers indicating occupied and virtual orbitals in molecules respectively. If the approximation is selected as $\hat{T} = \hat{T}_2$, we have the CCD (coupled-cluster doubles) method. Substituting $\hat{T} = \hat{T}_2$ into Equation 2.36 brings the formula for the CCD wave function

$$\Psi_{CCD} = e^{\hat{T}_2} \Psi_{HF} = \left(1 + \hat{T}_2 + \frac{\hat{T}_2^2}{2!} + \frac{\hat{T}_2^3}{3!} + \dots + \frac{\hat{T}_2^k}{k!} \right) \Psi_{HF}. \quad (2.39)$$

Note that if both \hat{T}_1 and \hat{T}_2 are included in the \hat{T} operator, this is called the CCSD (coupled-cluster singles and doubles) method, a widely-used coupled-cluster approach. Combination of \hat{T}_3 , namely CCSDT, requires high computational costs, but it is possible to treat its effects by perturbation theory. The resulting method CCSD(T) is robust and very accurate for single reference calculations although the triples correction is slightly overestimated.

Multiconfiguration Self-consistent Field Theory

Multiconfiguration self-consistent field (MCSCF) is a method based on the CI method mentioned above. In this method, the Hartree-Fock wave function is expanded as a linear combination of Slater determinants including excited electronic configurations.^{20,21} The difference between MCSCF and CI methods is that MCSCF optimizes both determinant coefficients c_i (Equation 2.40) and the MOs used for construction of the determinants

simultaneously.

$$\Psi = c_0 \Phi_0 + \sum c_S \Phi_S + \sum c_D \Phi_D + \sum c_T \Phi_T + \dots = \sum c_i \Phi_i \quad (2.40)$$

Therefore, the MCSCF wave function is more flexible in comparison to the HF wave function. The first improvement is to treat the so-called static electron correlation, which stems from multi-configurational systems with energetically degenerate states. Unfortunately, the MCSCF method is computationally expensive and rapidly increases its cost due to huge numbers of configurations, and thus it is difficult to expand Equation 2.40.

Moreover, MCSCF is not size-extensive which hinders its application to systems of chemical interest. Hence, the CASSCF method,^{22,23} which is a size-extensive MCSCF approach where the selection of the configurations is based on the partitioning of the molecular orbitals into *inactive*, *active* and *virtual* spaces. Inactive orbitals are always fully occupied with two electrons, while virtual orbitals are unoccupied. The remaining electrons are flexibly distributed in the active space taking into account all possible configurations. The decision on which orbitals to include in the active space requires chemical insight and is crucial to obtain an accurate description of the problem at hand.

For large systems, usually the employment of bigger active spaces is necessary; however, the number of electronic configurations in CASSCF raises very sharply. To include more orbitals in active spaces and reduce as much as possible determinants in the expansion of CASSCF wave functions, a variant of CASSCF in terms of configuration choice has been introduced, so-called the *Restricted Active Space Self-Consistent Field* (RASSCF) method.^{24,25} The key idea of the RASSCF method is to separate active spaces into three subspaces (RAS1, RAS2, RAS3) with distinguished occupation restrictions for each one. In a typical calculation model, a full CI generating the configurations or limitation to SDTQ excitations for RAS2 subspaces is applied, while RAS1 and RAS3 are relatively contrary to each other, rather doubly occupied and unoccupied MOs for RAS1 and RAS3 with exception of a maximum number of holes and allowed electrons in these subspaces, respectively. Figure 2.7 depicts the detailed schemes for CASSCF and RASSCF.

CASSCF and RASSCF methods can treat static correlation but does not include the so-called, dynamical correlation, which arises from the movements of individual electrons

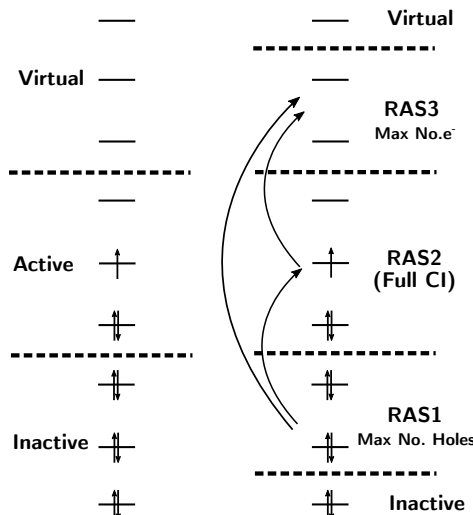


Figure 2.7: The schemes for electron distribution in the CASSCF and RASSCF methods

to avoid each other. Second-order perturbation theory is widely employed for this purpose which applies second-order perturbation on the top of the CASSCF and RASSCF Hamiltonian. Depending on specific types of Hamiltonian, the perturbation methods are named as CASPT2^{26,27} and RASPT2.²⁸ Since these two methods are capable of recovering most correlation energy, they have been applied to several systems, especially clusters containing transition metals. Note that because the results obtained from CASPT2 were found to be underestimated (0.13 to 0.28 eV, so-called error bars in the next chapters) for atomization energies,²⁹ an IPEA shift³⁰ of 0.25 a.u was proposed. We used this standard IPEA shift for all CASPT2 calculations in this dissertation. We also note that, in this thesis, multistate CASPT2 was employed on the basis of state-averaged CASSCF states for all higher-energy roots. Another way to recover dynamic correlation energy is to use the configuration interaction technique, resulting in multireference configuration interaction (MRCI). Instead of using an SCF wave function as reference, a reference space consisting multiple electronic configurations is used. The MRCI wave function is then constructed by exciting a specific number of electrons from all configurations in the reference space. In practical application, the common levels of excitation is singles and doubles, resulting in the multireference singles and doubles configuration interaction (MRSDCI), and the reference space of configurations is taken from CASSCF wave functions.

2.2.7 Density matrix renormalization group

Density matrix renormalization group (DMRG) algorithm is a numerical algorithm attracting attention from theoretical chemists and physicists due to its potential capability to tackle strongly correlated systems.³¹⁻³⁷ In the two-site DMRG algorithm, molecular orbitals in the active space can be represented as sites and form a superblock which is divided into two blocks, the left and right ones. There are also two sites inserted in between two blocks. Since there are four possible states ($|\uparrow\downarrow\rangle, |\uparrow\rangle, |\downarrow\rangle, |0\rangle$) that each spatial orbital can have, the total number of states for the left and right blocks are 4^{n_L} and 4^{n_R} , and 4^2 for two sites in the middle of the superblock, where n_L and n_R are the total number of correlated sites in the left and right blocks, respectively. Note that the total number of sites is $L = n_L + n_R + 2$. The superblock wave function can be constructed as a tensor product of all block states.

$$|\Psi\rangle = \sum_{\alpha_L \sigma_L \sigma_R \alpha_R} |\alpha_L\rangle \otimes |\sigma_L\rangle \otimes |\sigma_R\rangle \otimes |\alpha_R\rangle = \sum_{i_L i_R} |i_L\rangle \otimes |i_R\rangle \quad (2.41)$$

Each block state in Equation 2.41 can be represented as a matrix product state (MPS).³⁸⁻⁴⁰ DMRG energy of the system is variationally optimized by using a sweep algorithm.

In theory, the DMRG method can be understood as an approximation to the full configuration interaction (FCI) formalism. In the configuration interaction (CI) method, the electronic wave function is expanded in the determinantal space consisting of all possible electronic configurations starting from a reference one. The contribution of each configuration to the total electronic wave function can be recognized through its CI coefficients C_σ as follows,

$$|\Psi\rangle = \sum_{\sigma} C_{\sigma} |\sigma\rangle = \sum_{\sigma} C_{\sigma} |\sigma_1 \dots \sigma_L\rangle \quad (2.42)$$

where $\sigma_l = |\uparrow\downarrow\rangle, |\uparrow\rangle, |\downarrow\rangle, |0\rangle$ corresponding to four basis states is occupancy of the spatial orbital l th in the system. The CI coefficients C_{σ} can be exactly decomposed by using successive single value decompositions (SVDs) and then explicitly expressed as a product of L matrices M^{σ_i} . The FCI wave function can be written as

$$|\Psi\rangle = \sum_{\sigma} M^{\sigma_1} M^{\sigma_2} \dots M^{\sigma_L} |\sigma_1 \dots \sigma_L\rangle. \quad (2.43)$$

Note that the first and last matrices in Equation 2.43 have dimensions of $1 \times m_1$ and $m_{L-1} \times 1$, respectively, and all remaining matrices are $m_{l-1} \times m_l$ -dimensional matrices. Equation 2.43 is the wave function described in the language of MPS. The maximal dimensional value of these matrices is $O(4^{L/2})$.^{41,42} At the maximal level of matrix dimensions, there will be no approximation and the wave function in Equation 2.43 becomes exact. However, with this MPS representation of wave functions this method can be applied to small systems that the FCI method can handle.⁴³ As a result, there is no computational advantage obtained from the new MPS forms of wave functions in comparison to the FCI method. Therefore, to reduce the exponential scaling of the FCI method to a polynomial scaling of the MPS wave function method, the maximal dimension of the matrices M^{σ_i} is limited to m .⁴⁴ In this way, the size of all matrices M^{σ_i} are truncated, and the accuracy of MPS wave functions are totally controlled through a single parameter m , known as the number of renormalized block states. In practice, the value of m within the range of 1000 – 10000 can produce enough chemical accuracy.⁴⁵

The DMRG algorithm in combination with MPS can treat strongly correlated system with around 50 orbitals in the active space. However, the DMRG method cannot efficiently recover dynamic correlation energy. Dynamic correlation energy can be treated by perturbation theory (DMRG-CASPT2^{46,47} or DMRG-NEVPT2^{48,49}), configuration interaction (DMRG-MRCI), and the canonical transformation theory (DMRG-CT).^{50,51}

2.2.8 Density Functional Methods

Electronic wave functions are relatively complicated due to the number of variables to treat, including the spatial and spin coordinates of every electron. A different concept, so-called the density functional theory (DFT),⁵² was proposed originally in order to decrease the inherent complication in describing electronic wave functions by using the electron density instead. The electron density $\rho(\mathbf{r})$ is only dependent on three coordinate variables in space. More importantly, the energy of a system can be related directly to $\rho(\mathbf{r})$ ⁵³ by the following relationship

$$E[\rho(\mathbf{r})] = E_{elec} \quad (2.44)$$

$E[\rho(\mathbf{r})]$ is a functional taking the density function $\rho(\mathbf{r})$ as its argument and E_{elec} is the electronic energy. However, the exact expression of $E[\rho(\mathbf{r})]$ is not known and there are no systematic methods proposed to obtain the exact energy from electron density. The approximation to $E[\rho(\mathbf{r})]$ of the ground state, as it is formulated in Kohn-Sham theory,⁵⁴ is written as

$$E[\rho(\mathbf{r})] = T_e[\rho(\mathbf{r})] + V_{ne}[\rho(\mathbf{r})] + V_{ee}[\rho(\mathbf{r})] + V_{xe}[\rho(\mathbf{r})] \quad (2.45)$$

where the terms on the right hand side are, respectively, the kinetic energy of the non-interacting electrons, the nuclear-electron attraction, the classical electron-electron repulsion, and the *exchange-correlation* functional accounting for all remaining non-classical corrections. Three of the four functionals in Equation 2.45 are exactly known. The first one is given in an explicit formulation in terms of the Kohn-Sham orbital set $\{\phi_i\}$.

$$T_e[\rho(\mathbf{r})] = \sum_i \left\langle \phi_i \left| -\frac{1}{2} \nabla^2 \right| \phi_i \right\rangle \quad (2.46)$$

The second one is expressed as

$$V_{ne}[\rho(\mathbf{r})] = - \int \sum_N \frac{Z_N}{|\mathbf{r} - \mathbf{R}_N|} \rho(\mathbf{r}) d\mathbf{r} \quad (2.47)$$

and the classical electron-electron repulsion energy is

$$V_{ee}[\rho(\mathbf{r})] = \frac{1}{2} \int \int \frac{\rho(\mathbf{r}_1)\rho(\mathbf{r}_2)}{|\mathbf{r}_1 - \mathbf{r}_2|} d\mathbf{r}_1 d\mathbf{r}_2 \quad (2.48)$$

Theoretically, once the exact exchange-correlation functional is known, the Kohn-Sham DFT becomes an exact theory. However, an exact exchange-correlation is still unknown

and may be unknowable.⁵⁵

All developments in DFT hitherto are to find good functionals to approximate the universal functional. There are various levels of approximation to the exact functional according to Jacob's ladder.⁵⁶ The lowest rung in Jacob's ladder is Local Density Approximation (LDA). At this level, the exchange-correlation energy ($V_{xe}[\rho(\mathbf{r})] = E_{XC}$) is defined as a function of electron density,

$$E_{XC} = \int F(\rho(\mathbf{r}))d\mathbf{r}. \quad (2.49)$$

General Gradient Approximation (GGA) is the second lowest rung where the exchange-correlation energy is formulated as a function of both electron density and its gradients (the first derivative of electron density),

$$E_{XC} = \int F(\rho(\mathbf{r}), \nabla\rho(\mathbf{r}))d\mathbf{r}. \quad (2.50)$$

Higher order derivatives of electron density and/or the orbital kinetic energy density can be included in the exchange-correlation functional. The obtained functionals are categorized into meta-GGA with the following general form,

$$E_{XC} = \int F(\rho(\mathbf{r}), \nabla\rho(\mathbf{r}), \nabla^2\rho(\mathbf{r}), \tau(\mathbf{r}))d\mathbf{r}, \quad (2.51)$$

where $\tau(\mathbf{r})$ is the orbital kinetic energy density:

$$\tau(\mathbf{r}) = \frac{1}{2} \sum_i^{occ} |\nabla\phi_i|^2. \quad (2.52)$$

The fourth rung in Jacob's ladder is hybrid functionals. Hybrid functionals are basically GGA functionals with inclusion of a fraction of Hartree–Fock exchange.

$$E_{XC} = \int F(\rho(\mathbf{r}), \nabla\rho(\mathbf{r}))d\mathbf{r} + aE_X^{HF} \quad (2.53)$$

Double hybrid functionals are considered as the highest rung of Jacob's ladder. Double hybrid functionals take into account virtual Kohn-Sham orbital contribution under the form of perturbative second-order correlation making use of DFT orbitals and orbital energies.^{57,58}

$$E_{XC}^{DHDFT} = (1 - a_X)E_X^{DFT} + a_X E_X^{HF} + (1 - a_C)E_C^{DFT} + a_C E_C^{PT2} \quad (2.54)$$

where E_X^{DFT} , E_X^{HF} , E_C^{DFT} , and E_C^{PT2} are the DFT exchange, HF exchange, DFT correlation, and second-order perturbative energy, respectively.

Nowadays, there are many functionals developed, but none of these exchange-correlation functionals can be applied as the universal functional for all chemical systems. Nevertheless, among the developed functionals, some of them are widely-used and common in computational chemistry for instance PW91, BP86, TPSS, TPSSh, B3LYP, B3P86, CAM-B3LYP, M06, M06-2X, B2PLYP, and PBE0-DH.

References

- (1) Reinert, F.; Hüfner, S. *New J. Phys.* **2005**, *7*, 97.
- (2) Spicer, W. E.; Berglund, C. N. *Phys. Rev. Lett.* **1964**, *12*, 9–11.
- (3) Berglund, C. N.; Spicer, W. *Phys. Rev.* **1964**, *136*, A1030.
- (4) Turner, D. W.; Jobory, M. I. A. *J. Chem. Phys.* **1962**, *37*, 3007–3008.
- (5) Zhai, H.-J.; Wang, L.-S. *J. Chem. Phys.* **2006**, *125*, 164315.
- (6) Born, M.; Oppenheimer, R. *Ann. Phys.* **1927**, *389*, 457–484.
- (7) Piela, L. In; Elsevier: 2014, e109–e120.
- (8) Raffaele, B.; Amedeo, C.; Andrea, P. *Can. J. Chem.* **2013**, *91*, 495–504.
- (9) Ellis, A. M.; Feher, M.; Wright, T. G., *Electronic and photoelectron spectroscopy: fundamentals and case studies*; Cambridge University Press: 2005.
- (10) Fielicke, A.; Von Helden, G.; Meijer, G. *Eur. Phys. J. D* **2005**, *34*, 83–88.

- (11) Pham, L. N.; Claes, P.; Lievens, P.; Jiang, L.; Wende, T.; Asmis, K. R.; Nguyen, M. T.; Janssens, E. *J. Phys. Chem. C* **2018**, *122*, 27640–27647.
- (12) Schrödinger, E. *Phys. Rev.* **1926**, *28*, 1049–1070.
- (13) Szabo, A.; Ostlund, N. S., *Modern quantum chemistry: introduction to advanced electronic structure theory*; Dover Publications: Mineola, N.Y, 1996, p 466.
- (14) Lewars, E. G., *Computational chemistry: introduction to the theory and applications of molecular and quantum mechanics*, 2. ed; Springer: Dordrecht, 2011, p 664.
- (15) Slater, J. C. *Phys. Rev.* **1930**, *36*, 57.
- (16) Boys, S. F. In *Proceedings of the Royal Society of London A: Mathematical, Physical and Engineering Sciences*, 1950; Vol. 200, pp 542–554.
- (17) Sherrill, C. D.; Schaefer, H. F. *Adv. Quantum Chem.* **1999**, *34*, 143–269.
- (18) Møller, C.; Plesset, M. S. *Phys. Rev.* **1934**, *46*, 618.
- (19) Čížek, J. *J. Chem. Phys.* **1966**, *45*, 4256–4266.
- (20) Shepard, R. *Ab Initio Methods in Quantum Chemistry-II* **1987**, 63–200.
- (21) Szalay, P. G.; Müller, T.; Gidofalvi, G.; Lischka, H.; Shepard, R. *Chem. Rev.* **2011**, *112*, 108–181.
- (22) Roos, B. O.; Taylor, P. R.; Si, P. E., et al. *Chem. Phys.* **1980**, *48*, 157–173.
- (23) Roos, B. O. *Advances in Chemical Physics: Ab Initio Methods in Quantum Chemistry Part 2, Volume 69* **1987**, 399–445.
- (24) Olsen, J.; Roos, B. O.; Jo, P.; Jo, H., et al. *J. Chem. Phys.* **1988**, *89*, 2185–2192.
- (25) Malmqvist, P. A.; Rendell, A.; Roos, B. O. *J. Phys. Chem.* **1990**, *94*, 5477–5482.
- (26) Andersson, K.; Malmqvist, P.-Å.; Roos, B. O. *J. Chem. Phys.* **1992**, *96*, 1218–1226.
- (27) Andersson, K.; Malmqvist, P. A.; Roos, B. O.; Sadlej, A. J.; Wolinski, K. *J. Phys. Chem.* **1990**, *94*, 5483–5488.
- (28) Malmqvist, P. Å.; Pierloot, K.; Shahi, A. R. M.; Cramer, C. J.; Gagliardi, L. *J. Chem. Phys.* **2008**, *128*, 204109.
- (29) Andersson, K.; Roos, B. O. *Int. J. Quantum Chem.* **1993**, *45*, 591–607.
- (30) Ghigo, G.; Roos, B. O.; Malmqvist, P.-Å. *Chem. Phys. Lett.* **2004**, *396*, 142–149.
- (31) Mizukami, W.; Kurashige, Y.; Yanai, T. *J. Chem. Theory Comput.* **2012**, *9*, 401–407.

- (32) Yanai, T.; Kurashige, Y.; Mizukami, W.; Chalupský, J.; Lan, T. N.; Saitow, M. *Int. J. Quantum Chem.* **2015**, *115*, 283–299.
- (33) Liu, F.; Kurashige, Y.; Yanai, T.; Morokuma, K. *J. Chem. Theory Comput.* **2013**, *9*, 4462–4469.
- (34) Kurashige, Y.; Yanai, T. *J. Chem. Phys.* **2009**, *130*, 234114.
- (35) Kurashige, Y.; Chan, G. K.-L.; Yanai, T. *Nat. Chem.* **2013**, *5*, 660.
- (36) Ma, Y.; Knecht, S.; Keller, S.; Reiher, M. *J. Chem. Theory Comput.* **2017**, *13*, 2533–2549.
- (37) Phung, Q. M.; Wouters, S.; Pierloot, K. *J. Chem. Theory Comput.* **2016**, *12*, 4352–4361.
- (38) Schollwöck, U. *Ann. Phys.* **2011**, *326*, 96–192.
- (39) Wouters, S.; Limacher, P. A.; Van Neck, D.; Ayers, P. W. *J. Chem. Phys.* **2012**, *136*, 134110.
- (40) Lischka, H.; Nachtigallova, D.; Aquino, A. J.; Szalay, P. G.; Plasser, F.; Machado, F. B.; Barbatti, M. *Chem. Rev.* **2018**, *118*, 7293–7361.
- (41) Schollwöck, U. *Ann. Phys.* **2011**, *326*, 96–192.
- (42) Nakatani, N.; Guo, S. *J. Chem. Phys.* **2017**, *146*, 094102.
- (43) Moritz, G.; Reiher, M. *J. Chem. Phys.* **2007**, *126*, 244109.
- (44) White, S. R. *Phys. Rev. B* **1993**, *48*, 10345.
- (45) Olivares-Amaya, R.; Hu, W.; Nakatani, N.; Sharma, S.; Yang, J.; Chan, G. K.-L. *J. Chem. Phys.* **2015**, *142*, 034102.
- (46) Kurashige, Y.; Yanai, T. *J. Chem. Phys.* **2011**, *135*, 094104.
- (47) Kurashige, Y.; Chalupský, J.; Lan, T. N.; Yanai, T. *J. Chem. Phys.* **2014**, *141*, 174111.
- (48) Guo, S.; Watson, M. A.; Hu, W.; Sun, Q.; Chan, G. K.-L. *J. Chem. Theory Comput.* **2016**, *12*, 1583–1591.
- (49) Freitag, L.; Knecht, S.; Angeli, C.; Reiher, M. *J. Chem. Theory Comput.* **2017**, *13*, 451–459.
- (50) Yanai, T.; Kurashige, Y.; Neuscamman, E.; Chan, G. K.-L. *J. Chem. Phys.* **2010**, *132*, 024105.
- (51) Yanai, T.; Kurashige, Y.; Neuscamman, E.; Chan, G. K.-L. *Phys. Chem. Chem. Phys.* **2012**, *14*, 7809–7820.
- (52) Kohn, W.; Becke, A. D.; Parr, R. G. *J. Phys. Chem.* **1996**, *100*, 12974–12980.

- (53) Hohenberg, P.; Kohn, W. *Phys. Rev.* **1964**, *136*, B864.
- (54) Kohn, W.; Sham, L. J. *Phys. Rev.* **1965**, *140*, A1133.
- (55) Schuch, N.; Verstraete, F. *Nat. Phys.* **2009**, *5*, 732.
- (56) Perdew, J. P.; Ruzsinszky, A.; Tao, J.; Staroverov, V. N.; Scuseria, G. E.; Csonka, G. I. *J. Chem. Phys.* **2005**, *123*, 062201.
- (57) Grimme, S.; Neese, F. *J. Chem. Phys.* **2007**, *127*, 154116.
- (58) Goerigk, L.; Grimme, S. *Wiley Interdiscip. Rev.: Comput. Mol. Sci.* **2014**, *4*, 576–600.

Chapter 3

Electronic Structure of Neutral and Anionic Scandium Disilicon $\text{ScSi}_2^{-/0}$ Clusters

This chapter is based on the paper:

Pham, L. N.; Nguyen, M. T. Electronic Structure of Neutral and Anionic Scandium Disilicon $\text{ScSi}_2^{-/0}$ Clusters and the Related Anion Photoelectron Spectrum. *J. Phys. Chem. A* **2016**, 120, 9401–9410. *Reprinted with permission from Journal of Physical Chemistry A. Copyright 2016. American Chemical Society. The Supporting Information is available online.*

My contribution to this work was theoretical calculations, data analysis, discussion, writing of the first draft and revision.

3.1 Introduction

Silicon is one of the most used elements in the modern industry, because it, in different forms, has been applied in a diversity of domains, especially in electronic devices. Several additional interesting improvements and features such as higher stability,^{1–5} larger HOMO-LUMO gaps,⁶ magnetic moments,⁷ and optical properties⁸ can be obtained by doping pristine silicon structures with transition metals (TMs). Therefore, silicon clusters doped with TMs have extensively been studied both experimentally and theoretically. Of the list of 3d-block metals, scandium is known to be the simplest metal, and it can form stable structures with silicon clusters through strong interaction between its 3d orbitals and silicon orbitals.^{9,10}

Photoelectron (PE) spectroscopy is an efficient tool in determination of electronic structures of complexes and clusters.¹¹ In anion PE spectroscopy, under photon laser beams with high enough energy, electrons are removed from an anion, and in turn neutral clusters are generated. The characteristic signals of removed electrons can thus be recorded in anion PE spectra. From these spectra, the electronic structure of the neutral clusters can be revealed on the basis of ionization energies. For silicon clusters containing scandium impurities, various PE spectra of different sizes and shapes were recorded.^{12–15} Typically, two series of scandium-doped silicon clusters were reported,^{14,15} which included the smallest sizes of silicon clusters containing one and two scandium atoms. In the first series,¹⁴ the anionic ScSi_n^- with $n = 1 – 6$ clusters were synthesized and photodetached at two levels of photon energies of 193 and 266 nm. The same procedure was used for the second series of doubly doped Sc_2Si_n^- also with $n = 1 – 6$.¹⁵ In combination with quantum chemical calculations (mainly density functional theory), the geometrical and electronic structures of the measured clusters were predicted, on the basis of the first adiabatic and vertical detachment energies of the anionic clusters. More recently, three higher levels of theory including the ccCA-TM, G4, and G4(MP2) were used to investigate the electronic structure and ionization energies of $\text{ScSi}_n^{-/0}$ ($n = 1 – 6$).¹⁶ Basically, the computed geometrical structures of both anionic and neutral clusters were proved to be consistent with previous publications,^{9,14} but some inconsistencies persist in the determination of the true ground electronic states of the species considered.

From the experimental anion photoelectron spectra, higher-lying electronic structures corresponding to the bands with higher ionization energies in the spectra can also be identified, and it usually needs more effort to fully understand such excited electronic states.

One of the simple choices for interpreting the anion PE spectra is to use time dependent density functional theory (TDDFT) calculations, and such calculations have been applied extensively to study excited states of clusters and complexes.^{17–21} However, DFT is a single-reference method, and therefore it possesses inherent shortcomings, especially when one describes the energetically degenerate and quasi-degenerate states that are usually found in systems containing TMs, bond-breaking systems, and excited states.²² In addition, description of excited states is strongly dependent on the characteristic of the functionals used. For a better treatment, careful studies based on higher levels of wave function theory are necessary. To efficiently treat these systems, multireference wave function methods are the appropriate, but computationally demanding, alternative. Indeed, several recent studies employed the CASSCF/CASPT2 and MRCI to describe electronic structures and excited states of clusters containing transition metals.^{23–30} Detailed excited electronic structures and ionization energies of the $\text{VSi}_3^{-/0}$ system were studied³¹ making use of the CASSCF/CASPT2 approach. Another study of excited electronic structures and corresponding electron transitions in the anion PE spectra of the anionic ScSi_3^- cluster was reported.³²

As mentioned above, the anion PE spectrum of ScSi_2^- was experimentally determined.¹⁴ Under the photon laser beam of 266 nm, electron detachments from the anionic cluster ScSi_2^- were triggered off and recorded. There are two distinguishable regions recorded in the spectrum, which range from 1.20 to 3.00 eV. In particular, the lower-energy region splits into two bands in which the first band is characterized by an adiabatic detachment energy (ADE) of 1.28 eV and a vertical detachment energy (VDE) of 1.44 eV. The VDE of the next band was measured to be 1.69 eV. In the remaining region, three other bands with higher VDEs of 2.57, 2.75, and 2.97 eV were observed. Although geometrical and electronic structures were previously studied,^{14,16} there are still some conflicts on the identity of the true ground state of ScSi_2^- , namely, $^3\text{B}_1$ versus $^3\text{B}_2$. Besides, the characteristics of all higher one-electron ionization energies are still not determined yet.

In view of such uncertainty on the ground state of a small but basic TM doped Si cluster, we set out to investigate the ground and low-lying states related to the experimentally observed bands in the PE spectrum of the triatomic anion ScSi_2^- . We examine these states by means of the multiconfigurational multireference methods CASSCF/CASPT2. This sheds light on the identity of the ground and low-lying states, from which the DFT method (B3LYP, BP86, ...) and even coupled-cluster theory RCCSD(T) methods can be calibrated for determination of relative energies among low-lying states, and of detachment energies.

In conjunction with leading configurations, the possible electron transitions are revealed, and the elucidation of all bands in the anion photoelectron spectra of $\text{ScSi}_2^{-/0}$ are proposed. Harmonic frequencies and normal coordinates of the vibrational modes of all accessible states corresponding to particular bands in the spectrum are also used for multidimensional Franck-Condon factor integrations that suggest a clearer view on vibrational progressions along the appearance of the bands emerging in the spectrum.

3.2 Computational Details

The most stable geometrical structures of both anionic and neutral clusters need to be correctly determined, and this is the purpose of the first computational step. Starting from two possible geometrical isomers of $\text{ScSi}_2^{-/0}$ mentioned in previous studies,^{14,16} geometrical optimizations of both linear and cyclic isomers (Figure 3.1) are performed using DFT with the B3LYP^{33–35} and BP86^{34,36} functionals in conjunction with the correlation-consistent polarized basis set, aug-cc-pVTZ.^{37,38} This step takes into account all possible spin multiplicities of the anion (singlet, triplet, quintet, and septet) and the neutral (doublet, quartet, sextet, and octet). Optimization processes are totally free from any restrictions as no symmetry is imposed. After this step, the most stable geometric structures, and other energetically close ones on the potential surfaces of $\text{ScSi}_2^{0/-}$ are extracted. All the calculations in this step are conducted using the Gaussian 09 E.01 program package.³⁹

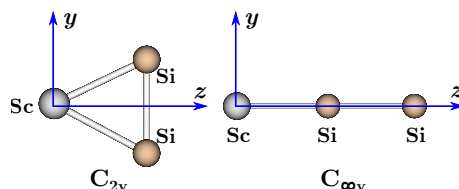


Figure 3.1: Two isomers of $\text{ScSi}_2^{-/0}$ clusters and the coordinate systems used.

In the second step, the ground states of both anionic and neutral clusters $\text{ScSi}_2^{-/0}$ are determined using several methods. Because the global ground states are crucial in solving the anion PE spectrum, the identity and location of such states should correctly be determined on the potential energy surfaces. All states with regard to a spatial symmetry of the most stable structure, which was previously found, are optimized at higher levels of

correlation energy. Owing to the employment of spatial symmetry, one needs to define a specific precoordinate system. Conventionally, the cyclic structure of $\text{ScSi}_2^{-/0}$, eventually proved to have C_{2v} point group, and to be the most stable one, is graphically defined in Figure 3.1, in which the Sc center is set to be the Cartesian coordinate origin and the yz -plane contains the cluster frame. Some additional CASPT2 calculations for the linear isomer (Figure 3.1) with symmetry of $C_{\infty v}$ are calculated within the spatial symmetry of C_{2v} because the nonabelian group $C_{\infty v}$ is not supported in the quantum chemical packages used in this work.

In this work, we use the complete active space self-consistent field (CASSCF) method to construct the wave functions that recover the nondynamic correlation well, and subsequently the second-order perturbation (CASPT2) method, based on CASSCF wave functions as references, that takes into account the dynamical correlation parts. Hence, geometry optimizations of different electronic states are carried out using the CASSCF/CASPT2.⁴⁰ This is in part because a few singlet open-shell states cannot be accessed by single reference methods, and consequently, cannot be geometrically optimized. From our preliminary evaluations, because the 3s and inner-shell orbitals of Si atoms are found not to be involved in the ionization processes causing experimental PE bands, and more importantly to reduce computational costs of CASPT2 optimizations, the 3s and all inner-shell orbitals of Si are not treated in the active space. Instead, six valence 3p orbitals of two Si atoms, together with six valence orbitals (five 3d and one 4s) of the scandium atom are included in the active space of CASSCF calculations. Depending on the charge states of ScSi_2 , the number of electrons included in the active space amounts to 7 and 8 for the neutral and anion, respectively. As a result, there are 12 orbitals in the active space for variable occupancy by 7 or 8 electrons. The number of configuration state functions produced in our CASSCF calculations can be over 28.000 (for singlet states).

For calibration, single-point electronic energies at restricted single and double coupled cluster theory plus the perturbative contributions of connected triple excitations RCCSD(T) are also calculated at CASPT2 geometries. A few additional multiconfigurational reference computations using internally contracted configuration interaction (MRCI(Q)) on the basis of CASSCF wave functions making use of CASPT2 geometries are also conducted to check further the conclusion on the global ground states. To obtain more reliable MRCI(Q) energies, each MRCI calculation takes into account all configuration state functions with coefficients larger than or equal to 0.01, and then the MRCI energies are corrected using the Davidson correction for the quadrupole contributions to correlation energies. At

this step, the correlation consistent triple- ζ basis set aug-cc-PVTZ-DK is used for all single reference and MRCI calculations; the atomic natural orbital basis set ANO-RCC contracted to [7s6p4d3f2g]⁴¹ for Sc and to [5s4p3d2f]⁴² for Si is used in the CASSCF and CASPT2 calculations. In the evaluation of ADEs and VDEs, single-point B3LYP, BP86 and RCCSD(T) energies are equally obtained using a larger quintuple- ζ aug-cc-PV5Z-DK basis set,^{37,38} in which DK stands for the relativistic account. It should be noted that the ADEs are calculated at CASPT2 optimized geometries of the corresponding states, whereas all the VDEs are evaluated at the CASPT2 optimal geometry of the anionic ground state. For RCCSD(T), MRCI, and CASPT2 computations, the inner-shell orbitals 1s, 2s, and 2p of Sc and 1s of Si atoms are not correlated. Scalar relativistic effects are treated by the mean of the second-order Douglas–Kroll–Hess Hamiltonian.⁴³ Single-point and optimization CASPT2 calculations are performed using the MOLCAS 8.1 package,⁴⁴ and DFT, RCCSD(T), and MRCI are carried out with the aid of the MOLPRO 2012 package.⁴⁵ The true energy minima obtained from optimizations are confirmed by all positive harmonic vibrational frequencies.

The last step of the present study is to simulate the band progressions in the anion photoelectron spectrum of ScSi_2^- . Harmonic vibrational frequencies of four accessible neutral states corresponding to the X, A, B, and D bands are calculated at the B3LYP level as mentioned above. Such calculations also provide the equilibrium geometries and normal modes of vibration. By carrying out all possible integrations of the multidimensional Franck-Condon factors up to 15 quanta of many modes, we can theoretically evaluate relative intensities of peaks within each progression, as well as the width of such progressions. This result reveals a more detailed visualization of the bands in the spectrum. The calculations of integrals are implemented with the MolFC program.⁴⁶

3.3 Results and Discussion

3.3.1 Ground States and Low-Lying States of $\text{ScSi}_2^{-/0}$

To ensure that the cyclic isomer with C_{2v} point group corresponds to the most stable structures of both the anionic and neutral clusters as reported elsewhere,^{9,14,16} optimization energies of many different spin-multiplicity states at the B3LYP and BP86 are calculated and visualized in Figure S1 of the [Supporting Information](#) (available online). Apparently,

the cyclic C_{2v} isomer is found to be in each state more stable than the linear isomer. To be more detailed, a triplet and a doublet state are found to be the ground states of the anionic and the neutral clusters, respectively. It should be mentioned here that all high-spin states of the cyclic isomers (sextet, septet, and octet states), which are energetically much higher than the low-spin states of the anion and the neutral, are no longer considered in the next step.

From previous calculations, the cyclic C_{2v} form of the anion and the neutral have been determined as the most stable isomer, and therefore this geometrical structure is believed to be involved in experimental photodetachments. However, the ground state of the anionic cluster from which one electron is removed needs to be exactly known. For this reason, four triplet states (3A_1 , 3B_1 , 3B_2 and 3A_2) of the cyclic isomer are taken into account in the geometrical optimizations. Four doublet states of the neutral cluster are also geometrically optimized for the search of the ground state. Geometrical optimizations of other energetic neighbors on the potential surfaces of the anion and the neutral are performed as well. The relative energies at the B3LYP, BP86, RCCSD(T), and CASPT2 levels, and the CASPT2 geometries used to compute RCCSD(T) energies are presented in Table 3.1. To be safer, we also calculated the relative energies of all singlet and triplet states of the linear isomer at the CASPT2 level by doing geometrical optimizations and provide them in Table S1 of the [ESI](#) file.

Relative energies listed in Table 3.1 indicate that the triplet 3B_2 has the lowest energy of the anion ScSi_2^- . Indeed, all the remaining low-lying singlet and triplet states, as well as the higher spin states are higher in energy than that of the 3B_2 state at all levels considered. The CASPT2 and RCCSD(T) adiabatically place the 3A_2 at 0.24 eV above the 3B_2 , whereas the 3A_1 is positioned at \sim 0.1 eV higher than 3A_2 at the RCCSD(T) level. When the four singlet states are considered, CASPT2 calculations reveal that the open-shell 1B_2 state is just 0.07 eV above the 3B_2 ; such a small difference in energy is within the error margin of the CASPT2 method. Additionally, the RCCSD(T) energy of the 1A_1 is only 0.03 eV above that of the 3B_2 , although CASPT2 energy of this state is 0.28 eV higher than that of the 3B_2 state. Such small differences in relative energies motivate us to perform additional multireference configuration interaction (MRCI) calculations for the states 1A_1 , 1B_2 , and 3B_2 . The internally contracted MRCI calculations, for a specific state, include more than one billion uncontracted configurations (being over 87 million contracted configurations) and are therefore very computationally expensive. Hence, MRCI calculations are only carried out for the necessary states mentioned above. MRCI

Table 3.1: Relative Energies and Structural Parameters of the Ground and Low-Lying States^(a)

cluster	state	CASPT2 geometry (Å)		relative energy (eV)			
		Sc-Si	Si-Si	B3LYP	BP86	RCCSD(T)	CASPT2
cyclic	¹ A ₁	2.666	2.142	0.54	0.64	0.03	0.28
	¹ B ₁	2.404	2.356				0.81
	¹ B ₂	2.500	2.237				0.07
	¹ A ₂	2.694	2.143				0.37
	³ A ₁	2.725	2.138	0.45	0.68	0.34	0.30
	³ B ₁	2.408	2.439	0.59	0.48	0.72	0.50
	³ B ₂	2.479	2.250	0.00	0.00	0.00	0.00
	ScSi ₂ ⁻	³ A ₂	2.701	2.140	0.31	0.43	0.24
	⁵ A ₁	2.601	2.345	1.28	1.21	1.37	1.49
	⁵ B ₁	2.423	2.415	1.32	1.24	1.63	1.56
cyclic	ScSi ₂ ⁰	⁵ B ₂	2.746	2.173	1.49	1.57	1.59
	⁵ A ₂	2.748	2.167	1.58	1.64	1.64	1.80
	² A ₁	2.560	2.160	1.61	1.81	1.60	1.57
	² B ₁	2.600	2.160	2.10	2.46	2.13	1.98
	² B ₂	2.435	2.286	1.34	1.50	1.41	1.09
ScSi ₂ ⁰	² A ₂	2.540	2.168	1.65	1.89	1.73	1.63
	⁴ A ₁	2.480	2.538	2.50	2.63	2.77	2.50
	⁴ B ₁	2.366	2.453	2.53	2.66	2.94	2.57
	⁴ B ₂	2.608	2.159	2.29	2.50	2.46	2.33
	⁴ A ₂	2.599	2.490	2.36	2.63	2.77	2.63

^(a) Single-point RCCSD(T) energies were calculated using CASPT2 optimized geometries. At the B3LYP, BP86, and CASPT2 levels, energies are obtained with optimized geometries at the same level. These values are electronic energies without ZPEs. The basis sets aug-cc-PVTZ-DK (for single reference methods DFT and RCCSD(T)) and ANO-RCC (for CASSCF/CASPT2) were used including the scalar relativistic effects.

calculations for the anion indicate that the ³B₂ state is 0.17 and 0.09 eV lower in energy than the ¹A₁ and ¹B₂ states, respectively. Overall, all results from DFT, RCCSD(T), CASPT2, and MRCI calculations allow us to conclude that the triplet ³B₂ is the ground state of the anionic cluster ScSi₂⁻, which confirms the result of a previous report.¹⁶ This state exhibits the following orbital configuration: ³B₂ ... (12a₁)² (4b₁)² (13a₁)¹ (8b₂)¹. As for the neutral cluster, determination of its ground state appears to be more straightforward because all the doublet and quartet states are accessible from all quantum chemical methods. The DFT (using B3LYP, BP86 functionals) and coupled-cluster theory RCCSD(T) methods identify

Table 3.2: CASSCF Leading Configurations and Possible Ionization Processes Starting from the Anionic Ground State $^3\text{B}_2$, and from the Nearly Degenerate State $^1\text{B}_2$.

state	leading configuration	weight (%)	ionization	ionization orbital
$^3\text{B}_2$	11a ₁ ² 12a ₁ ² 13a ₁ ¹ 4b ₁ ² 5b ₁ ⁰ 8b ₂ ¹ 2a ₂ ⁰	87		
$^1\text{B}_2$	11a ₁ ² 12a ₁ ² 13a ₁ ¹ 4b ₁ ² 5b ₁ ⁰ 8b ₂ ¹ 2a ₂ ⁰	87		
$^2\text{A}_1$	11a ₁ ² 12a ₁ ² 13a ₁ ¹ 4b ₁ ² 5b ₁ ⁰ 8b ₂ ⁰ 2a ₂ ⁰	85	$^3\text{B}_2 \longrightarrow ^2\text{A}_1$ $^1\text{B}_2 \longrightarrow ^2\text{A}_1$ ^(b)	8b ₂ (Sc: 3d _{yz})
$^2\text{B}_1$	11a ₁ ² 12a ₁ ² 13a ₁ ⁰ 4b ₁ ² 5b ₁ ¹ 8b ₂ ⁰ 2a ₂ ⁰	88		
$^2\text{B}_2$	11a ₁ ² 12a ₁ ² 13a ₁ ⁰ 4b ₁ ² 5b ₁ ⁰ 8b ₂ ¹ 2a ₂ ⁰	85	$^3\text{B}_2 \longrightarrow ^2\text{B}_2$	13a ₁ (Sc: 4s)
$^2\text{A}_2$	11a ₁ ² 12a ₁ ² 13a ₁ ⁰ 4b ₁ ² 5b ₁ ⁰ 8b ₂ ⁰ 2a ₂ ¹	87		
$^1\text{A}_1$	11a ₁ ² 12a ₁ ² 13a ₁ ⁰ 4b ₁ ¹ 5b ₁ ⁰ 8b ₂ ¹ 2a ₂ ¹	83		
$^1\text{B}_1$	11a ₁ ¹ 12a ₁ ² 13a ₁ ⁰ 4b ₁ ² 5b ₁ ⁰ 8b ₂ ¹ 2a ₂ ¹	87		
$^1\text{B}_2$	11a ₁ ² 12a ₁ ¹ 13a ₁ ¹ 4b ₁ ² 5b ₁ ⁰ 8b ₂ ¹ 2a ₂ ⁰	89	$^3\text{B}_2 \longrightarrow ^1\text{B}_2$	12a ₁ (Si: 3p _y)
$^2\text{B}_2$	11a ₁ ¹ 12a ₁ ² 13a ₁ ¹ 4b ₁ ² 5b ₁ ⁰ 8b ₂ ¹ 2a ₂ ⁰	84	$^3\text{B}_2 \longrightarrow ^2\text{B}_2$	11a ₁ (Si: 3p _z)
$^1\text{A}_2$	11a ₁ ² 12a ₁ ² 13a ₁ ¹ 4b ₁ ¹ 5b ₁ ⁰ 8b ₂ ¹ 2a ₂ ⁰	86	$^3\text{B}_2 \longrightarrow ^1\text{A}_2$	4b ₁ (Si: 3p _x)

^(b) This transition is considered when the nearly degenerate state $^1\text{B}_2$ is supposed to be populated.

the low-spin $^2\text{B}_2$ at ~ 0.20 eV lower in energy than the $^2\text{A}_1$ state. CASPT2 optimizations also determine the energy of $^2\text{B}_2$ to be lower than that of $^2\text{A}_1$, but the CASPT2 relative energy gap is slightly larger with a difference of ~ 0.5 eV between the $^2\text{B}_2$ and $^2\text{A}_1$. All high-spin quartet states of the cyclic neutral ScSi_2 are about 1.20 eV energetically higher than $^2\text{B}_2$ at the DFT, RCCSD(T) and CASPT2 levels. Unambiguously, the $^2\text{B}_2$ can be assigned as the ground state of the neutral cluster ScSi_2 .¹⁶

3.3.2 Electronic Structures and Possible One-Electron Detachments

Because the electronic configurations of states decide the ionization processes, all of them are now thoroughly analyzed. By extracting leading configurations from the CASSCF levels, we reveal the detailed electronic structures of possible initial and final states involving the ionization processes. In going from the ground states of both the anionic and neutral clusters $\text{ScSi}_2^{-/0}$, all other low-lying states that follow one-electron detachments, are investigated. All the leading configurations of selected states are tabulated in Table 3.2.

The $^3\text{B}_2$ ground state has three doubly and two singly occupied orbitals in the active space. Whereas two singly occupied orbitals $13a_1$ and $8b_2$ are mostly contributed from Sc valence

orbitals $4s$ and $3d_{yz}$, three doubly occupied ones originate from π_u ($11a_1$ and $4b_1$) and σ_g ($12a_1$) orbitals of the Si_2^- ligand. These ligand orbitals dominantly constitute the $3p$ orbitals from Si atoms, which are $3p_x$ and $3p_z$ for the case of two π_u orbitals, and are $3p_y$ for the case of σ_g .

The leading configuration of ${}^3\text{B}_2$ can also be written as $[... \pi_{3p_z}^2 \sigma_{3p_y}^2 4s^1 \pi_{3p_x}^2 3d_{yz}^1]$ in terms of dominant orbital contributions. Similarly, the ${}^2\text{B}_2$ state can be analyzed from its obtained leading configuration. Most features of active orbitals are the same as those of the ${}^3\text{B}_2$. Nevertheless, instead of two metallic singly occupied orbitals as the case of ${}^3\text{B}_2$, the ${}^2\text{B}_2$ state has only one singly occupied one ($8b_2$). This is originally the $3d_{yz}$ orbital of Sc. It means that an electron in the $4s$ orbital is removed from the ${}^3\text{B}_2$ state to form the ${}^2\text{B}_2$ if the ionization process happens during the measurement of anion photoelectron spectra. This one-electron removal can obviously be seen by comparing the leading configurations between these states. As a result, the leading configuration of ${}^2\text{B}_2$ can be described as $[... \pi_{3p_z}^2 \sigma_{3p_y}^2 4s^0 \pi_{3p_x}^2 3d_{yz}^1]$. For an intuitive visualization, the pseudonatural active orbitals of these two states are plotted in Figure 3.2. The ionization process is thus denoted as ${}^3\text{B}_2 \longrightarrow {}^2\text{B}_2$ together with the corresponding ionization orbital $13a_1$ (Sc: $4s$) in Table 3.2.

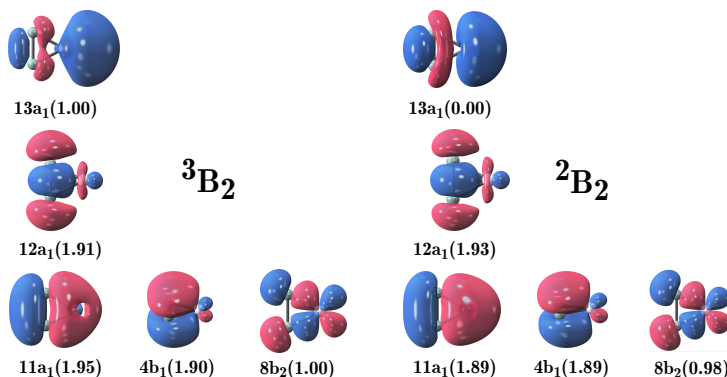


Figure 3.2: Occupied CASSCF pseudonatural active orbitals of ${}^3\text{B}_2$ and corresponding active orbitals of ${}^2\text{B}_2$. Average occupation numbers are given in parentheses. Scandium atoms are on the right-hand side of each cluster.

As mentioned above, with regard to the one-electron detachment process, if the ${}^3\text{B}_2$ state is the ground state of the anionic cluster, the final state can be a state of doublet and of quartet. Thus, besides the neutral ground state ${}^2\text{B}_2$, other doublet states and the quartet

states should be examined. By considering the leading configurations, we can predict the 2A_1 state as a final state of the ionization process starting from the 3B_2 . In fact, two leading configurations of 3B_2 and 2A_1 are just distinguishable from each other through the 8b_2 orbital, which is singly occupied in the state of 3B_2 and unoccupied in the latter state. Therefore, this one-electron detachment should appear somewhere in the anion photoelectron spectrum of ScSi_2^- . For two other leading configurations 2B_1 and 2A_2 , both cannot be the final states, because these leading configurations are not the consequences of one-electron detachments starting from the anionic ground state 3B_2 . Up to now, two ionization processes can happen upon excitation of the 4s and $3d_{yz}$ electrons, which are valence orbitals of Sc.

Concerning the quartet states, three singly occupied orbitals with particular symmetrical orbitals decide the electronic state of the neutral cluster. When comparing the leading configurations of both 1A_1 and 1B_1 with the anionic ground state 3B_2 , one can point out that no one-electron detachments from 3B_2 are possible to produce these two leading configurations. This can be understood by electron occupation in the orbital $2a_2$, which has a large contribution from the $3d_{xy}(\text{Sc})$ orbital. Indeed, though the orbital $2a_2$ is unoccupied in the 3B_2 state, it is singly occupied in both 1A_1 and 1B_1 states. There are also differences in occupancy of orbitals in the representations a_1 and b_1 between the 3B_2 and these two quartet states. Let us recall that two metallic orbitals $13a_1$ and 8b_2 are found to be the key orbitals involving in the above-mentioned ionization processes. Therefore, removals of electrons from the $3p(\text{Si})$ orbitals are expected to appear in the photoelectron spectrum of ScSi_2^- as well.

With the electronic structure of the 3B_2 state, the tentative final states corresponding to three one-electron removals from three bonding orbitals π_{3p_x} , π_{3p_z} , σ_{3p_y} can be predicted. Clearly, if the ionization happens upon removal of one electron from the bonding orbital σ_{3p_y} ($12a_1$) in the ligand, the obtained leading configuration is that of 1B_2 . Similarly, if one-electron transition starts from the bonding orbital π_{3p_z} ($11a_1$), the electronic structure of 2B_2 is observed. For the 1A_1 state, the one-electron transition is out of the totally symmetrical a_1 orbitals but not the b_1 one. Instead of a doubly occupied orbital, the $4b_1$ orbital, dominantly composed of the π_{3p_x} orbital of the Si_2 moiety, is a singly occupied one. This suggests that removal of one electron can occur at the $4b_1$ orbital, and this should be reflected in the photoelectron spectrum of ScSi_2^- . All the one-electron transitions and ionization orbitals can be found in Table 3.2.

The charge distribution among the atoms in the anionic ground state $^3\text{B}_2$ can be drawn from its electronic structure. First, the electronic structure of Si_2^- should be considered. The ground state of the diatomic anion Si_2^- was, originally, reported to be $2\pi_u$, whose configuration was written as $[...\pi_u^3\sigma_g^2]$.⁴⁷ Later, a revision suggested that the nearly degenerate state $^2\Sigma_g^+$ with configuration of $[...\pi_u^4\sigma_g^1]$ is the ground state.⁴⁸ This result is in better agreement with a previous study.⁴⁹ Technically, these configurations can be interpreted as the states $[...(\pi_{3p_x}\pi_{3p_z})^3\sigma_{3p_y}^2]$ and $[(\pi_{3p_x}\pi_{3p_z})^4\sigma_{3p_y}^1]$ for $^2\pi_u$ and $^2\Sigma_g^+$, respectively, if the coordinate system of the C_{2v} isomer presented in Figure 3.1 is applied to the Si_2^- unit. In each of these two nearly degenerate configurations, there are in total five electrons occupying two degenerate π_u orbitals and a σ_g one. Because these two nearly degenerate states are believed to be experimentally populated,⁴⁸ they can be involved in the formation process of the anion ScSi_2^- . As seen in the electronic configuration of the $^3\text{B}_2$ ground state $[...\pi_{3p_z}^2\sigma_{3p_y}^24s^1\pi_{3p_x}^23d_{yz}^1]$, all orbitals of the Si_2^- ligand are doubly occupied. The electronic configurations of two nearly degenerate states of Si_2^- and the ground state of ScSi_2^- provide unequivocal evidence proving that one electron in the valence orbitals of Sc is attracted and captured by the Si_2 moiety, even though the mechanism of electron transfer is different with regard to which state of Si_2^- reacting with Sc atoms. This allows us to suggest the formal oxidation states of each components in the anionic cluster ScSi_2^- as $(\text{Sc})^{+1}(\text{Si}_2)^{-2}$. With the same line of thought, the formal oxidation states of the Sc and Si_2 parts in two neutral states $^2\text{A}_1$ and $^2\text{B}_2$ can be described as $(\text{Sc})^{+2}(\text{Si}_2)^{-2}$, because one electron is removed from the metallic orbitals of Sc during the ionization. It becomes different for three quartet states, $^1\text{B}_2$, $^2\text{B}_2$, and $^1\text{A}_2$. As the ionization processes start from $\sigma_{3p_y}^2$, $\pi_{3p_x}^2$ and $\pi_{3p_z}^2$ of the ligand, the formal oxidation states of Si_2 moiety should be -1. As a result, the formal oxidation states of these three quartet states can be described as $(\text{Sc})^{+1}(\text{Si}_2)^{-1}$.

These charge distributions can also be easily obtained from population analyses. The Bader charges of Sc and Si atoms analyzed at the CASSCF wave functions are provided in Table 3.3. The AIM charge values afford a better description of charge distribution among Sc and Si atoms. The most obvious feature is the actual values of charge correctly reflect the signs of formal oxidation states, which are positive for Sc and negative for Si. The absolute values of charge also well demonstrate the charge redistribution when one electron is removed from a specific moiety of the anionic ground state $^3\text{B}_2$. To be more detailed, the absolute charge value on the Sc atom is somewhat in balance with that on each Si atom (0.56 versus 0.78) as their formal oxidation states are. When one electron is removed from Sc to form the doublet states $^2\text{A}_1$ and $^2\text{B}_2$, the positive charge of Sc increases to

around +1.0 electron. This is what can be expected after considering changes in the formal oxidation states given above. A point of interest here is that the negative charge on Si tends to decrease. This can be understood by relaxation happening immediately after ionization. For a charge redistribution after detachments of an electron from Si_2 moiety, the absolute value of negative charge on Si atoms is significantly reduced to approximate 0.4 electron as observed in two quartet states 1^4B_2 and 1^4A_2 .

Table 3.3: Atomic Net Charges of Sc and Si (CASSCF)

state	AIM charge (electron)		
	Sc	Si	Si
$^3\text{B}_2$	+0.56	-0.78	-0.78
$^2\text{A}_1$	+0.96	-0.48	-0.48
$^2\text{B}_2$	+1.06	-0.53	-0.53
1^4B_2	+0.82	-0.41	-0.41
1^4A_2	+0.84	-0.42	-0.42

3.3.3 Anion photoelectron Spectrum and Band Assignments

With all possible one-electron ejections analyzed above, one can now evaluate the number of the first few anion photoelectron bands that can appear in the experimental spectrum of ScSi_2^- . However, this type of qualitative information cannot be used to locate the energetic range of each one-electron detachment. In other words, the experimentally recorded bands cannot be assigned without extra ionization energies of these one-electron transitions. Thus, the ADEs and VDEs are of utmost importance in band assignments. Before considering this, for the sake of convenience, five experimental bands in the spectrum of ScSi_2^- , reproduced in Figure 3.3, can be labeled as X – D. All calculated ADEs and VDEs at the DFT, RCCSD(T) and CASPT2 levels of theory are presented in Table 3.4.

Normally, the lowest band X in an anion PE spectrum is expected to be the result of a one-electron transition between the anionic and neutral ground states. For ScSi_2^- , the transition $^3\text{B}_2 \rightarrow ^2\text{B}_2$ is responsible for such a band. The calculated ADE and VDE at DFT, RCCSD(T), and CASPT2 levels are in fact in good agreement with experimental values. All single reference methods predict the ADE and VDE deviations of about 0.10 eV from the experimental ones. Indeed, the experimental ADE of the X band is 1.28 eV, and

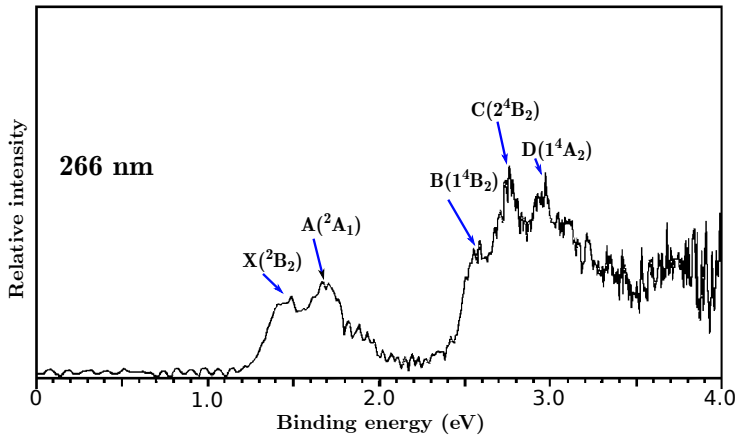


Figure 3.3: Anion photoelectron spectrum of ScSi_2^- recorded at the photon energy of 266 nm (reproduced with permission from ref 14. Copyright 2011, CPS). Five bands in the spectrum are labeled as the traditional nomenclature of anion photoelectron bands (X – D).

the B3LYP, BP86, and RCCSD(T) ADEs are, respectively, estimated to be 1.31, 1.47, and 1.40 eV. The B3LYP and RCCSD(T) estimated values are much closer to the experimental ADE of 1.47 eV reported elsewhere.¹⁶ The VDEs calculated again confirm the assignment for the X band when they are quite close to the experimental VDE of 1.44 eV. It is worth mentioning here that the CASPT2 energy predictions of the ADE and VDE are slightly underestimated in comparison to the experimental ionization values (1.09 versus 1.28 eV for the ADE, and 1.17 versus 1.44 eV for the VDE). However, the differences in ADE and VDE between the CASPT2 and experimental values (0.19 and 0.27 eV) are all below the error margin of the CASPT2 method. All estimated VDEs and ADEs from single-reference methods for this band are in good agreement with experiment. This can be, in part, explained by the strong single-reference feature of the anionic and neutral ground states, which are quantitatively determined by the leading configurations weights listed in Table 3.2. For the other low-lying doublet states, the VDEs and ADEs are significantly higher than the experimental values. Therefore, $^2\text{B}_2$ is the unique state leading to the X band.

Table 3.4: Adiabatic Detachment Energies and Vertical Detachment Energies Calculated at CASPT2 Geometries in Table 3.2^(c)

state	ADE (eV)				VDE (eV)				exptl	
	B3LYP	BP86	RCCSD(T)	CASPT2	exptl	B3LYP	BP86	RCCSD(T)	CASPT2	
$^3\text{B}_2$	0.00	0.00	0.00	0.00		0.00	0.00	0.00	0.00	0.00
$^1\text{B}_2$				0.07						0.08
$^2\text{A}_1$	1.54	1.76	1.63	1.57 (1.51)		1.68	1.88	1.75	1.65 (1.55)	1.69 (A)
$^2\text{B}_1$	2.02	2.40	2.08	1.98		2.24	2.56	2.28	2.14	
$^2\text{B}_2$	1.31	1.47	1.40	1.09	1.28	1.26	1.44	1.36	1.17	1.44 (X)
$^2\text{A}_2$	1.57	1.84	1.68	1.63		1.65	1.86	1.75	1.69	
$^1\text{A}_1$	2.50	2.62	2.82	2.50		2.56	2.74	2.90	2.67	
$^1\text{B}_1$	2.65	2.73	2.92	2.57		2.50	2.63	2.82	2.71	
$^1\text{B}_2$	2.22	2.45	2.50	2.33		2.42	2.62	2.67	2.57	2.57 (B)
$^2\text{A}_2$									2.70	2.75 (C)
$^1\text{A}_2$	2.45	2.71	2.83	2.63		2.51	2.78	2.89	2.91	2.79 (D)

^(c) All single reference calculations use the quintuple- ζ basis set aug-cc-pV5Z-DK. CASPT2 energies are calculated by employing the same ANO-RCC basis set used in determination of the ground states. The values in the parentheses are the ADE and VDE of the supposed electronic transition $^1\text{B}_2 \rightarrow ^2\text{A}_1$.

Because there are no experimental ADEs of the four bands A, B, C, and D, their assignments can only be made on the basis of VDEs. As stated above, removal of one electron from the 4s(Sc) orbital of the anionic ground state $^3\text{B}_2$ was proved to cause the appearance of the X band. In a logical aspect, removal of an electron from the 3d(Sc) orbital is expected to be the insight of the A band, because this band has the second lowest ionization energy. This view is reinforced by the detachment energies calculated at DFT, RCCSD(T), and CASPT2 levels. The experimental VDE of the A band is 1.69 eV, which is very close to the B3LYP, RCCSD(T), and CASPT2 values of 1.68, 1.75, and 1.65 eV, respectively, for the transition $^3\text{B}_2 \rightarrow ^2\text{A}_1$. The pure exchange-correlation functional BP86 is not as accurate as the other methods, but its evaluation is still valuable as the deviation is 0.19 eV. As a consequence, the A band is safely attributed to the transition $^3\text{B}_2 \rightarrow ^2\text{A}_1$, which is totally allowed by the one-electron detachment rule mentioned above. It is noticeable to mention that the leading configuration's weight of the state $^2\text{A}_1$ is 85%, which is the same as that of the neutral ground state $^2\text{B}_2$. As a result, this neutral state can electronically and energetically be well described with a single electron configuration.

Three remaining bands in the experimental spectrum are expected to be the results of detachments starting from three occupied orbitals π_{3p_z} , π_{3p_x} and σ_{3p_y} that are mainly located in the ligand Si_2^- . When only the energies of orbitals in the intact diatomic anion Si_2^- are considered, two degenerate orbitals π_{3p_z} and π_{3p_x} are the HOMOs; and the orbital σ_{3p_y} is the HOMO-1.⁴⁷⁻⁴⁹ When Si_2^- combines with a Sc atom to form ScSi_2^- , these orbitals slightly change, in part due to the interference of the same symmetrical orbitals from the transition metal Sc. Particularly, the CASSCF pseudonatural orbitals show that σ_{3p_y} has tiny contribution from the $3d_{z^2}$ orbital; the π_{3p_z} is contaminated by the 4s orbital, and the $3d_{xz}$ partially places itself into the π_{3p_x} . As a result, the π_{3p_z} and π_{3p_x} which are actually the orbitals 11a_1 and 4b_1 in the leading configuration of the state $^3\text{B}_2$, are no longer degenerate, as these two orbitals are contributed by two types of orbitals with different levels of energy (4s and 3d). Because the level of 4s energy is lower than that of the 3d in the first-row TMs, the energy level of π_{3p_z} (11a_1) should be predictably lower than that of the π_{3p_x} (4b_1). Thus, removal of an electron from the orbital 11a_1 of the anionic ground state $^3\text{B}_2$ needs less energy than that from the 4b_1 orbital. These basic considerations yield a clearer route to reach the final assignments for three remaining bands B, C and D.

First, we find out the insight of the B band. Our calculated results identify that the transition $^3\text{B}_2 \rightarrow 1^4\text{B}_2$, which corresponds to the removal of an electron from the orbital σ_{3p_y}

(12a₁), has the lowest VDE. The methods BP86, RCCSD(T), and CASPT2 predict this VDE to be 2.62, 2.67, and 2.57 eV, whereas the experimental VDE is 2.57 eV. In this case, the B3LYP value of 2.42 eV is underestimated. For the C and D bands, we can undoubtedly assign them to the formation of the 2⁴B₂ and 1⁴A₂ states, respectively, by taking the above analysis into account. For the state 2⁴B₂, the VDE of the transition 3B₂ → 2⁴B₂ is well obtained at RCCSD(T) and CASPT2 levels but not at DFT levels. Specifically, the RCCSD(T) detachment energy gives the best value of 2.77 eV for this ionization, which is only 0.02 eV larger than the experimental value of 2.75 eV and is larger than the CASPT2 ionization energy an amount of 0.07 eV.

With regard to the last band D, both RCCSD(T) and CASPT2 values of 2.89 and 2.91 eV again accurately reproduce the experimental VDEs of 2.79 eV for the transition 3B₂ → 1⁴A₂. The pure BP86 functional also can correctly predict the detachment energy of 2.78 eV for the excited state 1⁴A₂ of the neutral cluster ScSi₂. The hybrid B3LYP functional seriously underestimates this VDE by up to 0.30 eV below the experimental counterpart, though it predicts better detachment energies for the lower excited states. In summary, all the anion PE bands in the spectrum of ScSi₂⁻ are now assigned, and these assignments are denoted in Figure 3.3.

As mentioned above, the ¹B₂ is a nearly degenerate state of the ground state ³B₂. Therefore, this state can be populated during the anion PE measurement. From the leading configuration of ¹B₂, which is quite similar to that of ³B₂ except for spin of the electron in the singly occupied orbital 8b₂, and from other neutral states given in Table 3.2 we can infer that the tentative state ²A₁ can be obtained only by removing the 3d_{y_z} electron from the 8b₂ orbital of ¹B₂. Our CASPT2 calculation predicted the transition ¹B₂ → ²A₁ has a VDE of 1.55 eV, which is energetically located in the range between X and A bands in the spectrum of ScSi₂⁻. On the basis of Maxwell-Boltzmann statistics, the energy splitting of two anionic nearly degenerate states and the cooled condition of ScSi₂⁻ clusters obtained from the experiment,¹⁴ one can expect that the population of ¹B₂ (a few percent) is very small in comparison to the ground state ³B₂. Therefore, one-electron transitions, if experimentally observed, starting from ¹B₂ are believed to be not intense compared to those starting from the ground state ³B₂. This allows us to expect the intensity of the transition ¹B₂ → ²A₁ is negligible and can be overshadowed by the allowed transitions underlying the X and A bands in the spectrum.

It is clear that most single reference methods can closely reproduce the experimental

ionization energies of ScSi_2^- . In conjunction with the leading configurations weights, around 85% for all states as listed in Table 3.2, one can safely conclude that the electronic structure of $\text{ScSi}_2^{-/0}$ are basically single configurations. And thus, single-reference methods such as DFT, which are computationally more economic, can be used to correctly describe the ground and low-lying electronic states of $\text{ScSi}_2^{-/0}$ clusters, except for the singlet open-shell states which are inaccessible by single reference methods.

3.3.4 Franck-Condon Factor Simulations

In an attempt to provide a clearer view of the photoelectron spectrum, simulations of multidimensional Franck–Condon factors for the four observed bands, whose harmonic vibrations of normal modes of the final states are computationally accessible, are carried out. Table 3.5 collects the vibrational frequencies of normal modes and equilibrium geometries of relevant states for the Franck–Condon factor integration. On the basis of multidimensional Franck–Condon factors, the progressions occurring along the appearance of the four specific electronic transitions underlying the X, A, B, and D bands are depicted (Figure 3.4).

Table 3.5: Equilibrium geometries and harmonic vibrational frequencies (B3LYP/aug-cc-pVTZ-DK) for the initial anionic state ${}^3\text{B}_2$ and four neutral final states corresponding to the bands X, A, B and D in the PE spectrum

state	B3LYP geometry (\AA)		B3LYP frequencies (cm^{-1})	band
	Sc-Si	Si-Si		
${}^3\text{B}_2$	2.59	2.21	227, 289, 450	
${}^2\text{A}_1$	2.59	2.16	220, 327, 547	A
${}^2\text{B}_2$	2.50	2.23	233, 334, 489	X
${}^1\text{B}^2$	2.67	2.17	246, 265, 517	B
${}^1\text{A}^2$	2.68	2.30	218, 256, 444	D

In the experimental bands, the exact number of peaks cannot be obtained and relative intensities of peaks within every band are not well-resolved. Thus, it is not possible to draw a detailed comparison between the experimental and the simulated bands. Theoretically, the X, B, and D band progressions are broader than band A, as visualized in Figure 3.4. Such a difference in the progression broadening is due to the geometrical differences between the anionic ground state ${}^3\text{B}_2$ and the corresponding final neutral states. Particularly, at

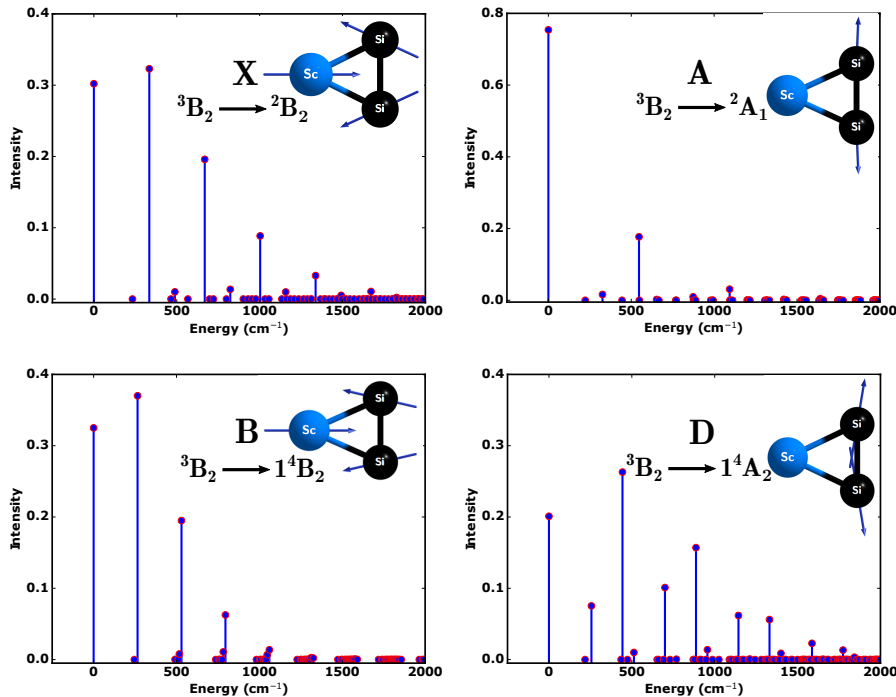


Figure 3.4: Franck-Condon factor simulations for the four bands X, A, B, and D of the photoelectron spectrum of ScSi_2^- .

the vibrational frequency of 334 cm^{-1} , the reduction of the $\text{Sc}-\text{Si}$ bond from 2.59 \AA to 2.50 \AA seems to be a key factor deciding the wide progression of the ionization ${}^3\text{B}_2 \longrightarrow {}^2\text{B}_2$. Similarly, for the ionization ${}^3\text{B}_2 \longrightarrow {}^4\text{B}_2$, the increase of $\text{Sc}-\text{Si}$ bond by 0.08 \AA results in a broadening of this progression at the vibrational frequency of 265 cm^{-1} . For the simulation of the D band, different aspects can be noticed. Significant changes of 0.09 \AA in both $\text{Sc}-\text{Si}$ and $\text{Si}-\text{Si}$ bonds are why the progression of the band D is broader than the others. In contrast, the simulated band A is not broad with two clear peaks, in which the first one's intensity is stronger than that of the second one. This can be understood by the insignificant change in the $\text{Si}-\text{Si}$ bond length of the state ${}^2\text{A}_1$ in comparison to the initial state ${}^3\text{B}_2$. The vibrational frequency of the final state ${}^2\text{A}_1$ is mainly involved in this vibronic transition amounts to 547 cm^{-1} , which is larger than the counterparts. The vibrational modes of four corresponding final states are depicted as the insets in Figure 3.4.

It should be again stressed that the experimental bands are not so clear-cut and well-resolved, which makes it difficult for a detailed comparison between the widths of experimental bands and those from our simulations. In addition, for the specific band A, the electronic transition $^1\text{B}_2 \longrightarrow ^2\text{A}_1$ is believed to somewhat affect its shape, because the relevant ionization energy ($^1\text{B}_2 \longrightarrow ^2\text{A}_1$) is quite close to that derived from the band A. More interestingly the $^2\text{A}_1$ state of this secondary transition is also the final ionized state defining the band A.

3.4 Concluding Remarks

In the present theoretical study, several quantum chemical methods were used, including density functional theory (DFT with B3LYP and BP86 functionals), coupled-cluster theory RCCSD(T), and multiconfigurational methods CASSCF/CASPT2 and MRCI to determine the global minima structures and the ground electronic states of the anionic and neutral forms of the triatomic ScSi_2 species.

The $^3\text{B}_2$ state was determined to be the ground state of the anion ScSi_2^- whereas the low-spin $^2\text{B}_2$ state is the ground state of the neutral ScSi_2 . The formal oxidation states of the Si_2 ligand in the anionic and neutral ground states are -2, whereas those of the scandium atom are +1 and +2. These formal oxidation states are well described with the AIM charges. More importantly, on the basis of electronic structures of the ground and low-lying states, all experimentally observed bands in the photoelectron spectrum of ScSi_2^- are now fully understood. All ionization processes originate from the anionic ground state $^3\text{B}_2$. The band assignments can be divided into two levels with regard to the electronic insights of the ionization. The first level is the removals of one electron from the scandium orbitals, and the second one is the detachments of an electron from the Si_2 orbitals. For the former, the X and A band are the results of one-electron transitions $^3\text{B}_2 \longrightarrow ^2\text{B}_2$ and $^3\text{B}_2 \longrightarrow ^2\text{A}_1$, in which the ionization processes start from the 4s and 3d orbitals of Sc, respectively. As for the latter, the B band is attributed to the transition $^3\text{B}_2 \longrightarrow ^1\text{B}_2$ as the consequence of a one-electron removal from the σ_{3p_y} of the Si_2 moiety. The C band was ascribed to the formation of the $^2\text{B}_2$ state and the D band was assigned to that of the $^1\text{A}_2$. These two bands are the results of one-electron photodetachments from the π_{3p_z} , π_{3p_x} orbitals of the Si_2 ligand, respectively. Franck-Condon simulations of four accessible bands in the spectra of ScSi_2^- revealed more detailed features of the band progressions and relative

intensities of peaks within each progression.

References

- (1) Andriotis, A. N.; Mpourmpakis, G.; Froudakis, G. E.; Menon, M. *New J. Phys.* **2002**, *4*, 78.
- (2) Menon, M.; Andriotis, A. N.; Froudakis, G. *Nano Lett.* **2002**, *2*, 301–304.
- (3) Uchida, N.; Miyazaki, T.; Kanayama, T. *Phys. Rev. B* **2006**, *74*, 205427.
- (4) Beck, S. M. *J. Chem. Phys.* **1987**, *87*, 4233–4234.
- (5) Jaeger, J. B.; Jaeger, T. D.; Duncan, M. A. *J. Phys. Chem. A* **2006**, *110*, 9310–9314.
- (6) Kumar, V.; Kawazoe, Y. *Phys. Rev. Lett.* **2001**, *87*, 045503.
- (7) Ngan, V. T.; Janssens, E.; Claes, P.; Lyon, J. T.; Fielicke, A.; Nguyen, M. T.; Lievens, P. *Chem. - Eur. J.* **2012**, *18*, 15788–15793.
- (8) McVey, B. F. P.; Butkus, J.; Halpert, J. E.; Hodgkiss, J. M.; Tilley, R. D. *J. Phys. Chem. Lett.* **2015**, *6*, 1573–1576.
- (9) Xiao, C.; Abraham, A.; Quinn, R.; Hagelberg, F.; Lester, W. A. *J. Phys. Chem. A* **2002**, *106*, 11380–11393.
- (10) He, J.; Wu, K.; Liu, C.; Sa, R. *Chem. Phys. Lett.* **2009**, *483*, 30–34.
- (11) Reinert, F.; Hüfner, S. *New J. Phys.* **2005**, *7*, 97.
- (12) Koyasu, K.; Akutsu, M.; Mitsui, M.; Nakajima, A. *J. Am. Chem. Soc.* **2005**, *127*, 4998–4999.
- (13) Koyasu, K.; Atobe, J.; Furuse, S.; Nakajima, A. *J. Chem. Phys.* **2008**, *129*, 214301.
- (14) Hong-Guang, X.; Miao-Miao, W.; Zeng-Guang, Z.; Qiang, S.; Wei-Jun, Z. *Chin. Phys. B* **2011**, *20*, 043102.
- (15) Xu, H.-G.; Zhang, Z.-G.; Feng, Y.; Zheng, W. *Chem. Phys. Lett.* **2010**, *498*, 22–26.
- (16) Lu, J.; Yang, J.; Kang, Y.; Ning, H. *J. Mol. Model.* **2014**, *20*, 2114.
- (17) Dreuw, A.; Head-Gordon, M. *Chem. Rev.* **2005**, *105*, 4009–4037.
- (18) Stratmann, R. E.; Scuseria, G. E.; Frisch, M. J. *J. Chem. Phys.* **1998**, *109*, 8218–8224.
- (19) Vlček, A.; Záliš, S. *Coord. Chem. Rev.* **2007**, *251*, 258–287.

- (20) Zhai, H.-J.; Döbler, J.; Sauer, J.; Wang, L.-S. *J. Am. Chem. Soc.* **2007**, *129*, 13270–13276.
- (21) Yuan, Y.; Deng, K.; Liu, Y.; Tang, C.; Lu, G.; Yang, J.; Wang, X. *Eur. Phys. J. D* **2006**, *40*, 243–246.
- (22) Cohen, A. J.; Mori-Sánchez, P.; Yang, W. *Science* **2008**, *321*, 792–794.
- (23) Tran, V. T.; Iftner, C.; Hendrickx, M. F. A. *J. Phys. Chem. A* **2013**, *117*, 5613–5619.
- (24) Tran, V. T.; Hendrickx, M. F. A. *J. Phys. Chem. A* **2013**, *117*, 3227–3234.
- (25) Tran, V. T.; Hendrickx, M. F. A. *J. Chem. Phys.* **2011**, *135*, 094505.
- (26) Tran, V. T.; Hendrickx, M. F. A. *J. Chem. Theory Comput.* **2011**, *7*, 310–319.
- (27) Hou, X.-J.; Gopakumar, G.; Lievens, P.; Nguyen, M. T. *J. Phys. Chem. A* **2007**, *111*, 13544–13553.
- (28) Ivanov, A. S.; Zhang, X.; Wang, H.; Boldyrev, A. I.; Gantefoer, G.; Bowen, K. H.; Černušák, I. *J. Phys. Chem. A* **2015**, *119*, 11293–11303.
- (29) Rayón, V. M.; Redondo, P.; Barrientos, C.; Largo, A. *J. Phys. Chem. A* **2007**, *111*, 6345–6353.
- (30) Majumdar, D.; Roszak, S.; Balasubramanian, K. *J. Chem. Phys.* **2003**, *118*, 130–141.
- (31) Tran, V. T.; Tran, Q. T. *J. Phys. Chem. A* **2016**, *120*, 5950–5957.
- (32) Tran, Q. T.; Tran, V. T. *J. Chem. Phys.* **2016**, *144*, 214305.
- (33) Lee, C.; Yang, W.; Parr, R. G. *Phys. Rev. B* **1988**, *37*, 785–789.
- (34) Becke, A. D. *Phys. Rev. A* **1988**, *38*, 3098–3100.
- (35) Becke, A. D. *J. Chem. Phys.* **1993**, *98*, 5648–5652.
- (36) Perdew, J. P. *Phys. Rev. B* **1986**, *33*, 8822–8824.
- (37) Woon, D. E.; Dunning, T. H. *J. Chem. Phys.* **1993**, *98*, 1358–1371.
- (38) Balabanov, N. B.; Peterson, K. A. *J. Chem. Phys.* **2005**, *123*, 064107.

- (39) Frisch, M. J.; Trucks, G. W.; Schlegel, H. B.; Scuseria, G. E.; Robb, M. A.; Cheeseman, J. R.; Scalmani, G.; Barone, V.; Mennucci, B.; Petersson, G. A.; Nakatsuji, H.; Caricato, M.; Li, X.; Hratchian, H. P.; Izmaylov, A. F.; Bloino, J.; Zheng, G.; Sonnenberg, J. L.; Hada, M.; Ehara, M.; Toyota, K.; Fukuda, R.; Hasegawa, J.; Ishida, M.; Nakajima, T.; Honda, Y.; Kitao, O.; Nakai, H.; Vreven, T.; Montgomery Jr., J. A.; Peralta, J. E.; Ogliaro, F.; Bearpark, M.; Heyd, J. J.; Brothers, E.; Kudin, K. N.; Staroverov, V. N.; Kobayashi, R.; Normand, J.; Raghavachari, K.; Rendell, A.; Burant, J. C.; Iyengar, S. S.; Tomasi, J.; Cossi, M.; Rega, N.; Millam, J. M.; Klene, M.; Knox, J. E.; Cross, J. B.; Bakken, V.; Adamo, C.; Jaramillo, J.; Gomperts, R.; Stratmann, R. E.; Yazyev, O.; Austin, A. J.; Cammi, R.; Pomelli, C.; Ochterski, J. W.; Martin, R. L.; Morokuma, K.; Zakrzewski, V. G.; Voth, G. A.; Salvador, P.; Dannenberg, J. J.; Dapprich, S.; Daniels, A. D.; Farkas, Ö.; Foresman, J. B.; Ortiz, J. V.; Cioslowski, J.; Fox, D. J. Gaussian-09 Revision E.01., Gaussian Inc. Wallingford CT 2009.
- (40) Andersson, K.; Malmqvist, P.-Å.; Roos, B. O. *J. Chem. Phys.* **1992**, *96*, 1218–1226.
- (41) Roos, B. O.; Lindh, R.; Malmqvist, P.-Å.; Veryazov, V.; Widmark, P.-O. *J. Phys. Chem. A* **2005**, *109*, 6575–6579.
- (42) Roos, B. O.; Lindh, R.; Malmqvist, P.-Å.; Veryazov, V.; Widmark, P.-O. *J. Phys. Chem. A* **2004**, *108*, 2851–2858.
- (43) Reiher, M.; Wolf, A. *J. Chem. Phys.* **2004**, *121*, 10945–10956.
- (44) Aquilante, F.; Autschbach, J.; Carlson, R. K.; Chibotaru, L. F.; Delcey, M. G.; De Vico, L.; Fdez. Galván, I.; Ferré, N.; Frutos, L. M.; Gagliardi, L.; Garavelli, M.; Giussani, A.; Hoyer, C. E.; Li Manni, G.; Lischka, H.; Ma, D.; Malmqvist, P. Å.; Müller, T.; Nenov, A.; Olivucci, M.; Pedersen, T. B.; Peng, D.; Plasser, F.; Pritchard, B.; Reiher, M.; Rivalta, I.; Schapiro, I.; Segarra-Martí, J.; Stenrup, M.; Truhlar, D. G.; Ungur, L.; Valentini, A.; Vancoillie, S.; Veryazov, V.; Vysotskiy, V. P.; Weingart, O.; Zapata, F.; Lindh, R. *J. Comput. Chem.* **2016**, *37*, 506–541.
- (45) Werner, H.-J.; Knowles, P. J.; Knizia, G.; Manby, F. R.; Schütz, M. *Wiley Interdiscip. Rev.: Comput. Mol. Sci.* **2012**, *2*, 242–253.
- (46) Raffaele, B.; Amedeo, C.; Andrea, P. *Can. J. Chem.* **2013**, *91*, 495–504.
- (47) Kitsopoulos, T. N.; Chick, C. J.; Zhao, Y.; Neumark, D. M. *J. Chem. Phys.* **1991**, *95*, 1441–1448.
- (48) Arnold, C. C.; Kitsopoulos, T. N.; Neumark, D. M. *J. Chem. Phys.* **1993**, *99*, 766–768.
- (49) Nimlos, M. R.; Harding, L. B.; Ellison, G. B. *J. Chem. Phys.* **1987**, *87*, 5116–5124.

Chapter 4

Electronic Structures of Titanium Digermanium and Its Anion

This chapter is based on the paper:

Pham, L. N.; Nguyen, M. T. Titanium Digermanium: Theoretical Assignment of Electronic Transitions Underlying Its Anion Photoelectron Spectrum. *J. Phys. Chem. A* 2017, 121, 1940–1949. Reprinted with permission from *Journal of Chemical Theory and Computation*. Copyright 2018. American Chemical Society. [The Supporting Information is available online.](#)

My contribution to this work was theoretical calculations, data analysis, discussion, writing of the first draft and revision.

4.1 Introduction

Germanium is well-known for its use as semiconductor materials in electronic devices.^{1–3} Because of the high p-type mobility, germanium has been placed under consideration for potential future high-performance electronic transistors.¹ Similar to silicon-based

materials, metal-doped germanium materials are believed to bring in improved properties in comparison to the pure ones.^{4–11} In the intensive search for such new materials, several transition metal-doped germanium clusters have been experimentally synthesized and characterized.^{12–21}

In the above-mentioned experimental syntheses, photoelectron (PE) spectroscopy has frequently been used as a powerful technique to characterize both geometrical and electronic structures of the clusters found, in conjunction with ab initio quantum chemical calculations.^{13–16,19,21} Accordingly, the existence of several small germanium clusters containing metals has been confirmed. In fact, properties of a few series of metal-doped germanium clusters were systematically reported,^{15,16,19,21–23} such as $\text{TiGe}_n^{-/0}$, $\text{VGe}_n^{-/0}$, $\text{CoGe}_n^{-/0}$, $\text{RuGe}_n^{-/0}$, and $\text{AuGe}_n^{-/0}$. Besides, complicated germanium clusters doped with transition or lanthanide metals were also studied.¹⁴ Alongside the lowest ionization energies (IEs) that are usually responsible for electronic transitions between anionic and neutral ground states recorded in anion PE spectra, other higher IEs are obtained as well. These higher IEs correspond to different excited states of neutral clusters.

Of the series of germanium clusters doped with transition metals mentioned above, the triatomic anion TiGe_2^- was the simplest cluster to experimentally synthesize and characterize.²² After being generated in a laser vaporization source, the mass-selected anion TiGe_2^- was guided into the laser beam with an energy of 266 nm to measure detachment energies. Measurement at this level of photon energy showed four ionization bands in the PE spectrum of TiGe_2^- . The lowest band had an adiabatic detachment energy (ADE) of 0.78 eV and a vertical detachment energy (VDE) of 1.06 eV. There were also three more bands observed with higher electron binding energies of 1.44, 2.05, and 2.49 eV. Previous DFT calculations using both B3LYP and HSE06 functionals on geometrical structures of $\text{TiGe}_2^{-/0}$ pointed out that both states have a cyclic C_{2v} structure.^{22,24} The anionic and neutral ground electronic states were believed to be the $^2\text{A}_2$ and $^3\text{B}_1$, respectively.²² Therefore, the lowest-lying band in the PE spectrum of TiGe_2^- was assigned to the $^2\text{A}_2 \longrightarrow ^3\text{B}_1$ transition.

As far as we are aware, there is no information about the excited states and corresponding electronic transitions underlying the bands in PE spectra of any germanium cluster containing transition metals. As TiGe_2^- is the simplest experimentally obtained species among the metal-doped germanium clusters reported, we surprisingly recognized from preliminary calculations that a low-spin doublet state cannot be the ground state of the

anion TiGe_2^- , as reported in the previous DFT study. In this context, we set out to more deeply investigate the electronic structure of the triatomic TiGe_2 in both anionic and neutral states. All electronic states of the neutral TiGe_2 were determined in order to elucidate the four bands seen in the PE spectrum of TiGe_2^- .

4.2 Computational Details

As $\text{TiGe}_2^{-/0}$ clusters have two low-lying isomers, being the cyclic and the linear ones, depicted in Figure 4.1, the simplest step of our calculation scheme is to confirm the higher stability of the cyclic isomer in both anionic and neutral forms.^{22,24} Because our preliminary calculations showed that the M06-L functional appears to be more suitable than other popular functionals in the determination of IEs for TiGe_2^- and this functional also performs well for transition metals,^{25,26} we use the M06-L functional²⁶ to rapidly locate the equilibrium geometries of two low-lying isomers (Figure 4.1) of $\text{TiGe}_2^{-/0}$. Because the primary purpose of this step is to identify the global energy minimum, geometries of all spin multiplicities from singlet to octet of $\text{TiGe}_2^{-/0}$ are taken into account during DFT geometry optimizations. All unrestricted open-shell DFT calculations in this step are carried out using the Gaussian 09E.01 suite of program packages²⁷ and employ the correlation consistent polarized triple- ζ basis set aug-cc-pVTZ,^{28,29} unless otherwise noted. Although the cyclic isomers of $\text{TiGe}_2^{-/0}$ previously proved to have spatial symmetry of C_{2v} ,²² no geometrical symmetry is imposed during this optimization step, which allows both linear and cyclic low-lying isomers to be fully optimized (Figure 4.1).

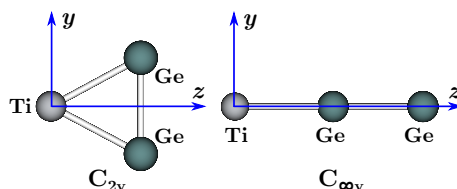


Figure 4.1: Two low-lying isomers of $\text{TiGe}_2^{-/0}$ and the Cartesian coordinate axes.

As our investigated systems contain transition metals, all spatial states of $\text{TiGe}_2^{-/0}$ are again optimized at a higher level of theory, namely, the CASPT2,³⁰ which is able to better treat correlation energy. To perform such calculations, predefined coordinate systems should be applied to the target $\text{TiGe}_2^{-/0}$. As seen in Figure 4.1, for the cyclic isomer, the molecular

plane is chosen to be the yz -plane, and the titanium atom is located at the origin of the Cartesian coordinate system; the Ge–Ge bonding is perpendicular to the z -axis. The active space and numbers of electrons included in the active space should also be defined. For germanium, all of the 4p valence orbitals are treated in the active space because our probing calculations indicated that 4s and inner orbitals do not involve in electronic transitions. As for titanium, six valence orbitals including one 4s and five 3d ones are taken into account. In total, 12 orbitals in the active space are statically correlated. Because titanium has a total of four electrons in the 4s and 3d subshells and there are two electrons in the 4p subshell of germanium, the total number of electrons in the active space amounts to eight for the neutral TiGe_2 and nine for the anion TiGe_2^- . The ANO-RCC basis set with [7s6p4d3f2g] contraction for titanium³¹ and [6s5p3d1f] contraction for germanium³² is used for this geometry optimization step with the assistance of the Molcas 8.1 package.³³

To increase the reliability of relative energies in the determination of the global ground states, one more geometry optimization using the single-reference functional M06-L is then conducted in conjunction with the triple- ζ basis set aug-cc-pVTZ-DK on the basis of leading configurations drawn above. In addition, single-point calculations using CASPT2-optimized geometries are also carried out, utilizing the coupled-cluster theory RCCSD(T) and the n -electron valence state perturbation theory NEVPT2. The latter is used to synergistically draw out the ground states of $\text{TiGe}_2^{-/0}$ because a few lower spin states cannot be described with single-reference methods, and more importantly, there is a competition for the anionic ground state at the CASPT2 level among the energetically nearly degenerate states. For the sake of convenience, RCCSD(T) calculations use the same triple- ζ basis set used in M06-L optimizations. Multireference single-point CASSCF/NEVPT2³³ calculations employ the larger quintuple- ζ basis set, aug-cc-pV5Z-DK. All obtained energies for low-lying states allow us to confidently identify the ground states of both anionic and neutral forms. Once the ground states are identified, both ADEs and VDEs can be evaluated. The difference between VDE and ADE procedures concerns the geometries of final states, which are the CASPT2-optimized geometrical parameters of every involved neutral state and the CASPT2 optimal geometry of the anionic initial state for ADEs and VDEs, respectively. To efficiently reproduce the correlation energy at single-reference levels, such as M06-L and RCCSD(T), we increase the basis set size to the quintuple- ζ aug-cc-pV5Z-DK when evaluation of ADEs and VDEs is conducted. All single-reference DFT and RCCSD(T), and CASSCF/NEVPT2 calculations are carried out using Molpro 2012.³⁴ Because both germanium and titanium are heavy elements, all electron scalar relativistic effects are taken into account by making use of the second-

order Douglas-Kroll-Hess Hamiltonian (denoted as DK).³⁵ All relative energies are derived without ZPE corrections because for these small species their ZPEs are quite similar and do not significantly affect the relative positions on the potential surfaces.³⁶

It should be mentioned that the true energy minima obtained from geometrical optimizations at the M06-L and CASPT2 levels are confirmed by subsequent vibrational frequency analyses (without any negative vibrational frequency). This step not only ensures the identity of each structure, but also provides us with coordinates of the vibration normal modes, which are in turn used for multidimensional Franck-Condon factor integrations. Our basic evaluation shows that single-reference methods are not energetically efficient to describe $\text{TiGe}_2^{-/0}$, and hence, we use vibrational frequencies of the normal modes computed at the CASPT2 level. At this level, several final states that are responsible for the bands in the PE spectrum of TiGe_2^- can be accessed, and their normal modes of vibrations are numerically obtained. The multidimensional Franck-Condon factors are simulated with the MolFC code.³⁷

4.3 Results and Discussion

4.3.1 Ground and Low-Lying States of $\text{TiGe}_2^{-/0}$.

Relative energies of the cyclic and linear isomers in several spin multiplicities are collected and graphically visualized in Figure S1 of the [Supporting Information](#) (available online). The cyclic isomer is confirmed to be more stable than the linear counterpart for both anionic and neutral forms. For the anion, a quartet state of the cyclic isomer emerges as the most stable one using the M06-L functional. Surprisingly, this result completely disagrees with the conclusion previously reported²² that the doublet state ${}^2\text{A}_2$ of the cyclic isomer is the most stable anionic form. Such a discrepancy in the identity of the anionic ground state stimulates us to proceed a further step to construct more elaborated TiGe_2 hypersurfaces in both low- and high-spin states.

Figure S2a ([ESI](#)) shows the adiabatic potential surface of both doublet and quartet states using the M06-L functional when the Ti–Ge bond length increases from 2.1 to 3.1 Å. Both potential energy surfaces strongly support the conclusion mentioned above. Therefore, a quartet state can be probed as the anionic ground state. In addition, one can rule out

the high-spin states such as the sextet and octet because they are located at quite high energy levels on the potential surface of TiGe_2^- . Thus, these spin states are ignored in the following discussion.

Turning now to the neutral form, a triplet cycle is clearly the most stable isomer. Conversely, the high-spin septet states are characterized to be quite high relative energies in comparison to the triplet state. This high-spin state as well as the linear isomer is therefore not considered in subsequent steps because they are not significantly populated in photodetachment processes.

In order to safely identify the global ground states, further optimization is performed using two methods, CASPT2 and M06-L, and single-point electronic energies of the obtained states at the RCCSD(T) and CASSCF/NEVPT2 levels are also calculated. These relative energies and CASPT2 geometries are tabulated in Table 4.1. In this step, all methods consistently identify the $^4\text{B}_1$ and $^3\text{B}_1$ states as the ground states of the anion and the neutral, respectively. Both single-reference methods also point toward the $^4\text{B}_1$ as the energetically lowest anionic state. M06-L and RCCSD(T) estimate that the $^4\text{B}_1$ is 0.33 and 0.12 eV more stable than the first excited state $^2\text{A}_1$ of the anion. There is also a significant difference of 0.19 eV between the $^4\text{B}_1$ and the second excited state $^2\text{A}_2$ of TiGe_2^- at the RCCSD(T) level. Note that the $^2\text{A}_2$ was assigned to be the ground anionic state in a previous study.²²

The situation gets more complex at the CASPT2 and NEVPT2 levels, in which the ground, first, and second excited states of TiGe_2^- are determined to lie very close to each other. The $^2\text{A}_1$ state is only 0.01 and 0.02 eV higher than the $^4\text{B}_1$ at the CASPT2 and NEVPT2 levels, respectively. For the $^2\text{A}_2$ state, the CASPT2 and NEVPT2 produce relative energies of 0.08 and 0.06 eV, respectively. Accordingly, these three states are quasi-degenerate at multireference theory.

Such a degeneracy of many states is encountered as well in the neutral TiGe_2 . Our calculated relative energies confirm the neutral ground state $^3\text{B}_1$, in full agreement with previous conclusions,^{22,24} even though both $^3\text{B}_1$ and $^3\text{B}_2$ states seem to be nearly degenerate at several levels (RCCSD(T), CASPT2, and NEVPT2). The $^3\text{B}_1$ state is \sim 0.05 eV lower in energy than the $^3\text{B}_2$. With regard to higher-lying excited states, three singlet states $^1\text{A}_1$, $^1\text{B}_1$, and $^1\text{B}_2$ are determined to lie higher than the ground $^3\text{B}_1$ by an amount of \sim 0.50 eV at both CASPT2 and NEVPT2 levels. Interestingly, these three singlet states seem also nearly degenerate, and hence, this could result in a complicated determination of

Table 4.1: Determination of Ground States of Both Anionic and Neutral TiGe_2 at Different Levels

species	state	CASPT2 geometry (\AA)		relative energy (eV) ^(a)			
		Ti-Ge	Ge-Ge	M06L	RCCSD(T)	NEVPT2	CASPT2
cyclic TiGe_2^-	$^2\text{A}_1$	2.44	2.50	0.33	0.12	0.02	0.01
	$^2\text{B}_1$	2.50	2.35			0.22	0.25
	$^2\text{B}_2$	2.47	2.36	0.70	0.31	0.26	0.28
	$^2\text{A}_2$	2.40	2.58	0.33	0.19	0.06	0.08
	$^4\text{A}_1$	2.46	2.42	0.43	0.47	0.39	0.39
	$^4\text{B}_1$	2.50	2.35	0.00	0.00	0.00	0.00
	$^4\text{B}_2$	2.49	2.37	0.48	0.18	0.22	0.26
	$^4\text{A}_2$	2.57	2.33	0.42	0.34	0.49	0.38
cyclic TiGe_2	$^1\text{A}_1$	2.41	2.48	1.81	1.65	1.50	1.38
	$^1\text{B}_1$	2.42	2.43			1.57	1.35
	$^1\text{B}_2$	2.45	2.39			1.62	1.33
	$^1\text{A}_2$	2.44	2.54			2.31	2.15
	$^3\text{A}_1$	2.59	2.33	2.16	2.74	2.18	2.07
	$^3\text{B}_1$	2.43	2.41	1.15	1.33	1.07	0.90
	$^3\text{B}_2$	2.44	2.39	1.37	1.37	1.14	0.94
	$^3\text{A}_2$	2.54	2.34	1.94	1.98	2.10	1.98
	$^5\text{A}_1$	2.57	2.33	2.19	2.76	2.53	2.37
	$^5\text{B}_1$	2.54	2.54	2.54	2.72	2.53	2.28
	$^5\text{B}_2$	2.79	2.25	2.64	2.65	2.92	2.75
	$^5\text{A}_2$	2.81	2.34	2.82	2.88	3.34	3.01

^(a) RCCSD(T) and NEVPT2 energies were obtained with the use of CASPT2-optimized geometries. All relative energies were determined without ZPE corrections.

electronic transitions (final states).

4.3.2 Electronic Structures and One-Electron Electronic Transitions

Investigation into the electronic structure of both anionic and neutral ground states allows us to know whether the one-electron transition between two ground states, which gives rise to the lowest recorded band in the anion spectrum of TiGe_2^- , is possible. The leading

configurations of many states obtained from CASSCF wave functions and their weights are given in Table 4.2.

Let us first thoroughly examine the anionic ground state because most bands that appeared in the PE spectrum originate from it. The anionic state ${}^4\text{B}_1$ is determined by three singly occupied orbitals a_1 , b_2 , and a_2 and three doubly occupied ones as noted in Table 4.2. The three singly occupied orbitals are largely contributed to by valence orbitals of titanium. On the basis of the CASSCF wave function, the totally symmetric orbital 19a_1 , one of three singly occupied molecular orbitals (MOs), is composed mainly of the metallic 4s orbital, while the other two MOs 14b_2 and 5a_2 are dominantly contributed to by 3d_{yz} and 3d_{xy} orbitals, respectively. The doubly occupied MOs 17a_1 , 18a_1 , and 7b_1 are based on the six 4p orbitals of the Ge_2 moiety. Similar to the electronic structure of Ge_2 ,³⁸ the six 4p orbitals of the Ge_2 moiety can form one bonding σ_g and two π_u MOs. With graphic assistance from the orbital shape in Figure 4.2, it is able to exactly map the original components of these MOs. Apparently, the two π_u orbitals 18a_1 and 7b_1 are built up from 4p_z and 4p_x atomic orbitals (AOs) of Ge, and the σ_g , being the 17a_1 , is from an overlap between two 4p_y AOs. For the sake of convenience in solving PE bands in a following step, the leading configuration of ${}^4\text{B}_1$ can be formulated in another form as $[... \sigma_g^2 \pi_{4p_z}^2 4s^1 \pi_{4p_x}^2 3d_{yz}^1 3d_{xy}^1]$.

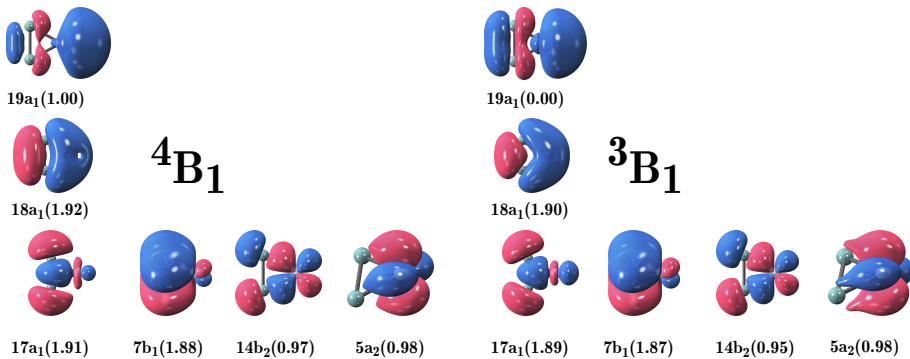


Figure 4.2: Occupied pseudonatural orbitals in the active spaces of states ${}^4\text{B}_1$ and ${}^3\text{B}_1$ (CASSCF wave functions). The average occupation numbers are given in parentheses. The metal atom Ti is located on the right-hand side.

Table 4.2: Leading Configurations of the Two Most Stable Anionic Ground States and of Neutral Ones

state	leading configuration	weight (%)	transition	ionization orbital
$^4\text{B}_1$	$17\text{a}_1^2 18\text{a}_1^2 19\text{a}_1^0 20\text{a}_1^0 21\text{a}_1^0 7\text{b}_1^2 8\text{b}_1^0 14\text{b}_2^1 5\text{a}_2^1$	83		
$^2\text{A}_1$	$17\text{a}_1^2 18\text{a}_1^2 19\text{a}_1^0 20\text{a}_1^1 21\text{a}_1^0 7\text{b}_1^2 8\text{b}_1^0 14\text{b}_2^2 5\text{a}_2^0$	71		
$^2\text{A}_2$	$17\text{a}_1^2 18\text{a}_1^2 19\text{a}_1^0 20\text{a}_1^0 21\text{a}_1^0 7\text{b}_1^2 8\text{b}_1^0 14\text{b}_2^2 5\text{a}_2^1$	73		
$^1\text{A}_1$	$17\text{a}_1^2 18\text{a}_1^2 19\text{a}_1^0 20\text{a}_1^0 21\text{a}_1^0 7\text{b}_1^2 8\text{b}_1^0 14\text{b}_2^2 5\text{a}_2^0$	76	$^2\text{A}_1 \longrightarrow ^1\text{A}_1$	20a_1 (Ti: $3\text{d}_{x^2-y^2}$)
			$^2\text{A}_2 \longrightarrow ^1\text{A}_1$	$^5\text{a}_2$ (Ti: 3d_{xy})
$^1\text{B}_1$	$17\text{a}_1^2 18\text{a}_1^2 19\text{a}_1^0 20\text{a}_1^0 21\text{a}_1^0 7\text{b}_1^2 8\text{b}_1^0 14\text{b}_2^1 5\text{a}_2^1$	74		
$^1\text{B}_2$	$17\text{a}_1^2 18\text{a}_1^2 19\text{a}_1^0 20\text{a}_1^1 21\text{a}_1^0 7\text{b}_1^2 8\text{b}_1^0 14\text{b}_2^1 5\text{a}_2^0$	72		
$^1\text{A}_2$	$17\text{a}_1^2 18\text{a}_1^1 19\text{a}_1^0 20\text{a}_1^0 21\text{a}_1^0 7\text{b}_1^2 8\text{b}_1^0 14\text{b}_2^2 5\text{a}_2^1$	57		
$^3\text{A}_1$	$17\text{a}_1^2 18\text{a}_1^2 19\text{a}_1^0 20\text{a}_1^1 21\text{a}_1^1 7\text{b}_1^2 8\text{b}_1^0 14\text{b}_2^0 5\text{a}_2^0$	85		
$^3\text{B}_1$	$17\text{a}_1^2 18\text{a}_1^2 19\text{a}_1^0 20\text{a}_1^0 21\text{a}_1^0 7\text{b}_1^2 8\text{b}_1^0 14\text{b}_2^1 5\text{a}_2^1$	80	$^4\text{B}_1 \longrightarrow ^3\text{B}_1$	19a_1 (Ti: 4s)
			$^2\text{A}_2 \longrightarrow ^3\text{B}_1$	14b_2 (Ti: 3d_{yz})
$^1\text{B}_2$	$17\text{a}_1^2 18\text{a}_1^2 19\text{a}_1^0 20\text{a}_1^1 21\text{a}_1^0 7\text{b}_1^2 8\text{b}_1^0 14\text{b}_2^1 5\text{a}_2^0$	83		
$^2\text{B}_2$	$17\text{a}_1^2 18\text{a}_1^2 19\text{a}_1^1 20\text{a}_1^0 21\text{a}_1^0 7\text{b}_1^2 8\text{b}_1^0 14\text{b}_2^1 5\text{a}_2^0$	41	$^4\text{B}_1 \longrightarrow ^2\text{B}_2$	5a_2 (Ti: 3d_{xy})
$^3\text{B}_2$	$17\text{a}_1^2 18\text{a}_1^2 19\text{a}_1^0 20\text{a}_1^0 21\text{a}_1^0 7\text{b}_1^2 8\text{b}_1^1 14\text{b}_2^1 5\text{a}_2^1$	44		
$^1\text{A}_2$	$17\text{a}_1^2 18\text{a}_1^2 19\text{a}_1^0 20\text{a}_1^0 21\text{a}_1^1 7\text{b}_1^2 8\text{b}_1^0 14\text{b}_2^0 5\text{a}_2^1$	86		
$^2\text{A}_2$	$17\text{a}_1^2 18\text{a}_1^2 19\text{a}_1^1 20\text{a}_1^0 21\text{a}_1^0 7\text{b}_1^2 8\text{b}_1^0 14\text{b}_2^0 5\text{a}_2^1$	60	$^4\text{B}_1 \longrightarrow ^2\text{A}_2$	14b_2 (Ti: 3d_{yz})
$^3\text{A}_2$	$17\text{a}_1^2 18\text{a}_1^2 19\text{a}_1^0 20\text{a}_1^0 21\text{a}_1^0 7\text{b}_1^2 8\text{b}_1^1 14\text{b}_2^1 5\text{a}_2^0$	79		
$^1\text{A}_1$	$17\text{a}_1^2 18\text{a}_1^2 19\text{a}_1^0 20\text{a}_1^0 21\text{a}_1^0 7\text{b}_1^2 8\text{b}_1^1 14\text{b}_2^1 5\text{a}_2^1$	83		
$^2\text{A}_1$	$17\text{a}_1^2 18\text{a}_1^2 19\text{a}_1^1 20\text{a}_1^0 21\text{a}_1^0 7\text{b}_1^2 8\text{b}_1^0 14\text{b}_2^1 5\text{a}_2^1$	78	$^4\text{B}_1 \longrightarrow ^2\text{A}_1$	7b_1 (Ge: 4p_x)

Continued on next page

Table 4.2 – continued from previous page

state	leading configuration	weight (%)	transition	ionization orbital
3 ⁵ A ₁	17a ₁ ² 18a ₁ ² 19a ₁ ⁰ 20a ₁ ⁰ 21a ₁ ¹ 7b ₁ ¹ 8b ₁ ⁰ 14b ₂ ¹ 5a ₂ ¹	76		
1 ⁵ B ₁	17a ₁ ² 18a ₁ ² 19a ₁ ⁰ 20a ₁ ⁰ 21a ₁ ⁰ 7b ₁ ¹ 8b ₁ ¹ 14b ₂ ¹ 5a ₂ ¹	81		
2 ⁵ B ₁	17a ₁ ² 18a ₁ ¹ 19a ₁ ¹ 20a ₁ ⁰ 21a ₁ ⁰ 7b ₁ ² 8b ₁ ⁰ 14b ₂ ¹ 5a ₂ ¹	74	⁴ B ₁ → ² 5B ₁	18a ₁ (Ge: 4p _y)
3 ⁵ B ₁	17a ₁ ¹ 18a ₁ ² 19a ₁ ¹ 20a ₁ ⁰ 21a ₁ ⁰ 7b ₁ ² 8b ₁ ⁰ 14b ₂ ¹ 5a ₂ ¹	75	⁴ B ₁ → ³ 5B ₁	17a ₁ (Ge: 4p _z)
1 ⁵ B ₂	17a ₁ ² 18a ₁ ¹ 19a ₁ ¹ 20a ₁ ¹ 21a ₁ ⁰ 7b ₁ ² 8b ₁ ⁰ 14b ₂ ¹ 5a ₂ ⁰	89		
1 ⁵ A ₂	17a ₁ ² 18a ₁ ² 19a ₁ ¹ 20a ₁ ¹ 21a ₁ ⁰ 7b ₁ ¹ 8b ₁ ⁰ 14b ₂ ¹ 5a ₂ ⁰	91		

As analyzed above, the anionic 2A_1 is a nearly degenerate state of the state 4B_1 at both levels CASPT2 and NEVPT2. In this situation, multireference methods are expected to reproduce more reliable results because many states of $TiGe_2^{-/0}$ cannot be well-described by single-reference wave functions. Therefore, we believe that the 2A_1 state can be somehow populated in experiment and thereby involved in the spectral appearance. As expected, the leading configuration of the 2A_1 state (Table 4.2) is dominated by the singly occupied orbital $20a_1$. The relevant pseudonatural orbital is constructed from a primary part $3d_{x^2-y^2}$ and a minor amount of $4s$, which are both valence orbitals of titanium. The four doubly occupied orbitals of 2A_1 include the $17a_1$, $18a_1$, $7b_1$, and $14b_2$. Thus, electronic components are chiefly the same as those of the anionic ground state 4B_1 . In terms of orbital components, the nearly degenerate state 2A_1 can be rewritten as $[... \sigma_g^2 \pi_{4p_z}^2 3d_{(x^2-y^2)}^1 \pi_{4p_x}^2 3d_{yz}^2]$.

Normally, the lowest-lying band in an anion PE spectrum is the result of a one-electron transition between the anionic and neutral ground states. Let us briefly consider the electronic structure of the neutral 3B_1 . In Table 4.2, the leading orbital configuration of the 3B_1 shows a similarity of its orbital components in comparison to the anionic state 4B_1 . Indeed, the neutral state has two singly occupied MOs $14b_2$ and $5a_2$, together with three doubly occupied MOs $17a_1$, $18a_1$, and $7b_1$ (quite similar to those of 4B_1). In principle, the electron located in orbital $19a_1$ of 4B_1 can be removed, giving rise to the neutral 3B_1 , and therefore, the neutral leading configuration of the state 3B_1 can be assigned as $[... \sigma_g^2 \pi_{4p_z}^2 4s^0 \pi_{4p_x}^2 3d_{yz}^1 3d_{xy}^1]$. The $4s$ electron of titanium can thus be ionized from the anionic state 4B_1 under the high-energy laser beam to generate neutral 3B_1 .

Within the scope of the treated active spaces, we can predict six possible one-electron ionizations starting from the anionic ground state 4B_1 . Six electrons located in six occupied orbitals can be removed, one by one, to form six corresponding final states, including the neutral ground state 3B_1 . Two 3d MOs ($14b_2$ and $5a_2$) can participate in one-electron photodetachment, and the proposed final electronic states are $^2^3A_2$ and $^2^3B_2$, respectively, whose leading configurations can be found in Table 4.2. Out of the metallic valence orbitals, three other one-electron ionizations can individually occur in three doubly occupied orbitals σ_g^2 , $\pi_{4p_z}^2$, and $\pi_{4p_x}^2$, noted as $17a_1$, $18a_1$, and $7b_1$ in the 4B_1 leading configuration, respectively. The corresponding electronic states are $^3^5B_1$, $^2^5B_1$, and $^2^5A_1$, whose leading configurations are also listed in Table 4.2. Apart from the above-mentioned states, other low-lying states cannot theoretically be final states of one-electron photoionization, simply because their electronic structures (as presented by leading configurations) cannot be the final leading configurations of one-electron detachments starting from the anionic ground

state.

The coefficient weights of leading configurations can quantitatively give an additional evaluation of the nature of corresponding states. When a system is well-described with single-reference wave functions,³⁶ all coefficient weights of leading configurations amount to $\geq 85\%$ and are nearly equal to each other. For $\text{TiGe}_2^{-/0}$ (Table 4.2) most leading configurations of the states potentially taking part in one-electron transitions contribute to the corresponding electronic wave functions with coefficient weights of $\leq 80\%$. The only one over 80% (83% to be accurate) belongs to the anionic ground state $^4\text{B}_1$. This gives a reason why the anionic ground state, the nearly degenerate state, and all other final low-lying states are not well-described by single-reference wave functions. In other words, single-reference quantum chemical methods are again confirmed to be inappropriate for treating systems like $\text{TiGe}_2^{-/0}$.

Taking a closer look at electronic structures of the anionic states $^4\text{B}_1$, $^2\text{A}_1$, and $^2\text{A}_2$, remarkable quantitative differences between the leading coefficient weights of $^4\text{B}_1$ (83%) and those of two other states $^2\text{A}_1$ and $^2\text{A}_2$ (71 and 73%, respectively) can be noticed. A difference of $>10\%$ implies that single-reference methods cannot recover the correlation energy of these two excited states well. This explains why the previous single-reference study²² failed in locating the global ground state of TiGe_2^- on the potential hypersurface. On the basis of CASPT2 and NEVPT2 relative energies listed in Table 4.1, three state $^4\text{B}_1$, $^2\text{A}_1$, and $^2\text{A}_2$ are very close to each other in terms of energy and can accordingly be treated as quasi-degenerate states.

From the analysis above, three states $^4\text{B}_1$, $^2\text{A}_1$, and $^2\text{A}_2$ are energetically close and hence can be populated in the PE experiment. However, the anions TiGe_2^- were cooled down after being synthesized. On the basis of Maxwell-Boltzmann statistics, the population of $^2\text{A}_2$ (relative energy of ~ 0.1 eV at the CASPT2 level) is predicted to be negligible, and thus, insignificant intensities of PE signals originating from this state are expected. Two remaining states have closer relative energies, and the difference is ~ 0.01 eV. These two states could thus be more populated in the PE experiment, especially the anionic ground state $^4\text{B}_1$, and therefore could be taking part in possible electronic transitions underlying bands in the PE spectrum of TiGe_2^- .

We predict possible final neutral states in the situation that electronic transitions start from the anionic ground state $^4\text{B}_1$. If the nearly degenerate state $^2\text{A}_1$ is significantly populated in a PE experiment, signals of its one-electron ionizations can be observed in

the PE spectrum of TiGe_2^- . The relevant question is thus about the final states. On the basis of all low-lying neutral leading configurations, it is easy to add ${}^1\text{A}_1$ to the list of final states. In this case, the unique singly occupied MO 20a_1 , also known as $3d_{x^2-y^2}^1$, of the ${}^2\text{A}_1$ is detached, and the final state is expected to be ${}^1\text{A}_1$. This ionization arises from a 3d AO of titanium, and hence, its IE cannot be high in comparison to those starting from the Ge_2 moiety's orbitals. This electronic transition is listed in Table 4.2. The electronic transitions that hypothetically start from the second excited state (${}^2\text{A}_2$) of the anion can also be found in Table 4.2.

All possible one-electron transitions discussed in detail above are based on electronic configurations of involved states. To understand how charge distribution varies during the ionization processes, population analyses of all potential initial and final states are conducted. Mulliken atomic charge values are tabulated in Table 4.3. Formal oxidation states of each atom of the involved states are also figured out. Formal oxidation states can be inferred by considering the electronic structures of Ge_2^- and TiGe_2^- . Although there are still arguments over the electronic ground state of Ge_2^- , the two lowest-lying states are theoretically and experimentally established as nearly degenerate.^{38–42} Both states ${}^2\Pi_u$ [...] and ${}^2\Sigma_g^+$ [...] have one singly occupied orbital and can combine with titanium atoms to form TiGe_2^- . By comparing the leading orbital configurations of two lowest nearly degenerate states ${}^4\text{B}_1$ and ${}^2\text{A}_1$ of the triatomic species with that of Ge_2^- , one can recognize that the singly occupied orbital (π_u and/or σ_g) of the Ge_2^- moiety becomes doubly occupied in TiGe_2^- , which means that one electron is actually transferred from titanium to the Ge_2 moiety. Overall, the formal oxidation states of the Ti and Ge_2 parts are +1 and -2. The formal oxidation states of each part can be rewritten as $(\text{Ti})^{+1}(\text{Ge}_2)^{-2}$. As for the case of TiGe_2 , because the ground state ${}^3\text{B}_1$ is formed upon removal of one electron from the titanium 4s orbital, the positive oxidation number of Ti increases by +1. As a result, the stoichiometry with the formal oxidation numbers of Ti and Ge_2 for the neutral cluster can be formulated as $(\text{Ti})^{+2}(\text{Ge}_2)^{-2}$. When one electron is removed from Ge_2 , the formal oxidation number of the Ge_2 moiety is expected to be -1, and the formal charge of Ti is +1. This is the situation occurring in three neutral excited states ${}^2\text{A}_1$, ${}^2\text{B}_1$, and ${}^3\text{B}_1$ (cf. Table 4.2 for the corresponding leading configurations).

The Mulliken atomic charge values in Table 4.3 partially reflect the predicted formal oxidation numbers of atoms. The titanium atom always has a positive charge, whereas the germanium atom bears a negative one in all states considered. Especially, these well describe charge redistribution upon removal of one electron from the anionic TiGe_2^- .

The positive charge of Ti increases from +0.3 to +0.6 e because one-electron removal occurs from titanium's orbitals in the transition $^4\text{B}_1 \rightarrow ^3\text{B}_1$. A different situation occurs when one electron is removed from the Ge_2 ligand. Negative charge on the Ge atom is significantly reduced from -0.6 to -0.3 e in quintet states. Along with the changes of charge on directly related components from which one electron is removed (Ti and/or Ge_2), charge values on the remaining parts also vary upon relaxation to counteract one electron ionization happening in the other part. All of these changes can be seen in Table 4.3.

Table 4.3: Mulliken Atomic Charges of Ti and Ge Analyzed from CASSCF Wave Functions

state	Mulliken charge (e)		
	Ti	Ge	Ge
$^4\text{B}_1$	+0.28	-0.64	-0.64
$^2\text{A}_1$	+0.28	-0.64	-0.64
$^3\text{B}_1$	+0.64	-0.32	-0.32
$^1\text{A}_1$	+0.64	-0.32	-0.32
$^2\text{B}_2$	+0.64	-0.32	-0.32
$^2\text{A}_2$	+0.64	-0.32	-0.32
$^2\text{A}_1$	+0.50	-0.25	-0.25
$^2\text{B}_1$	+0.56	-0.28	-0.28
$^3\text{B}_1$	+0.54	-0.27	-0.27

4.3.3 Anion PE Spectrum and Band Assignments

All possible one-electron transition processes allowed by relevant selection rules are analyzed in detail above. Accordingly, nine totally allowed transitions are given in Table 4.2. Two transitions start from the lowly populated state $^2\text{A}_2$, whose ionization signals are believed to be overshadowed in part by other transitions and to be weak. The seven remaining transitions can be used as corresponding final states for four experimental bands, namely, X, A, B, and C bands seen in Figure 4.3. This makes our assignment more complicated, and it suffers from difficulties because the number of allowed transitions is about double the number of experimental bands. There should be more than one excited state of the neutral TiGe_2 simultaneously corresponding to a single experimental band. To fully understand all bands in the PE spectrum, we calculate the detachment energies (ADEs and VDEs) of all allowed transitions, and these values are presented in Table 4.4.

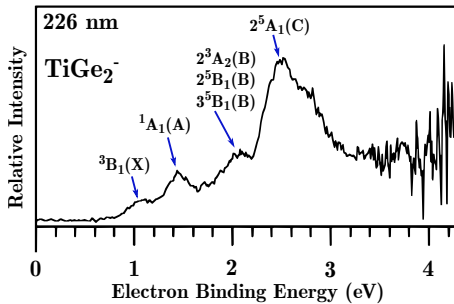


Figure 4.3: Experimental anion PE spectrum of TiGe_2^- (reproduced with permission from ref 22, Copyright 2014, RSC Publisher).

In general, two types of one-electron detachments can be theoretically predicted, as noted in Table 4.2. The ionization of one electron occurs, first from titanium's 4s and 3d orbitals, and second from germanium's 4p orbitals. Conventionally, the lowest ionization band X in an anion PE spectrum is the result of one-electron transition between the anionic and neutral ground states. For the case of TiGe_2^- , the X band can unambiguously be assigned to the electronic transition $^4\text{B}_1 \longrightarrow ^3\text{B}_1$, in which a 4s electron of titanium is detached under the laser beam of the photon.

A closer look at the ADEs (Table 4.4, values in parentheses) reveals that all single-reference methods substantially overestimate ADEs in comparison to the experimental value. To be more detailed, the experimental ADE is 0.78 eV, while the M06-L and RCCSD values are 1.15 and 1.34 eV, respectively. On the other hand, the CASPT2 estimate of 0.90 eV for this ADE is 0.12 eV larger than the experimental one. The NEVPT2 ADE is larger than the CASPT2 ADE by an amount of 0.17 eV. In comparison to experiment, the NEVPT2 value is not in good agreement with experiment, even though its deviation is within the error bar. Clearly, neither DFT nor RCCSD(T) methods are able to reproduce the ADE of the X band on the basis of the electronic transition $^4\text{B}_1 \longrightarrow ^3\text{B}_1$. This result makes us carefully reconsider the experimental band X of the PE spectrum.

The X band has not been well-resolved and is not clear enough to be a normal PE band (Figure 4.3). Thus, it would lead to a less precise determination of the ADE value. Although all of the states of $\text{TiGe}_2^{-/0}$ bear multireference features, this is the lowest-lying band, and an assignment for this X band is rather straightforward without much doubt of the basis of two ground states. Turning to the computed VDEs for this band, multireference

Table 4.4: Calculated VDE of TiGe_2^-

state	VDE (eV) ^(b)					state transition
	M06L	RCCSD(T)	NEVPT2	CASPT2	exptl.	
$^1\text{A}_1$	1.48	1.57	1.51	1.38	1.44 (A)	$^2\text{A}_1 \longrightarrow ^1\text{A}_1$
	1.51	1.54	1.53	1.34		$^2\text{A}_2 \longrightarrow ^1\text{A}_1$
$^3\text{A}_1$	2.42	2.23	2.22	2.13		
$^3\text{B}_1$	1.18 (1.15)	1.35 (1.34)	1.10 (1.07)	0.96 (0.90)	1.06 (X) (0.78) (X)	$^4\text{B}_1 \longrightarrow ^3\text{B}_1$ $^4\text{B}_1 \longrightarrow ^3\text{B}_1$
	0.94	1.33	1.21	0.92		$^2\text{A}_2 \longrightarrow ^3\text{B}_1$
	(0.82)	(1.14)	(1.01)	(0.82)		$^2\text{A}_2 \longrightarrow ^3\text{B}_1$
$^1\text{^3B}_2$	1.35	1.37	1.18	0.98		
$^2\text{^3B}_2$				0.92	1.06 (X)	$^4\text{B}_1 \longrightarrow 2^3\text{B}_2$
$^3\text{^3B}_2$				1.69		
$^1\text{^3A}_2$	1.95	2.00	2.11	1.99		
$^2\text{^3A}_2$				1.90	2.05 (B)	$^4\text{B}_1 \longrightarrow 2^3\text{A}_2$
$^3\text{^3A}_2$				1.48		
$^1\text{^5A}_1$	2.23	2.47	2.22	2.03		
$^2\text{^5A}_1$		2.62		2.31	2.49 (C)	$^4\text{B}_1 \longrightarrow 2^5\text{A}_1$
$^3\text{^5A}_1$				2.94		
$^1\text{^5B}_1$	2.60	2.78	2.56	2.42		
$^2\text{^5B}_1$				2.03	2.05 (B)	$^4\text{B}_1 \longrightarrow 2^5\text{B}_1$
$^3\text{^5B}_1$				2.16	2.05 (B)	$^4\text{B}_1 \longrightarrow 3^5\text{B}_1$
$^5\text{B}_2$	2.88	2.86	3.30	3.08		
$^5\text{A}_2$	3.13	3.04	3.58	3.16		

^(b) Values without ZPE corrections, calculated at single-reference methods (M06-L, RCCSD(T)) and second-order perturbation theories (NEVPT2 and CASPT2) on the basis of CASSCF wave functions. CASPT2-optimized geometries of final states are used for all VDE calculations. All single-reference methods and NEVPT2 employ the quintuple- ζ basis set aug-cc-pV5Z-DK. CASPT2 energies are computed with the ANO-RCC basis set used in geometry optimizations. Values in parentheses are adiabatic ADEs calculated with the use of CASPT2-optimized geometries of involving states.

wave function methods NEVPT2 and CASPT2 again prove their capability in dealing with multireference systems like $\text{TiGe}_2^{-/0}$. Indeed, while NEVPT2 reproduces a VDE of 1.10 eV, which is only 0.04 eV higher than the experimental VDE of 1.06 eV, CASPT2 gives a deviation of 0.10 eV below the experimental VDE. Of the single-reference methods, the M06-L functional seems to be a good option for reproducing the X band VDE with a

deviation of 0.12 eV.

The situation becomes more interesting as another electronic transition $^4B_1 \rightarrow 2^3B_2$ starting from the anionic ground state involves a detachment energy of 0.92 eV at the CASPT2 level, which lies in the region of the X band. However, the leading configuration of the final state 2^3B_2 has a coefficient weight of only 41%. Therefore, this state does not strongly contribute to the photodetachment signal observed. If the 2A_2 state, another nearly degenerate state of the anionic state 4B_1 at both CASPT2 and NEVPT2 levels, is somehow populated in experiment, the transition $^2A_2 \rightarrow 3^3B_1$ should be observable in the spectrum. Because all of the ADEs and VDEs predicted by CASPT2 and NEVPT2 methods place signals of this transition in the X band's range, its intensity is expected to be in part overshadowed by signals from the transition $^4B_1 \rightarrow 3^3B_1$. Overall, three electronic transitions can contribute to the X band, in which the ground-ground transition $^4B_1 \rightarrow 3^3B_1$ is mainly responsible for the observed intensity.

Starting from the 4B_1 , the next vertical IE is estimated to be ~ 2.0 eV (CASPT2). Indeed, seven final low-lying neutral states are positioned for this electron detachment (cf. Table 4.4 for these neutral states). However, only three of them, 2^3A_2 , 2^5B_1 , and 3^5B_1 , are allowed by the selection rule as analyzed above. At first, similar IEs of these states are quite surprising because the ionization processes occurring from two different formal types of orbitals with different levels of energy, 3d (14b₂) orbitals of Ti for 2^3A_2 and 4p (17a₁ and 18a₁) orbitals of the ligand Ge₂ for 2^5B_1 and 3^5B_1 , need equal amounts of photon energy (2.0 eV). Nevertheless, a closer look at the pseudonatural orbitals can explain the situation. As a matter of fact, the ionized orbitals are not pure 3d or 4p orbitals. On the one hand, two ionized orbitals σ_g (17a₁) and π_{4p_z} (18a₁) have significant contributions from the 4s and 3d AOs, and on the other hand, $3d_{yz}$ (14b₂) is interfered substantially with the 4p_z orbital of Ge₂ (cf. Figure 4.2 for more intuitive plots). Such contamination elevates energy levels of the MOs σ_g (17a₁) and π_{4p_z} (18a₁) and reduces that of the $3d_{yz}$ (14b₂) to new levels. As a consequence, three related ionization processes $^4B_1 \rightarrow 2^3A_2$, $^4B_1 \rightarrow 2^5B_1$, and $^4B_1 \rightarrow 3^5B_1$ are computed to have VDEs of 1.90, 2.03, and 2.16 eV, which all correspond to the experimental VDE of 2.05 eV of the B band. Because all three transitions start from the anionic ground state and are totally allowed by selection rules, they are likely to be simultaneously responsible for the experimental B band.

Beyond the B band, there is one band with higher detachment energy. This band has the highest experimental IE of 2.49 eV. Because it has a high VDE, one-electron detachments

underlying this band are expected to originate from the ligand orbitals. Correspondingly, our electronic analysis using the active space of CASSCF calculations proves that a one-electronic transition can give a high IE corresponding to the C band. This electronic transition, namely, $^4\text{B}_1 \longrightarrow 2^5\text{A}_1$, is the result of one-electron removals from the π_{4p_x} orbital of $^4\text{B}_1$. Unlike the features of other MOs originating from the Ge_2 moiety, the π_{4p_x} orbital is purely from $4p_x$. Thus, photodetachment of one electron from this MO is predicted to need a larger energy than that from the σ_g (17a_1) and π_{4p_z} (18a_1). The CASPT2 VDE of this transition (2.31 eV) is ~ 0.18 eV smaller than the experimental value of 2.49 eV. The RCCSD(T) value of 2.62 eV is ~ 0.13 eV above the experimental value, and this supports our attribution of the neutral state 2^5A_1 to the C band. In this context, the transition $^4\text{B}_1 \longrightarrow 2^5\text{A}_1$ is a key contributor to the C band appearance.

There is still one unsolved band, which is the A band characterized by a VDE of 1.44 eV in the experimental PE spectrum of TiGe_2^- . All possible one-electron transitions starting from the state $^4\text{B}_1$ were already taken into account to assign other bands of the spectrum. In addition, no appropriate allowed transitions would correspond to this band energetically. Therefore, the degenerate state $^2\text{A}_1$ of the anionic ground state can now be invoked as the likely initial state from which one-electron ionization can occur. As the IE associated with the A band is not so high (1.44 eV), one electron is expected to be removed from a 4s or a 3d orbital of titanium. This likely happens in the electronic transition $^2\text{A}_1 \longrightarrow ^1\text{A}_1$. More importantly, all predicted VDEs of this transition (in Table 4.4), at either single-reference or NEVPT2 and CASPT2 levels, are in good correlation with the experimental VDE of 1.44 eV. Deviation of theoretical estimates is around 0.10 eV. Accordingly, the A band is ascribed to the emergence of the low-spin state $^1\text{A}_1$. This result is quite similar to the situation of anionic vanadium dicarbide where a nearly degenerate anionic ground state is experimentally populated and gives rise to PE bands.⁴³ Another electronic transition $^2\text{A}_2 \longrightarrow ^1\text{A}_1$ should also be mentioned because it is totally allowed by transition rules and has a predicted VDE properly corresponding to the A band. Nevertheless, this transition originating from the less populated state $^2\text{A}_2$ cannot substantially affect the intensity of the transition $^2\text{A}_1 \longrightarrow ^1\text{A}_1$.

4.3.4 Franck-Condon Factor Simulations

As seen previously, three of the four bands in the PE spectrum of TiGe_2^- are proved to be the results of more than one electronic transitions. The only band purely caused by a

one-electron transition is the C band. Complicated contributions of multiple transitions to a band make multidimensional Franck-Condon factor simulations more difficult to give accurate reflection to a specific experimental band. Therefore, to simulate PE bands of TiGe_2^- more accurately, normal coordinates and vibrational frequencies of all accessible states underlying and/or contributing to these bands are utilized to calculate multidimensional Franck-Condon factors with up to 15 quanta. Technically, the vibrations of first two bands (X and A) are accessible, and hence, the simulations are conducted for these two bands. For the X band, two electronic transitions including $^4\text{B}_1 \longrightarrow ^3\text{B}_1$ and $^2\text{A}_2 \longrightarrow ^3\text{B}_1$ are simulated, and for band A, Franck-Condon factor integration of two one-electron detachments $^2\text{A}_1 \longrightarrow ^1\text{A}_1$ and $^2\text{A}_2 \longrightarrow ^1\text{A}_1$ is performed. In doing so, vibrational frequencies of all electronic states underlying bands X and A need to be observed, and these values obtained at the numerical CASPT2 level are given in Table 4.5. Simulations of the Franck-Condon factor also need equilibrium geometries of involved states given in Table 4.1. Simulation results are illustrated in Figure 4.4.

Table 4.5: Vibrational frequencies of involving states underlying two X and A bands in the PE spectrum calculated at the CASPT2 level of theory

state	CASPT2 frequency (cm^{-1})	band	ionization
$^4\text{B}_1$	184, 277, 354		
$^2\text{A}_1$	200, 238, 369		
$^2\text{A}_2$	211, 271, 362		
$^3\text{B}_1$	217, 226, 339	X	$^4\text{B}_1 \longrightarrow ^3\text{B}_1$
		X	$^2\text{A}_2 \longrightarrow ^3\text{B}_1$
$^1\text{A}_1$	208, 242, 348	A	$^2\text{A}_1 \longrightarrow ^1\text{A}_1$
		A	$^2\text{A}_2 \longrightarrow ^1\text{A}_1$

Our Franck-Condon factor simulations are in excellent agreement with both experimental X and A bands in regard to relative intensities between both bands. Apparently, the intensities of two simulated progressions underlying the X band are quite low in comparison to those of the A band. This obvious relative intensity is experimentally observed in the TiGe_2^- PE spectrum displayed in Figure 4.3. The X band is characterized with quite low intensity because of the considerable difference in equilibrium geometries (cf. Table 4.1) between the initial and final states underlying this band. Franck-Condon factor simulations also reveal more detailed information about the vibrational modes of final states participating in electronic transitions. In particular, all involved vibrational modes of final states include the vibration of titanium. This vibration is actually expected

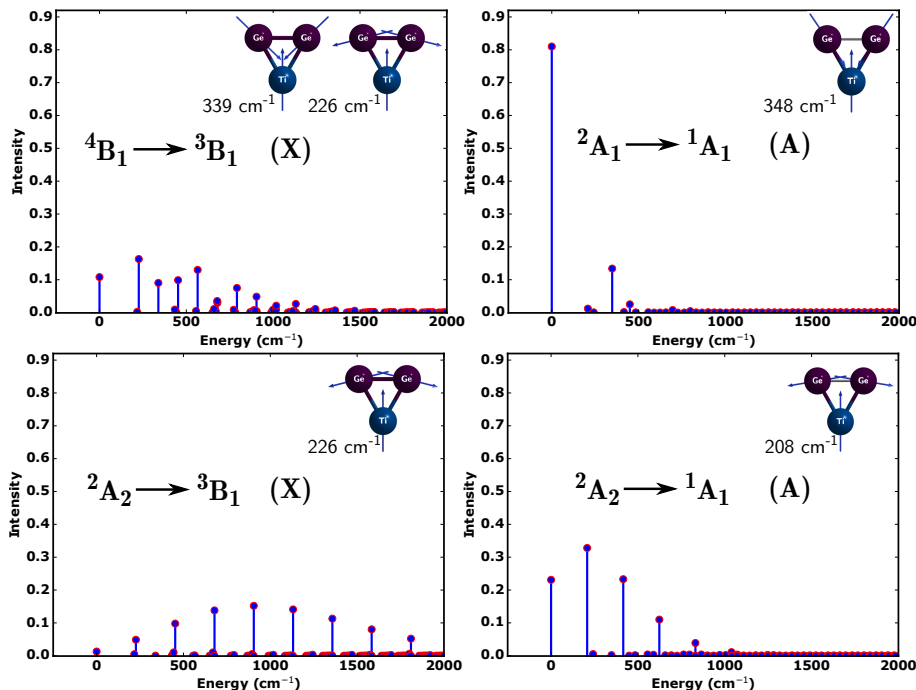


Figure 4.4: Franck-Condon factor simulations of two bands X and A making use of CASPT2 vibrational frequencies given in Table 4.5 and of related equilibrium geometries in Table 4.1. Each band is simulated with two simultaneous electronic transitions.

upon knowing about the types of electrons being removed from initial states. In all simulated progressions, one-electron detachments are determined to arise from 4s and 3d orbitals of titanium. Such ionizations of metallic electrons essentially provoke vibrations of titanium. Vibrational frequencies and associated normal modes chiefly making Franck-Condon factor integrals significant are given in the insets in Figure 4.4.

4.4 Concluding Remarks

By employing a combination of different quantum chemical methods, the electronic structures of the triatomic species $\text{TiGe}_2^{-/0}$ were thoroughly studied. Most states of $\text{TiGe}_2^{-/0}$ appearing in the anion PE experiment have multireference features. With the

support from multireference wave functions, electronic structures of all states underlying the anion PE spectrum were described. Our results firmly established that the ground state of the anion TiGe_2^- is the high-spin state $^4\text{B}_1$. This conclusion disagrees with a previous theoretical study using DFT methods (B3LYP and HSE06 functionals), which concluded that $^2\text{A}_2$ is the anionic ground state.

Two other nearly degenerate anionic states $^2\text{A}_1$ and $^2\text{A}_2$ could be populated during the experiment, in which $^2\text{A}_1$ was proved to be the initial state for band A in the PE spectrum of TiGe_2^- while the other one is likely lesser populated but can affect the width of the observed bands.

Both the anion and neutral have several nearly degenerate states that significantly participate in the formation of PE bands. Four bands in the spectrum of TiGe_2^- were proved to originate from the two most likely degenerate states $^4\text{B}_1$ and $^2\text{A}_1$, and state $^2\text{A}_2$ could also affect the first two X and A bands. More specifically, the X, B, and C bands were mainly attributed to electronic transitions starting from the anionic ground state $^4\text{B}_1$, while the A band was ascribed to removal of one electron from the nearly degenerate state $^2\text{A}_1$ to form the neutral low-spin $^1\text{A}_1$.

Our Franck-Condon simulations of the first two X and A bands, on the basis of all possible transitions, gave additional understanding of normal modes and vibrational frequencies of the final neutral states. Concerning the quantum chemical methods, although multireference methods need to be used for this type of small clusters, our calculations suggested that the DFT/M06-L functional could be appropriate for treatment of systems such as TiGe_2 if a single-reference method should be used.

References

- (1) Pillarisetty, R. *Nature* **2011**, *479*, 324.
- (2) Kamata, Y. *Mater. Today* **2008**, *11*, 30–38.
- (3) Brunco, D. P.; De Jaeger, B.; Eneman, G.; Mitard, J.; Hellings, G.; Satta, A.; Terzieva, V.; Souriau, L.; Leys, F. E.; Pourtois, G.; Houssa, M.; Winderickx, G.; Vrancken, E.; Sioncke, S.; Opsomer, K.; Nicholas, G.; Caymax, M.; Stesmans, A.; Van Steenbergen,

- J.; Mertens, P. W.; Meuris, M.; Heyns, M. M. *J. Electrochem. Soc.* **2008**, *155*, H552–H561.
- (4) Li, X.; Ma, Y.; Dai, Y.; Huang, B. *J. Mater. Chem. C* **2013**, *1*, 4565–4569.
- (5) Wang, J.; Han, J.-G. *J. Chem. Phys.* **2005**, *123*, 244303.
- (6) Kumar, V.; Kawazoe, Y. *Phys. Rev. Lett.* **2002**, *88*, 235504.
- (7) Jing, Q.; Tian, F.-y.; Wang, Y.-x. *J. Chem. Phys.* **2008**, *128*, 124319.
- (8) Kumar, V.; Kawazoe, Y. *Appl. Phys. Lett.* **2002**, *80*, 859–861.
- (9) Hou, X.-J.; Gopakumar, G.; Lievens, P.; Nguyen, M. T. *J. Phys. Chem. A* **2007**, *111*, 13544–13553.
- (10) Wang, J.; Han, J.-G. *J. Phys. Chem. A* **2006**, *110*, 12670–12677.
- (11) Tai, T. B.; Nguyen, M. T. *J. Phys. Chem. A* **2011**, *115*, 9993–9999.
- (12) Zhang, X.; Li, G.; Gao, Z. *Rapid Commun. Mass Spectrom.* **15**, 1573–1576.
- (13) Furuse, S.; Koyasu, K.; Atobe, J.; Nakajima, A. *J. Chem. Phys.* **2008**, *129*, 064311.
- (14) Atobe, J.; Koyasu, K.; Furuse, S.; Nakajima, A. *Phys. Chem. Chem. Phys.* **2012**, *14*, 9403–9410.
- (15) Deng, X.-J.; Kong, X.-Y.; Xu, X.-L.; Xu, H.-G.; Zheng, W.-J. *ChemPhysChem* **2014**, *15*, 3987–3993.
- (16) Lu, S.-J.; Hu, L.-R.; Xu, X.-L.; Xu, H.-G.; Chen, H.; Zheng, W.-J. *Phys. Chem. Chem. Phys.* **2016**, *18*, 20321–20329.
- (17) Zhou, B.; Denning, M. S.; Kays, D. L.; Goicoechea, J. M. *J. Am. Chem. Soc.* **2009**, *131*, 2802–2803.
- (18) Espinoza-Quintero, G.; Duckworth, J. C. A.; Myers, W. K.; McGrady, J. E.; Goicoechea, J. M. *J. Am. Chem. Soc.* **2014**, *136*, 1210–1213.
- (19) Jin, Y.; Lu, S.; Hermann, A.; Kuang, X.; Zhang, C.; Lu, C.; Xu, H.; Zheng, W. *Sci. Rep.* **2016**, *6*, 30116.
- (20) Wang, J.-Q.; Stegmaier, S.; Fässler, T. F. *Angew. Chem., Int. Ed.* **2009**, *48*, 1998–2002.
- (21) Deng, X.-J.; Kong, X.-Y.; Xu, H.-G.; Xu, X.-L.; Feng, G.; Zheng, W.-J. *J. Phys. Chem. C* **2015**, *119*, 11048–11055.
- (22) Deng, X.-J.; Kong, X.-Y.; Xu, X.-L.; Xu, H.-G.; Zheng, W.-J. *RSC Adv.* **2014**, *4*, 25963–25968.

- (23) Deng, X.-J.; Kong, X.-Y.; Xu, X.-L.; Xu, H.-G.; Zheng, W.-J. *Chin. J. Chem. Phys.* **2016**, *29*, 123–128.
- (24) Kumar, M.; Bhattacharyya, N.; Bandyopadhyay, D. *J. Mol. Model.* **2012**, *18*, 405–418.
- (25) Zhao, Y.; Truhlar, D. G. *Acc. Chem. Res.* **2008**, *41*, 157–167.
- (26) Zhao, Y.; Truhlar, D. G. *J. Chem. Phys.* **2006**, *125*, 194101.
- (27) Frisch, M. J.; Trucks, G. W.; Schlegel, H. B.; Scuseria, G. E.; Robb, M. A.; Cheeseman, J. R.; Scalmani, G.; Barone, V.; Mennucci, B.; Petersson, G. A.; Nakatsuji, H.; Caricato, M.; Li, X.; Hratchian, H. P.; Izmaylov, A. F.; Bloino, J.; Zheng, G.; Sonnenberg, J. L.; Hada, M.; Ehara, M.; Toyota, K.; Fukuda, R.; Hasegawa, J.; Ishida, M.; Nakajima, T.; Honda, Y.; Kitao, O.; Nakai, H.; Vreven, T.; Montgomery Jr., J. A.; Peralta, J. E.; Ogliaro, F.; Bearpark, M.; Heyd, J. J.; Brothers, E.; Kudin, K. N.; Staroverov, V. N.; Kobayashi, R.; Normand, J.; Raghavachari, K.; Rendell, A.; Burant, J. C.; Iyengar, S. S.; Tomasi, J.; Cossi, M.; Rega, N.; Millam, J. M.; Klene, M.; Knox, J. E.; Cross, J. B.; Bakken, V.; Adamo, C.; Jaramillo, J.; Gomperts, R.; Stratmann, R. E.; Yazyev, O.; Austin, A. J.; Cammi, R.; Pomelli, C.; Ochterski, J. W.; Martin, R. L.; Morokuma, K.; Zakrzewski, V. G.; Voth, G. A.; Salvador, P.; Dannenberg, J. J.; Dapprich, S.; Daniels, A. D.; Farkas, Ö.; Foresman, J. B.; Ortiz, J. V.; Ciosowski, J.; Fox, D. J. Gaussian-09 Revision E.01., Gaussian Inc. Wallingford CT 2009.
- (28) Balabanov, N. B.; Peterson, K. A. *J. Chem. Phys.* **2005**, *123*, 064107.
- (29) Wilson, A. K.; Woon, D. E.; Peterson, K. A.; Dunning, T. H. *J. Chem. Phys.* **1999**, *110*, 7667–7676.
- (30) Anderson, M. W.; Occelli, M. L.; Klinowski, J. *J. Phys. Chem.* **1992**, *96*, 388–392.
- (31) Roos, B. O.; Lindh, R.; Malmqvist, P.-Å.; Veryazov, V.; Widmark, P.-O. *J. Phys. Chem. A* **2005**, *109*, 6575–6579.
- (32) Roos, B. O.; Lindh, R.; Malmqvist, P.-Å.; Veryazov, V.; Widmark, P.-O. *J. Phys. Chem. A* **2004**, *108*, 2851–2858.
- (33) Angeli, C.; Cimiraglia, R.; Evangelisti, S.; Leininger, T.; Malrieu, J.-P. *J. Chem. Phys.* **2001**, *114*, 10252–10264.
- (34) Werner, H.-J.; Knowles, P. J.; Knizia, G.; Manby, F. R.; Schütz, M. *Wiley Interdiscip. Rev.: Comput. Mol. Sci.* **2012**, *2*, 242–253.
- (35) Reiher, M.; Wolf, A. *J. Chem. Phys.* **2004**, *121*, 10945–10956.
- (36) Pham, L. N.; Nguyen, M. T. *J. Phys. Chem. A* **2016**, *120*, 9401–9410.

- (37) Raffaele, B.; Amedeo, C.; Andrea, P. *Can. J. Chem.* **2013**, *91*, 495–504.
- (38) Burton, G. R.; Xu, C.; Arnold, C. C.; Neumark, D. M. *J. Chem. Phys.* **1996**, *104*, 2757–2764.
- (39) Deutsch, P.; Curtiss, L.; Blaudeau, J.-P. *Chem. Phys. Lett.* **2001**, *344*, 101–106.
- (40) Shim, I.; Baba, M. S.; Gingerich, K. *Chem. Phys.* **2002**, *277*, 9–20.
- (41) Archibong, E. F.; St-Amant, A. *J. Chem. Phys.* **1998**, *109*, 962–972.
- (42) Arnold, C. C.; Xu, C.; Burton, G. R.; Neumark, D. M. *J. Chem. Phys.* **1995**, *102*, 6982–6989.
- (43) Pham, L. N.; Hendrickx, M. F. A. *J. Phys. Chem. A* **2016**, *120*, 9465–9475.

Chapter 5

Geometric and Electronic Structures of $\text{VGe}_3^{-/0}$

This chapter is based on the paper:

Pham, L. N.; Nguyen, M. T. Insights into Geometric and Electronic Structures of $\text{VGe}_3^{-/0}$ Clusters from Anion Photoelectron Spectrum Assignment. *J. Phys. Chem. A* 2017, 121, 6949–6956. Reprinted with permission from *Journal of Chemical Theory and Computation*. Copyright 2017. American Chemical Society. [The Supporting Information is available online.](#)

My contribution to this work was theoretical calculations, data analysis, discussion, writing of the first draft and revision.

5.1 Introduction

Germanium is one of the potential candidates for high-performance electronic transistors.¹ With a search for new materials based on germanium, several types of pure and metal-doped clusters of germanium have been theoretically studied and experimentally synthesized.^{2–12} Usually, germanium clusters are doped with transition metals, and the obtained clusters can

be detected and characterized by, among others, anion photoelectron (PE) spectroscopy. In principle, mass-selected anionic clusters irradiated with high-energy beams of photons are ionized, and signals of removed electrons are then recorded in anion PE spectra. Dozens of germanium clusters doped with metals such as Sc, V, Ti, Co, Ru, Nb, and Au have been studied by this method.^{2,6–9,11}

Typically, experimentalists can identify with anion PE spectroscopy in conjunction with mass spectroscopy the sizes and ionization energies of clusters. For clusters containing transition metals, electronic structures and insights of their excited states are usually quite complicated. As can be seen from previous reports^{13–15} on pure germanium clusters and our recent study on digermanium doped with titanium,¹⁶ energy degeneracy of states significantly affects the anion PE spectra. In such cases, more than one electronic transition can cause one visible band in the spectrum. Thus, although the measured anion PE spectrum seems to be simple to understand, elucidation of the electronic transitions underlying it is not straightforward. In light of the reports mentioned, it is reasonable to expect that energetically degenerate states exist in other doped germanium clusters and are involved in the generation of anion PE spectra.

Of the germanium clusters doped with metals, vanadium trigermanium is one of the simplest clusters spectroscopically characterized using the PE technique.⁶ For the sake of comprehension, Figure 5.1 reproduces the experimental spectrum reported in ref 6. Accordingly, five distinguishable bands are recorded corresponding to five ionizations of the anion VGe₃⁻. First, the lowest vertical ionization is located at 2.02 eV whose adiabatic ionization energy is 1.73 eV. At higher levels, inner electrons are photodetached, and thereby four more PE bands are obtained. One of the latter bands has an ionization energy of 2.80 eV, and three remaining ones are >3.0 eV (3.13, 3.40, and 3.60 eV). On the basis of ionization energy and density functional theory (DFT) calculations, the most stable isomers of both anionic and neutral VGe₃^{-/0} were claimed to have a rhombic form (Figure 5.2a). A quintet state (⁵A) and a quartet one (⁴A) are determined to be the ground states of the anionic and neutral clusters, respectively.⁶ A recent DFT study using the B3LYP functional¹⁷ pointed out that the most stable isomers of VGe₃^{-/0} are both in the tetrahedral shape (Figure 5.2c). While a quartet state (⁴A) is the neutral global minimum, a singlet state (C_{3v}, ¹A₁) is the anionic ground state.

Beside the confusing notations of electronic states assigned in the two previous reports,^{6,17} one can recognize a disagreement on the identity of the most stable isomers and their

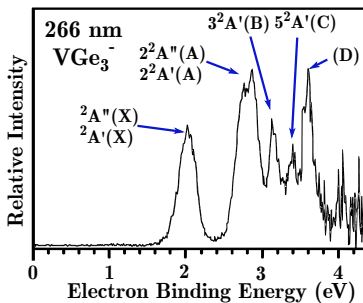


Figure 5.1: Anion photoelectron spectrum of VGe_3^- with five distinguishable bands denoted as X, A, B, C, and D is taken from ref 6. Reproduced with permission from ref 6. Copyright 2015 American Chemical Society.

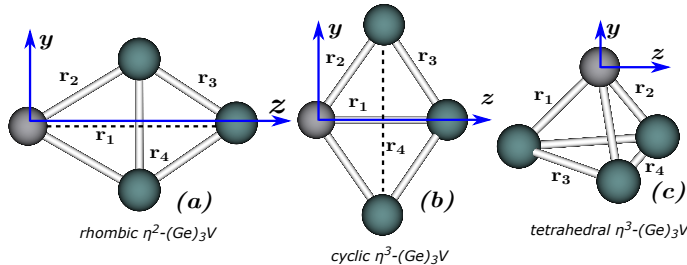


Figure 5.2: Three possible geometries of $\text{VGe}_3^{-/0}$ and the coordinate systems employed.

ground states. Furthermore, the conclusions on the ground states given in the latter report are doubtful, as they simply violate the spin selection rule. In fact, starting from a singlet state, one cannot obtain a quartet state upon ionization. Apart from such doubtful conclusions, our pre-evaluations also reveal that the rhombic isomer is not the most stable geometry of $\text{VGe}_3^{-/0}$ as reported in a previous report.⁶ More importantly, other excited experimental bands appearing in the spectrum of the anion VGe_3^- still need to be fully understood. In this context, we set out to reinvestigate the geometric and electronic structures of both anionic and neutral clusters $\text{VGe}_3^{-/0}$ making use of several reliable methods of quantum chemical theory.

5.2 Computational Details

Geometrical structures of VGe₃^{-/0} clusters are optimized using the multireference CASSCF/CASPT2¹⁸ method. In this method, the correlation energy is expected to be well-recovered, and therefore, the global minima of both the anion and neutral can definitely be identified from relative energies. From previous reports^{6,17} and our preliminary evaluations (data given in Figure S1 of the [Supporting Information](#)), three low-lying isomers of VGe₃^{-/0} (Figure 5.2) are more stable than the others, and hence, these isomers are considered in this optimization step. The coordinate systems used in our calculations are displayed in Figure 5.2.

For CASPT2 calculations, all five 3d and one 4s orbitals of vanadium are included in the active space of CASSCF wave functions. We should note that 4s orbitals of three germanium atoms are likely involved in photodetachment processes which appear as the highest band in the spectrum of VGe₃⁻. Nonetheless, inclusion of all 4s orbitals in the active space would make the CASSCF/CASPT2 calculations practically prohibited. As a consequence, only nine 4p orbitals of three germanium atoms are taken into account. As vanadium has 5 valence electrons and three germanium atoms have 6 4p valence ones, complete configuration state functions (CSFs) are generated on the basis of CASSCF(11,15) and CASSCF(12,15) wave functions including 11 (for the neutral) and 12 (for the anion) electrons distributed in 15 active orbitals, respectively. Since the relative energies obtained are of paramount importance in determination of the global minima, and moreover the optimal geometrical structures are going to be used in all extra single-point calculations afterward, subsequent CASPT2 optimization is implemented in conjunction with relatively large basis sets. The ANO-RCC basis set with contraction of [7s6p4d3f2g]¹⁹ and of [6s5p3d1f]²⁰ is used for vanadium and germanium, respectively. All geometry optimizations are conducted with the MOLCAS 8.0 code.²¹ All 3p and inner-core electrons of both vanadium and germanium are kept frozen in the recovery of dynamic correlation under treatment of second-order perturbation.

To confirm the results obtained above, several additional single-point electronic energies are computed making use of CASPT2 optimal geometries. For the purpose of ground-state identification, the coupled-cluster theory RCCSD(T) is an obvious choice. For finding of appropriate DFT functionals to treat a system like VGe₃^{-/0}, the pure exchange-correlation generalized gradient approximation (GGA) functional BP86^{22,23} is selected because it performs better than other tested functionals (refer to Table S1 for more details). All

computations using these two single-reference methods are done with regard to the electronic structure of each state emerged from CASSCF wave functions. In addition to single-reference methods (DFT and RCCSD(T)), single-point multireference configuration interaction (MRCI) energies of a few accessible states are also calculated to further support the assignment. The Davidson correction for the quadruple contributions is used to improve MRCI energies as well. For a balance between accuracy and our computing resources, the relatively large basis set (quadruple- ζ aug-cc-pVQZ-DK^{24,25}) is employed for both vanadium and germanium atoms. All RCCSD(T) calculations utilize the same electron-correlation schemes used in previous CASPT2 calculations. In MRCI(Q) calculations, due to technical shortcomings we cannot include 15 3d orbitals of three germanium atoms, and they are not correlated in MRCI(Q) calculations. Only 4s and 4p orbitals of Ge atoms are thus included. In the internally contracted MRCI(Q) calculations, all CSFs with coefficients larger than or equal to 0.05 generated from prior CASSCF calculations are taken into account.

On the basis of optimal geometries of the ground and low-lying states obtained from CASPT2 optimizations, vertical (VDEs) and adiabatic (ADEs) detachment energies can be drawn. VDEs are calculated by making use of the initial state (usually the anionic ground state). RCCSD(T) and MRCI(Q) single-point energies are computed using the program MOLPRO 2012.²⁶ We should stress that, for small clusters, ZPE corrections are not important as proved elsewhere;²⁷ this is because ZPEs of all isomers considered are small and nearly the same. Hence all relative energies are derived from pure electronic energies without ZPE corrections. Corrections of scalar relativistic effects are taken into consideration using the second-order Douglas–Kroll–Hess Hamiltonian of all electrons.²⁸

Symmetry plays a vital role in most calculations in this work. As seen in Figure 5.2a,b, the rhombic or cyclic symmetry is simple. Our pre-evaluation shows that both isomers exhibit a C_{2v} spatial symmetry. For the tetrahedral isomer (Figure 5.2c) $VGe_3^{-/0}$ can be in a C_{3v} form (indeed VGe_3^- is). However, spatial symmetrical wave functions of this point group (non-Abelian) cannot be treated in the currently used program packages. Therefore, we use the lower-symmetry C_s point group. All symmetrical operations for these three isomers can be deduced from Figure 5.2.

Finally, Franck–Condon factors of electronic transitions which contribute to the first band in the anion PE spectrum of VGe_3^- are simulated as a further confirmation of our assignment. The first band can be simulated because only harmonic frequencies

of the involved states underlying this band can be accessed. To obtain equilibrium geometrical parameters and analytic vibrational frequencies of involved states, geometries of considered states are optimized using the BP86 functional in conjunction with the basis set def2-TZVP²⁹ as implemented in the TURBOMOLE 7.1 package,³⁰ and harmonic vibrational frequencies are calculated analytically at the same level. We choose the BP86 pure exchange-correlation GGA functional because this functional reproduces quite well experimental detachment energies of VGe₃⁻ as presented later in this work. All parameters are provided as input for simulations up to 10 quanta, which are done with the aid of the MolFC code.³¹

5.3 Results and Discussion

5.3.1 The Most Stable Isomer and Ground States

The most stable isomers of VGe₃^{-/0} are identified on the basis of relative energies obtained after geometry optimizations. Optimized CASPT2 bond lengths of the three low-lying isomers of VGe₃^{-/0} and CASPT2 relative energies of several low-lying states are given in Table 5.1. Relative energies calculated using the BP86 functional and RCCSD(T) are also provided in this table. Unequivocally, the ¹A' state (with respect to C_s symmetry, but C_{3v} point group being the true spatial symmetry of this state) of the tetrahedral isomer is positioned at the lowest point on the potential surface of VGe₃⁻. At the CASPT2 level, the second-lowest states of the anion are the two nearly degenerate ³A' and ³A" states of the tetrahedral η^3 -(Ge₃)V⁻. Both triplet states are \sim 0.6 eV higher in energy than the ¹A'. The most stable cyclic anion (Figure 5.2b) is the ³B₂, which is energetically higher than the ground state ¹A' by \sim 0.7 eV, whereas the high-spin ⁵B₂ state is determined to be \sim 1.0 eV less stable.

As for the neutral ground state, two states ²A' and ²A" have the lowest relative energies and are nearly degenerate. Relative energies of ²A' and ²A" states with respect to the anionic ground state ¹A' are 1.70 and 1.69 eV, respectively. Their degeneracy is reconfirmed with relative energies calculated at the BP86 and RCCSD(T) levels as seen in Table 5.1. In this case, the CASPT2 method reproduces excellently the experimental ADE of the first band, being 1.70 versus 1.73 eV. This agreement between the calculated and experimental ionization energy strongly reinforces our conclusion on the global minima of VGe₃^{-/0}.

Table 5.1: Determination of the Ground States at BP86, RCCSD(T), and CASPT2 Levels^(a)

isomer	state	sym	CASPT2 geometry (Å)	relative energy (eV)		
			r ₁ , r ₂ , r ₃ , r ₄	BP86	RCCSD(T)	CASPT2
tetrahedral $\eta^3\text{-}(\text{Ge}_3)\text{V}^-$	¹ A'	C _s	2.35, 2.35, 2.70, 2.70	0.00	0.00	0.00
	¹ A"	C _s	2.37, 2.44, 2.70, 2.52			0.89
	³ A'	C _s	2.46, 2.39, 2.60, 2.83	0.40	0.83	0.60
	³ A"	C _s	2.37, 2.44, 2.75, 2.52	0.39	0.82	0.60
	⁵ A'	C _s	2.53, 2.48, 2.58, 2.71	0.80	1.29	1.21
	⁵ A"	C _s	2.55, 2.53, 2.56, 2.56	0.84	1.27	1.07
rhombic $\eta^2\text{-}(\text{Ge}_3)\text{V}^-$	⁵ B ₂	C _{2v}	4.34, 2.63, 2.42, 2.57	0.41	0.62	1.01
	⁵ A ₂	C _{2v}	4.40, 2.69, 2.42, 2.60	0.84	0.83	1.28
cyclic $\eta^3\text{-}(\text{Ge}_3)\text{V}^-$	¹ A ₁	C _{2v}	2.74, 2.39, 2.42, 3.95	0.87	0.48	0.80
	³ B ₂	C _{2v}	2.63, 2.37, 2.47, 4.07	0.52	0.87	0.68
	³ A ₂	C _{2v}	2.72, 2.39, 2.47, 4.03	0.89	1.23	1.09
	⁵ A ₁	C _{2v}	2.90, 2.43, 2.44, 3.91	1.67	1.07	0.88
	⁵ B ₁	C _{2v}	3.25, 2.45, 2.43, 3.64	0.76	1.18	0.89
	⁵ B ₂	C _{2v}	2.64, 2.45, 2.41, 4.09	0.89	1.29	1.02
tetrahedral $\eta^3\text{-}(\text{Ge}_3)\text{V}$	² A'	C _s	2.42, 2.36, 2.59, 2.79	1.88	1.89	1.70
	² A"	C _s	2.34, 2.40, 2.72, 2.53	1.89	1.88	1.69
	⁴ A'	C _s	2.46, 2.44, 2.60, 2.72	2.40	2.84	2.39
	⁴ A"	C _s	2.47, 2.47, 2.61, 2.61	2.13	2.56	2.15
	⁶ A'	C _s	2.80, 2.57, 2.41, 3.29	2.88	3.26	2.96
	⁶ A"	C _s	2.50, 2.63, 2.57, 2.64	3.00	3.36	3.00
rhombic $\eta^2\text{-}(\text{Ge}_3)\text{V}$	⁴ B ₂	C _{2v}	4.21, 2.47, 2.44, 2.52	2.39	2.55	2.25
	⁴ A ₂	C _{2v}	4.15, 2.52, 2.42, 2.69	2.37	2.46	2.29
cyclic $\eta^3\text{-}(\text{Ge}_3)\text{V}$	² B ₂	C _{2v}	2.55, 2.36, 2.50, 4.12	2.86	2.84	2.70
	⁴ B ₁	C _{2v}	2.84, 2.42, 2.44, 3.95	2.54	3.03	2.50
	⁴ B ₂	C _{2v}	2.51, 2.46, 2.41, 4.17	2.61	3.05	2.56
	⁶ A ₁	C _{2v}	2.64, 2.53, 2.38, 4.13	2.57	3.01	2.59

^(a) RCCSD(T) and BP86 energies are obtained using CASPT2-optimized geometries. The true symmetrical point group for the anion is C_{3v}, but C_s is used. All values are calculated from total electronic energies without ZPE.

The remaining low-lying states of the neutral including those of the rhombic and cyclic isomers are all significantly higher than both degenerate states $^2A'$ and $^2A''$. Finally, as an extra confirmation, all values of relative energies calculated at the BP86 and RCCSD(T) levels support CASPT2 results that the $^1A'$ state of the tetrahedral $\eta^3\text{-}(\text{Ge}_3)\text{V}^-$ is the ground state of the anion VGe₃⁻ (1A_1 for the anion under C_{3v}) and the neutral has two competitive doublet states for its ground state.

All the results above can give us a clear conclusion that the tetrahedral geometry of both anion and neutral are the most stable isomers. Under the cooled experimental condition, the tetrahedral structures of VGe₃^{-/0} are likely to be much more populated in comparison to the others. This result disagrees with the conclusion reported elsewhere⁶ that the rhombic form is the most stable one of VGe₃^{-/0}. The more recent DFT computations¹⁷ using the B3LYP functional somewhat agree with our results in terms of the stable geometrical structures, and the ground state of the anionic VGe₃⁻ ($^1A'$), but not for the neutral ground state. Note that the neutral ground state has a C_s symmetry (determined by our calculations) instead of a C_{3v} as reported in ref 17. Geometrical structure is changed from C_{3v} to C_s upon ionization. Such a change will be analyzed in the next section.

5.3.2 Electronic Structures and One-Electron Electronic Transitions

As proven above, the tetrahedral isomer, namely, tetrahedral $\eta^3\text{-}(\text{Ge}_3)\text{V}^{-/0}$, is the most stable geometrical structure of both anionic and neutral VGe₃^{-/0}. Using spatial symmetry C_s, the anionic ground state is $^1A'$, and both doublet $^2A'$ and $^2A''$ states are nearly degenerate, vying for the competitive ground state of the neutral. Therefore, to predict the electronic transitions that do not violate the selection rule, electronic structures of ground states and other possibly excited ones of the tetrahedral $\eta^3\text{-}(\text{Ge}_3)\text{V}^{-/0}$ need to be understood.

The leading configurations of both anionic and neutral ground states obtained from CASSCF wave functions are presented in Table 5.2. Some other low-lying states of the tetrahedral $\eta^3\text{-}(\text{Ge}_3)\text{V}^0$ are also given in this table. The occupied pseudonatural orbitals of $^1A'$ (C_s tetrahedral $\eta^3\text{-}(\text{Ge}_3)\text{V}^-$) are displayed in Figure 5.3. In general, these active-space orbitals are quite complex in terms of their original components. Indeed, each of them has a contribution from valence atomic orbitals (AOs) of vanadium and germanium, but the schemes of contributions are expected to be not the same for all orbitals. While the

molecular orbitals (MOs) $34a'$ and $37a'$ are remarkably dominated with the trigermanium moiety's 2p orbitals, all the remaining ones are largely contributed by valence AOs of vanadium (3d and 4s AOs). A graphic visualization in Figure 5.3 gives more details of the components of these MOs.

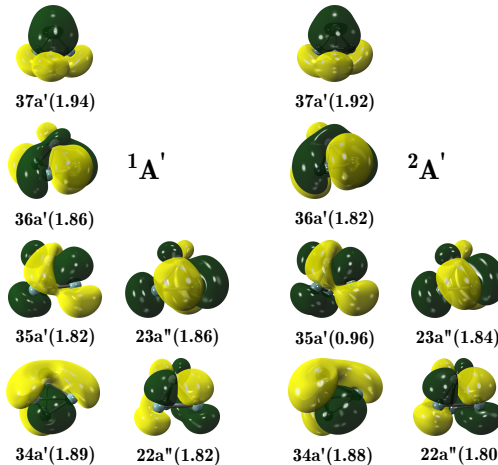


Figure 5.3: Occupied pseudonatural orbitals in the active space of $^1A'$ (C_s) and corresponding active orbitals of $^2A'$. Orbitals are obtained from CASSCF wave functions. The average occupation numbers are given in parentheses. The metal atom V is on the top of the tetrahedral $\eta^3\text{-}(\text{Ge}_3)\text{V}$ isomer.

Our analyses show that both MOs $35a'$ and $22a''$ mainly have, one by one, contributions from two 3d orbitals of vanadium ($3d_{yz}$, $3d_{x^2-y^2}$) and ($3d_{xy}$, $3d_{xz}$). Both MOs $36a'$ and $23a''$ possess stronger components of the metallic orbitals $3d_{yz}$ and $3d_{xz}$, respectively. Appearance of the 4s and $3d_{z^2}$ orbitals of vanadium in occupied orbitals of the anionic ground state is not significant. Figure 5.3 shows the tiny contributions of these two metallic orbitals in the MOs $34a'$ and $37a'$.

The similarity of features between neutral and anionic ground states can be observed from the visualization in Figure 5.3. The two MO sets of $^1A'$ and $^2A'$ reflect these similar features in each pair of MOs, except for the occupation number of MOs $35a'$ (1.82 versus 0.96). Such a similarity suggests that ionization can occur from the MO $35a'$ of the anionic ground state $^1A'$ with removal of one electron, and the expected state $^2A'$ is formed. This ionization process is noted as $^1A' \longrightarrow ^2A'$ in Table 5.2, and the ionized orbital can be implicitly withdrawn by comparing two leading configurations of both $^1A'$ and $^2A'$. Besides,

one can also find major components of the singly occupied orbital noted as [3d_{yz}, 3d_{x²-y²} + 4p] for this ionization process.

Table 5.2: CASSCF Leading Configurations of Anionic and Neutral Ground States, and Electronic Transitions Allowed by Selection Rules

isomer	state	leading configuration	weight (%)	ionization	ionized orbital ^(b)
tetrahedral η^3 - $(\text{Ge}_3)\text{V}$	${}^1\text{A}'$	$34\text{a}''^2 35\text{a}''^2 36\text{a}''^2 37\text{a}''^2 38\text{a}''^0 22\text{a}''^2 23\text{a}''^2$	67	${}^1\text{A}' \longrightarrow 1^2\text{A}'$	$35\text{a}' [3\text{d}_{yz}, 3\text{d}_{x^2-y^2} + 4\text{p}]$
	${}^1\text{D}'$	$34\text{a}''^2 35\text{a}''^1 36\text{a}''^2 37\text{a}''^2 38\text{a}''^0 22\text{a}''^2 23\text{a}''^2$	67	${}^1\text{A}' \longrightarrow 2^2\text{A}'$	$36\text{a}' [3\text{d}_{yz} + 4\text{p}]$
	${}^2\text{A}'$	$34\text{a}''^2 35\text{a}''^2 36\text{a}''^1 37\text{a}''^2 38\text{a}''^0 22\text{a}''^2 23\text{a}''^2$	66	${}^1\text{A}' \longrightarrow 3^2\text{A}'$	$37\text{a}' [4\text{s} + 4\text{p}]$
	${}^3\text{A}'$	$34\text{a}''^2 35\text{a}''^2 36\text{a}''^2 37\text{a}''^1 38\text{a}''^0 22\text{a}''^2 23\text{a}''^2$	46		
	${}^4\text{F}'$	$34\text{a}''^2 35\text{a}''^2 36\text{a}''^0 37\text{a}''^1 38\text{a}''^2 22\text{a}''^2 23\text{a}''^2$	31		
	${}^5\text{P}'$	$34\text{a}''^1 35\text{a}''^2 36\text{a}''^2 37\text{a}''^2 38\text{a}''^0 22\text{a}''^2 23\text{a}''^2$	49	${}^1\text{A}' \longrightarrow 5^2\text{A}'$	$34\text{a}' [3\text{d}_{z^2} + 4\text{p}]$
	${}^1\text{D}''$	$34\text{a}''^2 35\text{a}''^2 36\text{a}''^2 37\text{a}''^2 38\text{a}''^0 22\text{a}''^1 23\text{a}''^2$	66	${}^1\text{A}' \longrightarrow 1^2\text{A}''$	$22\text{a}'' [3\text{d}_{xy}, 3\text{d}_{xz} + 4\text{p}]$
	${}^2\text{D}''$	$34\text{a}''^2 35\text{a}''^2 36\text{a}''^2 37\text{a}''^2 38\text{a}''^0 22\text{a}''^2 23\text{a}''^1$	66	${}^1\text{A}' \longrightarrow 2^2\text{A}''$	$23\text{a}'' [3\text{d}_{xz} + 4\text{p}]$

(b) 3d and 4s orbitals originate from vanadium, and 4p orbitals are from three germanium atoms. 4s and 3d_{z²} AOs of vanadium have rather minor contributions to two MOs 37a' and 34a', respectively.

Most of the bands appearing in the anion PE spectrum of VGe₃⁻ are expected to have originated from the anionic ground state. Hence, prediction of possible electronic transitions starting from the anionic ground state can aid us in understanding the bands of the anion PE spectrum. From the orbital configuration of the ¹A' state (considered under C_s, being ¹A₁ under real C_{3v}), one can predict six possible transitions including the transition ¹A' → ¹D₂, and six final neutral states can be obtained. Six possible transitions are listed in Table 5.2 together with corresponding ionized orbitals and their main original AOs.

With regard to the a' spatial symmetry, apart from the 35a' MO, three more doubly occupied MOs (34a', 36a', and 37a'), one by one, can be ionized, and three final states (2²A', 3²A', and 5²A') are theoretically observed. The leading orbital configurations of these three neutral states can be found in Table 5.2. Because three ionized MOs are composed of different AO components from the vanadium and Ge₃ moiety, ionization energies are expected to be different from each other, and different from the ionization energy of MO 35a' analyzed above. Particularly, within the a' representation, the orbital 35a' is expected to have the lowest ionization energy, because this orbital is largely contributed to by two valence 3d orbitals of vanadium (3d_{yz} and 3d_{x²-y²}). The orbital 36a' is underlying the next level of ionization energy, as this MO has strong 3d_{yz} character. The two remaining MOs 37a' and 34a' exhibit minor features of the metallic 4s and 3d_{xy} orbitals, respectively, but not the Ge 4p orbitals, and thus need higher photon energies for photodetachments. Taking a closer look at the components of two latter MOs, we can roughly estimate the ionization energy order. Because the MO 37a' comprises the vanadium 4s AO, which is energetically higher than the 3d counterparts, the MO 37a' is expected to be ionized with a lower energy compared to that of the MO 34a'.

With respect to the a'' spatial orbitals, the MO 22a'' dominantly consists of major metallic features of two 3d AOs (3d_{xy} and 3d_{xz}), and the other one, 23a'', has lesser metallic character (3d_{xz}) in comparison to that of the MO 22a''. Therefore, we can estimate that ionization energy from the MO 22a'' is lower than that from 23a''. As for a comparison, the huge contributions of 3d metallic orbitals to the MOs 35a' and 22a'' are most likely the same, and a similar situation happens for both MOs 36a' and 23a'' with lesser metallic contributions. As a matter of fact, the CASPT2-optimized geometrical structure of the anionic ground state ¹A' is identified to be in the form of C_{3v} (trigonal pyramid). In this respect, the anionic ground state is the ¹A₁ as mentioned previously. As a result, the two orbitals 35a' and 22a'' must be the HOMOs of the 2-fold degenerate irreducible representations (irrep) e,

and two HOMOs - 1 ($36a'$ and $23a''$) are also degenerate within another 2-fold irrep e. Consequently, one can suggest the leading MO diagram of the $^1A'$ ground state as the one plotted in Figure 5.4.

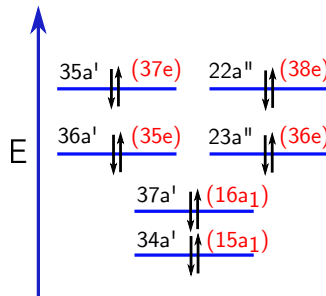


Figure 5.4: MO diagram of the anionic ground state $^1A'$ (1A_1) within the treated active space. Orbital labels with respect to a C_{3v} spatial symmetry are placed in parentheses. The energy ordering is figured out on the basis of the corresponding single-reference wave functions.

Turning back to the optimized geometrical structures of tetrahedral $\eta^3\text{-}(Ge_3)V^{-/0}$, we can see that the geometry is distorted upon removal of one electron from the anionic ground state (C_{3v} , 1A_1), giving the neutral ground state ($^2A'$ and $^2A''$, C_s). Such a distortion occurs under a Jahn-Teller effect. This effect does not happen in the anionic ground state 1A_1 , because the two 2-fold degenerate HOMOs are doubly occupied, and there is no degeneracy of electronic configurations and no distorted geometry. When one-electron photodetachments take place from one of the degenerate HOMOs, two possible electronic configurations of the final state are obtained with the same energy. A Jahn-Teller effect is thus expected to happen inducing a relaxation of the neutral geometry leading to geometry distortion. The distortion directions taking place upon two lowest one-electron ionizations, yielding two distinct $^2A'$ and $^2A''$ states, are plotted in Figure 5.5. This is proved in our CASPT2 geometry optimization of both $^2A'$ and $^2A''$ states.

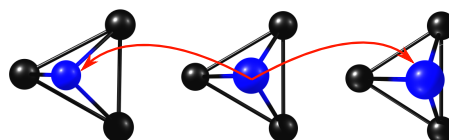


Figure 5.5: Two distortion directions under a Jahn-Teller effect upon one-electron photodetachments at the degenerate HOMO. The blue atom is vanadium.

5.3.3 Anion Photoelectron Spectrum and Band Assignments

As mentioned above, there are six possible allowed one-electron transitions from the anionic ground state $^1A'$ (being 1A_1). The experimental spectrum points out five distinguished bands of ionization with ADEs ranging from ~ 2.0 to 3.6 eV, noted as X, A, B, C, and D in Figure 5.1. However, from the electronic structure of the anionic ground state, we know only four levels of ionization energy because the first two levels involve degenerate transitions starting from degenerate orbitals. Thus, the identity of one experimental band cannot be solved. This band is the last one denoted as D with a high detachment energy of 3.60 eV. To assign this band, we need larger active space including all $4s$ orbitals of three germanium atoms, and the resulting calculations become, at the time being, computationally intractable at the CASSCF levels. Therefore, this band will not explicitly be assigned here, but some possible ionization features can be proposed on the basis of an analysis of electronic structure.

To assign bands in the spectrum, we calculate the VDEs of all possible electronic transitions analyzed above using several methods including DFT/BP86, RCCSD(T), MRCI(Q), and CASPT2. These values are provided in Table 5.3 together with the calculated ADEs of two lowest transitions. The following point has been discussed in a previous section, but for the sake of completeness in spectral assignment, let us state it again.

First of all, ionization energies (ADEs and VDEs) again quantitatively confirm the MO diagram of the 1A_1 state in Figure 5.4. There are clearly two pairs of degenerate MOs with hierarchical levels of ionization energy. Usually, a ground-ground electronic transition is responsible for the first level of ionization energy, namely, the band X, in PE spectra. In the present situation, two transitions from the anionic ground state 1A_1 to two competitive neutral ground states $^2A'$ and $^2A''$ are responsible for the X band. Because these two electronic transitions, $^1A_1 \rightarrow ^1A'$ and $^1A_1 \rightarrow ^1A''$, simultaneously start from the same anionic ground state, they should have equal probability to appear in the anion PE spectrum. As stated above, our calculated ADEs of these two transitions amount to ~ 1.70 eV at the CASPT2 level, which are in excellent agreement with the experimental ADE of 1.73 eV of the X band. The MRCI(Q) also reproduces these ADEs quite well, being 1.78 and 1.80 eV, respectively.

As additional synergism, two single-reference methods give deviations of ~ 0.16 eV in

Table 5.3: VDEs of Electronic Transitions Originating from the Anionic Ground State ${}^1\text{A}_1$

isomer	state	VDE (eV) ^(c)				
		BP86	RCCSD(T)	MRCI(Q)	CASPT2	expt ^(d)
$\eta^3\text{-}(\text{Ge}_3)\text{V}$	${}^1\text{A}'$	0.00	0.00	0.00	0.00	
	${}^1\text{A}'$	1.93 (1.88)	2.02 (1.89)	1.87 (1.78)	1.78 (1.70)	2.02 (X) (1.73)
	${}^1\text{A}''$	1.94 (1.89)	2.02 (1.88)	1.87 (1.80)	1.77 (1.69)	
	${}^2\text{A}'$	2.76	2.75		2.59	2.80 (A)
	${}^2\text{A}''$	2.75	2.71		2.60	
	${}^3\text{A}'$	3.16			2.95	3.13 (B)
	${}^4\text{A}'$				2.98	
	${}^5\text{A}'$	3.53	3.38		3.13	3.40 (C)

^(c) Values are calculated without ZPE; in the parentheses are ADEs. ADEs and VDEs are calculated making use of the CASPT2-optimized geometries of involved states.

^(d) Experimental values are taken from ref 6.

comparison to experiment. With respect to the VDE, the MRCI(Q) and CASPT2 slightly underestimate the experimental VDE (1.87 and 1.78 versus 2.02 eV). Better results are obtained using DFT/BP86 and especially the coupled-cluster theory RCCSD(T). The RCCSD(T) almost recovers the experimental VDE value of 2.02 eV. Again, these results explicitly point toward two transitions ${}^1\text{A}_1 \longrightarrow {}^1\text{A}'$ and ${}^1\text{A}_1 \longrightarrow {}^1\text{A}''$ being responsible for the X band.

The next level of ionization energy belongs to band A with an experimental VDE of 2.80 eV. From the MO diagram of ${}^1\text{A}'$ (Figure 5.4), two ionization processes happening from two degenerate MOs $36\text{a}'$ and $23\text{a}''$ are expected to underlie this band. Indeed, the CASPT2 method predicts two transitions ${}^1\text{A}_1 \longrightarrow {}^2\text{A}'$ and ${}^1\text{A}_1 \longrightarrow {}^2\text{A}''$ having VDEs of 2.59 and 2.60 eV, respectively. These are in good correlation with experimental data of 2.80 eV. Moreover, with calculated values being \sim 0.05 eV below experiment, both DFT/BP86 and RCCSD(T) results again reinforce our assignment for this band. Hence, the two states ${}^2\text{A}'$ and ${}^2\text{A}''$ are concurrently attributed to the emergence of the A band.

The MO diagram within the treated active space suggests that two more levels of ionization

are expected to be occurring under irradiation of suitable photon energy. Two ionization processes corresponding to these two levels are predicted to be $^1\text{A}_1 \longrightarrow 3^2\text{A}'$ and $^1\text{A}_1 \longrightarrow 5^2\text{A}'$. Our calculated DFT/BP86 and CASPT2 VDEs of the transition $^1\text{A}_1 \longrightarrow 3^2\text{A}'$ are 3.16 and 2.95 eV, which are in good agreement with the B band's experimental VDE of 3.13 eV. For the C band, the experimental VDE of 3.40 eV is most likely reflected from the RCCSD(T) VDE of 3.38 eV for the $^1\text{A}_1 \longrightarrow 5^2\text{A}'$ transition. The DFT/BP86 method can recover a VDE of this inner ionization with a difference of 0.13 eV with respect to the experimental value. The CASPT2 prediction of this band is somewhat underestimated by 0.27 eV. Nonetheless, this CASPT2 VDE is still within the error bar of the CASPT2 method. Such a CASPT2 underestimation of deep ionization levels for transition $^1\text{A}_1 \longrightarrow 5^2\text{A}'$ is not surprising because similar situations were encountered in previous studies of clusters containing vanadium³² and germanium.¹⁶ All in all, beyond any doubt, the two higher consecutive bands B and C are attributed to two electronic transitions $^1\text{A}_1 \longrightarrow 3^2\text{A}'$ and $^1\text{A}_1 \longrightarrow 5^2\text{A}'$, respectively. There is still one more band, namely, D, in the spectrum of VGe₃⁻ with a VDE of 3.6 eV. As stated above, a larger active space up to or more than 18 orbitals needs to be considered. As for a prediction, transitions underlying this band can be probed from MOs possessing large contributions from 4s(Ge) AOs.

In this paragraph, we would like to take a further discussion on the relatively low intensities of two experimental bands B and C. All explanations are based on the coefficient weights of leading configurations extracted from the CASSCF wave functions listed in Table 5.2. On one hand, the coefficient weights of states participating in the first two bands X and A are $\sim 65\%$, and on the other hand those of $3^2\text{A}'$ and $5^2\text{A}'$ are below 50%. Relative values of these coefficients implicitly unveil lower probabilities of electronic transitions $^1\text{A}_1 \longrightarrow 3^2\text{A}'$ and $^1\text{A}_1 \longrightarrow 5^2\text{A}'$. As a result, lower intensities of the two latter bands B and C in comparison to those of the former bands are understandable.

5.3.4 Franck-Condon Factor Simulations

To further support our assignment for the band X and to reveal additional details about this band's progression, multidimensional Franck-Condon factor simulations are carried out, and the results are visualized in Figure 5.6. All parameters used to simulate both electronic transitions underlying the X band are given in Table S2 of the SI. The general form of these two simulated progressions is quite similar to that of the experimental band X, which is basically in the shape of typical normal PE bands. Paying a deeper attention to

the simulated progressions, we can see that each progression is the results of numerous vibrational transitions from the initial state to the final counterpart. Theoretically, the wide progressions of two simulated transitions can be explained by taking a geometrical distortion of the final states subjected to a Jahn-Teller effect (refer to Table 5.2 for more details) into account. More interestingly, as discussed above, ionization occurs from two degenerate orbitals whose components are chiefly from 3d orbitals of vanadium and secondarily from 4p orbitals of germanium. Hence, vibration of the metal atom is expected as a result of ionization processes, and germanium atoms' vibrations can also occur. Such vibrations are the main factors governing band X's progression. These vibrations are observable throughout Franck-Condon factor simulations as noted in the insets of Figure 5.6.

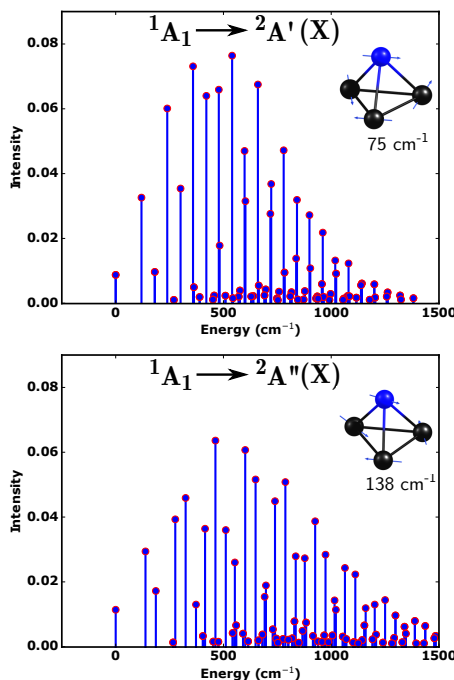


Figure 5.6: Franck–Condon factor simulations of two transitions underlying the PE band X.

5.4 Concluding Remarks

Several geometrical and electronic structures of the tetratomic cluster VGe₃^{-/0} were investigated using both single-reference and multireference quantum chemical methods. The tetrahedral shape was found to be the most stable isomer of both anionic and neutral VGe₃^{-/0}. While the anion exhibits a C_{3v} point group, the neutral cluster has a C_s spatial symmetry, due to the Jahn-Teller effect. This result is completely different from previously reported results that the rhombic isomer is the most stable one. Furthermore, a low-spin state ¹A₁ (C_{3v}) is the global ground state of the anionic cluster VGe₃⁻. Subjected to a Jahn-Teller distortion in two different directions, both resulting ²A' and ²A" states are the nearly degenerate and competitive ground state of the neutral VGe₃.

On the basis of the anionic ground state ¹A₁'s electron configuration, four of the five bands experimentally recorded in the anion photoelectron spectrum of VGe₃⁻ were energetically and electronically assigned. The first band X is the result of two simultaneous electronic transitions from the anionic ground state. The A band was assigned to two other transitions with higher ionization energy. The bands B and C were ascribed to two energetically deeper transitions. The identity of the last band D cannot be assigned, as larger CASSCF wave functions are needed to be constructed, and this is presently out of our computing resources. We believe that electronic transitions forming this band likely start from MOs with larger contributions from the 4s orbitals of germanium atoms. Multidimensional Franck-Condon factor simulations give rise to additional confirmation of the X band's assignment and provide more details about the progression of this band.

As for an energetically reasonable and computationally less demanding theory to treat doped germanium cluster systems like VGe₃^{-/0}, the pure density functional BP86 emerges as our suggestion for a reliable method.

References

- (1) Pillarisetty, R. *Nature* **2011**, *479*, 324.
- (2) Atobe, J.; Koyasu, K.; Furuse, S.; Nakajima, A. *Phys. Chem. Chem. Phys.* **2012**, *14*, 9403–9410.

- (3) Hou, X.-J.; Gopakumar, G.; Lievens, P.; Nguyen, M. T. *J. Phys. Chem. A* **2007**, *111*, 13544–13553.
- (4) Li, X.; Ma, Y.; Dai, Y.; Huang, B. *J. Mater. Chem. C* **2013**, *1*, 4565–4569.
- (5) Tai, T. B.; Nguyen, M. T. *J. Phys. Chem. A* **2011**, *115*, 9993–9999.
- (6) Deng, X.-J.; Kong, X.-Y.; Xu, H.-G.; Xu, X.-L.; Feng, G.; Zheng, W.-J. *J. Phys. Chem. C* **2015**, *119*, 11048–11055.
- (7) Jin, Y.; Lu, S.; Hermann, A.; Kuang, X.; Zhang, C.; Lu, C.; Xu, H.; Zheng, W. *Sci. Rep.* **2016**, *6*, 30116.
- (8) Deng, X.-J.; Kong, X.-Y.; Xu, X.-L.; Xu, H.-G.; Zheng, W.-J. *RSC Adv.* **2014**, *4*, 25963–25968.
- (9) Deng, X.-J.; Kong, X.-Y.; Xu, X.-L.; Xu, H.-G.; Zheng, W.-J. *ChemPhysChem* **2014**, *15*, 3987–3993.
- (10) Espinoza-Quintero, G.; Duckworth, J. C. A.; Myers, W. K.; McGrady, J. E.; Goicoechea, J. M. *J. Am. Chem. Soc.* **2014**, *136*, 1210–1213.
- (11) Lu, S.-J.; Hu, L.-R.; Xu, X.-L.; Xu, H.-G.; Chen, H.; Zheng, W.-J. *Phys. Chem. Chem. Phys.* **2016**, *18*, 20321–20329.
- (12) Burton, G. R.; Xu, C.; Arnold, C. C.; Neumark, D. M. *J. Chem. Phys.* **1996**, *104*, 2757–2764.
- (13) Burton, G. R.; Xu, C.; Neumark, D. M. *Surf. Rev. Lett.* **1996**, *3*, 383–388.
- (14) Dai, D.; Sumathi, K.; Balasubramanian, K. *Chem. Phys. Lett.* **1992**, *193*, 251–257.
- (15) Arnold, C. C.; Xu, C.; Burton, G. R.; Neumark, D. M. *J. Chem. Phys.* **1995**, *102*, 6982–6989.
- (16) Pham, L. N.; Nguyen, M. T. *J. Phys. Chem. A* **2017**, *121*, 1940–1949.
- (17) Shi, S.-P.; Liu, Y.-L.; Deng, B.-L.; Zhang, C.-Y.; Jiang, G. *Int. J. Mod. Phys. B* **2017**, *31*, 1750022.
- (18) Andersson, K.; Malmqvist, P.-Å.; Roos, B. O. *J. Chem. Phys.* **1992**, *96*, 1218–1226.
- (19) Roos, B. O.; Lindh, R.; Malmqvist, P.-Å.; Veryazov, V.; Widmark, P.-O. *J. Phys. Chem. A* **2005**, *109*, 6575–6579.
- (20) Roos, B. O.; Lindh, R.; Malmqvist, P.-Å.; Veryazov, V.; Widmark, P.-O. *J. Phys. Chem. A* **2004**, *108*, 2851–2858.

- (21) Aquilante, F.; De Vico, L.; Ferré, N.; Ghigo, G.; Malmqvist, P.-Å.; Neogrády, P.; Pedersen, T. B.; Pitoňák, M.; Reiher, M.; Roos, B. O., et al. *J. Comput. Chem.* **2010**, *31*, 224–247.
- (22) Becke, A. D. *Phys. Rev. A* **1988**, *38*, 3098–3100.
- (23) Perdew, J. P. *Phys. Rev. B* **1986**, *33*, 8822–8824.
- (24) Wilson, A. K.; Woon, D. E.; Peterson, K. A.; Dunning, T. H. *J. Chem. Phys.* **1999**, *110*, 7667–7676.
- (25) Balabanov, N. B.; Peterson, K. A. *J. Chem. Phys.* **2005**, *123*, 064107.
- (26) Werner, H.-J.; Knowles, P. J.; Knizia, G.; Manby, F. R.; Schütz, M. *Wiley Interdiscip. Rev.: Comput. Mol. Sci.* **2012**, *2*, 242–253.
- (27) Pham, L. N.; Nguyen, M. T. *J. Phys. Chem. A* **2016**, *120*, 9401–9410.
- (28) Reiher, M.; Wolf, A. *J. Chem. Phys.* **2004**, *121*, 10945–10956.
- (29) Weigend, F.; Ahlrichs, R. *Physical Chemistry Chemical Physics* **2005**, *7*, 3297–3305.
- (30) TURBOMOLE V7.1 2016, a development of University of Karlsruhe and Forschungszentrum Karlsruhe GmbH, 1989–2007, TURBOMOLE GmbH, since 2007; available from <http://www.turbomole.com>. (accessed February 4, 2017).
- (31) Raffaele, B.; Amedeo, C.; Andrea, P. *Can. J. Chem.* **2013**, *91*, 495–504.
- (32) Pham, L. N.; Hendrickx, M. F. A. *J. Phys. Chem. A* **2016**, *120*, 9465–9475.

Chapter 6

Multireference Characters and Energetic Degeneracy in $\text{Cr}_2\text{O}_2^{-}/0$

This chapter is based on the paper:

Pham, L. N.; Nguyen, M. T. Another Look at Photoelectron Spectra of the Anion Cr_2O_2^- : Multireference Character and Energetic Degeneracy. *J. Chem. Theory Comput.* **2018**, *14*, 4833–4843. Reprinted with permission from *Journal of Chemical Theory and Computation*. Copyright 2018. American Chemical Society. [The Supporting Information is available online](#).

My contribution to this work was theoretical calculations, data analysis, discussion, writing of the first draft and revision.

6.1 Introduction

With several applications in industry^{1,2} and chemical reactions as catalysts,^{3–5} chromium oxides have been widely studied. Many new chromium oxide clusters were synthesized,^{6–14} and their properties such as magnetic behaviors, geometrical structures and electronic

states were also investigated.^{6–9,14–17} Several electronic, magnetic, and energetic features of chromium oxides are known to be dependent on chemical compositions and geometrical structures. Therefore, geometries of their lowest-lying states must be accurately identified. For this purpose, calculated results obtained using reliable quantum chemical methods still need to be rechecked by comparison with experimental data such as infrared signals and ionization energies.

Similar to a large number of clusters containing transition metals, theoretical studies of unsaturated chromium oxides are known to be computationally challenging. In fact, such clusters need to be described by wave functions that can accurately address their inherently strong multireference characters. As a result, specific methods, such as the multireference configuration interaction (MRCI), multiconfigurational complete active space followed by perturbation theory (CASSCF/CASPT2), and *n*-electron valence state perturbation theory (NEVPT2), are necessary to recover enough correlation energy. When lower levels of theory (usually single-reference methods) were employed, the results obtained for geometric and electronic structures of chromium oxides were frequently not consistent with each other, leading to confusing conclusions.^{6,7,11,15–19}

A case in point in which a typical chromium oxide gives rise to conflicting results is dichromium dioxide ($\text{Cr}_2\text{O}_2^{-/0}$). Two independent groups probed the electronic structures and magnetic interactions of Cr_2O_2 by using anion photoelectron spectroscopy.^{6,11} The anion photoelectron spectra recorded by Wang and co-workers¹¹ in general reproduced all four distinguished bands reported previously by Tono et al.,⁶ and interestingly, two additional clear bands were also observed.^{6,11} On the one hand, studies of both groups agreed with each other that both the anionic and neutral clusters $\text{Cr}_2\text{O}_2^{-/0}$ have high-spin ground states of 10 and 9, respectively, in which two chromium atom sites are ferromagnetically coupled. On the other hand, both reports completely disagreed on the band assignments. In addition to the two above reports, several theoretical reports pointed out low-spin-state (singlet) electronic ground states of Cr_2O_2 .^{16–18,20} In contrast, some more recent studies again reached the conclusion of a high-spin ground state (decet) for Cr_2O_2^- .^{16,21} Even more surprisingly, the geometrical form of Cr_2O_2 determined by Ashman and co-workers²⁰ is not consistent with those given in other reports mentioned.^{6,16–18,20}

As summarized above, although experimental spectra obtained from two studies^{6,11} appear quite similar, the band assignments differed completely from each other. Tono et al.⁶ used energies obtained from density functional theory (DFT) for assignments of the four

visible bands noted as X' (1.20 vs. 1.40 eV), X (1.69 vs. 1.80 eV), A (2.52 vs. 2.60 eV), B (2.99 vs. 3.10 eV) or C (3.14 vs. 3.10 eV) as shown in Figure 6.1¹¹ (the first and second values given in parentheses are vertical detachment energies (VDEs) taken from refs 11 and 6, respectively). Wang and co-workers¹¹ applied an energetic shift of 0.56 eV to VDEs calculated⁶ to ascribe all transition bands including two new observed ones (B or C and D (3.81 eV), leading to a complete disregard of the very first band X' located at ~1.20 eV. As a consequence, the identity of the first band (X') with extremely low intensity remains to be determined. While this low-intensity band was believed in ref 11 to be raised from a lowly populated isomer,¹¹ it was attributed in ref 6 to a transition from a highly populated isomer.⁶

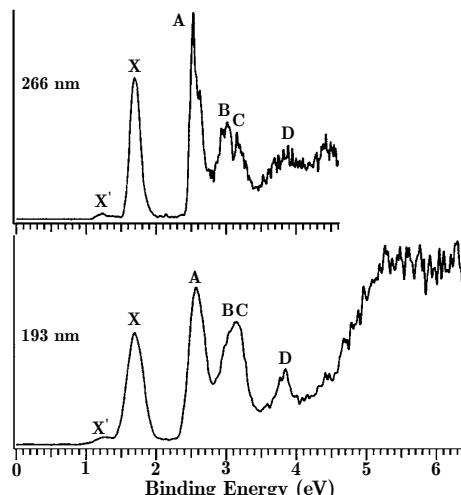


Figure 6.1: Anion photoelectron spectra of Cr_2O_2^- at two different photon energies of 266 and 193 nm (reproduced with permission from ref 11, Copyright 2006, AIP Publisher).

Overall, correct and reliable conclusions on the most stable isomers, electronic ground states, and ionization processes appearing in the anion photoelectron spectra of Cr_2O_2^- are still a matter of debate. In this context, we set out to carry out a set of high-accuracy quantum chemical computations with the aim of reinvestigating the geometrical and electronic structures of both $\text{Cr}_2\text{O}_2^{-/0}$. Subsequently, all electronic transitions causing the appearance of bands in the photoelectron spectra of the anion Cr_2O_2^- are predicted and assigned. A further step, which is multidimensional Franck-Condon factor simulations of the first two bands with lowest ionization energies, is also conducted to corroborate our band assignments.

6.2 Computational Methods

Generally, the computational procedure includes three steps involving geometry optimizations, additional energy single-point calculations, and Franck–Condon factor simulations. The RASSCF/RASPT2 method was first used to optimize geometries of the oxides in both charge states $\text{Cr}_2\text{O}_2^{-/0}$. Single-point electronic energy calculations were subsequently conducted using the density-matrix renormalization group DMRG method, also followed by second-order perturbation treatment CASPT2 and DFT computations using different functionals. The last step involving Franck–Condon simulations was performed on the basis of equilibrium structures and harmonic vibrational frequencies obtained from DFT optimizations. To treat the $\text{Cr}_2\text{O}_2^{-/0}$ clusters with the RASSCF/RASPT2 method,²² a predefined coordinate system was applied to a particular isomer of $\text{Cr}_2\text{O}_2^{-/0}$. The four different isomers considered with their predefined coordinate systems are given in Figure 6.2.

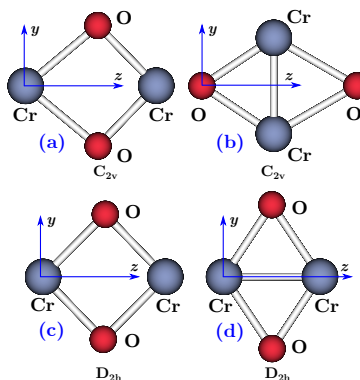


Figure 6.2: Coordinate systems used for RASSCF/RASPT2 calculations of four different Cr_2O_2 isomers in both neutral and anionic states.

All RASSCF/RASPT2²² calculations were conducted using the OpenMolcas program.²³ The active space used for generations of RASSCF wave functions consists of three subspaces, noted as RAS1, RAS2, and RAS3. While RAS1 contains all six 2p orbitals of two oxygen atoms, RAS3 has no orbitals. Theoretically, some more virtual orbitals can be added to the RAS3 subspace. For transition metals with a more-than-half-filled 3d shell, a set of additional 4d orbitals should be the first choice to account for the 3d double-shell effect.²⁴ The inclusion of such an additional d shell would make our computations harder to get convergence and require higher computing resources. More importantly, all metallic

3d molecular orbitals (MOs) of $\text{Cr}_2\text{O}_2^{-/0}$ are singly occupied and unoccupied, and as a result, occupation numbers of all 4d orbitals are negligible. Hence, these 4d MOs are not important, and RAS3 is kept empty with insignificant sacrifice of accuracy. RAS2 is basically comprised of 12 metallic orbitals arising from two chromium atoms, namely, two 4s orbitals and ten 3d ones. A maximum of two electrons were excited from RAS1 to take further static correlation energy into account. Depending on the charged state of Cr_2O_2 , the total number of electrons in the active spaces is 20 (for the neutral) or 21 (for the anion). Two RASSCF calculation schemes can be written in a short way as RAS(20,2,0;6,12,0) and RAS(21,2,0;6,12,0) for the neutral and anionic clusters, respectively. The dynamic correlation energy was subsequently calculated employing second-order perturbation theory on the basis of RASSCF wave functions obtained above. All core orbitals of oxygen (1s) and chromium (3p and inner ones) atoms were not considered in the perturbative step. Because the optimization step can only be performed using numerical gradient evaluations at the RASPT2 level, many electronic states of the mentioned isomers were, first, roughly optimized with a small basis set ANO-RCC-VDZ,^{25,26} and some selected low-lying states were reoptimized with a larger basis set ANO-RCC-VQZP.^{25,26} Energetic minima of optimizations were subsequently confirmed by vibrational calculations. However, due to technical shortcomings, only the totally symmetric vibrational modes with respect to the molecular symmetries (C_{2v} and D_{2h}) were obtained at the RASPT2 level.

The first result revealed from RASSCF calculations is strong multireference features of the wave functions of the $\text{Cr}_2\text{O}_2^{-/0}$ systems. Therefore, in order to ensure that the RASPT2 computations correctly identified ground and important low-lying states, some DMRG-CASPT2^{27–31} single-point calculations were also conducted. Single-point energies of some selected low-lying states were thus calculated employing the previously optimized RASPT2 geometries. A larger active space with 28 orbitals including all 2s and 2p ones of two oxygen atoms and 3s, 3p, 3d, and 4s orbitals of two chromium atoms was used for DMRG calculations. The numbers of electrons in the active space amount to 40 and 41 for the neutral and anionic clusters, respectively. The number of the renormalized state m in all DMRG calculations was set to $m = 2000$. It is known that to obtain more accurate energies m needs to be >2000 , but the resulting DMRG-CASPT2 calculations become computationally expensive, and they go beyond our computing resources. The correlation energy recovered from CASPT2 calculations on the basis of DMRG wave functions did not include the core orbitals excluded in the DMRG step. The ANO-RCC-VQZP basis set was used for all DMRG-CASPT2 calculations that were done with the CHEMPS2 code³² interfaced with the OpenMolcas package.

Dozens of DFT single-point calculations were also conducted using the TPSS³³ and BP86^{34,35} functionals in combination with the correlation-consistent quintuple- ζ aug-cc-pV5Z (for Cr)³⁶ and cc-pV5Z (for O)³⁷ basis sets implemented in the Molpro 2015 package.³⁸ All single-point energy calculations and RASPT2 optimizations took all electron scalar relativistic effects into account by use of the second Douglas–Kroll–Hess Hamiltonian (DKH2).³⁹ As proven elsewhere, the zero-point vibrational energies (ZPEs) insignificantly affect positions of small cluster states on their potential energy hypersurfaces;⁴⁰ hence, all energies considered in this work are purely electronic energies without ZPE corrections.

To give more details to and support the photoelectron band assignments, equilibrium geometries and corresponding harmonic vibrational frequencies of four states involved in the first two bands X' and X were calculated analytically using DFT with the TPSS functional in conjunction with the def2-TZVP basis set⁴¹ available in the Gaussian 09 program.⁴² All obtained information was used to simulate the Franck–Condon factors. The integrals between vibrational wave functions were calculated with the MolFC program.⁴³ As a side note, optimal geometrical parameters of these four states obtained at this DFT level were compared to those optimized at the RASPT2 level (see Table S3) to ensure that the TPSS functional is appropriate for Franck-Condon factor simulations.

6.3 Results and Discussion

6.3.1 Ground-State Identification

Electronic ground states of both Cr₂O₂^{-/0} clusters were determined after two rounds of optimizations. The results of the first round employing the ANO-RCC-VDZ basis set are collected in Table S1 of the [Supporting Information](#) (available online). We can rule out all low-spin states as candidates for the ground states of both the neutral and anionic clusters. Some high-spin states of the isomers *a*, *b* and *d* (Figure 6.2) tended to geometrically converge to the same motif of geometry *c* in Figure 6.2, belonging to the D_{2h} point group. Therefore, in the second round of optimizations, only high-spin states of the isomer *c* with spatial symmetry of D_{2h} were selected for geometry reoptimizations using the larger ANO-RCC-VQZP basis set.

As mentioned above, all electronic states with spin multiplicities of 8, 9, 10, and 11 were reoptimized using the RASPT2 method with the ANO-RCC-VQZP basis set, and their relative energies are given in Table 6.1. Clearly, the RASPT2 method identified a decet state $^{10}A_g$ as the most stable electronic structure of the anionic cluster Cr_2O_2^- . Interestingly, another decet state of Cr_2O_2^- , namely, $^{10}\text{B}_{2g}$, was determined to be energetically very close to $^{10}A_g$, being about 0.02 eV less stable than the state $^{10}A_g$ computed with the RASPT2 method. The RASPT2 potential energy curves for the two lowest-lying states of the anionic cluster Cr_2O_2^- in Figure 6.3 strongly corroborate their degeneracy. Due to the very small difference in energy between two lowest-lying anionic states, DMRG-CASPT2 calculations were carried out, and the results obtained confirmed the RASPT2 finding. Additionally, to ensure that ZPE corrections do not affect energetic ordering of these two lowest-lying states, their RASPT2 and DMRG-CASPT2 energies corrected with the CASSCF and TPSS ZPEs were evaluated (see Table ??). Both states $^{10}A_g$ and $^{10}\text{B}_{2g}$ are nearly degenerate, in which the $^{10}\text{B}_{2g}$ state is only 0.01 eV energetically higher than the ground state. With DFT methods, the results calculated with the TPSS functional seem to be consistent with the RASPT2 and DMRG-CASPT2 methods, whereas the BP86 produced a bit of confusion over the ground state of Cr_2O_2^- . Overall, one can conclude that the two high-spin decet states $^{10}A_g$ and $^{10}\text{B}_{2g}$ are degenerate with a marginal energy difference in favor of the $^{10}A_g$ state as the ground state of the anionic cluster Cr_2O_2^- .

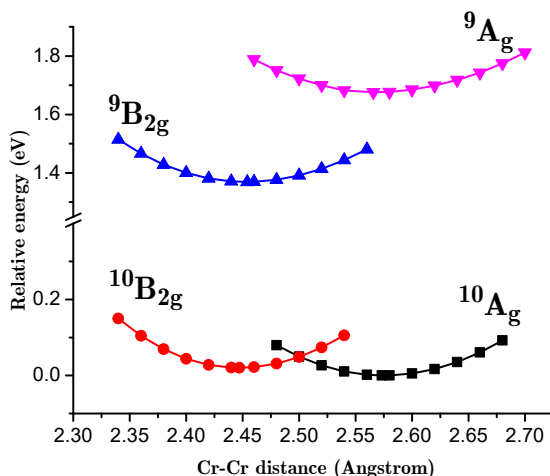


Figure 6.3: Potential energy curves for the ground and first excited states of $\text{Cr}_2\text{O}_2^{-/0}$ along the Cr–Cr distance at the RASPT2 level.

Table 6.1: Relative Energies (eV) of All Electronic States with Spin Multiplicities of 8, 9, 10, and 11 Determined Using Different Methods^(a)

isomer	wt.	state	RASPT2 geometry (Å)	method		
			r_{Cr-Cr}, r_{Cr-O}	RASPT2 ^(b)	TPSS ^(c)	BP86 ^(c)
c-anion	0.26	⁸ A _g	2.55, 1.83	1.10		
	0.08	⁸ B _{3u}	2.42, 1.84	0.62		
	0.09	⁸ B _{2u}	2.23, 1.84	1.32		
	0.10	⁸ B _{1g}	2.65, 1.82	1.20		
	0.10	⁸ B _{1u}	2.60, 1.82	1.45		
	0.14	⁸ B _{1g}	2.39, 1.83	0.78		
	0.16	⁸ B _{3g}	2.53, 1.83	2.45		
	0.13	⁸ A _u	2.63, 1.81	1.24		
	0.44	¹⁰ A _g	2.57, 1.84	0.00 (0.00)	0.00	0.00
	0.21	¹⁰ B _{3u}	2.54, 1.88	1.53	1.51	1.40
	0.36	¹⁰ B _{2u}	2.48, 1.86	1.26	0.84	0.70
	0.34	¹⁰ B _{1g}	2.48, 1.87	1.29	1.14	1.08
	0.96	¹⁰ B _{1u}	2.66, 1.85	3.47		
	0.34	¹⁰ B _{2g}	2.45, 1.83	0.02 (0.01)	0.11	-0.01
	0.42	¹⁰ B _{3g}	2.25, 1.84	2.24	0.67	0.57
	0.34	¹⁰ A _u	2.29, 1.92	2.28	0.96	0.99
c-neutral	0.59	⁹ A _g	2.56, 1.82	1.68 (1.40)	1.38	1.43
	0.30	⁹ B _{3u}	2.53, 1.87	3.13	2.41	2.41
	0.69	⁹ B _{2u}	2.39, 1.85	3.04	1.92	2.01
	0.32	⁹ B _{1g}	2.36, 1.88	2.21	1.67	1.83
	0.34	⁹ B _{1u}	2.39, 1.90	2.90	2.41	2.50
	0.37	⁹ B _{2g}	2.45, 1.83	1.35 (1.25)	1.28	1.33
	0.34	⁹ B _{3g}	2.61, 1.83	2.42	2.18	2.25
	0.36	⁹ A _u	2.56, 1.84	2.81	2.70	2.87
	0.41	¹¹ A _g	2.50, 1.93	6.46	5.70	5.83
	0.53	¹¹ B _{3u}	2.40, 2.02	6.77	5.12	5.33
	0.72	¹¹ B _{2u}	2.66, 2.25	5.76	4.30	4.56
	0.65	¹¹ B _{1g}	2.45, 2.00	5.97	4.49	4.73
	0.60	¹¹ B _{1u}	2.90, 1.90	7.52	6.03	6.24
	0.46	¹¹ B _{2g}	2.58, 1.91	5.99	4.37	4.50
	0.80	¹¹ B _{3g}	2.51, 2.19	6.78	5.91	6.13
	0.40	¹¹ A _u	2.51, 1.93	6.59	6.05	6.33

^(a) Coefficient weights of leading configurations are noted as wt.

^(b) Values in parentheses are the DMRG-CASPT2 relative energies.

^(c) Because coefficient weights (wt.) of some octet states are too small, their DFT energies are not calculated.

Table 6.2: Insignificant Effects of ZPEs on Energetic Ordering of the Two Lowest Anionic States^(d)

method	without ZPE		with CASSCF ZPE ^(e)		with TPSS ZPE	
	¹⁰ A _g	¹⁰ B _{2g}	¹⁰ A _g	¹⁰ B _{2g}	¹⁰ A _g	¹⁰ B _{2g}
RASPT2	0.000	0.020	0.000	0.022	0.000	0.023
DMRG-CASPT2	0.000	0.010	0.000	0.012	0.000	0.013

^(d) All relative energies are in eV.

^(e) To obtain CASSCF ZPE values, CASSCF calculations were conducted using 12 orbitals (two 4s and ten 3d) only.

For the neutral cluster, all used methods consistently agree with each other that the ⁹B_{2g} state is the most stable one. The difference in energy of this state with respect to the anionic ground state ¹⁰A_g yielded an adiabatic electron affinity of ~1.30 eV for the neutral oxide. The first excited state of the neutral Cr₂O₂ was determined to be the ⁹A_g state at all employed levels of theory. The RASPT2 relative energy of this state with respect to the neutral ground state is 0.33 eV, placing it at the first excited position on the potential surface of the neutral Cr₂O₂. The other levels (DMRG-CASPT2, TPSS, and BP86) estimated that this relative energy is ~0.15 eV.

Our results on the ground state of the anion Cr₂O₂⁻ are in agreement with those of previous reports,⁶ whereas the ground state ⁹B_{2g} of the neutral is completely different from that given in the same report (⁹A_g).⁶ In a recent work,¹⁶ the neutral ground state was identified using DFT computations to have a low-spin multiplicity of 1 (singlet state), which is totally different from our present results. For the anion, the difference becomes more significant because a twisted geometrical chain of the anion Cr₂O₂⁻ was found in ref 16 to be the most stable one.¹⁶ Such an inconsistency in the most stable geometry and electronic ground states can be explained by strong multireference characters of wave functions describing the clusters Cr₂O₂^{-/0}, which can be deduced from the small coefficient weights of the dominant configuration state functions listed in Table 6.1. These values are around 0.30 – 0.50 for important states (ground and some excited states involved in the anion photoelectron processes). This suggests that quantum chemical methods with high capability of recovering the static correlation energy are necessary for treatments of Cr₂O₂^{-/0} systems. Single-reference methods are less suitable for the study of Cr₂O₂, resulting in less accurate, if not confusing, results. This is the reason why several DFT studies are not consistent with each other in determination of the geometric and electronic

structures of Cr_2O_2^- as mentioned above.

6.3.2 Electronic Structures and One-Electron Removals

The two most stable anionic states $^{10}\text{A}_g$ and $^{10}\text{B}_{2g}$ are now analyzed on the basis of their leading electronic configurations extracted from corresponding RASSCF wave functions. Table 6.3 lists the leading configurations of these two anionic and some selected neutral states. Detailed analysis of the anionic ground state from pseudonatural active orbitals points out that all nine singly occupied orbitals are strongly metallic, in which the 11a_g MO is mainly composed of the metallic 4s atomic orbitals (AOs) of chromium atoms and other singly occupied ones originate from 3d AOs. Within the active space used, there are also six doubly occupied MOs resulting from six 2p AOs of the two oxygen atoms. The orbital features of the nearly degenerate state $^{10}\text{B}_{2g}$ are quite similar to those of the ground state, except for the occupation schemes of two MOs 2b_{1g} and 4b_{3g} . Figure ?? shows some characteristics of the 18 active-space MOs of both lowest-lying anionic states.

It is worth noting that from the leading configurations in Table 6.3 and the electronic features in Figure 6.4, one can easily figure out the formal oxidation states of both oxygen and chromium atoms in each state of $\text{Cr}_2\text{O}_2^{-/0}$. For example, the anionic ground state $^{10}\text{A}_g$ has nine singly metallic occupied orbitals and six doubly 2p occupied ones, which means that each oxygen atom captures two electrons and two chromium atoms donate three electrons. Thus, the formal oxidation state of oxygen in the anionic ground state $^{10}\text{A}_g$ is -2, and that of each chromium atom is +1.5. Formal oxidation states of oxygen and chromium in the anionic $^{10}\text{B}_{2g}$ state are also -2 and +1.5, respectively. Because one metallic electron is removed from Cr_2O_2^- to form the neutral ground state $^9\text{B}_{2g}$, the formal oxidation state of oxygen is unchanged (-2), and the formal oxidation state of each chromium atom is +2.

Generally, one can divide the 15 occupied orbitals into 3 different types (4s, 3d, and 2p types) depending on their original AOs. Such origins of orbitals can somehow explain the ionization ordering of MOs in the photoelectron spectroscopic measurements. With three types of MOs found, electrons in the 4s-type MOs are associated with the lowest ionization energy, while the 2p-type MOs are expected to be at the highest ionization energy. The 3d-type orbitals are in the middle range of ionization energies. This is understandable because for a specific transition metal atom the 4s AO is energetically higher than 3d orbitals, and as a result, ionization from 4s-type MOs likely occurs first. Therefore, three

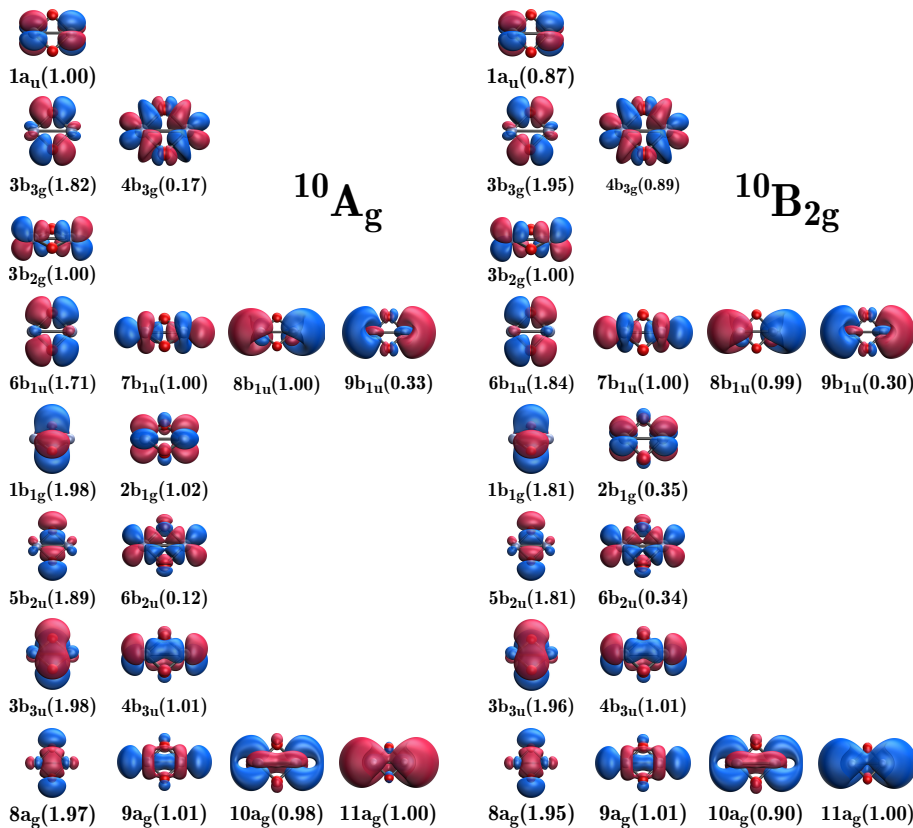


Figure 6.4: Pseudonatural orbitals within the active spaces of the ground and first excited states of Cr_2O_2^- . In parentheses are the occupation numbers.

ranges of electron signals are expected to be observed in the anion photoelectron spectra of Cr_2O_2^- , in which the first and second band regions correspond to electrons removed from the 4s-type and 3d-type MOs, respectively. The last region of anion photoelectron spectra is expected to be higher in terms of energy because all relevant electrons correspond to higher ionization energies of O(2p) electrons. It should be noted that all predictions are made on the basis of active orbitals constructed and are for a certain upper limit of ionization energy.

Table 6.3: Leading Configurations of the Two Most Stable Anionic Ground States and of Neutral Ones. Continuous bands are noted as con.

state	wt.	leading configuration	ionization	orbital
¹⁰ A _g	0.44	8a _g ³ 9a _g ¹ 10a _g ¹ 11a _g ¹ 3b _{3u} ² 4b _{3u} ¹ 5b _{2u} ² 6b _{2u} ¹ 1b _{1g} ² 2b _{1g} ¹ 6b _{1u} ² 7b _{1u} ¹ 8b _{1u} ¹ 9b _{1u} ⁰ 3b _{1g} ¹ 3b _{3g} ² 4b _{3g} ⁰ 1a _u		
¹⁰ B _{2g}	0.34	8a _g ² 9a _g ¹ 10a _g ¹ 11a _g ¹ 3b _{3u} ² 4b _{3u} ¹ 5b _{2u} ² 6b _{2u} ¹ 1b _{1g} ² 2b _{1g} ⁰ 6b _{1u} ² 7b _{1u} ¹ 8b _{1u} ¹ 9b _{1u} ⁰ 3b _{1g} ¹ 3b _{3g} ² 4b _{3g} ¹ 1a _u	¹⁰ A _g → ¹ 9A _g	11a _g (X)
¹ 9A _g	0.59	8a _g ² 9a _g ¹ 10a _g ¹ 11a _g ¹ 3b _{3u} ² 4b _{3u} ¹ 5b _{2u} ² 6b _{2u} ¹ 1b _{1g} ² 2b _{1g} ¹ 6b _{1u} ² 7b _{1u} ¹ 8b _{1u} ¹ 9b _{1u} ⁰ 3b _{1g} ¹ 3b _{3g} ² 4b _{3g} ⁰ 1a _u	¹⁰ A _g → ² 9A _g	9a _g (C)
² 9A _g	0.21	8a _g ² 9a _g ⁰ 10a _g ¹ 11a _g ¹ 3b _{3u} ² 4b _{3u} ¹ 5b _{2u} ² 6b _{2u} ¹ 1b _{1g} ² 2b _{1g} ¹ 6b _{1u} ² 7b _{1u} ¹ 8b _{1u} ¹ 9b _{1u} ⁰ 3b _{1g} ¹ 3b _{3g} ² 4b _{3g} ⁰ 1a _u	¹⁰ A _g → ² 9A _g	9a _g (C)
³ 9A _g	0.16	8a _g ² 9a _g ¹ 10a _g ¹ 11a _g ¹ 3b _{3u} ² 4b _{3u} ¹ 5b _{2u} ² 6b _{2u} ¹ 1b _{1g} ² 2b _{1g} ⁰ 6b _{1u} ² 7b _{1u} ¹ 8b _{1u} ¹ 9b _{1u} ⁰ 3b _{1g} ¹ 3b _{3g} ² 4b _{3g} ¹ 1a _u	¹⁰ B _{2g} → ³ 9A _g	3b _{2g} (D')
⁴ 9A _g	0.24	8a _g ² 9a _g ¹ 10a _g ⁰ 11a _g ¹ 3b _{3u} ² 4b _{3u} ¹ 5b _{2u} ² 6b _{2u} ¹ 1b _{1g} ² 2b _{1g} ¹ 6b _{1u} ² 7b _{1u} ¹ 8b _{1u} ¹ 9b _{1u} ⁰ 3b _{1g} ¹ 3b _{3g} ² 4b _{3g} ⁰ 1a _u	¹⁰ A _g → ⁴ 9A _g	10a _g (D)
¹ 9B _{3u}	0.22	8a _g ² 9a _g ¹ 10a _g ¹ 11a _g ¹ 3b _{3u} ² 4b _{3u} ¹ 5b _{2u} ² 6b _{2u} ¹ 1b _{1g} ² 2b _{1g} ¹ 6b _{1u} ² 7b _{1u} ¹ 8b _{1u} ¹ 9b _{1u} ⁰ 3b _{1g} ¹ 3b _{3g} ² 4b _{3g} ⁰ 1a _u	¹⁰ A _g → ¹ 9B _{3u}	4b _{3u} (C)
² 9B _{3u}	0.22	8a _g ² 9a _g ¹ 10a _g ¹ 11a _g ¹ 3b _{3u} ² 4b _{3u} ¹ 5b _{2u} ² 6b _{2u} ¹ 1b _{1g} ² 2b _{1g} ⁰ 6b _{1u} ² 7b _{1u} ¹ 8b _{1u} ¹ 9b _{1u} ⁰ 3b _{1g} ¹ 3b _{3g} ² 4b _{3g} ¹ 1a _u	¹⁰ B _{2g} → ² 9B _{3u}	8b _{1u} (B)
³ 9B _{3u}	0.14	8a _g ² 9a _g ¹ 10a _g ¹ 11a _g ¹ 3b _{3u} ² 4b _{3u} ¹ 5b _{2u} ² 6b _{2u} ¹ 1b _{1g} ² 2b _{1g} ¹ 6b _{1u} ² 7b _{1u} ¹ 8b _{1u} ¹ 9b _{1u} ⁰ 3b _{1g} ¹ 3b _{3g} ² 4b _{3g} ¹ 1a _u	¹⁰ B _{2g} → ³ 9B _{3u}	7b _{1u} (D')
¹ 9B _{2u}	0.69	8a _g ² 9a _g ¹ 10a _g ¹ 11a _g ⁰ 3b _{3u} ² 4b _{3u} ¹ 5b _{2u} ² 6b _{2u} ¹ 1b _{1g} ² 2b _{1g} ¹ 6b _{1u} ² 7b _{1u} ¹ 8b _{1u} ¹ 9b _{1u} ⁰ 3b _{1g} ¹ 3b _{3g} ² 4b _{3g} ⁰ 1a _u	¹⁰ B _{2g} → ² 9B _{3u}	8b _{1u} (B)
² 9B _{2u}	0.36	8a _g ² 9a _g ¹ 10a _g ¹ 11a _g ⁰ 3b _{3u} ² 4b _{3u} ¹ 5b _{2u} ² 6b _{2u} ¹ 1b _{1g} ² 2b _{1g} ⁰ 6b _{1u} ² 7b _{1u} ¹ 8b _{1u} ¹ 9b _{1u} ⁰ 3b _{1g} ¹ 3b _{3g} ² 4b _{3g} ⁰ 1a _u	¹⁰ B _{2g} → ³ 9B _{3u}	7b _{1u} (D')
³ 9B _{2u}	0.30	8a _g ² 9a _g ¹ 10a _g ¹ 11a _g ¹ 3b _{3u} ² 4b _{3u} ¹ 5b _{2u} ² 6b _{2u} ¹ 1b _{1g} ² 2b _{1g} ⁰ 6b _{1u} ² 7b _{1u} ¹ 8b _{1u} ¹ 9b _{1u} ⁰ 3b _{1g} ¹ 3b _{3g} ² 4b _{3g} ¹ 1a _u	¹⁰ B _{2g} → ³ 9B _{2u}	1a _u (C')
¹ 9B _{1g}	0.32	8a _g ² 9a _g ¹ 10a _g ¹ 11a _g ¹ 3b _{3u} ² 4b _{3u} ¹ 5b _{2u} ² 6b _{2u} ¹ 1b _{1g} ² 2b _{1g} ¹ 6b _{1u} ² 7b _{1u} ¹ 8b _{1u} ¹ 9b _{1u} ⁰ 3b _{1g} ¹ 3b _{3g} ² 4b _{3g} ⁰ 1a _u	¹⁰ A _g → ¹ 9B _{1g}	2b _{1g} (A)
² 9B _{1g}	0.32	8a _g ² 9a _g ¹ 10a _g ¹ 11a _g ¹ 3b _{3u} ² 4b _{3u} ¹ 5b _{2u} ² 6b _{2u} ¹ 1b _{1g} ² 2b _{1g} ⁰ 6b _{1u} ² 7b _{1u} ¹ 8b _{1u} ¹ 9b _{1u} ⁰ 3b _{1g} ¹ 3b _{3g} ² 4b _{3g} ¹ 1a _u	¹⁰ B _{2g} → ² 9B _{1g}	4b _{3g} (A)
¹ 9B _{1u}	0.34	8a _g ² 9a _g ¹ 10a _g ¹ 11a _g ¹ 3b _{3u} ² 4b _{3u} ¹ 5b _{2u} ² 6b _{2u} ¹ 1b _{1g} ² 2b _{1g} ⁰ 6b _{1u} ² 7b _{1u} ¹ 8b _{1u} ¹ 9b _{1u} ⁰ 3b _{1g} ¹ 3b _{3g} ² 4b _{3g} ¹ 1a _u	¹⁰ A _g → ¹ 9B _{1u}	8b _{1u} (B)
² 9B _{1u}	0.19	8a _g ² 9a _g ¹ 10a _g ¹ 11a _g ¹ 3b _{3u} ² 4b _{3u} ¹ 5b _{2u} ² 6b _{2u} ¹ 1b _{1g} ² 2b _{1g} ¹ 6b _{1u} ² 7b _{1u} ¹ 8b _{1u} ¹ 9b _{1u} ⁰ 3b _{1g} ¹ 3b _{3g} ² 4b _{3g} ⁰ 1a _u	¹⁰ A _g → ² 9B _{1u}	7b _{1u} (B)
³ 9B _{1u}	0.19	8a _g ² 9a _g ¹ 10a _g ¹ 11a _g ¹ 3b _{3u} ² 4b _{3u} ¹ 5b _{2u} ² 6b _{2u} ¹ 1b _{1g} ² 2b _{1g} ⁰ 6b _{1u} ² 7b _{1u} ¹ 8b _{1u} ¹ 9b _{1u} ⁰ 3b _{1g} ¹ 3b _{3g} ² 4b _{3g} ¹ 1a _u	¹⁰ B _{2g} → ³ 9B _{1u}	4b _{3u} (D')
¹ 9B _{2g}	0.37	8a _g ² 9a _g ¹ 10a _g ¹ 11a _g ⁰ 3b _{3u} ² 4b _{3u} ¹ 5b _{2u} ² 6b _{2u} ¹ 1b _{1g} ² 2b _{1g} ⁰ 6b _{1u} ² 7b _{1u} ¹ 8b _{1u} ¹ 9b _{1u} ⁰ 3b _{1g} ¹ 3b _{3g} ² 4b _{3g} ¹ 1a _u	¹⁰ B _{2g} → ¹ 9B _{2g}	11a _g (X)
² 9B _{2g}	0.11	8a _g ² 9a _g ¹ 10a _g ¹ 11a _g ¹ 3b _{3u} ² 4b _{3u} ¹ 5b _{2u} ² 6b _{2u} ¹ 1b _{1g} ² 2b _{1g} ¹ 6b _{1u} ² 7b _{1u} ¹ 8b _{1u} ¹ 9b _{1u} ⁰ 3b _{1g} ¹ 3b _{3g} ² 4b _{3g} ⁰ 1a _u	¹⁰ A _g → ² 9B _{2g}	3b _{2g} (C)
³ 9B _{2g}	0.14	8a _g ² 9a _g ¹ 10a _g ¹ 11a _g ¹ 3b _{3u} ² 4b _{3u} ¹ 5b _{2u} ² 6b _{2u} ¹ 1b _{1g} ² 2b _{1g} ⁰ 6b _{1u} ² 7b _{1u} ¹ 8b _{1u} ¹ 9b _{1u} ⁰ 3b _{1g} ¹ 3b _{3g} ² 4b _{3g} ¹ 1a _u	¹⁰ B _{2g} → ³ 9B _{2g}	10ag(D')

Continued on next page

Table 6.3 – continued from previous page

state	wt.	leading configuration	ionization	orbital
4^9B_{2g}	0.17	$8a_g^2 9a_g^0 10a_g^1 11a_g^1 3b_{3u}^2 4b_{3u}^1 5b_{2u}^0 6b_{2u}^0 1b_{1g}^2 2b_{1g}^0 6b_{2u}^1 7b_{1u}^1 8b_{1u}^1 9b_{1u}^0 3b_{2g}^1 3b_{3g}^2 4b_{3g}^1 1a_u^1$	$10^0\text{B}_{2g} \longrightarrow 4^9\text{B}_{2g}$	$9a_g (\text{D}')$
1^9B_{3g}	0.34	$8a_g^2 9a_g^1 10a_g^0 11a_g^0 3b_{3u}^1 4b_{3u}^1 5b_{2u}^2 6b_{2u}^0 1b_{1g}^2 2b_{1g}^1 6b_{2u}^1 7b_{1u}^1 8b_{1u}^1 9b_{1u}^0 3b_{2g}^1 3b_{3g}^2 4b_{3g}^1 1a_u^1$		
1^9A_u	0.34	$8a_g^2 9a_g^1 10a_g^1 11a_g^1 3b_{3u}^2 4b_{3u}^1 5b_{2u}^0 6b_{2u}^1 1b_{1g}^2 2b_{1g}^0 6b_{2u}^1 7b_{1u}^1 8b_{1u}^1 9b_{1u}^0 3b_{2g}^1 3b_{3g}^2 4b_{3g}^0 1a_u^1$		
2^2B_{3u}	0.15	$8a_g^2 9a_g^1 10a_g^0 11a_g^1 3b_{3u}^2 4b_{3u}^0 5b_{2u}^2 6b_{2u}^0 1b_{1g}^1 2b_{1g}^1 6b_{2u}^1 7b_{1u}^1 8b_{1u}^1 9b_{1u}^0 3b_{2g}^1 3b_{3g}^2 4b_{3g}^1 1a_u^1$		
2^2A_u	0.17	$8a_g^2 9a_g^0 10a_g^1 11a_g^1 3b_{3u}^2 4b_{3u}^1 5b_{2u}^2 6b_{2u}^0 1b_{1g}^2 2b_{1g}^1 6b_{2u}^1 7b_{1u}^1 8b_{1u}^1 9b_{1u}^0 3b_{2g}^1 3b_{3g}^2 4b_{3g}^1 1a_u^1$		
3^9A_u	0.17	$8a_g^2 9a_g^0 10a_g^1 11a_g^1 3b_{3u}^2 4b_{3u}^1 5b_{2u}^0 6b_{2u}^1 1b_{1g}^2 2b_{1g}^1 6b_{2u}^1 7b_{1u}^1 8b_{1u}^1 9b_{1u}^0 3b_{2g}^1 3b_{3g}^2 4b_{3g}^1 1a_u^1$		
4^9A_u	0.12	$8a_g^2 9a_g^1 10a_g^0 11a_g^1 3b_{3u}^2 4b_{3u}^1 5b_{2u}^2 6b_{2u}^0 1b_{1g}^2 2b_{1g}^1 6b_{2u}^1 7b_{1u}^1 8b_{1u}^1 9b_{1u}^0 3b_{2g}^1 3b_{3g}^2 4b_{3g}^0 1a_u^0$	$10\text{A}_g \longrightarrow 4^9\text{A}_u$	$1a_u (\text{con.})$
1^{11}A_g	0.50	$8a_g^1 9a_g^0 10a_g^1 11a_g^1 3b_{3u}^2 4b_{3u}^1 5b_{2u}^2 6b_{2u}^0 1b_{1g}^1 2b_{1g}^0 6b_{2u}^1 7b_{1u}^1 8b_{1u}^1 9b_{1u}^0 3b_{2g}^1 3b_{3g}^2 4b_{3g}^0 1a_u^1$	$10\text{A}_g \longrightarrow 1^{11}\text{A}_g$	$8a_g (\text{con.})$
1^{11}B_{3u}	0.53	$8a_g^2 9a_g^1 10a_g^0 11a_g^1 3b_{3u}^1 4b_{3u}^1 5b_{2u}^2 6b_{2u}^0 1b_{1g}^2 2b_{1g}^1 6b_{2u}^1 7b_{1u}^1 8b_{1u}^1 9b_{1u}^0 3b_{2g}^1 3b_{3g}^2 4b_{3g}^0 1a_u^1$	$10\text{A}_g \longrightarrow 1^{11}\text{B}_{3u}$	$3b_{3u} (\text{con.})$
2^{11}B_{3u}	0.18	$8a_g^2 9a_g^1 10a_g^1 11a_g^0 3b_{3u}^1 4b_{3u}^1 5b_{2u}^2 6b_{2u}^0 1b_{1g}^2 2b_{1g}^0 6b_{2u}^1 7b_{1u}^1 8b_{1u}^1 9b_{1u}^0 3b_{2g}^1 3b_{3g}^2 4b_{3g}^1 1a_u^1$	$10\text{B}_{2g} \longrightarrow 2^{11}\text{B}_{3u}$	$6b_{1u} (\text{con.})$
1^{11}B_{2u}	0.72	$8a_g^2 9a_g^1 10a_g^1 11a_g^0 3b_{3u}^2 4b_{3u}^1 5b_{2u}^1 6b_{2u}^0 1b_{1g}^2 2b_{1g}^1 6b_{2u}^1 7b_{1u}^1 8b_{1u}^1 9b_{1u}^0 3b_{2g}^1 3b_{3g}^2 4b_{3g}^0 1a_u^1$	$10\text{A}_g \longrightarrow 1^{11}\text{B}_{2u}$	$5b_{2u} (\text{con.})$
1^{11}B_{1g}	0.65	$8a_g^2 9a_g^1 10a_g^0 11a_g^1 3b_{3u}^1 4b_{3u}^1 5b_{2u}^2 6b_{2u}^0 1b_{1g}^1 2b_{1g}^0 6b_{2u}^1 7b_{1u}^1 8b_{1u}^1 9b_{1u}^0 3b_{2g}^1 3b_{3g}^2 4b_{3g}^0 1a_u^1$	$10\text{A}_g \longrightarrow 1^{11}\text{B}_{1g}$	$1b_{1g} (\text{con.})$
2^{11}B_{1g}	0.33	$8a_g^2 9a_g^1 10a_g^0 11a_g^1 3b_{3u}^2 4b_{3u}^1 5b_{2u}^0 6b_{2u}^1 1b_{1g}^2 2b_{1g}^0 6b_{2u}^1 7b_{1u}^1 8b_{1u}^1 9b_{1u}^0 3b_{2g}^1 3b_{3g}^2 4b_{3g}^1 1a_u^1$	$10\text{B}_{2g} \longrightarrow 2^{11}\text{B}_{1g}$	$3b_{3g} (\text{con.})$
1^{11}B_{1u}	0.60	$8a_g^2 9a_g^1 10a_g^1 11a_g^0 3b_{3u}^1 4b_{3u}^0 5b_{2u}^2 6b_{2u}^0 1b_{1g}^2 2b_{1g}^1 6b_{2u}^1 7b_{1u}^1 8b_{1u}^1 9b_{1u}^0 3b_{2g}^1 3b_{3g}^2 4b_{3g}^0 1a_u^1$	$10\text{A}_g \longrightarrow 1^{11}\text{B}_{1u}$	$6b_{1u} (\text{con.})$
2^{11}B_{1u}	0.23	$8a_g^2 9a_g^1 10a_g^1 11a_g^0 3b_{3u}^1 4b_{3u}^1 5b_{2u}^0 6b_{2u}^1 1b_{1g}^2 2b_{1g}^0 6b_{2u}^1 7b_{1u}^1 8b_{1u}^1 9b_{1u}^0 3b_{2g}^1 3b_{3g}^2 4b_{3g}^1 1a_u^1$	$10\text{B}_{2g} \longrightarrow 2^{11}\text{B}_{1u}$	$3b_{3u} (\text{con.})$
1^{11}B_{2g}	0.19	$8a_g^1 9a_g^0 10a_g^1 11a_g^1 3b_{3u}^2 4b_{3u}^1 5b_{2u}^2 6b_{2u}^0 1b_{1g}^1 2b_{1g}^0 6b_{2u}^1 7b_{1u}^1 8b_{1u}^1 9b_{1u}^0 3b_{2g}^1 3b_{3g}^2 4b_{3g}^1 1a_u^1$	$10\text{B}_{2g} \longrightarrow 11\text{B}_{2g}$	$8a_g (\text{con.})$
1^{11}B_{3g}	0.80	$8a_g^2 9a_g^1 10a_g^1 11a_g^0 3b_{3u}^1 4b_{3u}^0 5b_{2u}^2 6b_{2u}^0 1b_{1g}^2 2b_{1g}^1 6b_{2u}^1 7b_{1u}^1 8b_{1u}^1 9b_{1u}^0 3b_{2g}^1 3b_{3g}^2 4b_{3g}^0 1a_u^1$	$10\text{A}_g \longrightarrow 1^{11}\text{B}_{3g}$	$3b_{3g} (\text{con.})$
2^{11}B_{3g}	0.28	$8a_g^2 9a_g^1 10a_g^1 11a_g^0 3b_{3u}^2 4b_{3u}^1 5b_{2u}^1 6b_{2u}^0 1b_{1g}^1 2b_{1g}^0 6b_{2u}^1 7b_{1u}^1 8b_{1u}^1 9b_{1u}^0 3b_{2g}^1 3b_{3g}^2 4b_{3g}^1 1a_u^1$	$10\text{B}_{2g} \longrightarrow 2^{11}\text{B}_{3g}$	$1b_{1g} (\text{con.})$
1^{11}A_{1u}	0.40	$8a_g^2 9a_g^1 10a_g^0 11a_g^1 3b_{3u}^1 4b_{3u}^1 5b_{2u}^1 6b_{2u}^0 1b_{1g}^2 2b_{1g}^0 6b_{2u}^1 7b_{1u}^1 8b_{1u}^1 9b_{1u}^0 3b_{2g}^1 3b_{3g}^2 4b_{3g}^0 1a_u^1$	$10\text{B}_{2g} \longrightarrow 11\text{A}_{1u}$	$5b_{2u} (\text{con.})$

In an anion photoelectron spectrum, the strongest bands in the spectra are caused by removal of electrons from an anionic ground state. Let us stress again that in this analysis all inner core orbitals of Cr_2O_2^- were not considered. A close look at the leading configurations of the anionic ground state (${}^{10}\text{A}_g$) in Table 6.3 reveals all possible one-electron removals. In detail, 9 singly occupied orbitals (9a_g , 10a_g , 11a_g , 4b_{3u} , 2b_{1g} , 7b_{1u} , 8b_{1u} , 3b_{2g} , and 1a_u) ionized at relatively low energy and 6 doubly occupied counterparts (8a_g , 3b_{3u} , 5b_{2u} , 1b_{1g} , 6b_{1u} , and 3b_{3g}) with higher one-electron removal energy give rise to 15 ionization processes. Because all ionization processes originate from the most populated anionic ground state ${}^{10}\text{A}_g$ of the anion, they should all be observed in the anion photoelectron spectra of Cr_2O_2^- .

As the ${}^{10}\text{B}_{2g}$ state is very close to the anionic ground state in terms of its relative energy, this state will have a significant population. Thus, one-electron removals from this nearly degenerate state can also give rise to observed bands in the experimental spectra. This phenomenon was observed elsewhere.^{44,45} Taking into account all occupied MOs of the ${}^{10}\text{B}_{2g}$ state, another set of 15 orbitals can be equally ionized under a relevant energy of laser beams. Because these 15 ionization processes are predicted to start from a formal excited state, their signals are also predicted to be relatively lower in comparison to those from the anionic ground state. This means that some weak signals can be seen if the experimental spectra are well resolved. Also, these signals can be overshadowed by signals of electrons removed from the ground state or even by the noise. For the sake of understanding, 30 ionization processes and corresponding ionized MOs are given in Table 6.3, in which the coefficient weights of several final neutral states are also collected, which will be analyzed in a following section on the low-intensity bands caused by electrons of the ground state.

6.3.3 Anion Photoelectron Spectra

The anion photoelectron spectra of Cr_2O_2^- recorded at four photon beam energies¹¹ (two of them are provided in Figure 6.1) look more complicated than those measured earlier.⁶ In the earlier report,⁶ two energetic regions of electron signals, in which one region is below 2.0 eV and the other one is over 2.5 eV, were recorded. In the more recent report, one more continuous region over 4.0 eV is present (see Figure 6.1).¹¹ As predicted above, electron removals from three different types of orbitals can give signals to the anion spectra. Obviously, ionization from these three types of MOs are completely reflected by the observation of three visible regions of signals in the experimental spectra of Cr_2O_2^- .¹¹

This also implies that the active spaces used in our RASSCF calculations are sufficient to allow us to assign all visible bands.

In the range of under 2.00 eV, starting from the anionic ground state ${}^{10}\text{A}_g$, one electronic transition ${}^{10}\text{A}_g \longrightarrow {}^{19}\text{A}_g$ was predicted at the RASPT2 level. The ${}^{10}\text{A}_g \longrightarrow {}^{19}\text{A}_g$ VDE and ADE were determined to both be 1.68 eV, which corresponds to the X band with its experimental VDE and ADE of 1.69 and 1.65 eV, respectively (see Table 6.4). In this range of ionization energy, starting from the first excited state ${}^{10}\text{B}_{2g}$, one more ionization ${}^{10}\text{B}_{2g} \longrightarrow {}^{19}\text{B}_{2g}$ was found. The calculated VDE of this electronic transition is 1.35 eV. The experimental spectra recorded one band at around 1.20–1.40 eV, noted as X' in Table 6.4 and in Figure 6.1. Therefore, this band can be energetically ascribed to the ${}^{10}\text{B}_{2g} \longrightarrow {}^{19}\text{B}_{2g}$ transition.

One more interesting fact that further supports such assignments for the first two bands is the relative intensities between two experimental bands in the spectra. The X' band is much less intense as compared to the X band. This suggests that the X' band is likely caused by an experimentally less populated electronic state. Indeed, the ${}^{10}\text{B}_{2g} \longrightarrow {}^{19}\text{B}_{2g}$ transition originates from the first excited state ${}^{10}\text{B}_{2g}$, which may have, according to Maxwell–Boltzmann statistics, $\sim 10\%$ of probability populated in the ionization region of the spectrometer at 110 K,⁶ the lowest temperature of the cluster-growth room reported in ref 6. As a result, all ionization signals coming from this anionic excited state are expected to be lower in intensity, and this is probably what happened to the X' band. To make all electronic transitions starting from the first anionic excited state ${}^{10}\text{B}_{2g}$ clear with regard to band assignments, corresponding bands are noted with the prime symbol in Table 6.4.

The second region ranging from 2.00 to 4.00 eV in the spectra (Figure 6.1) shows four visible bands, denoted as A, B, C, and D, in which the B and C bands are not well resolved. At first, for the A band, the electronic transition ${}^{10}\text{A}_g \longrightarrow {}^{19}\text{B}_{1g}$ has a calculated VDE of 2.41 eV, which is ~ 0.10 eV smaller than the experimental VDE of the A band. The neutral ${}^{19}\text{B}_{3g}$ state with a VDE of 2.66 eV energetically matches the band A, but a comparison between the leading configurations of ${}^{10}\text{A}_g$ and ${}^{19}\text{B}_{3g}$ listed in Table 6.3 indicates this ionization is not a one-electron process. Hence, the A band is assigned to the ${}^{10}\text{A}_g \longrightarrow {}^{19}\text{B}_{1g}$ ionization. Let us note that the ${}^{29}\text{B}_{1g}$ state, formed by the ${}^{10}\text{B}_{2g} \longrightarrow {}^{29}\text{B}_{1g}$ ionization process can also be ascribed to the A band in view of its relative energy. However, this ionization is caused by a transition from the first excited state, and therefore, its signal can be overshadowed by ionization processes from the ground state.

Table 6.4: RASPT2 ADE and VDE Values of Electronic Transitions Starting from the Nearly Degenerate Anionic States^(f)

state	ADE (eV)	VDE (eV)	expt. VDE (eV)		band ^(h)	ionization
			ref 11 ^(g)	ref 6		
1 ⁹ A _g	1.68	1.68	1.69 (1.65)	1.80	X	¹⁰ A _g → 1 ⁹ A _g
2 ⁹ A _g		3.16	3.16	3.10	C	¹⁰ A _g → 2 ⁹ A _g
3 ⁹ A _g		3.88	3.81		D'	¹⁰ B _{2g} → 3 ⁹ A _g
4 ⁹ A _g		4.06	3.81		D	¹⁰ A _g → 4 ⁹ A _g
1 ⁹ B _{3u}	2.67	3.02	3.16	3.10	C	¹⁰ A _g → 1 ⁹ B _{3u}
2 ⁹ B _{3u}		2.90	2.99	3.10	B'	¹⁰ B _{2g} → 2 ⁹ B _{3u}
3 ⁹ B _{3u}		3.97	3.81		D'	¹⁰ B _{2g} → 3 ⁹ B _{3u}
1 ⁹ B _{2u}		3.04				
2 ⁹ B _{2u}		3.11				
3 ⁹ B _{2u}		3.33	3.16	3.10	C'	¹⁰ B _{2g} → 3 ⁹ B _{2u}
1 ⁹ B _{1g}	2.22	2.41	2.52	2.60	A	¹⁰ A _g → 1 ⁹ B _{1g}
2 ⁹ B _{1g}	2.18	2.49	2.52	2.60	A'	¹⁰ B _{2g} → 2 ⁹ B _{1g}
1 ⁹ B _{1u}	2.9	2.93	2.99	3.10	B	¹⁰ A _g → 1 ⁹ B _{1u}
2 ⁹ B _{1u}		3.01	2.99	3.10	B	¹⁰ A _g → 2 ⁹ B _{1u}
3 ⁹ B _{1u}		3.78	3.81		D'	¹⁰ B _{2g} → 3 ⁹ B _{1u}
1 ⁹ B _{2g}	1.35	1.35	1.20	1.40	X'	¹⁰ B _{2g} → 1 ⁹ B _{2g}
2 ⁹ B _{2g}		3.21	3.16	3.10	C	¹⁰ A _g → 2 ⁹ B _{2g}
3 ⁹ B _{2g}		3.58	3.81		D'	¹⁰ B _{2g} → 3 ⁹ B _{2g}
4 ⁹ B _{2g}		4.06	3.81		D'	¹⁰ B _{2g} → 4 ⁹ B _{2g}
1 ⁹ B _{3g}	2.42	2.66				
1 ⁹ A _u	2.81	3.25				
2 ⁹ A _u		3.37				
3 ⁹ A _u		4.38				
4 ⁹ A _u		4.53	> 4.00		con.	¹⁰ A _g → 4 ⁹ A _u
1 ¹¹ A _g		7.69	> 4.00		con.	¹⁰ A _g → 1 ¹¹ A _g
1 ¹¹ B _{3u}	6.77	7.07	> 4.00		con.	¹⁰ A _g → 1 ¹¹ B _{3u}
2 ¹¹ B _{3u}		8.49	> 4.00		con.	¹⁰ B _{2g} → 2 ¹¹ B _{3u}
1 ¹¹ B _{2u}	5.76	6.66	> 4.00		con.	¹⁰ A _g → 1 ¹¹ B _{2u}
1 ¹¹ B _{1g}	5.97	6.36	> 4.00		con.	¹⁰ A _g → 1 ¹¹ B _{1g}
2 ¹¹ B _{1g}		8.15	> 4.00		con.	¹⁰ B _{2g} → 2 ¹¹ B _{1g}
1 ¹¹ B _{1u}	7.52	7.78	> 4.00		con.	¹⁰ A _g → 1 ¹¹ B _{1u}
2 ¹¹ B _{1u}		7.76	> 4.00		con.	¹⁰ B _{2g} → 2 ¹¹ B _{1u}
1 ¹¹ B _{2g}		8.25	> 4.00		con.	¹⁰ B _{2g} → 1 ¹¹ B _{2g}
1 ¹¹ B _{3g}		7.58	> 4.00		con.	¹⁰ A _g → 1 ¹¹ B _{3g}
2 ¹¹ B _{3g}		8.09	> 4.00		con.	¹⁰ B _{2g} → 2 ¹¹ B _{3g}
1 ¹¹ A _u		7.73	> 4.00		con.	¹⁰ B _{2g} → 1 ¹¹ A _u

^(f) Formal bands with the prime symbol are due to transitions starting from the state ¹⁰B_{2g}.

^(g) The value in parentheses is the experimental ADE.

^(h) Continuous bands are noted as con.

Moving on to the next two bands B and C, these bands are energetically quite close to each other, with a difference in energy of ~ 0.15 eV. Such a difference in energy is too small to make distinguishable band assignments. Thus, the assignments for the B and C bands can be interchangeable within the error bar of the RASPT2 method. To assign these two bands, all electronic transitions from the anionic ground state should be considered first. Within the range of experimental VDEs from 2.99 to 3.16 eV, our calculated VDEs show that five ionization processes, namely, ${}^{10}\text{A}_g \rightarrow {}^1\text{B}_{1u}$, ${}^{10}\text{A}_g \rightarrow {}^2\text{B}_{1u}$, ${}^{10}\text{A}_g \rightarrow {}^2\text{A}_g$, ${}^{10}\text{A}_g \rightarrow {}^1\text{B}_{3u}$, and ${}^{10}\text{A}_g \rightarrow {}^2\text{B}_{2g}$ from the anionic ground state, can be attributed to these two bands. Each calculated VDE value of these five electronic transitions lies within an energetic range of 2.93 – 3.21 eV. Electronic transitions corresponding to each band noted as B and C in this region are listed in Table 6.4, and the assignments here are in fact totally interchangeable. Besides, two more additional ionization processes ${}^{10}\text{B}_{2g} \rightarrow {}^2\text{B}_{3u}$ and ${}^{10}\text{B}_{2g} \rightarrow {}^3\text{B}_{2u}$ arising from two singly occupied 3d-type MOs of the nearly degenerate state ${}^{10}\text{B}_{2g}$ are likely to take place and give rise to lower-intensity bands (noted as B' and C') dominated by the bands B and C.

The last well-resolved band in the anion photoelectron spectra of Cr_2O_2^- was centered at ~ 3.81 eV. Because of its relatively high ionization energy, this band could not be observed in the earlier report, where the limit was set to ~ 3.20 eV.⁶ The intensity of this band is obviously lower than those of the X, A, B, and C bands. However, it is much higher than the intensity of the X' band (see Figure 6.1). Such a relative intensity of the D band suggests that a one-electron transition starting from the ground state ${}^{10}\text{A}_g$ may underlie this band. Because the D band vertically lies at 3.81 eV, the ${}^{10}\text{A}_g \rightarrow {}^4\text{A}_g$ transition with a computed VDE of 4.06 eV seems to be a good candidate to be responsible for this band. Such a predicted VDE slightly overestimates the experimental value, but this is the only energetically appropriate transition in Table 6.4. The D band is assigned to the ${}^{10}\text{A}_g \rightarrow {}^4\text{A}_g$ ionization process. In Table 6.4, five electronic transitions starting from the lowly populated state ${}^{10}\text{B}_{2g}$ are theoretically found in the range of 3.78 – 4.06 eV. Although all of them can contribute to the experimental band D, their low intensities would be overshadowed by signals of the ${}^{10}\text{A}_g \rightarrow {}^4\text{A}_g$ transition. Note that the leading configuration of the final state ${}^4\text{A}_g$ has a relatively smaller coefficient weight than those of other final states causing X and A bands. Therefore, the intensity of the D band is lower than those of both the X and A bands.

In Figure 6.1, a continuous region of signals is present at over 4.00 eV. As analyzed above, due to higher ionization energy, these unwell-resolved signals are expected to

come from the ionization processes of electrons in 2p-type MOs. In Table 6.4, twelve 2p-type electronic transitions are listed together with their calculated VDEs of above 6.30 eV. All 12 one-electron transitions lead to the high-spin 11-tet states of the neutral Cr₂O₂. In addition, one 3d-type transition (¹⁰A_g → ⁴A_u) contributes to the continuous region. The vertical ionization energy of this transition was computed to be 4.53 eV. If the anion photoelectron spectrum of Cr₂O₂⁻ is more resolved, this band is believed to become pronounced and appear more clearly in the spectrum.

Obviously, most of our present band assignments are different from those reported in two previous studies.^{6,11} The nearly degenerate state of the anion Cr₂O₂⁻, causing the extremely low intensity X' band, was not recognized and was completely ignored in these two reports. A detailed comparison of relative energies between the present RASPT2 results and those of Tono and co-workers shows that DFT relative energies reported by these authors are significantly underestimated. This tends to explain the remarkable difference in band assignments. Using an empirical energetic shift of 0.56 eV, Wang and co-workers ruled out the ⁹A_g as the final state underlying the X' band identified by Tono et al., but considered the X band, which is in agreement with our present RASPT2 assignment for this band. However, such an empirical energy correction seems not completely effective for the remaining bands (see Table 6.5).

Let us note that the electronic transition, ¹⁰A_g → ¹B_{3g}, is not a one-electron process as found in Tono's report but a two-electron one. A few additional two-electron processes involving electronic transitions from both degenerate anionic states to the unassigned neutral counterparts can be predicted from Table 6.3. Two-electron processes usually appear as low-intensity peaks in anion photoelectron spectra.⁴⁶⁻⁴⁸ Because of low intensities, two-electron signals can be overshadowed by strong and well-resolved bands of the same energy regions. If spectra of strong electron correlation anionic systems are well-resolved and no one-electron processes underlie bands in the energy region of two-electron processes, two-electron detachment signals can be seen even clearly like those in the UO₂⁻ and Cu⁻ anion photoelectron spectra reported by Wang and co-workers.^{47,49}

Table 6.5: Comparison of Band Assignments from This Work and Two References 11 and 6⁽ⁱ⁾

band	assignment		
	this work	ref 11	ref 6
X'	${}^{10}\text{B}_{2g} \longrightarrow {}^1\text{B}_{2g}$		${}^{10}\text{A}_g \longrightarrow {}^1\text{A}_g$
X	${}^{10}\text{A}_g \longrightarrow {}^1\text{A}_g$	${}^{10}\text{A}_g \longrightarrow {}^1\text{A}_g$	${}^{10}\text{A}_g \longrightarrow {}^1\text{B}_{3g}$
A	${}^{10}\text{A}_g \longrightarrow {}^1\text{B}_{1g}$	${}^{10}\text{A}_g \longrightarrow {}^1\text{B}_{3g}$	${}^{10}\text{A}_g \longrightarrow {}^1\text{B}_{3u}$ ${}^{10}\text{A}_g \longrightarrow {}^1\text{B}_{1u}$
B	${}^{10}\text{A}_g \longrightarrow {}^1\text{B}_{1u}$ ${}^{10}\text{A}_g \longrightarrow {}^2\text{B}_{1u}$	${}^{10}\text{A}_g \longrightarrow {}^1\text{B}_{3u}$ ${}^{10}\text{A}_g \longrightarrow {}^1\text{B}_{1u}$	
C	${}^{10}\text{A}_g \longrightarrow {}^2\text{A}_g$ ${}^{10}\text{A}_g \longrightarrow {}^1\text{B}_{3u}$ ${}^{10}\text{A}_g \longrightarrow {}^2\text{B}_{2g}$	${}^{10}\text{A}_g \longrightarrow {}^2\text{A}_g$	${}^{10}\text{A}_g \longrightarrow {}^1\text{B}_{2g}$ ${}^{10}\text{A}_g \longrightarrow {}^2\text{B}_{3u}$
D	${}^{10}\text{A}_g \longrightarrow {}^4\text{A}_g$	${}^{10}\text{A}_g \longrightarrow {}^1\text{B}_{2g}$ ${}^{10}\text{A}_g \longrightarrow {}^2\text{B}_{3u}$	
con.	${}^{10}\text{A}_g \longrightarrow {}^4\text{A}_u$ ${}^{10}\text{A}_g \longrightarrow {}^{11}\text{A}_g$ ${}^{10}\text{A}_g \longrightarrow {}^{11}\text{B}_{3u}$ ${}^{10}\text{A}_g \longrightarrow {}^{11}\text{B}_{2u}$ ${}^{10}\text{A}_g \longrightarrow {}^{11}\text{B}_{1g}$ ${}^{10}\text{A}_g \longrightarrow {}^{11}\text{B}_{1u}$ ${}^{10}\text{A}_g \longrightarrow {}^{11}\text{B}_{3g}$		

⁽ⁱ⁾ All electronic transitions starting from the anionic ground state ${}^{10}\text{A}_g$ and one giving rise to the X' band are listed.

6.3.4 Franck-Condon Factor Simulations

To further support the band assignments discussed above and give more details to band progressions, multidimensional Franck-Condon factor simulations were conducted. Because only the harmonic vibrational frequencies of four states involved in the first two bands (${}^{10}\text{A}_g$, ${}^9\text{A}_g$, ${}^{10}\text{B}_{2g}$, and ${}^9\text{B}_{2g}$) were accessible from DFT computations, both X' and X bands were simulated. The equilibrium structures and harmonic vibrational frequencies of the involved states are tabulated in the SI. Two simulated bands are presented in Figure 6.5. The intensity of the X band is much higher than that of the X' band, which is in good agreement with the experiment (Figure 6.5). With regard to band broadening, although the simulated bands do not reproduce well the absolute values of band widths, their relative bandwidth is in good correlation with the experiment. The simulation results

not only reflect well the experiment in terms of relative intensities and band widths but also confirm the band assignments for these two bands.

As explained before, the first two bands are the results of one-electron removals from 4s-type MOs of Cr_2O_2^- . Therefore, vibrational modes including vibrations of Cr atoms are expected in the final states. Indeed, all vibrational modes in the insets show harmonic vibrations of Cr atoms. A deeper investigation into the integrals describing the intensity of the band X' indicates significant involvement of the first excited vibrational state of the Cr–Cr stretching mode, while for the X band, the results mainly come from 0 to 0 transitions of the same mode.

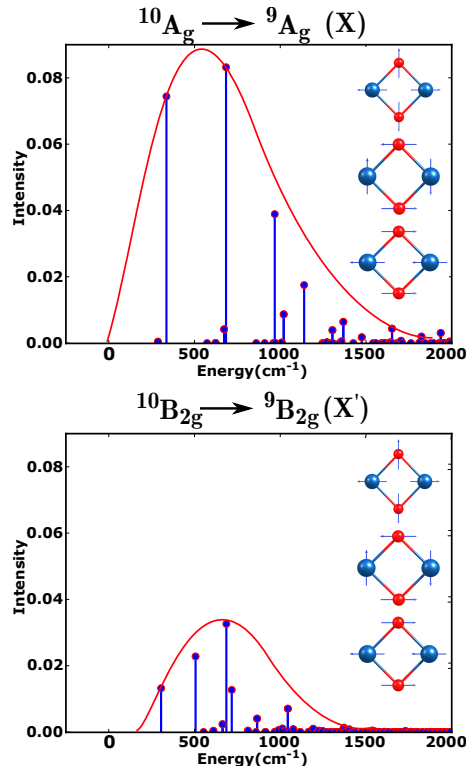


Figure 6.5: Franck–Condon factor simulations of the first two bands X' and X in the anion photoelectron spectra of Cr_2O_2^- . Vibrational modes obtained from DFT computations giving rise to significant integrals can be seen in the insets.

6.4 Concluding Remarks

In the present theoretical study, detailed electronic and geometrical structures of the chromium oxides $\text{Cr}_2\text{O}_2^{0/-}$ were reinvestigated. Geometrical structures of both anionic and neutral clusters of Cr_2O_2 have a D_{2h} diamond form. Competition for the anionic ground state of the anion Cr_2O_2^- between the two lowest-lying electronic states ${}^{10}\text{A}_g$ and ${}^{10}\text{B}_{2g}$ was found, in which the ${}^{10}\text{A}_g$ state is marginally more stable and within the expected accuracy of the methods employed both states are basically degenerate.

A high-spin state ${}^9\text{B}_{2g}$ is confirmed to be the ground state of the neutral cluster. Both lowest anionic states (${}^{10}\text{A}_g$ and ${}^{10}\text{B}_{2g}$) have contributions to the anion photoelectron spectra of the anion Cr_2O_2^- . All well-resolved bands with high intensities denoted as X, A, B, C, and D were determined to be the results of one-electron transitions starting from the anionic ground state ${}^{10}\text{A}_g$. The lower-intensity X' band is likely caused by the nearly degenerate state ${}^{10}\text{B}_{2g}$ when one electron is removed to form the neutral ground state ${}^9\text{B}_{2g}$. The degenerate state ${}^{10}\text{B}_{2g}$ is also found to undergo several ionization processes and to produce photoelectron signals overshadowed by those originating from the anionic ground state. Overall, most of our spectral assignments for Cr_2O_2^- done in this work turn out to be completely different from those given in previous reports. Additionally, band simulations for the first two bands X' and X confirm the anionic ground state and reinforce the band assignments for these two bands.

References

- (1) Lunk, H.-J. *ChemTexts* **2015**, *1*, 6.
- (2) McDaniel, M. P. *Adv. Catal.* **2010**, *53*, 123–606.
- (3) Rivalta, I.; Russo, N.; Sicilia, E. *J. Comput. Chem.* **2006**, *27*, 174–187.
- (4) Maeda, K.; Domen, K. *J. Phys. Chem. C* **2007**, *111*, 7851–7861.
- (5) Zhang, Y. J.; Wang, Y. C.; Yan, W.; Li, T.; Li, S.; Hu, Y. R. *Appl. Surf. Sci.* **2009**, *255*, 9508–9511.
- (6) Tono, K.; Terasaki, A.; Ohta, T.; Kondow, T. *J. Chem. Phys.* **2003**, *119*, 11221–11227.
- (7) Tono, K.; Terasaki, A.; Ohta, T.; Kondow, T. *Phys. Rev. Lett.* **2003**, *90*, 133402.

- (8) Janssens, E.; Hou, X. J.; Neukermans, S.; Wang, X.; Silverans, R. E.; Lievens, P.; Nguyen, M. T. *J. Phys. Chem. A* **2007**, *111*, 4150–4157.
- (9) Bañobre-López, M.; Vázquez-Vázquez, C.; Rivas, J.; López-Quintela, M. A. *Nanotechnology* **2003**, *14*, 318.
- (10) Gutsev, G. L.; Jena, P.; Zhai, H.-J.; Wang, L.-S. *J. Chem. Phys.* **2001**, *115*, 7935–7944.
- (11) Zhai, H.-J.; Wang, L.-S. *J. Chem. Phys.* **2006**, *125*, 164315.
- (12) Zhai, H.-J.; Li, S.; Dixon, D. A.; Wang, L.-S. *J. Am. Chem. Soc.* **2008**, *130*, 5167–5177.
- (13) Chertihin, G. V.; Bare, W. D.; Andrews, L. *J. Chem. Phys.* **1997**, *107*, 2798–2806.
- (14) Moriyama, R.; Sato, R.; Nakano, M.; Ohshima, K.; Misaizu, F. *J. Phys. Chem. A* **2017**, *121*, 5605–5613.
- (15) Reddy, B. V.; Khanna, S. N. *Phys. Rev. Lett.* **1999**, *83*, 3170–3173.
- (16) Gutsev, G. L.; Bozhenko, K. V.; Gutsev, L. G.; Utenshev, A. N.; Aldoshin, S. M. *J. Phys. Chem. A* **2017**, *121*, 845–854.
- (17) Veliah, S.; Xiang, K.-h.; Pandey, R.; Recio, J. M.; Newsam, J. M. *J. Phys. Chem. B* **1998**, *102*, 1126–1135.
- (18) Wang, Y.; Gong, X.; Wang, J. *J. Chem. Phys.* **2010**, *12*, 2471–2477.
- (19) Li, S.; Dixon, D. A. *J. Phys. Chem. A* **2007**, *111*, 11908–11921.
- (20) Reddy, B. V.; Khanna, S. N.; Ashman, C. *Phys. Rev. B* **2000**, *61*, 5797–5801.
- (21) Paul, S.; Misra, A. *J. Mol. Struct.: THEOCHEM* **2009**, *895*, 156–160.
- (22) Malmqvist, P. Å.; Pierloot, K.; Shahi, A. R. M.; Cramer, C. J.; Gagliardi, L. *J. Chem. Phys.* **2008**, *128*, 204109.
- (23) Aquilante, F.; Autschbach, J.; Carlson, R. K.; Chibotaru, L. F.; Delcey, M. G.; De Vico, L.; Fdez. Galván, I.; Ferré, N.; Frutos, L. M.; Gagliardi, L.; Garavelli, M.; Giussani, A.; Hoyer, C. E.; Li Manni, G.; Lischka, H.; Ma, D.; Malmqvist, P. Å.; Müller, T.; Nenov, A.; Olivucci, M.; Pedersen, T. B.; Peng, D.; Plasser, F.; Pritchard, B.; Reiher, M.; Rivalta, I.; Schapiro, I.; Segarra-Martí, J.; Stenrup, M.; Truhlar, D. G.; Ungur, L.; Valentini, A.; Vancoillie, S.; Veryazov, V.; Vysotskiy, V. P.; Weingart, O.; Zapata, F.; Lindh, R. J. *Comput. Chem.* **2016**, *37*, 506–541.
- (24) Pierloot, K. *Int. J. Quantum Chem.* **2011**, *111*, 3291–3301.
- (25) Roos, B. O.; Lindh, R.; Malmqvist, P.-Å.; Veryazov, V.; Widmark, P.-O. *J. Phys. Chem. A* **2005**, *109*, 6575–6579.

- (26) Roos, B. O.; Lindh, R.; Malmqvist, P.-Å.; Veryazov, V.; Widmark, P.-O. *J. Phys. Chem. A* **2004**, *108*, 2851–2858.
- (27) Mizukami, W.; Kurashige, Y.; Yanai, T. *J. Chem. Theory Comput.* **2012**, *9*, 401–407.
- (28) Yanai, T.; Kurashige, Y.; Mizukami, W.; Chalupský, J.; Lan, T. N.; Saitow, M. *Int. J. Quantum Chem.* **2015**, *115*, 283–299.
- (29) Liu, F.; Kurashige, Y.; Yanai, T.; Morokuma, K. *J. Chem. Theory Comput.* **2013**, *9*, 4462–4469.
- (30) Kurashige, Y.; Yanai, T. *J. Chem. Phys.* **2009**, *130*, 234114.
- (31) Kurashige, Y.; Chan, G. K.-L.; Yanai, T. *Nat. Chem.* **2013**, *5*, 660.
- (32) Wouters, S.; Poelmans, W.; Ayers, P. W.; Van Neck, D. *Comput. Phys. Commun.* **2014**, *185*, 1501–1514.
- (33) Tao, J.; Perdew, J. P.; Staroverov, V. N.; Scuseria, G. E. *Phys. Rev. Lett.* **2003**, *91*, 146401.
- (34) Becke, A. D. *Phys. Rev. A* **1988**, *38*, 3098–3100.
- (35) Perdew, J. P. *Phys. Rev. B* **1986**, *33*, 8822–8824.
- (36) Balabanov, N. B.; Peterson, K. A. *J. Chem. Phys.* **2005**, *123*, 064107.
- (37) Dunning, T. H. *J. Chem. Phys.* **1989**, *90*, 1007–1023.
- (38) Werner, H.-J.; Knowles, P. J.; Knizia, G.; Manby, F. R.; Schütz, M. *Wiley Interdiscip. Rev.: Comput. Mol. Sci.* **2012**, *2*, 242–253.
- (39) Reiher, M.; Wolf, A. *J. Chem. Phys.* **2004**, *121*, 10945–10956.
- (40) Pham, L. N.; Nguyen, M. T. *J. Phys. Chem. A* **2016**, *120*, 9401–9410.
- (41) Weigend, F.; Ahlrichs, R. *J. Chem. Phys.* **2005**, *7*, 3297–3305.
- (42) Frisch, M. J.; Trucks, G. W.; Schlegel, H. B.; Scuseria, G. E.; Robb, M. A.; Cheeseman, J. R.; Scalmani, G.; Barone, V.; Mennucci, B.; Petersson, G. A.; Nakatsuji, H.; Caricato, M.; Li, X.; Hratchian, H. P.; Izmaylov, A. F.; Bloino, J.; Zheng, G.; Sonnenberg, J. L.; Hada, M.; Ehara, M.; Toyota, K.; Fukuda, R.; Hasegawa, J.; Ishida, M.; Nakajima, T.; Honda, Y.; Kitao, O.; Nakai, H.; Vreven, T.; Montgomery Jr., J. A.; Peralta, J. E.; Ogliaro, F.; Bearpark, M.; Heyd, J. J.; Brothers, E.; Kudin, K. N.; Staroverov, V. N.; Kobayashi, R.; Normand, J.; Raghavachari, K.; Rendell, A.; Burant, J. C.; Iyengar, S. S.; Tomasi, J.; Cossi, M.; Rega, N.; Millam, J. M.; Klene, M.; Knox, J. E.; Cross, J. B.; Bakken, V.; Adamo, C.; Jaramillo, J.; Gomperts, R.; Stratmann, R. E.; Yazyev, O.; Austin, A. J.; Cammi, R.; Pomelli, C.; Ochterski, J. W.; Martin, R. L.; Morokuma, K.;

- Zakrzewski, V. G.; Voth, G. A.; Salvador, P.; Dannenberg, J. J.; Dapprich, S.; Daniels, A. D.; Farkas, Ö.; Foresman, J. B.; Ortiz, J. V.; Cioslowski, J.; Fox, D. J. Gaussian-09 Revision E.01., Gaussian Inc. Wallingford CT 2009.
- (43) Raffaele, B.; Amedeo, C.; Andrea, P. *Can. J. Chem.* **2013**, *91*, 495–504.
- (44) Pham, L. N.; Hendrickx, M. F. A. *J. Phys. Chem. A* **2016**, *120*, 9465–9475.
- (45) Pham, L. N.; Nguyen, M. T. *J. Phys. Chem. A* **2017**, *121*, 1940–1949.
- (46) Wu, H.; Wang, L.-S. *J. Phys. Chem. A* **1998**, *102*, 9129–9135.
- (47) Li, W.-L.; Su, J.; Jian, T.; Lopez, G. V.; Hu, H.-S.; Cao, G.-J.; Li, J.; Wang, L.-S. *J. Chem. Phys.* **2014**, *140*, 094306.
- (48) Wu, H.; Wang, L.-S. *J. Chem. Phys.* **1997**, *107*, 8221–8228.
- (49) Wu, H.; Desai, S. R.; Wang, L.-S. *J. Phys. Chem. A* **1997**, *101*, 2103–2111.

Chapter 7

Geometric, Electronic, and magnetic properties of Small Chromium oxide clusters

This chapter is based on the paper:

Pham, L. N.; Claes, P.; Lievens, P.; Jiang, L.; Wende, T.; Asmis, K. R.; Nguyen, M. T.; Janssens, E. Geometric Structures and Magnetic Interactions in Small Chromium Oxide Clusters. *J. Phys. Chem. C* 2018, 122, 27640-27647. Reprinted with permission from *Journal of Physical Chemistry C*. Copyright 2018. American Chemical Society. [The Supporting Information is available online](#)

My contribution to this work was theoretical calculations, data analysis, discussion, writing of the first draft and revision.

7.1 Introduction

Bulk chromium is an antiferromagnetic material at room temperature (its Néel temperature is about 308 K) and behaves paramagnetically at higher temperatures.¹ The chromium atom has, in the ground state, six unpaired electrons in its $3d$ and $4s$ orbitals. In the smallest possible cluster of chromium atoms, the Cr₂ dimer, the total magnetic moment is zero as a result of antiferromagnetic coupling of the local moments.^{2–4} Interestingly, the Cr–Cr bond length is significantly increased and the local moments at the two chromium sites couple ferromagnetically if one electron is removed resulting in a high-spin ground state ($^{12}\Sigma$) for Cr₂.⁴ Triatomic and other small odd sized chromium clusters are subject to antiferromagnetic frustration.^{5,6} In a recent theoretical study, an energetic competition between low and high spin states (S = 1 and S = 6) was found in Cr₄ as a result of the highly correlated electron behavior.⁷

Magnetic interactions in pure chromium clusters can be altered by addition of oxygen atoms. Superexchange through bridging oxygen atoms induces a ferromagnetic coupling between the local moments on the two Cr atoms in Cr₂O_n^{-/0} (n = 1 – 3).^{8,9} Further addition of oxygen reduces, and even quenches, total magnetic moments of the dichromium clusters (Cr₂O_n, n = 4 – 14).^{10,11} A similar observation was made for larger clusters; the local magnetic moments of chromium atoms are quenched in clusters with a high oxygen concentration, such as Cr₄O₁₀ and (CrO₃)_n (n = 1 – 5).^{12,13} Such quenching happens because all chromium valence electrons are involved in chemical bonds with oxygen atoms. In suboxide clusters, such as Cr₃O_n^{+/0} (n = 0 – 3), the magnetic interactions are controlled by the amount of oxygen.⁵ Besides the composition (chromium to oxygen atomic ratio), also the precise geometry of the cluster is important for the magnetic interaction. It was, for example, found that Cr_nO₂ (n = 2 – 5) clusters of the same size but with a different geometric structure can have different magnetic properties and interactions.^{14,15} Similar findings were reported for iron oxide clusters. For example, different magnetic states were predicted as lowest energy configuration of the neutral Fe₄O₆, although these isomers have similar geometries (T_d versus slightly distorted T_d symmetry), including a ferromagnetic state with a magnetic moment of 20 μ_B ,¹⁶ a ferrimagnetic 10 μ_B state,¹⁷ and most recently a singlet state (¹A₂, C_{2v}).^{18,19} Therefore, it is important to identify the geometry of clusters produced in the experiment before assessing their magnetic ground state configurations. The cluster geometry can be accurately obtained from infrared photodissociation (IRPD) spectroscopy experiments on cluster-rare gas atom complexes. The detachment of the rare

gas atoms is detected mass spectrometrically and signals resonant absorption of infrared photons. This spectroscopic technique, in combination with density functional theory (DFT) calculations, has been proven a powerful technique to identify the geometries of small metal oxide clusters.^{18,20–24}

To fully understand the interplay between chemical compositions, geometric arrangements, and magnetic properties of small chromium oxide clusters, we synthesized a series of cationic Cr_mO_n^+ ($m = 2, 3, 4$; $n \leq m$) clusters and studied them by a combination of infrared spectroscopy and quantum chemical calculations. Several quantum chemical methods were employed to locate ground-state and low-lying structures of the synthesized clusters. The magnetic interactions between and/or among local sites were studied. The evolution of magnetic moments through chemical control is discussed.

7.2 Experimental Methods

The experiments were carried out using a molecular beam setup consisting of a cluster source, an ion guide, a mass filter, an ion trap, and a time-of-flight mass spectrometer.²⁵ This setup was temporarily installed at the Free Electron Laser for Infrared eXperiments (FELIX) facility (The Netherlands).²⁶ The 2nd harmonic of a Nd:YAG laser is focused on a metallic Cr plate and creates a plasma, which is entrained in a pulse of 1% O₂ seeded in He carrier gas and expanded through a clustering channel. The chromium-oxide cluster beam is collimated and thermalized to room temperature by collisions with Ar atoms in a radio frequency (RF) decapole ion guide and mass-selected by a quadrupole mass filter. Mass-selected cationic clusters are accumulated in a ring electrode ion trap. To allow for continuous ion loading, ion thermalization, and cluster-rare gas (He, Ne) complex formation, the trap is continuously filled with a buffer gas of either pure He (for Cr₃O⁺ and Cr₃O₂⁺) or a mixture of 0.125% Ne in He (for Cr₂O₂⁺, Cr₃O₃⁺, and Cr₄O₄⁺) at ion trap temperatures in the range of 20 – 35 K. After filling the trap for 98 ms, all ions are extracted and focused both temporally and spatially into the center of the extraction region of an orthogonally mounted linear time-of-flight (TOF) mass spectrometer. Here, the ion packet can be irradiated with the IR laser pulse. The absorption of a few and often only a single IR photon(s) by the weakly bound cluster-rare gas ionic complex is sufficient for vibrational predissociation and loss of the rare gas messenger. Scanning the wavelength of the excitation laser light provides the IRPD spectra, which are obtained in the difference

mode of operation (laser on-laser off) and recorded by monitoring all ion intensities simultaneously. The infrared free electron laser FELIX is operated in the $400 - 750 \text{ cm}^{-1}$ spectral range at a repetition rate of 5 Hz, a bandwidth of 0.2% root-mean-square of the central wavelength and an average pulse energy of 10 mJ.

7.3 Computational Methods

The CALYPSO²⁷ tool was used to generate large numbers of initial structures at relatively low computational levels (B3LYP/3-21G and BP86/3-21G). The generated low-lying energetic structures were subsequently reoptimized with the larger cc-pVTZ basis set.^{28,29} Different spin multiplicities were tested for all structural isomers. Various density functionals (B3LYP,^{30–32} B3P86,^{32,33} B3PW91,³² BP86,^{31,33} TPSS,³⁴ TPSSh, and M06L³⁵) have been tested to ensure reliability of the obtained results. In addition, for Cr_2O_2^+ the restricted active space followed by second-order perturbation treatment (RASSCF/RASPT2) and coupled cluster (CCSD(T)-F12) methods have been used as benchmark for the DFT calculations. More details about these computational processes are provided in the [Supporting Information](#) (available online). Throughout the calculation process, the TPSS functional appears to be excellent in vibrational simulations of the obtained clusters in comparison to the other used functionals; therefore the simulated spectra from this functional are used as the basis for 4 out of 5 spectral assignments in this work. The B3P86 functional was used for Cr_2O_2^+ , since the IR spectrum of its ${}^8\text{B}_{1u}$ state could not be assessed at the TPSS level (see the [SI](#) for details). DFT energies were corrected for zero point energies (ZPEs) at corresponding levels of theory, unless otherwise stated. The harmonic vibrational frequencies of the ground and first excited states were analytically obtained after DFT optimizations. If not explicitly specified in the text, harmonic vibrational frequencies were calculated with the Gaussian 09 program.³⁶ The empirical dispersion correction GD3³⁷ (for supported functionals) for optimizations and spectral simulations was taken into account.

7.4 Results and Discussion

7.4.1 Structural Assignments

Starting from the simplest synthesized cluster Cr_2O_2^+ , two clear bands around 610 and 720 cm^{-1} were observed from the experimental IRPD spectrum of the $\text{Cr}_2\text{O}_2^+\cdot\text{Ne}$ complex. The ground, first excited states and other low-lying ones of Cr_2O_2^+ are listed in Table S1 of the SI. At all considered levels of theory the ${}^8\text{B}_{1g}$ and ${}^8\text{B}_{1u}$ states are much lower in energy, so we just focus on these two states. Comparing the geometrical structures of the ${}^8\text{B}_{1g}$ ground and the ${}^8\text{B}_{1u}$ excited states, small differences are found. The Cr–O bond is 0.01 Å longer when Cr_2O_2^+ is stimulated from the ${}^8\text{B}_{1g}$ ground state to the ${}^8\text{B}_{1u}$ first excited state. The bonding angles $\widehat{\text{OCrO}}$ and $\widehat{\text{CrOCr}}$ also stretch and bend, respectively, 5 degrees in comparison to the ones of the ground state. In terms of electronic structures, these two states differentiate from each other in the occupation of electrons in b_{1g} and b_{1u} orbitals. The leading configurations of these different electronic states are given in Table S2 of the SI.

The difference in energy between the ground state ${}^8\text{B}_{1g}$ and first excited state ${}^8\text{B}_{1u}$ at the RASPT2 level is 0.38 eV. Assuming Maxwell-Boltzmann statistics, occupancy of an excited state at +0.38 eV would be small. However, besides uncertainty on the calculated relative energy of the excited state, also the attachment of messenger rare gases may affect the energy differences between isomers. Because of shortcomings of the implementation of the RASPT2 calculational technique, the effect of rare gas messenger atoms on the excited states of Cr_2O_2^+ cannot be examined precisely. Taking into account the computational uncertainty of RASPT2 and other quantum chemical methods, the differences in geometrical structures of the ground and first excited states are insignificant, and it is well possible that both the ground and first excited state are populated in the experiment.

The experimental IRPD and simulated IR spectra of the Cr_2O_2^+ cluster are presented in Figure 7.1. Although the TPSS functional is used for simulating the vibrational spectra of most clusters studied in this work, the simulated IR spectrum of excited state ${}^8\text{B}_{1u}$ could not be accessed at this level; therefore, the simulated spectra of these two states at the B3P86 level are used in Figure 7.1b. The simulated IR spectrum in Figure 7.1b is consistent with those obtained for the same isomer using other DFT functionals (TPSSH, B3PW91,

B3P86, B3LYP, M06L, and BP86) (see Figure S9 of the SI). Note that the interaction of the cationic chromium oxide clusters with the rare gas messenger atoms (Ne and He) does not significantly affect the simulated IR spectra (see Figure S2 of the SI).

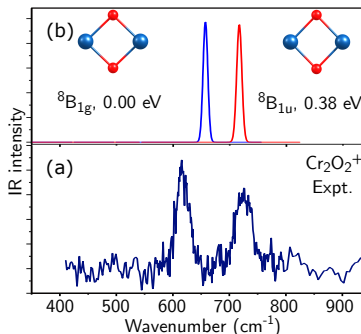


Figure 7.1: (a) Experimental IRPD spectra and (b) simulated harmonic IR spectra of Cr_2O_2^+ . The simulated spectrum of the ${}^8\text{B}_{1g}$ ground state is presented by the blue line, the spectrum of the ${}^8\text{B}_{1u}$ first excited state by the red line. The geometries of the lowest-lying states are shown as insets.

The simulated IR spectrum of the ground state (${}^8\text{B}_{1g}$) shows a single peak at around 630 cm^{-1} , which can only explain one of two experimental bands (Figure 7.1a). The first excited ${}^8\text{B}_{1u}$ state's simulated spectrum has a vibrational mode at around 700 cm^{-1} , 70 cm^{-1} above that of the ${}^8\text{B}_{1g}$ ground state (see Figure 7.1b). Their separation agrees reasonably well with the observed band separation of 90 cm^{-1} in the experimental spectrum. Therefore, both the ${}^8\text{B}_{1g}$ ground state and the ${}^8\text{B}_{1u}$ first excited state are proposed to be populated in the experiment. A similar observation has been made for $\text{Cr}_2\text{O}_2^{-/0}$.³⁸

Figure 7.2 presents experimental and simulated spectra of the Cr_3O_n^+ ($n = 1 - 3$) series. The IR spectrum of $\text{Cr}_3\text{O}^+\cdot\text{He}_2$ has a rather low signal-to-noise ratio, but shows a pronounced peak at 700 cm^{-1} (see Figure 7.2c). The lowest state is found to be ${}^6\text{A}'$ for a propeller-like isomer within the C_s symmetry. A D_{3h} isomer with a high spin ${}^{16}\text{A}'$ electronic state is identified as the first excited state. The predicted IR spectrum of the ${}^6\text{A}'$ ground state is in agreement with the experimental IRPD spectrum, i.e. the IR-active peak observed at 700 cm^{-1} is reproduced at 707 cm^{-1} . The IR spectrum of the first excited state does not match the experimental spectrum, because its intense mode is about 150 cm^{-1} red-shifted from the experimental feature.

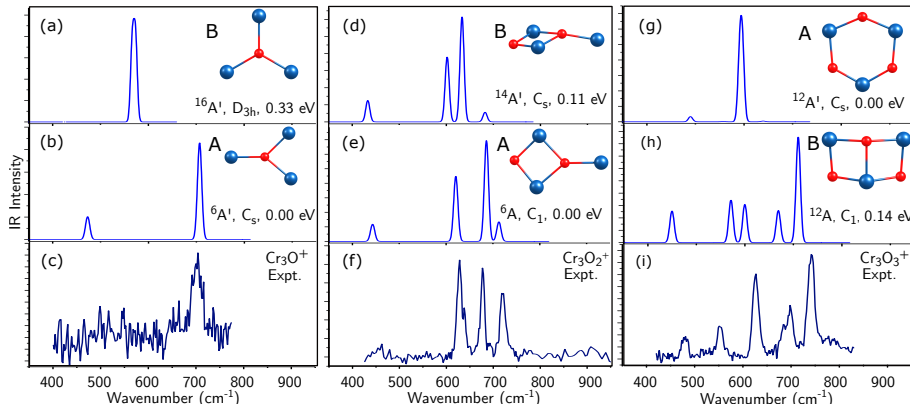


Figure 7.2: Experimental IRPD spectra and simulated harmonic IR spectra of Cr_3O^+ , Cr_3O_2^+ , and Cr_3O_3^+ . The geometries of lowest-lying states for each cluster are shown as insets.

The IRPD spectrum of Cr_3O_2^+ , measured on the $\text{Cr}_3\text{O}_2^+\cdot\text{He}$ complex, has three clear bands at 630, 680, and 725 cm^{-1} . The simulated IR spectra of the sextet ground and a 14-et first excited state (see Figure 7.2d and 7.2e) were used to determine the experimentally populated structure of Cr_3O_2^+ . For the ^6A state, the TPSS method reproduces the three main experimental infrared active vibrations. Simulated spectra of these isomers using other DFT functionals are similar and can be found in the SI (Figure S11). We note that calculated harmonic IR spectra are typically reliable to reproduce the number and the frequencies of the vibrational modes that are seen experimental, but are less accurate for predicting the relative intensities of those modes. The main reasons for this are the multiple photon aspect and the statistical dissociation of the cluster-rare gas complexes in the experiment, which are not included in the computations. A detailed discussion of the consequences of those effects can be found in ref 39. So we conclude that the sextet state is likely the isomer that is observed in the experiment. However, the first excited state $^{14}\text{A}'$ is quite close to the ground state in terms of energy (+0.11 eV at the TPSS level), and its simulated spectrum is similar to the one of the ^6A state. Therefore, both isomers may coexist in the experiment.

For Cr_3O_3^+ two isomers with a high spin 12-tet (noted as A and B in Figure 7.2 parts g and h, respectively) are energetically competitive. Although the calculated relative energy of isomer B (+0.14 eV) is slightly higher than that of isomer A, its simulated IR spectrum agrees much better with the experiment performed on the $\text{Cr}_3\text{O}_3^+\cdot\text{Ne}$ complex with regard

to the frequency of the modes and the number of peaks. We, therefore, assign the spectrum to isomer B. Note that the relative energy difference is comparable to the accuracy of the computational method. As reported in Table S6 of the SI, different hybrid and metaGGA functionals either predict isomer A (TPSS, B3LYP, B3PW91, TPSSH) or isomer B (M06L, B3P86) as most stable isomer with a maximal energy difference of 0.17 eV.

The IRPD spectrum of Cr_4O_4^+ (see Figure 7.3) shows several vibrational bands, which are grouped in three ranges: 550-600 cm^{-1} , 650-710 cm^{-1} and 750-790 cm^{-1} . In the computational study, many different local minima were obtained for Cr_4O_4^+ . Two structural motifs were found to be more stable: a cage-like structure (isomer A) and a ring-like structure (isomer B). Two most stable isomers of Cr_4O_4^+ , their lowest energy electronic states, and corresponding simulated IR spectra are visualized in Figure 7.3. The simulated IR spectrum of isomer A in the octet state is in substantially better agreement with the experiment performed on the $\text{Cr}_4\text{O}_4^+\cdot\text{Ne}$ complex, than that of isomer B. The only discrepancy is a redshift of the simulated spectrum by 40 cm^{-1} , particularly for the intense bands in the 670-760 cm^{-1} range. However, with the B3LYP, B3PW91 and B3P86 functional (see Figure S13 in the SI), the redshift for these bands is much smaller ($< 10 \text{ cm}^{-1}$). The IR spectrum of the cyclic isomer B only predicts two IR-active bands and cannot explain the more complex spectrum observed in the experiment.

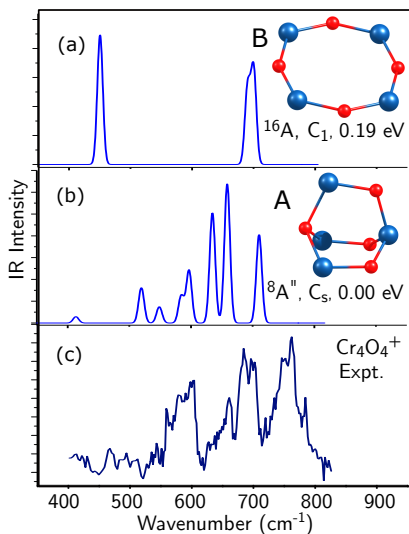


Figure 7.3: Experimental IRPD spectra and simulated harmonic IR spectra of Cr_4O_4^+ . The geometries of the two most stable isomers are shown as insets.

From the above results, one can recognize that different structural motifs result in different IR spectra. In certain cases also similar structural motifs with a different spin state and thus different magnetic configurations can be distinguished by their IR spectra. This is the case for Cr_4O_4^+ . Figure 7.4 presents four different spin configurations (quartet, sextet, octet, and dectet) of structural isomer A of Cr_4O_4^+ , with the octet spin state having the lowest energy. The simulated IR spectra of those different spin states are distinct from each other. This implies that the IRPD technique is, in this specific case, a suitable tool to not only probe the geometric structure but also spin configurations. This constitutes clear evidence of the direct relationship between the identification of vibrational spectra with the IRPD technique and magnetic properties.

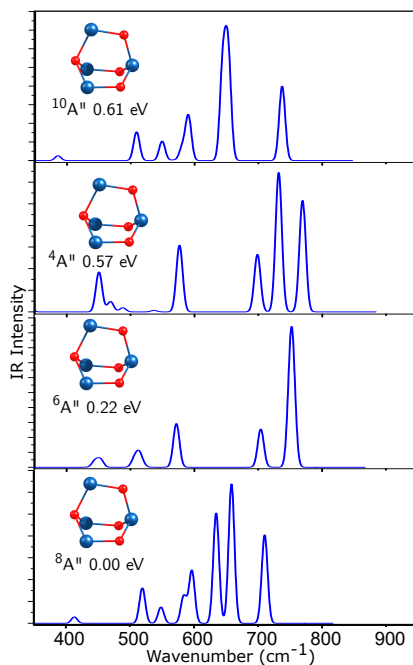


Figure 7.4: Simulated harmonic IR spectra of structural isomer A of Cr_4O_4^+ in four different spin states.

7.4.2 Magnetic Properties

After assigning the geometric structures and the electronic states of the chromium oxide clusters by comparing the measured with simulated IR spectra, computations can be used to analyze the magnetic properties of the clusters. Local spin moments of individual atoms, which combine to give total spin magnetic moments of clusters, are graphically presented in Figure 7.5. Values of these local spin magnetic moments are given in Table 7.1. Also Cr_3^+ , Cr_3O_4^+ and Cr_3O_5^+ are added to the figure and the table. For these sizes, we only have computational results and no assignment of their structure based on the infrared spectra was performed. The spin magnetic configurations of the clusters can be divided into two groups: (i) clusters in which chromium spin moments are ferromagnetically coupled (Cr_2O_2^+ , Cr_3O_3^+ , Cr_3O_4^+ , and Cr_3O_5^+) and (ii) clusters in which metallic spin moments are ferrimagnetically coupled (Cr_3^+ , Cr_3O^+ , Cr_3O_2^+ , and Cr_4O_4^+). In the ground-state structures of Cr_2O_2^+ , Cr_3O_3^+ , Cr_3O_4^+ , and Cr_3O_5^+ all spin magnetic moments of the chromium atoms are parallel, which leads to high values of 7, 11, 9, and 7 μ_B , respectively. In Cr_3^+ , Cr_3O^+ , Cr_3O_2^+ and Cr_4O_4^+ the total spin magnetic moment is reduced compared to the maximal values, resulting in spin moments of 3, 5, 5 and 7 μ_B , respectively.

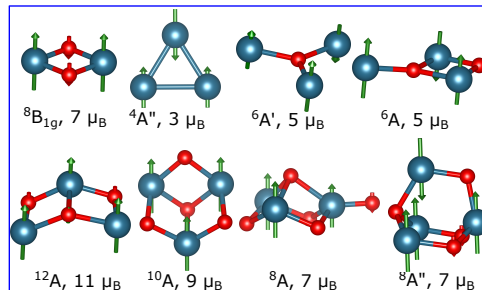


Figure 7.5: Structures of Cr_2O_2^+ , Cr_3O^+ , Cr_3O_2^+ , Cr_3O_3^+ , and Cr_4O_4^+ as assigned by comparison of simulated IR spectra with the experimental IRPD spectra. In addition, the structures of Cr_3^+ , Cr_3O_4^+ and Cr_3O_5^+ , for which no IRPD data is available, are added to the figure. Spin magnetic moments of Cr_3^+ , Cr_3O_4^+ and Cr_3O_5^+ were calculated from their energetically lowest geometry and electronic states. Chromium and oxygen atoms are represented by blue and red balls, respectively. Green (red) arrows indicate the orientation of the local spin magnetic moments ($> 0.05 \mu_B$) on the chromium (oxygen) atoms.

Table 7.1: Total Spin Magnetic Moments of Clusters and Local Spin Magnetic Moments of Chromium and Oxygen Atoms^(a)

cluster	state	spin magnetic moment (μ_B)	local spin magnetic moment (μ_B)						
			Cr ₁	Cr ₂	Cr ₃	Cr ₄	O ₁	O ₂	O ₃
Cr ₂ O ₂ ⁺	⁸ B _{1g}	7	+3.6	+3.6	-0.07	-0.07			
Cr ₃ ⁺	⁴ A	3	-4.5	+3.8	+3.8				
Cr ₃ O ⁺	⁶ A'	5	+4.6	-4.5	+4.9	-0.02			
Cr ₃ O ₂ ⁺	⁶ A	5	+4.9	+3.9	-3.7	-0.03	0.00		
Cr ₃ O ₂ ⁺	¹² A	11	+3.1	+4.0	+4.0	-0.06	-0.06	+0.01	
Cr ₃ O ₃ ⁺	¹⁰ A	9	+3.0	+3.0	+3.0	-0.02	-0.02	-0.02	+0.06
Cr ₃ O ₄ ⁺	⁸ A	7	+1.3	+2.9	+2.9	-0.12	-0.01	+0.02	+0.02
Cr ₃ O ₅ ⁺	⁸ A''	7	+3.8	-3.1	+3.8	+2.6	-0.08	-0.01	+0.03
Cr ₄ O ₄ ⁺									

(a) All values were calculated making use of natural bond orbital (NBO) analysis on the basis of the TPSS electron density.

3d-3d bonding-formation and superexchange-type interactions were demonstrated to underlie the corresponding magnetic properties in pure chromium clusters (Cr_2^0 , $\text{Cr}_3^{+/0}$)^{2,40,41} and dichromium oxide clusters ($\text{Cr}_2\text{O}_2^{-/0}$, and $\text{Cr}_2\text{O}_3^{-/0}$).^{8,9,42} In this work, we find small antiferromagnetic spin moments on the oxygen atoms in Cr_2O_2^+ and Cr_3O_3^+ . Coupling between the chromium and oxygen sites in these clusters occurs through the hybridization between Cr *3d* and O *2p* orbitals. Such an orbital interaction is known as superexchange, and it enhances the parallel spin coupling between chromium atoms.^{8,9,42} Figure 7.6 pictorially provides the total density of states (TDOS) and partial density of states (PDOS) of Cr_3O_3^+ and Cr_3O^+ . In the case of Cr_3O_3^+ , the PDOS (Figure 7.6c) reveals, particularly for the alpha occupied orbitals, strong hybridization between the chromium *3d* and the oxygen *2p* orbitals in the -15.0 to -9.0 eV range (-9.0 eV is the energy of the HOMO). The Cr_3^+ , Cr_3O^+ , Cr_3O_2^+ , and Cr_4O_4^+ clusters disclose ferrimagnetic magnetic behavior, in which one of chromium atoms has its magnetic moment in the reverse direction of the others. By analyzing interaction between the two closest chromium atoms in the C_s isomer of Cr_3O^+ , bonding-like features are found between those two chromium atoms (see Figure S14). The *3d* PDOS of the antiferromagnetically coupled chromium atoms of this cluster show energetic overlap between α and β *3d* occupied orbitals in the -10 to -8.5 eV range (Figure 7.6d). Therefore, *3d-3d*-like bonding between two closest chromium atoms causes an antiferromagnetic coupling of the local spin magnetic moments, similar as in the Cr₂ dimers.^{40,41} A similar bonding-type formation is believed to be present in Cr_3O_2^+ and Cr_4O_4^+ (see Figures S14 and S15), where the spin moment of one of the chromium atoms is in antiparallel to the other ones.

Next, we investigate the effect of atom-by-atom oxygen addition to the geometry and magnetism of the Cr_3^+ metallic cluster. Figure 7.7 presents the magnetic evolution of Cr_3O_n^+ ($n = 0 - 5$). With the addition of oxygen atoms, the total magnetic moment increases from $n = 0$ ($3 \mu_B$) to $n = 3$ ($11 \mu_B$). Such a strong increase of the total magnetic moment implies that direct *3d-3d* bonding-type interaction, which favors antiferromagnetic coupling, becomes weaker upon addition of oxygen atoms, reducing the *3d-3d* interaction. The *3d-3d* bonding-type formation is dominated by the superexchange interaction in Cr_3O_3^+ , leading to a high total spin magnetic moment ($11 \mu_B$). The total spin magnetic moment is gradually reduced if more oxygen atoms are added ($n = 4$ and $n = 5$). Finally, the magnetic moment is expected to be quenched, as was computationally found for the di-chromium oxides Cr_2O_n ¹¹ ($n \geq 6$). This result unravels how the oxygen concentration affects and controls the total magnetic properties of trichromium oxides.

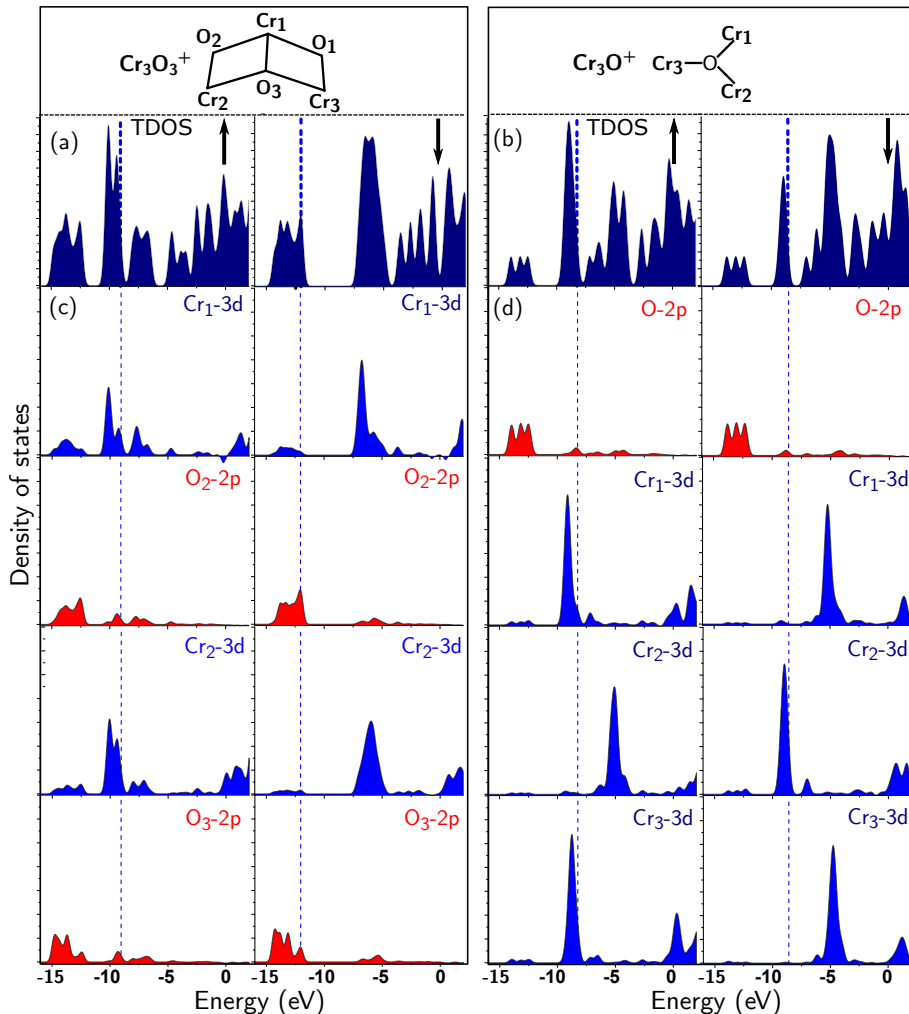


Figure 7.6: Total density of states (TDOS) and partial density of states (PDOS) of Cr_3O_3^+ (left part) and Cr_3O^+ (right part). For each part the left (right) side corresponds to alpha or up (beta or down) orbitals as indicated by the black arrows: (a) TDOS of Cr_3O_3^+ , (b) TDOS of Cr_3O^+ , (c) PDOS of Cr_3O_3^+ , and (d) PDOS of Cr_3O^+ . For PDOS, the projections in oxygen-2p (chromium-3d) orbitals are shown in red (blue). Atoms are numbered according to the structures shown in the insets. Vertical short dashed lines indicate the highest occupied alpha and beta orbitals.

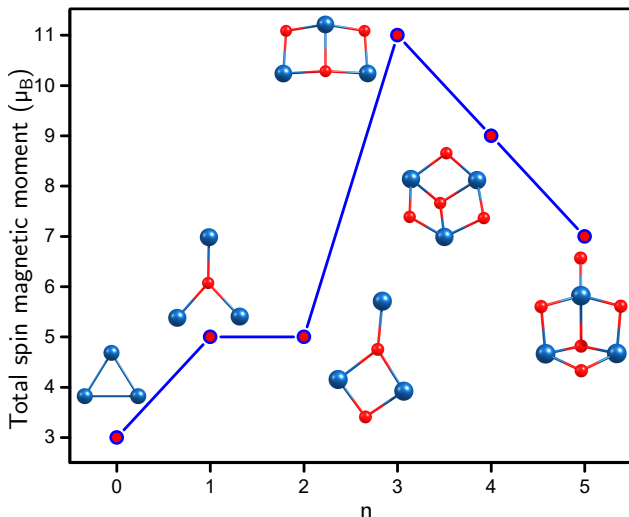


Figure 7.7: Evolution of the total spin magnetic moment for Cr_3O_n^+ ($n = 0 - 5$) clusters.

Overall the evolution of the structures and the magnetic configurations with the oxygen concentration indicates that the highest magnetic moments, i.e. parallel alignment of the local Cr spin magnetic moments, are obtained in suboxides that have enough oxygen atoms to form Cr–O–Cr bridges with a unique O atom between each pair of Cr atoms. For Cr_3O_n^+ this occurs in Cr_3O_3^+ . In this cluster the superexchange interaction is maximized and occurs without strong reduction of the local magnetic moments on the involved Cr atom (see Table 7.1). Addition of more oxygen atoms (i.e. in Cr_3O_4^+ and Cr_3O_5^+) results in the formation of Cr–O bonds with individual Cr atoms and the delocalization of the Cr 3d electrons in Cr–O shared orbitals. Such capturing of unpaired Cr 3d electrons reduces the Cr local magnetic moments. The observation of this magnetic configuration dependence on the oxygen concentration is empirical. An in-debt explanation may be the subject of follow-up studies.

7.5 Conclusion

In conclusion, several cationic chromium-rich oxides were synthesized and characterized through IR spectral characteristics. The magnetic states of these clusters were studied to reveal insights into their magnetic properties. Oxygen plays an important role in

controlling the magnetic configurations. Superexchange interaction through oxygen bridging sites causes ferromagnetic coupling of the chromium atoms in Cr_2O_2^+ and Cr_3O_3^+ . The ferrimagnetic behavior of Cr_3O^+ , Cr_3O_2^+ , and Cr_4O_4^+ is attributed to the bonds between the metal atoms, in which 3d orbitals of nearby chromium atoms directly interact with each other resulting in lower total spin magnetic moments. This study indicates that the highest possible total magnetic moments are obtained in suboxides with a comparable number of oxygen and chromium atoms that have a unique oxygen atom in a single Cr–O–Cr bridge between each pair of Cr atoms. The addition of more oxygen atoms enhances the delocalization of the Cr 3d electrons and reduces the magnetic moment.

References

- (1) Fawcett, E. *Rev. Mod. Phys.* **1988**, *60*, 209–283.
- (2) Bondybey, V.; English, J. *Chem. Phys. Lett.* **1983**, *94*, 443–447.
- (3) Riley, S. J.; Parks, E. K.; Pobo, L. G.; Wexler, S. *J. Chem. Phys.* **1983**, *79*, 2577–2582.
- (4) Zamudio-Bayer, V.; Hirsch, K.; Langenberg, A.; Niemeyer, M.; Vogel, M.; Ławicki, A.; Terasaki, A.; Lau, J. T.; von Issendorff, B. *Angew. Chem. Int. Ed.* **2015**, *54*, 4498–4501.
- (5) Janssens, E.; Hou, X. J.; Neukermans, S.; Wang, X.; Silverans, R. E.; Lievens, P.; Nguyen, M. T. *J. Phys. Chem. A* **2007**, *111*, 4150–4157.
- (6) Cheng, H.; Wang, L.-S. *Phys. Rev. Lett.* **1996**, *77*, 51–54.
- (7) López-Estrada, O.; López-Olay, S.; Aburto, A.; Orgaz, E. *J. Phys. Chem. C* **2016**, *120*, 23892–23897.
- (8) Tono, K.; Terasaki, A.; Ohta, T.; Kondow, T. *Phys. Rev. Lett.* **2003**, *90*, 133402.
- (9) Tono, K.; Terasaki, A.; Ohta, T.; Kondow, T. *J. Chem. Phys.* **2003**, *119*, 11221–11227.
- (10) Reddy, B. V.; Khanna, S. N.; Ashman, C. *Phys. Rev. B* **2000**, *61*, 5797–5801.
- (11) Gutsev, G. L.; Bozhenko, K. V.; Gutsev, L. G.; Utynshev, A. N.; Aldoshin, S. M. *J. Phys. Chem. A* **2017**, *121*, 845–854.
- (12) Li, S.; Zhai, H.-J.; Wang, L.-S.; Dixon, D. A. *J. Phys. Chem. A* **2012**, *116*, 5256–5271.
- (13) Zhai, H.-J.; Li, S.; Dixon, D. A.; Wang, L.-S. *J. Am. Chem. Soc.* **2008**, *130*, 5167–5177.
- (14) Pakiari, A. H.; Shariati, S. *Comput. Theor. Chem.* **2016**, *1084*, 169–178.

- (15) Shah, E. V.; Roy, D. R. *J. Magn. Magn. Mat.* **2018**, *451*, 32–37.
- (16) Ding, X.-L.; Xue, W.; Ma, Y.-P.; Wang, Z.-C.; He, S.-G. *J. Chem. Phys.* **2009**, *130*, 014303.
- (17) Kirilyuk, A.; Fielicke, A.; Demyk, K.; von Helden, G.; Meijer, G.; Rasing, T. *Phys. Rev. B* **2010**, *82*, 020405.
- (18) Logemann, R.; demWijns, A. A.; Katsnelson, M. I.; Kirilyuk, A. *Phys. Rev. B* **2015**, *92*, 144427.
- (19) Erlebach, A.; Huhn, C.; Jana, R.; Sierka, M. *Phys. Chem. Chem. Phys.* **2014**, *16*, 26421–26426.
- (20) Janssens, E.; Santambrogio, G.; Brümmer, M.; Wöste, L.; Lievens, P.; Sauer, J.; Meijer, G.; Asmis, K. R. *Phys. Rev. Lett.* **2006**, *96*, 233401.
- (21) Santambrogio, G.; Janssens, E.; Li, S.; Siebert, T.; Meijer, G.; Asmis, K. R.; Döbler, J.; Sierka, M.; Sauer, J. *J. Am. Chem. Soc.* **2008**, *130*, 15143–15149.
- (22) Brümmer, M.; Kaposta, C.; Santambrogio, G.; Asmis, K. R. *J. Chem. Phys.* **2003**, *119*, 12700–12703.
- (23) Asmis, K. R.; Sauer, J. *Mass Spectrom. Rev.* **2007**, *26*, 542–562.
- (24) Van Dijk, C. N.; Roy, D. R.; Fielicke, A.; Rasing, T.; Reber, A. C.; Khanna, S. N.; Kirilyuk, A. *Eur. Phys. J. D* **2014**, *68*, 357.
- (25) Goebbert, D. J.; Meijer, G.; Asmis, K. R. *AIP Conf. Proc.* **2009**, *1104*, 22–29.
- (26) Oepts, D.; Van der Meer, A.; Van Amersfoort, P. *Infrared Phys. Techn.* **1995**, *36*, 297–308.
- (27) Wang, Y.; Lv, J.; Zhu, L.; Ma, Y. *Phys. Rev. B* **2010**, *82*, 094116.
- (28) Balabanov, N. B.; Peterson, K. A. *J. Chem. Phys.* **2005**, *123*, 064107.
- (29) Dunning Jr., T. H. *J. Chem. Phys.* **1989**, *90*, 1007–1023.
- (30) Lee, C.; Yang, W.; Parr, R. G. *Phys. Rev. B* **1988**, *37*, 785–789.
- (31) Becke, A. D. *Phys. Rev. A* **1988**, *38*, 3098–3100.
- (32) Becke, A. D. *J. Chem. Phys.* **1993**, *98*, 5648–5652.
- (33) Perdew, J. P. *Phys. Rev. B* **1986**, *33*, 8822–8824.
- (34) Tao, J.; Perdew, J. P.; Staroverov, V. N.; Scuseria, G. E. *Phys. Rev. Lett.* **2003**, *91*, 146401.
- (35) Zhao, Y.; Truhlar, D. G. *J. Chem. Phys.* **2006**, *125*, 194101.

- (36) Frisch, M. J.; Trucks, G. W.; Schlegel, H. B.; Scuseria, G. E.; Robb, M. A.; Cheeseman, J. R.; Scalmani, G.; Barone, V.; Mennucci, B.; Petersson, G. A.; Nakatsuji, H.; Caricato, M.; Li, X.; Hratchian, H. P.; Izmaylov, A. F.; Bloino, J.; Zheng, G.; Sonnenberg, J. L.; Hada, M.; Ehara, M.; Toyota, K.; Fukuda, R.; Hasegawa, J.; Ishida, M.; Nakajima, T.; Honda, Y.; Kitao, O.; Nakai, H.; Vreven, T.; Montgomery Jr., J. A.; Peralta, J. E.; Ogliaro, F.; Bearpark, M.; Heyd, J. J.; Brothers, E.; Kudin, K. N.; Staroverov, V. N.; Kobayashi, R.; Normand, J.; Raghavachari, K.; Rendell, A.; Burant, J. C.; Iyengar, S. S.; Tomasi, J.; Cossi, M.; Rega, N.; Millam, J. M.; Klene, M.; Knox, J. E.; Cross, J. B.; Bakken, V.; Adamo, C.; Jaramillo, J.; Gomperts, R.; Stratmann, R. E.; Yazyev, O.; Austin, A. J.; Cammi, R.; Pomelli, C.; Ochterski, J. W.; Martin, R. L.; Morokuma, K.; Zakrzewski, V. G.; Voth, G. A.; Salvador, P.; Dannenberg, J. J.; Dapprich, S.; Daniels, A. D.; Farkas, Ö.; Foresman, J. B.; Ortiz, J. V.; Cioslowski, J.; Fox, D. J. Gaussian-09 Revision E.01., Gaussian Inc. Wallingford CT 2009.
- (37) Grimme, S.; Antony, J.; Ehrlich, S.; Krieg, H. *J. Chem. Phys.* **2010**, *132*, 154104.
- (38) Pham, L. N.; Nguyen, M. T. *J. Chem. Theory Comput.* **2018**, *14*, 4833–4843.
- (39) Calvo, F.; Li, Y.; Kiawi, D. M.; Bakker, J. M.; Parneix, P.; Janssens, E. *Phys. Chem. Chem. Phys.* **2015**, *17*, 25956–25967.
- (40) Vancoillie, S.; Malmqvist, P. Å.; Veryazov, V. *J. Chem. Theory Comput.* **2016**, *12*, 1647–1655.
- (41) Simard, B.; Lebeault-Dorget, M.-A.; Marijnissen, A.; ter Meulen, J. J. *J. Chem. Phys.* **1998**, *108*, 9668–9674.
- (42) Paul, S.; Misra, A. *J. Mol. Struc.: THEOCHEM* **2009**, *895*, 156–160.

Chapter 8

Geometric Structures, Structural Evolution, and Magnetic Properties of Hybrid Chromium Manganese Oxide Clusters

This chapter is based on the manuscript:

Pham, L. N.; van Dijk, C. N.; Kirilyuk, A.; Nguyen, M. T.; Janssens, E. et al. Bimetallic Oxide Clusters $\text{Cr}_x\text{Mn}_y\text{O}_z^+$: Geometric structures, structural evolution, and magnetic properties
Manuscript in preparation. The Supporting Information is available online.

My contribution to this work was theoretical calculations, data analysis, discussion, and writing of the first draft.

8.1 Introduction

Chromium and manganese are two first row transition metal elements with atomic elemental configurations that have five singly occupied $3d$ orbitals ($[Ar]3d^54s^1$ and $[Ar]3d^54s^2$). The electronic ground states of the neutral Cr_2 and Mn_2 dimers are singlets due to antiferromagnetic coupling between the local spin magnetic moments on the atoms.^{1–6} However, the ground states of the cationic dimers possess high-spin magnetic moments ($11\mu_B$) as a result of ferromagnetic coupling.^{6–8} Considering the bimetallic $CrMn$ dimer, the local magnetic moments are ferrimagnetically coupled, leading to a small net magnetic moment of $3\mu_B$.^{7,9} In larger clusters, the magnetic behaviors of chromium and manganese gradually diverge. Cr_3 was found to have a quartet ground state as a result of ferrimagnetic coupling,¹⁰ while in Mn_3 ferrimagnetic and ferromagnetic states were found to be energetically competitive.^{11–14} The energetic competition between ferrimagnetism and ferromagnetism as the ground state of Mn_4 is less clear.^{12,13} An energetic competition between two ferrimagnetic states ($S = 1$ vs. $S = 6$) was predicted for Cr_4 .¹⁵ In bulk materials, chromium is antiferromagnetic at room temperature,¹⁶ while the stable α phase of manganese is paramagnetic.¹⁷ Above 311 K, bulk chromium is paramagnetic as well.¹⁶

An effective way to modify and control magnetic properties of transition metal clusters is to introduce a different element, such as oxygen, into clusters. Indeed, total spin magnetic moments of small chromium oxide clusters (Cr_2O_n , $n = 1 – 3$ ^{18–20} and $Cr_3O_n^+$, $n = 0 – 5$ ¹⁰) were found to be strongly dependent on the number of oxygen atoms. Superexchange-type, $3d$ - $3d$ bonding-like interactions, and $3d$ - $2p$ delocalization were found to dominate the magnetic evolution of these clusters. As for manganese oxide clusters, total magnetic moments of $Mn_2O^{-/0}$ and $Mn_2O_2^+$ also seem to vary with the addition of oxygen atoms.^{21,22} Experiments indicated that ferromagnetic and antiferromagnetic configurations coexist for the case of $Mn_2O^{-/0}$.²¹ Computations predicted an energetic competition between 2-tet and 10-tet states in $Mn_2O_2^+$.²² For clusters with a larger number of oxygen atoms ($n = 3 – 7$), the total magnetic moments of $Mn_2O_n^{-/0/+}$ do not significantly change.²³ A systematic study has not been done for the series of $Mn_3O_n^+$, but for $Mn_3O_3^+$ a spin quintet state was theoretically predicted.²² In this case, the spin state of $Mn_3O_3^+$ is much lower than that of $Cr_3O_3^+$ (12-tet).¹⁰ In large manganese oxides clusters, addition of oxygen atoms is believed to cause alteration of total magnetic moments.²⁴

As can be seen from the abovementioned studies, two popular types of experimental signals possibly obtained from synthesized clusters are photoelectron spectra and infrared

photodissociation spectra. The latter gives direct information about the geometrical structures of studied clusters. Different magnetic configurations typically have (slightly) different geometric configurations, and as a result, their IR spectra are different. Surprisingly, for specific cases, the overall geometrical structures are similar, but a different magnetic configuration can lead to a different IR spectrum. The neutral Fe_4O_4 cluster is a good example of a cluster for which a single geometric motif can expose three magnetic moments of 0, 10 and $20 \mu_B$.^{25–28} Or in our very recent work, a small change in geometry of Co_nCr^+ ($n = 3, 4$) clusters can produce different total magnetic moments due to energetic degeneracy of several spin states.²⁹ Therefore, geometries of clusters need to be accurately determined. In doing so, IRMPD spectra are used as reference for finding the best match with simulated harmonic vibrational spectra of different structural isomers, obtained from quantum chemical calculations.^{10,27,30–34} For specific cases, IRMPD can be an appropriate tool used to distinguish spin configurations of clusters with a same or similar geometric motif,¹⁰ which sheds light on apparent relation between magnetic properties and IRMPD spectra.

While various studies on chromium and manganese oxide clusters have been performed, the corresponding bimetallic oxide clusters are unexplored. A few works were conducted to investigate magnetic properties and crystal structures of bulk chromium-manganese oxides such as CrMnO_3 and CrMnO_4 .^{35,36} In the current work, we synthesized multiple bimetallic oxide clusters and characterized them spectroscopically with the IRMPD technique. In combination with quantum chemical methods, geometrical and electronic structures of the synthesized clusters are unveiled. On the basis of obtained geometries and electronic features, magnetic interactions between metallic sites, and size and composition dependent magnetic evolution of $\text{Cr}_x\text{Mn}_y\text{O}_z^+$ ($x + y = 2 – 4$, $z = 4 – 9$) are disclosed.

8.2 Methodology

All the clusters in this chapter were synthesized by employing the same technique that was described in Chapter 7. The significant difference here is that the messenger species used is O_2 . After the synthesis and IRMPD measurement, quantum chemical computations were conducted. The computational procedure that was followed consists of three main steps. First, for each composition, a large numbers of initial isomers was generated by use of the CALYPSO tool,³⁷ and geometrically optimized at the fast B3LYP^{38–40} and BP86^{39,41}

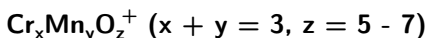
levels in combination with the small 3-21G basis set.^{42,43} For each size a maximum of 50 low-energy structures were screened and pushed to the next geometrical optimization step with a larger triple- ζ basis set def2-TZVP.⁴⁴ In the second step, three density functionals (TPSS,⁴⁵ BP86,^{39,41} and B3P86^{40,41}) were employed to reoptimize the geometries without any symmetry constraint. For clusters without experimental data, only the TPSS functional was employed. For the purpose of comparison, additional oxide clusters of chromium were also geometrically optimized making use of the TPSS functional.⁴⁵ To ensure that all low-lying isomers are minima on the potential energy hypersurface, harmonic vibrational frequencies were calculated analytically. The TPSS, BP86, and B3P86 functionals were used because these functionals were found to give good results on geometries and vibrational frequencies of chromium oxide clusters.¹⁰ Beside the use of the CALYPSO tool to generate initial structures, several isomers were also built on the basis of smaller cluster sizes. Especially, for clusters with the same number of metallic atoms but different metallic ratios, permutations were applied to the metal atoms to draw other low-lying isomers. This process increases our capability to correctly identify low-energy isomers. The third and last step of the computational approach dealt with simulating the effect of molecular oxygen on the vibration spectra, since the oxygen molecules are used in the experiment as messenger for the adsorption of the infrared red. Due to the energy used in the experiment to break two oxygen atoms attached on the clusters is in the range of 15–30 meV, we believe that the O₂ group weakly binds to the cluster. Therefore, the effect of oxygen gas messenger was, then, treated by considering the clusters Cr_xMn_yO_z⁺ with attached O₂ in simulation of IR spectra. Since all simulated frequencies of terminal metal-O vibrations are overestimated in comparison to the experimental ones, this mode of vibrations was scaled with a factor of 0.93. This scaling value was chosen because it gave better agreement with the experiment among several tested values. All remaining modes are kept unchanged. Quantum chemical calculations were done with the Gaussian 09 program,⁴⁶ and dispersion corrections were taken into account using the DFT-D3 parameters⁴⁷ for the supported functionals (TPSS and BP86).

8.3 Results and discussion

8.3.1 Structural assignments



In this work, CrMnO_4^+ is the smallest bimetallic cluster synthesized and spectroscopically characterized with well-resolved IRMPD signals. Its IRMPD spectrum is given in Figure 8.1. A quintet ${}^5\text{A}$ state was found to be the most stable for CrMnO_4^+ . The experimental IRMPD spectrum of CrMnO_4^+ , measured by depletion of $\text{CrMnO}_4^+\text{O}_2$ (Figure 8.1), has two clear bands at 670 and 1010 cm^{-1} . The simulated spectrum of the obtained ground state structure reproduces the band at 670 cm^{-1} , while the higher energy mode is blueshifted by 70 cm^{-1} in the simulation (without consideration of scaling). The simulated spectrum of $\text{CrMnO}_4^+\text{O}_2$ in Figure 8.1c has an additional band at around $\sim 1200\text{ cm}^{-1}$ corresponding to the O=O stretching mode, which is in good agreement with the experimental one even though the intensity of this band is much higher than that of the experiment. From all above features, we believe that the CrMnO_4^+ isomer with attached O_2 ($\text{CrMnO}_4^+\text{O}_2$) was measured in the experiment. Note that the other two isomers of CrMnO_4^+ shown in Figure S2 of the [Supporting Information \(SI\)](#) have a significantly higher relative energy and cannot reproduce the experimental IRMPD bands of $< 1100\text{ cm}^{-1}$ (see Figure S40).



Four bimetallic clusters containing three metal atoms were studied: $\text{CrMn}_2\text{O}_5^+$, $\text{CrMn}_2\text{O}_6^+$, $\text{Cr}_2\text{MnO}_6^+$, and $\text{Cr}_2\text{MnO}_7^+$. The experimental IRMPD spectra of these clusters are presented in Figures 8.2 and 8.3. Except for the spectrum of $\text{Cr}_2\text{MnO}_7^+$, their spectra reveal the O=O stretching mode around 1200 cm^{-1} , which is representative for the O_2 group that is used as messenger in the experiment. The vibrational modes around $\sim 1000\text{ cm}^{-1}$ correspond to vibrations of terminal oxygen atoms while the remaining lower-frequency modes are associated with vibrations of the main frames of the clusters.

The computed most stable isomers of $\text{CrMn}_2\text{O}_5^+$ and $\text{CrMn}_2\text{O}_6^+$ are given in subpanels b and e of Figure 8.2, respectively. Basically, the general frames of two clusters are similar with three metallic centers alternately binding to bridging oxygen atoms. The difference

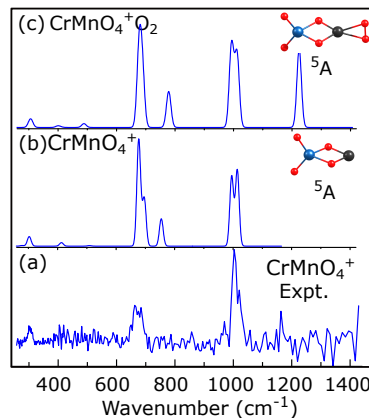


Figure 8.1: Experimental IRMPD and simulated (at the TPSS level) harmonic IR spectra of low-energy isomers of CrMnO_4^+ . The geometrical structures of selected low-lying states are given as inset with chromium (manganese) atoms represented by blue (black) balls.

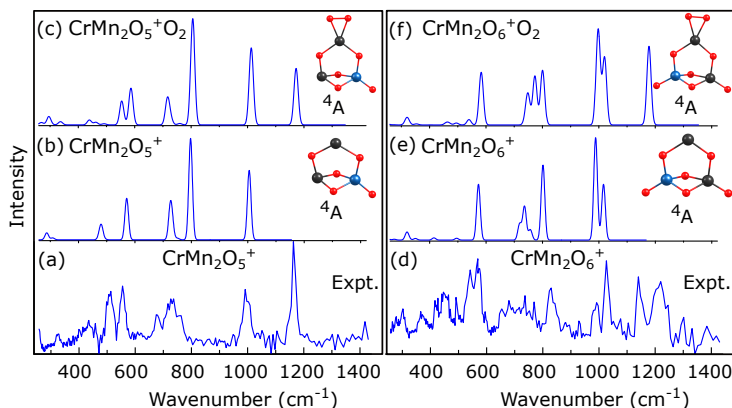


Figure 8.2: Experimental IRMPD and simulated (at the TPSS level) harmonic IR spectra of low-energy isomers of (left panel) $\text{CrMn}_2\text{O}_5^+$ and (right panel) $\text{CrMn}_2\text{O}_6^+$. The geometrical structures of selected low-lying states are given as insets with chromium (manganese) atoms represented by blue (black) balls.

here is that the $\text{CrMn}_2\text{O}_5^+$ has only one terminal oxygen atom binding to a chromium atom whereas in $\text{CrMn}_2\text{O}_6^+$ the terminal oxygen atoms are attached to the Cr and a Mn atom. The simulated spectra of these two clusters without effects of environmental $\text{O}=\text{O}$ fragments successfully reproduce the experiment in the spectral range below 1100 cm^{-1} . The measured vibrational modes around $\sim 1200 \text{ cm}^{-1}$, can be reproduced as well by adding the O_2 messenger molecule. The simulated $\text{O}=\text{O}$ stretching mode of attached oxygen fragment (O_2) reflects this region quite well (see parts c and f of Figure 8.2). Note that $\text{CrMn}_2\text{O}_5^+$ and $\text{CrMn}_2\text{O}_6^+$ have the same spin state (${}^4\text{A}$). Other nearly degenerate states and energetically close isomers of $\text{CrMn}_2\text{O}_5^+$ are provided in the SI.

For $\text{Cr}_2\text{MnO}_6^+$, two spin states (${}^5\text{A}$ and ${}^7\text{A}$) of the same geometrical motif, similar to the ground state of $\text{CrMn}_2\text{O}_6^+$, found to be energetically degenerate. Simulated vibrational spectra of those states are similar and nicely agree with the experiment spectrum if the O_2 messenger is included in the simulation (Figure 8.3a). Since both states are energetically degenerate and their simulated spectra are nearly identical, we predict that they are both populated in the experiment.

The experimental IRMPD spectrum of $\text{Cr}_2\text{MnO}_7^+$ does not show a band around 1200 cm^{-1} . This suggests that the O_2 group loosely binds to $\text{Cr}_2\text{MnO}_7^+$, and the symmetric stretching mode of $\text{O}=\text{O}$ is IR inactive (similar to the vibration of O_2 molecules). Therefore, effects of messenger is ignored in the IR simulation for this cluster. At the TPSS level, three geometrical motifs (noted as A, B, and C in Figure 8.3b) of $\text{Cr}_2\text{MnO}_7^+$ were found to be energetically competitive as the most stable isomer, in which the isomer A has two nearly degenerate spin states (${}^3\text{A}$ and ${}^5\text{A}$). Energetic ordering of these isomers is not consistent among the used functionals, however the differences are small (see Table S6). Four TPSS IR spectra of these isomers are given in the right panel of Figure 8.3. Among these four simulated spectra, two of them (${}^5\text{A}$ of isomers A and C) are in better agreement with the experimental one with regard to the number of active regions and vibrational frequencies. From the simulated IR spectrum of the isomer B in Figure 8.3b (${}^5\text{A}$), we can see that two peaks at $\sim 800 \text{ cm}^{-1}$ and $\sim 1050 \text{ cm}^{-1}$ can reflect the two corresponding experimental regions, but the peak at $\sim 520 \text{ cm}^{-1}$ has quite low intensity. Therefore, we believe that the ${}^5\text{A}$ state of the isomer B does not correspond to the experiment. Note that the simulated spectrum of the ${}^3\text{A}$ electronic state (isomer A) cannot be considered to be causing the experimental IRMPD spectra of $\text{Cr}_2\text{MnO}_7^+$ because its simulated spectrum (Figure 8.3b) cannot reproduce the experimental vibrational frequency of $\sim 520 \text{ cm}^{-1}$ reasonably.

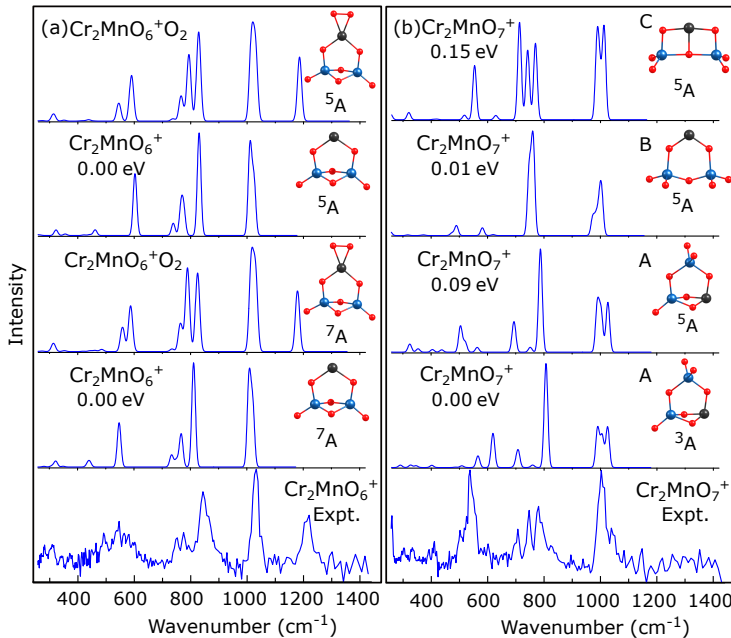


Figure 8.3: Experimental IRMPD and simulated (at the TPSS level) harmonic IR spectra of low-energy isomers of (a) $\text{Cr}_2\text{MnO}_6^+$ and (b) $\text{Cr}_2\text{MnO}_7^+$. The geometrical structures of selected low-lying states are given as insets with chromium (manganese) atoms represented by blue (black) balls.

$\text{Cr}_x\text{Mn}_y\text{O}_z^+ (x + y = 4, z = 6 - 9)$

Five bimetallic clusters containing four metal atoms were spectroscopically investigated $\text{CrMn}_3\text{O}_6^+$, $\text{Cr}_2\text{Mn}_2\text{O}_{7,8}^+$, and $\text{Cr}_3\text{MnO}_{8,9}^+$. The IRMPD spectra of these clusters seem to be different from each other with regard to the number of vibrational regions and relative intensities among each active vibrational regions; however in the experimental spectrum of each cluster, the terminal metal–O vibration ($\sim 1000 \text{ cm}^{-1}$) and vibrations of cluster frames ($\sim 800 \text{ cm}^{-1}$) usually appear although for specific clusters they are not so clear (refer to experimental subpanels in Figures 8.4, 8.5, and 8.6 for more details).

The IRMPD spectrum of $\text{CrMn}_3\text{O}_6^+$ (Figure 8.4a) has five clear regions (peaks) of vibrations with high signal-to-noise ratio. Computational determination of the most stable geometrical motif and the electronic ground state of this cluster is quite challenging. Three used functionals (TPSS, B3P86, and BP86) gave three different ground-state isomers (noted

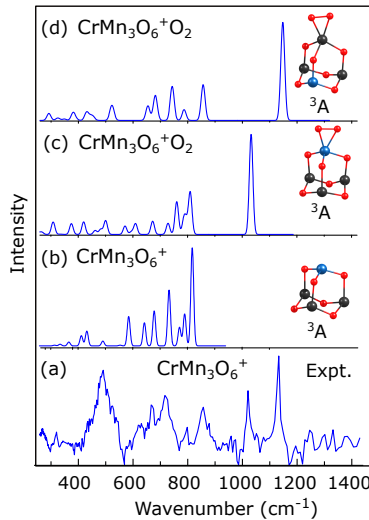


Figure 8.4: Experimental IRMPD and simulated harmonic IR spectra of $\text{CrMn}_3\text{O}_6^+$ at the TPSS level. The geometrical structures of selected low-lying states are given as insets with chromium (manganese) atoms represented by blue (black) balls.

as A, B, and C in Figure S7), in which two isomers B and C have terminal metal–O bonds. The isomer A ($S=1$) is determined as the most stable geometrical structures at the TPSS level. The predicted spectra of this isomer and its complexes with the O_2 group attached to the Cr and Mn atoms are provided in subpanels b, c, and d of Figure 8.4, respectively. Obviously, no single simulated spectra can reproduce two peaks at ~ 1010 and $\sim 1120 \text{ cm}^{-1}$. Interestingly, O=O attached to Cr and Mn atoms are computationally featured with two different wavenumbers (~ 1010 and $\sim 1120 \text{ cm}^{-1}$) as plotted in subpanels c and d of Figure 8.4. Suppose that two complexes of $\text{CrMn}_3\text{O}_6^+\text{O}_2$ were formed simultaneously and their vibrational features were observed experimentally. Two experimental peaks at ~ 1010 and $\sim 1120 \text{ cm}^{-1}$ can be caused by two stretching vibrations of the O_2 group. As a result, we believe that two complexes of $\text{CrMn}_3\text{O}_6^+$ with the attached O_2 at Mn and Cr sites can be populated in the experiment simultaneously to cause the complicated experimental spectrum. Note that the intensity of the vibrational region at $\sim 500 \text{ cm}^{-1}$ in the experimental spectrum is much higher than those of corresponding vibrational regions in the simulated spectra (see parts c and d of Figure 8.4).

The IRMPD spectrum of $\text{Cr}_2\text{Mn}_2\text{O}_7^+$ can be seen in Figure 8.5a and is well resolved with three vibrational regions. There is no characteristic band at $\sim 1200 \text{ cm}^{-1}$. Relative

energies calculated using three abovementioned functionals inconsistently pointed out two structural motifs as candidates for the most stable isomer, depending on the used functionals (see the SI for relative energies). The TPSS and B3P86 functionals determined the isomer A depicted in Figure S9 of the SI as the most stable isomer, while BP86 has a slight preference for the isomer B (see insets in parts b and c of Figure 8.5). A comparison between the experimental and simulated spectra rules out the isomer A and its O₂-attached clusters (Cr₂Mn₂O₇⁺O₂) as the populated structure in the experiment because only two clear simulated peaks at $\sim 770\text{ cm}^{-1}$ and $\sim 1005\text{ cm}^{-1}$ are present in the simulated spectra (see Figure S44). As mentioned above, no bands at $\sim 1200\text{ cm}^{-1}$ are observed in the experimental IRMPD spectrum. This can be due to very weak interaction between the cluster Cr₂Mn₂O₇⁺ and the O₂ group, resulting in totally symmetric stretching vibrations of O=O and then the inactive IR mode. This motivated us to focus more on the bare cluster Cr₂Mn₂O₇⁺ without the effects of gas messenger. A doublet state (²A) of the isomer B produces its simulated spectrum with three apparent active regions corresponding well to three pronounced experimental regions. Surprisingly, the cluster with attached O₂ group (see Figure 8.5d) also has three apparent active regions corresponding to three clear experimental bands but different relative intensity. The stretching vibration of the O=O group and terminal Cr-O vibration are in the same region of $\sim 1000\text{ cm}^{-1}$. Comparing two simulated spectra in parts c and d of Figure 8.5, one can conclude that the spectrum of the bare cluster is in better agreement with the experiment. Therefore, the doublet state of the isomer B is believed to be populated in the experiment and causes the observed experimental IRMPD spectrum of Cr₂Mn₂O₇⁺. One other state (⁴A) of the isomer B is $\sim 0.10\text{ eV}$ more stable than the ²A state, but its simulated IR spectrum and simulated spectra (see subpanels d and e of Figure S44) of cluster-O₂ are not in agreement with the experimental one; therefore this state is not populated in the experiment.

Addition of one more oxygen atom to Cr₂Mn₂O₇⁺ to form Cr₂Mn₂O₈⁺ does not significantly affect the main geometrical frame of clusters. Indeed, our calculations proved that the addition of one more oxygen atom creates one more terminal Cr—O bond (second one) on the main frame of oxide clusters (inset in Figure 8.5f). Such terminal Cr—O bonds underlie harmonic vibrational frequencies of $\sim 1020\text{ cm}^{-1}$ in the experimental IRMPD spectrum of Cr₂Mn₂O₈⁺ (Figure 8.5e). The vibrational peak at $\sim 1200\text{ cm}^{-1}$ in the experiment is attributed to the stretching vibration of the O=O group. IR simulation of the ²A ground-state structure taking account of O=O effects reasonably reproduces two peaks at $> 1000\text{ cm}^{-1}$ in Figure 8.5g. All remaining experimental peaks with frequencies of $< 900\text{ cm}^{-1}$ have rather low signal-to-noise ratio. Nevertheless, the TPSS simulated spectrum of the

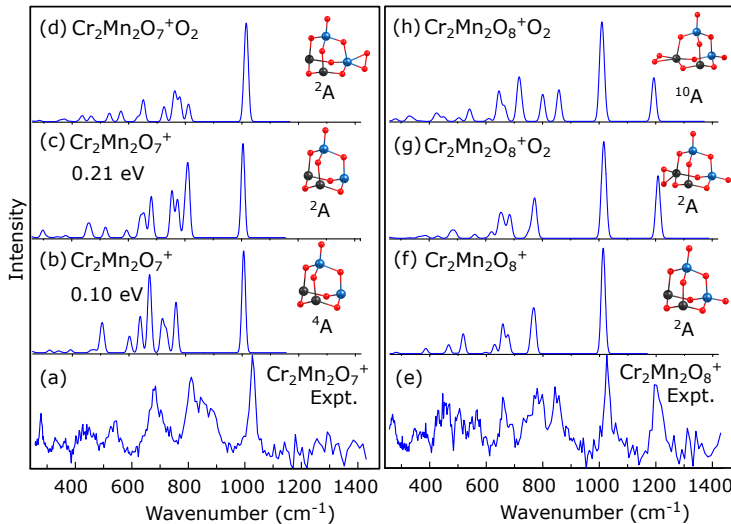


Figure 8.5: Experimental IRMPD and simulated harmonic IR spectra of $\text{Cr}_2\text{Mn}_2\text{O}_z^+$ ($z = 7, 8$) at the TPSS level. The geometrical structures of selected low-lying states are given as insets with chromium (manganese) atoms represented by blue (black) balls.

ground state also can reflect these features within this range. The simulated spectrum of a sextet state (the first excited state at the TPSS level) in Figure S45b has poor agreement with the experimental spectrum. Hence, it is not responsible for the experiment, although this state was determined to be the ground state of $\text{Cr}_2\text{Mn}_2\text{O}_8^+$ by the BP86 functional. From experimentally populated electronic states of two clusters $\text{Cr}_2\text{Mn}_2\text{O}_7^+$ and $\text{Cr}_2\text{Mn}_2\text{O}_8^+$, one can see that doublet spin states of these two clusters remain unchanged under variation of one oxygen atom.

The geometrical features of $\text{Cr}_3\text{MnO}_8^+$ and $\text{Cr}_3\text{MnO}_9^+$ are provided in Figure 8.6. Those clusters have a similar structural motif with the additional oxygen atom in $\text{Cr}_3\text{MnO}_9^+$ being attached to the third Cr atom via a terminal Cr—O bond. From experimental spectra done for the $\text{Cr}_3\text{MnO}_8^+$ and $\text{Cr}_3\text{MnO}_9^+$ clusters, we can see that vibrational signals recorded are not pronounced; nonetheless, the peak at $\sim 1000 \text{ cm}^{-1}$ can still be clear in both experimental spectra (Figures 8.6a and 8.6g). For $\text{Cr}_3\text{MnO}_8^+$, an unclear peak at $\sim 1200 \text{ cm}^{-1}$ seems to appear in the experimental spectrum. The same feature can be seen in the experimental spectrum of $\text{Cr}_3\text{MnO}_9^+$ but at $\sim 1250 \text{ cm}^{-1}$. Since these peaks have very low intensity, it is unsure to conclude whether gas messenger really affects the experimental spectra. As a result, we consider the simulation of both with and without gas messenger. Clearly, the

TPSS functional can predict the pronounced peak at $\sim 1000 \text{ cm}^{-1}$ successfully. With more attention to the experimental spectrum of $\text{Cr}_3\text{MnO}_8^+$, one recognizes all three remaining vibrational regions at $< 800 \text{ cm}^{-1}$ have the quite low signal-to-noise ratio. The ${}^3\text{A}$ ground-state of $\text{Cr}_3\text{MnO}_8^+$ can reproduce all these three regions of vibrations; however one of them is $\sim 100 \text{ cm}^{-1}$ redshifted (see Figure 8.6b). The IR simulated spectrum of a distorted structure depicted in Figure 8.6e seems to have better agreement with the experiment; however the ${}^3\text{A}$ state energy of this isomer is 1.52 eV less stable than the ground state. Taking into account of gas messenger (the O_2 group), the $\sim 1200\text{-cm}^{-1}$ peak can be reproduced but no improvements on all bands of $< \sim 1000 \text{ cm}^{-1}$ seen (see subpanels d and f in Figure 8.6). For $\text{Cr}_3\text{MnO}_9^+$, the simulated spectra of ${}^7\text{A}$ with and without gas messenger are in better agreement with the experiment than ${}^5\text{A}$ (see the right panel in Figure 8.6). The BP86 and B3P86 energies of these two states are nearly degenerate (see Table S12); therefore we propose that the ${}^7\text{A}$ state can be the ground state and it is populated in the experiment.

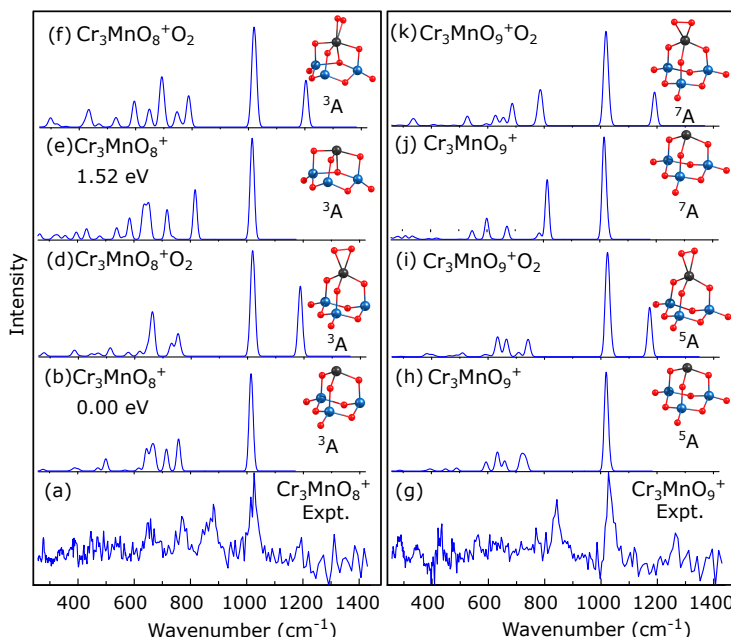


Figure 8.6: Experimental IRMPD and simulated harmonic IR spectra of $\text{Cr}_3\text{MnO}_z^+$ ($z = 8, 9$) at the TPSS level. The geometrical structures of selected low-lying states are given as insets with chromium (manganese) atoms represented by blue (black) balls.

8.3.2 Structural evolution

To explore the structural evolution of these bimetallic clusters ($\text{Cr}_x\text{Mn}_y\text{O}_z^+$, $x + y = 2 - 4$, $z = 2 - 10$), several additional clusters were investigated using the TPSS functional. Geometrical structures of the predicted clusters and the above studied ones are presented in Figure 8.7. Below, we discuss the effects of the oxygen content, the Cr to Mn metallic ratio, and numbers of metallic atoms on the geometrical structure of the clusters.

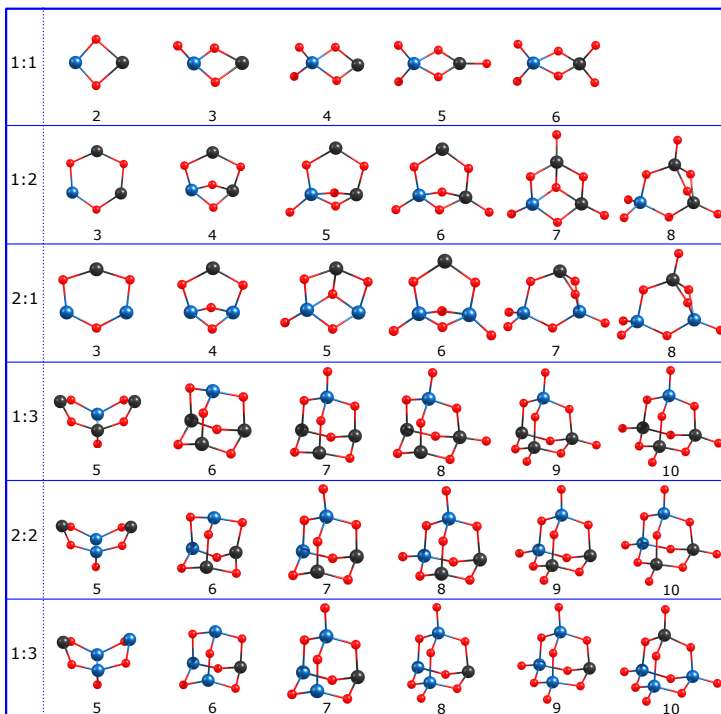


Figure 8.7: Structural evolution of $\text{Cr}_x\text{Mn}_y\text{O}_z^+$ ($x + y = 2 - 4$, $z = 2 - 10$). The numbers of chromium and manganese atoms are on the left-hand column, and the number of oxygen atoms is arranged horizontally below oxide structures. Chromium (manganese) balls are blue (black) balls.

The metallic frame of each Cr-Mn ratio oxide series does not change under addition of oxygen atoms. Adding more oxygen atoms to clusters increases the coordination of the metallic sites. 2-fold coordination becomes 3- and 4-fold coordination when more oxygen atoms are added to a specific series of clusters. The added oxygen atoms first go

to the chromium sites. Once a high oxygen coordination (3- and 4-fold) is reached for all chromium atoms, the oxygen coordination of the manganese atoms will subsequently increase under addition of more oxygen atoms. Additional oxygen atoms tend to bind first to chromium atoms and then to manganese ones. This bonding priority can be explained by the stronger Cr–O bond in comparison to the Mn–O one (461 ± 8.7 versus 362 ± 25 kJ mol^{-1}).⁴⁸ All oxygen atoms, except for those in terminal metal-O bonds, have 2-fold metal coordination.

The effects of metallic ratios can be evaluated within a specific range of oxygen atoms in $\text{Cr}_x\text{Mn}_y\text{O}_z^+$ ($x + y = 3 - 4$, $z = 3 - 10$). The metallic frame of series with three and four metallic atoms does not change when the metallic ratio varies. To be more specific, for the case of $\text{Cr}_x\text{Mn}_y\text{O}_z^+$ ($x + y = 3$) three metallic atoms are arranged to make a similar structural motif when the number of chromium atoms increases from 1 to 2. In $\text{CrMn}_3\text{O}_z^+$, $\text{Cr}_2\text{Mn}_2\text{O}_z^+$, and $\text{Cr}_3\text{MnO}_z^+$ ($z = 5 - 10$) the metallic frame is also unchanged over all possible ratios of metallic atoms.

8.3.3 Magnetic interactions

Figure 8.8 pictorially presents how total magnetic moments of each cluster series with two, three, and four metallic atoms varies under addition of oxygen atoms. Note that in order to see the effects of manganese on the magnetic properties, pure chromium oxide clusters with corresponding numbers of metallic atoms are also considered. For clusters with two metallic atoms, the total magnetic moment of CrMnO_z^+ ($z = 2 - 6$) behaves quite similarly to that of pure dichromium oxide clusters. Total magnetic moments of both series monotonically decrease under addition of oxygen atoms (see Figure 8.8a). In CrMnO_2^+ , superexchange interaction through bridging oxygen facilitates the maximum total magnetic moment as observed in $\text{Cr}_2\text{O}_2^{-/0/+}$.^{10,19,49} For series of clusters containing three metallic atoms, oxygen addition does not affect total magnetic moments of $\text{CrMn}_2\text{O}_z^+$ and $\text{Cr}_2\text{MnO}_z^+$ ($z = 3 - 8$) significantly (fluctuating within 2 to 5 μ_B), while that of the Cr_3O_z^+ ($z = 3 - 8$) linearly declines from 11 to 1 μ_B because 3d electrons of chromium are captured by additional oxygen atoms.¹⁰ Evolution of total magnetic moments in clusters with four metallic atoms is more complicated and likely dependent on the precise amount of both oxygen and chromium atoms. The addition of oxygen atoms has its stronger magnetic effects on clusters with dominant chromium ratio (3 and 4 atoms). This can be seen in Figure 8.8c where the total magnetic moments of these two series drastically go

down from ~ 11 to $\sim 2 \mu_B$ when the number of oxygen atom increases from 6 to 8. In the other two series of clusters $\text{Cr}_2\text{Mn}_2\text{O}_z^+$ and $\text{CrMn}_3\text{O}_z^+$ ($z = 6 - 8$), the total magnetic moment fluctuates around $2 \mu_B$. Through the evolution of total magnetic moments, we can see that introduction of manganese into oxide clusters keeps total magnetic moments lower and more stable under addition of oxygen atoms with respect to corresponding pure chromium oxide clusters. This kind of magnetic effects can be obviously observed in the series with three metallic atoms ($\text{CrMn}_2\text{O}_z^+$ and $\text{Cr}_2\text{MnO}_z^+$). In the series with four metallic atoms, manganese playing as magnetic reducer and stabilizer can be seen in clusters with significant ratio of manganese atoms such as $\text{Cr}_2\text{Mn}_2\text{O}_z^+$ and $\text{CrMn}_3\text{O}_z^+$. To see more details about the magnetic-reducer role of manganese in the manganese-rich clusters, total magnetic moments of four clusters (Cr_4O_6^+ , $\text{Cr}_3\text{MnO}_6^+$, $\text{Cr}_2\text{Mn}_2\text{O}_6^+$, and $\text{CrMn}_3\text{O}_6^+$) and the local magnetic orientation of metallic sites within each cluster are provided in Figure 8.9. Apparently, the total magnetic moment plunges from around 9 to $2 \mu_B$ when the number of manganese atoms becomes dominant in the clusters. In $\text{Cr}_2\text{Mn}_2\text{O}_6^+$ and $\text{CrMn}_3\text{O}_6^+$, antiferromagnetic coupling between two metallic sites appear resulting in reduction of total magnetic moments in these two clusters. Besides, moduli of local magnetic moments on the Cr sites, which are the main magnetic components causing high total magnetic moments in Cr_4O_6^+ and $\text{Cr}_3\text{MnO}_6^+$, are also significantly reduced (see Table S43).

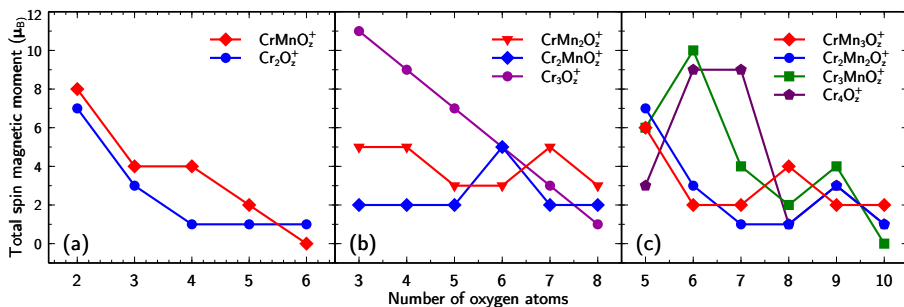


Figure 8.8: Total magnetic moments of $\text{Cr}_x\text{Mn}_y\text{O}_z^+$ ($x + y = 2 - 4$, $z = 2 - 10$)

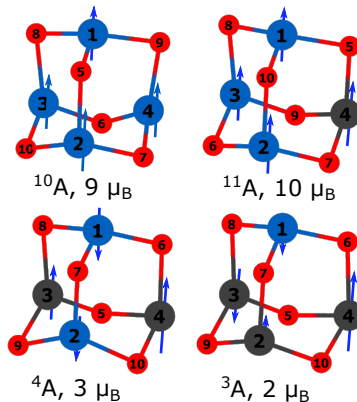


Figure 8.9: Total magnetic moments and the orientation of the local spin magnetic moments on the metallic sites (chromium and manganese) withdrawn from natural bond orbital (NBO) analysis using the TPSS electron density. Chromium (manganese) atoms are represented by blue (black) balls.

To see how local magnetic moments of manganese and chromium sites contribute to total magnetic moments and are affected upon the addition of oxygen atoms, averaged absolute local magnetic moments (ALMMs) of each metallic element (chromium and manganese) are calculated and graphically given in Figure 8.10. Apparently, ALMMs of both chromium and manganese are inversely proportional to the number of oxygen atoms. Local magnetic moments of metallic sites are quenched when the number of oxygen atoms is large enough (6, 8, and 10 for clusters containing 2, 3, and 4 metallic atoms, respectively). In most of the bimetallic clusters, ALMMs of manganese are higher than those of chromium, and ALMMs of chromium in the pure chromium oxide clusters are in between those of manganese and chromium in the bimetallic ones. This local magnetic ordering suggests that electron transfer from chromium atoms to manganese ones significantly controls total magnetic moments of hybrid Cr-Mn oxide clusters, and in these hybrid oxide clusters manganese sites predominantly cause magnetic behaviors. This result can be seen intuitively for the case of four metallic clusters Cr_4O_6^+ , $\text{Cr}_3\text{MnO}_6^+$, $\text{Cr}_2\text{Mn}_2\text{O}_6^+$, and $\text{CrMn}_3\text{O}_6^+$ in Figure 8.9.

8.3.4 Conclusion

Various hybrid Cr-Mn oxide clusters were synthesized and characterized with the IRMPD technique. In combination with DFT calculations, all experimentally synthesized clusters

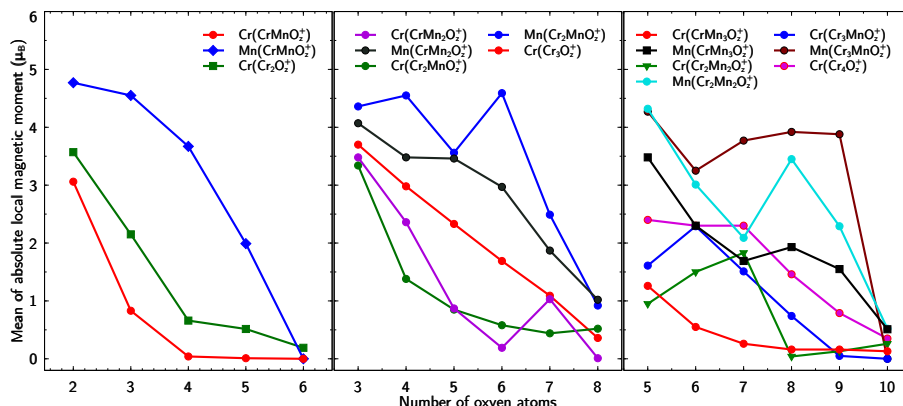


Figure 8.10: Averaged absolute local magnetic moments of Cr and Mn in $\text{Cr}_x\text{Mn}_y\text{O}_z^+$ ($x + y = 2 - 4$, $z = 2 - 10$). All values were calculated from natural bond orbital (NBO) analysis using the TPSS electron density.

with 2 to 4 metallic atoms were geometrically and electronically identified. Within studied clusters, general geometric frames of all series are not affected by additional oxygen atoms and metallic ratios. Several clusters possess nearly degenerate electronic states which are simultaneously populated and contribute to their experimental IRMPD spectra. Under addition of oxygen atoms, chromium sites tend to attract additional oxygen atoms first to reach 3- and 4-fold coordination and then to manganese sites.

While total magnetic moments of pure chromium oxide Cr_xO_y^+ and small hybrid oxide CrMnO_z^+ clusters strongly depend on amount of oxygen atoms, those of bigger bimetallic ones are more stable and smaller. In these hybrid clusters, manganese plays as magnetic stabilizer and reducer. Averaged absolute local magnetic moments of manganese are much higher than those of chromium in all bimetallic clusters and higher than those of chromium in corresponding pure chromium oxide clusters. This points out that electron transfer from chromium to manganese happens. This electron transfer process and electrons captured by oxygen atoms control magnetic behaviors of bimetallic Cr-Mn oxide clusters.

References

- (1) Baumann, C. A.; Van Zee, R. J.; Bhat, S. V.; Weltner, W. *J. Chem. Phys.* **1983**, *78*, 190–199.
- (2) Bier, K. D.; Haslett, T. L.; Kirkwood, A. D.; Moskovits, M. *J. Chem. Phys.* **1988**, *89*, 6–12.
- (3) Van Zee, R. J.; Baumann, C. A.; Weltner, W. *J. Chem. Phys.* **1981**, *74*, 6977–6978.
- (4) Yamamoto, S.; Tatewaki, H.; Moriyama, H.; Nakano, H. *J. Chem. Phys.* **2006**, *124*, 124302.
- (5) Bondybey, V.; English, J. *Chem. Phys. Lett.* **1983**, *94*, 443–447.
- (6) Zamudio-Bayer, V.; Hirsch, K.; Langenberg, A.; Niemeyer, M.; Vogel, M.; Ławicki, A.; Terasaki, A.; Lau, J. T.; von Issendorff, B. *Angew. Chem. Int. Ed.* **54**, 4498–4501.
- (7) Cheeseman, M.; Van Zee, R. J.; Flanagan, H. L.; Weltner, W. *J. Chem. Phys.* **1990**, *92*, 1553–1559.
- (8) Van Zee, R. J.; Weltner, W. *J. Chem. Phys.* **1988**, *89*, 4444–4446.
- (9) Desmarais, N.; Reuse, F. A.; Khanna, S. N. *J. Chem. Phys.* **2000**, *112*, 5576–5584.
- (10) Pham, L. N.; Claes, P.; Lievens, P.; Jiang, L.; Wende, T.; Asmis, K. R.; Nguyen, M. T.; Janssens, E. *J. Phys. Chem. C* **2018**, *122*, 27640–27647.
- (11) Gutsev, G. L.; Mochena, M. D.; Bauschlicher, C. W. *J. Phys. Chem. A* **2006**, *110*, 9758–9766.
- (12) Bobadova-Parvanova, P.; Jackson, K. A.; Srinivas, S.; Horoi, M. *Phys. Rev. A* **2003**, *67*, 061202.
- (13) Pederson, M. R.; Reuse, F.; Khanna, S. N. *Phys. Rev. B* **1998**, *58*, 5632–5636.
- (14) Longo, R. C.; Noya, E. G.; Gallego, L. J. *Phys. Rev. B* **2005**, *72*, 174409.
- (15) López-Estrada, O.; López-Olay, S.; Aburto, A.; Orgaz, E. *J. Phys. Chem. C* **2016**, *120*, 23892–23897.
- (16) Fawcett, E. *Rev. Mod. Phys.* **1988**, *60*, 209–283.
- (17) Hobbs, D.; Hafner, J.; Spišák, Phys. *Rev. B* **2003**, *68*, 014407.
- (18) Tono, K.; Terasaki, A.; Ohta, T.; Kondow, T. *Phys. Rev. Lett.* **2003**, *90*, 133402.
- (19) Tono, K.; Terasaki, A.; Ohta, T.; Kondow, T. *J. Chem. Phys.* **2003**, *119*, 11221–11227.

- (20) Paul, S.; Misra, A. *J. Mol. Struc.: THEOCHEM* **2009**, *895*, 156–160.
- (21) Khanna, S. N.; Jena, P.; Zheng, W.-J.; Nilles, J. M.; Bowen, K. H. *Phys. Rev. B* **2004**, *69*, 144418.
- (22) Marks, J. H.; Ward, T. B.; Duncan, M. A. *J. Phys. Chem. A* **2018**, *122*, 3383–3390.
- (23) Gutsev, G. L.; Bozhenko, K. V.; Gutsev, L. G.; Utenshev, A. N.; Aldoshin, S. M. *J. Chem. Phys. A* **2018**, *122*, 5644–5655.
- (24) Williams, K. S.; Hooper, J. P.; Horn, J. M.; Lightstone, J. M.; Wang, H.; Ko, Y. J.; Bowen, K. H. *J. Chem. Phys.* **2012**, *136*, 134315.
- (25) Ding, X.-L.; Xue, W.; Ma, Y.-P.; Wang, Z.-C.; He, S.-G. *J. Chem. Phys.* **2009**, *130*, 014303.
- (26) Kirilyuk, A.; Fielicke, A.; Demyk, K.; von Helden, G.; Meijer, G.; Rasing, T. *Phys. Rev. B* **2010**, *82*, 020405.
- (27) Logemann, R.; demWijs s., s. A.; Katsnelson, M. I.; Kirilyuk, A. *Phys. Rev. B* **2015**, *92*, 144427.
- (28) Erlebach, A.; Huhn, C.; Jana, R.; Sierka, M. *Phys. Chem. Chem. Phys.* **2014**, *16*, 26421–26426.
- (29) Jia, M.; van der Tol, J.; Li, Y.; Chernyy, V.; Bakker, J.; Pham, L. N.; Nguyen, M.; Janssens, E. *J. Phys.: Condens. Matter* **2018**.
- (30) Janssens, E.; Santambrogio, G.; Brümmer, M.; Wöste, L.; Lievens, P.; Sauer, J.; Meijer, G.; Asmis, K. R. *Phys. Rev. Lett.* **2006**, *96*, 233401.
- (31) Santambrogio, G.; Janssens, E.; Li, S.; Siebert, T.; Meijer, G.; Asmis, K. R.; Döbler, J.; Sierka, M.; Sauer, J. *J. Am. Chem. Soc.* **2008**, *130*, 15143–15149.
- (32) Brümmer, M.; Kaposta, C.; Santambrogio, G.; Asmis, K. R. *J. Chem. Phys.* **2003**, *119*, 12700–12703.
- (33) Asmis, K. R.; Sauer, J. *Mass Spectrom. Rev.* **2007**, *26*, 542–562.
- (34) Van Dijk, C. N.; Roy, D. R.; Fielicke, A.; Rasing, T.; Reber, A. C.; Khanna, S. N.; Kirilyuk, A. *Eur. Phys. J. D* **2014**, *68*, 357.
- (35) Nalbandyan, V. B.; Zvereva, E. A.; Yalovega, G. E.; Shukaev, I. L.; Ryzhakova, A. P.; Guda, A. A.; Stroppa, A.; Picozzi, S.; Vasiliev, A. N.; Whangbo, M.-H. *Inorg. Chem.* **2013**, *52*, 11850–11858.
- (36) Chamberland, B. L.; Kafalas, J. A.; Goodenough, J. B. *Inorg. Chem.* **1977**, *16*, 44–46.

- (37) Wang, Y.; Lv, J.; Zhu, L.; Ma, Y. *Phys. Rev. B* **2010**, *82*, 094116.
- (38) Lee, C.; Yang, W.; Parr, R. G. *Phys. Rev. B* **1988**, *37*, 785–789.
- (39) Becke, A. D. *Phys. Rev. A* **1988**, *38*, 3098–3100.
- (40) Becke, A. D. *J. Chem. Phys.* **1993**, *98*, 5648–5652.
- (41) Perdew, J. P. *Phys. Rev. B* **1986**, *33*, 8822–8824.
- (42) Gordon, M. S.; Binkley, J. S.; Pople, J. A.; Pietro, W. J.; Hehre, W. J. *J. Am. Chem. Soc.* **1982**, *104*, 2797–2803.
- (43) Dobbs, K. D.; Hehre, W. J. *J. Comput. Chem.* **8**, 861–879.
- (44) Weigend, F.; Ahlrichs, R. *Phys. Chem. Chem. Phys.* **2005**, *7*, 3297–3305.
- (45) Tao, J.; Perdew, J. P.; Staroverov, V. N.; Scuseria, G. E. *Phys. Rev. Lett.* **2003**, *91*, 146401.
- (46) Frisch, M. J.; Trucks, G. W.; Schlegel, H. B.; Scuseria, G. E.; Robb, M. A.; Cheeseman, J. R.; Scalmani, G.; Barone, V.; Mennucci, B.; Petersson, G. A.; Nakatsuji, H.; Caricato, M.; Li, X.; Hratchian, H. P.; Izmaylov, A. F.; Bloino, J.; Zheng, G.; Sonnenberg, J. L.; Hada, M.; Ehara, M.; Toyota, K.; Fukuda, R.; Hasegawa, J.; Ishida, M.; Nakajima, T.; Honda, Y.; Kitao, O.; Nakai, H.; Vreven, T.; Montgomery Jr., J. A.; Peralta, J. E.; Ogliaro, F.; Bearpark, M.; Heyd, J. J.; Brothers, E.; Kudin, K. N.; Staroverov, V. N.; Kobayashi, R.; Normand, J.; Raghavachari, K.; Rendell, A.; Burant, J. C.; Iyengar, S. S.; Tomasi, J.; Cossi, M.; Rega, N.; Millam, J. M.; Klene, M.; Knox, J. E.; Cross, J. B.; Bakken, V.; Adamo, C.; Jaramillo, J.; Gomperts, R.; Stratmann, R. E.; Yazyev, O.; Austin, A. J.; Cammi, R.; Pomelli, C.; Ochterski, J. W.; Martin, R. L.; Morokuma, K.; Zakrzewski, V. G.; Voth, G. A.; Salvador, P.; Dannenberg, J. J.; Dapprich, S.; Daniels, A. D.; Farkas, Ö.; Foresman, J. B.; Ortiz, J. V.; Cioslowski, J.; Fox, D. J. Gaussian-09 Revision E.01., Gaussian Inc. Wallingford CT 2009.
- (47) Grimme, S.; Antony, J.; Ehrlich, S.; Krieg, H. *J. Chem. Phys.* **2010**, *132*, 154104.
- (48) Luo, Y.-R., *Comprehensive handbook of chemical bond energies*; CRC Press: Boca Raton, 2007; 1655 pp.
- (49) Pham, L. N.; Nguyen, M. T. *J. Chem. Theory Comput.* **2018**, *14*, 4833–4843.

Chapter 9

Conclusions and Outlook

9.1 Conclusions

This dissertation presents the main results achieved during my PhD research. Briefly, the contents of this dissertation focus on studies of small clusters containing 3d-block metals. The dissertation stream can be divided into two sequential parts: (i) the study of small 3d-metal doped clusters by using highly accurate levels of theory, and (ii) the identification of geometric, electronic structures, and related properties of larger clusters containing more than one transition metal atom. In the first part, clusters were studied in the increasing order of multireference characteristics by raising the number of electrons one by one in the 3d subshell of the doping metals. Additionally, several DFT functionals were also employed to assist in the determination of stable geometrical structures, ground and excited states. Furthermore, the use of various density functionals provided basic assessment on how well density functionals perform for systems with increasing magnitude of multireference features. As an inherent shortcoming of multiconfigurational approaches, CASSCF-based methods cannot be used for larger systems (larger active spaces needed), and therefore density functional theory remains the choice at the time being. Some density functionals, screened from the first part of this dissertation, were tentatively utilized for next larger clusters chemically composed of multiple transition metal atoms. However, utilization of more than a half-dozen functionals (to ensure accurate results) for large clusters is still

time consuming and requires a large amount of computing resources. Hence, another purpose in the second part of this dissertation is to confine the range of functionals that can handle strong multireference systems to less than a few for the study of future related systems.

Chapter 2 gave a brief outline of the methodologies employed in this work. In Chapter 3, geometry, electronic ground and excited states on the energetic hypersurface of the experimentally known $\text{ScSi}_2^{-/0}$ were investigated and reported. Scandium has one electron in its $3d$ subshell, and therefore, the electronic structures of $\text{ScSi}_2^{-/0}$ are characterized with single-configurational features as expected. Indeed, all dominant electronic configurations of ground and excited states have contributions of $\geq 80\%$ to the wave functions. All tested density functionals can consistently locate ground states of the neutral and anion in accordance with the CASPT2 method. All experimental detachment energies obtained from the experimental spectra were also produced correctly as well at several single-reference levels (DFT and RCCSD(T)), and confirmed at the CASPT2 level. The point here is that single-reference methods cannot be used to reliably probe low-lying states represented by hyper open-shell electronic configurations¹ ($n \geq 2S + 2$ where n is the number of unpaired electrons and S is the total electronic spin). And for the anionic cluster ScSi_2^- , the hyper open-shell configuration of the state ${}^1\text{B}_2$ (C_{2v}) is energetically competitive with the ordinary open-shell configuration of ${}^3\text{B}_2$. In this case, DFT methods are not the effective choices for treatment of such electronic degeneracy.

Titanium digermanium and its anionic form were studied and reported in Chapter 4. Because there are more electrons in the $3d$ subshell and the moiety Ge_2 is considered electronically more complex than the Si_2 moiety, electronic structures of $\text{TiGe}_2^{-/0}$ were found to be more complicated than those of $\text{ScSi}_2^{-/0}$. Leading HF configurations of few wave functions of $\text{TiGe}_2^{-/0}$ are found to have $\geq 80\%$ contribution, and several leading configurations of other wave functions possess contributions in a range of 40 – 76%. With different magnitudes of leading configurations, especially for some states with low magnitudes, the multiconfigurational methods used in this chapter (CASSCF/CASPT2 and CASSCF/NEVPT2) and the golden standard method CCSD(T) simultaneously gave the same ground states of the neutral and anionic $\text{TiGe}_2^{-/0}$. Other nearly degenerate states and low-lying states were also identified at these levels. Multiple electronic transitions were proven to cause visible anion photoelectron bands in the experiment. Due to the wide range of leading coefficients, several states of $\text{TiGe}_2^{-/0}$ are believed to be challenging to DFT methods. By comparing electronic energies calculated using several DFT functionals, we

found that the M06-L functional can give the same energetic ordering of several electronic states as CASPT2, and NEVPT2, and RCCSD(T) did.

In Chapter 5, multiconfigurational characters of $\text{VGe}_3^{-/0}$ were found to be relatively stronger than those of $\text{TiGe}_2^{-/0}$. The CASPT2 method determined that VGe_3^- in the ground state (${}^1\text{A}_1$) has a tetrahedral form with a spatial symmetry of C_{3v} . All electronic transitions forming the ground and excited states of the neutral cluster start from the anionic ground state ${}^1\text{A}_1$. Upon removal of one frontier electron from the ground state, the resulting neutral cluster undergoes a Jahn-Teller effect, and there are two nearly degenerate electronic states generated. This means that the first band in the experimental spectra is induced by two electronic transitions from the anionic ground state. The same effect is also believed to contribute to the second band. In dealing with multiconfigurational features, the BP86 functional is found to be appropriate for the treatment of $\text{VGe}_3^{-/0}$.

To raise the level of multiconfigurational features, in Chapter 6 clusters containing two chromium atoms were thoroughly studied. Leading electron configurations of most electronic states have quite small coefficients. These values imply that the $\text{Cr}_2\text{O}_2^{-/0}$ clusters have very strong multireference features. This is why several tested functionals, except for the pure TPSS functional, cannot produce state energies that are consistent with the RASPT2 energies. By using two multireference methods RASPT2 and DMRG-CASPT2, two 10-tet states (${}^{10}\text{A}_g$ and ${}^{10}\text{B}_{2g}$) of Cr_2O_2^- were identified to be nearly degenerate and proven to be populated simultaneously in the experiment. Two nearly degenerate states were found to cause two first bands in the anion photoelectron spectra. Because of small difference in relative energy, the less-populated anionic ground state ${}^{10}\text{B}_{2g}$ causes the very low intensity band X', and the removal of one electron from the true ground state ${}^{10}\text{A}_g$ induces the X band with higher intensity in the anion photoelectron spectrum of Cr_2O_2^- . 30 electronic transitions (within the active space used) starting from two nearly degenerate states of the anion Cr_2O_2^- were predicted to be the origin of removed electrons recorded as several anion photoelectron bands in the spectra.

We can see that for single-reference clusters like $\text{ScSi}_2^{-/0}$ single-reference methods are good choices. The DFT options for single-reference clusters are quite plentiful. For systems with stronger multireference characters, we found that there can be appropriate functionals for studying these systems. Therefore, we believe that for larger systems containing multiple metallic atoms there will be also good density functionals for investigating these systems. In the next chapter (Chapter 7), several functionals were, thereby, used to identify geometric

and electronic structures of chromium oxide clusters.

Various unsaturated chromium oxide clusters (Cr_mO_n^+ , $m = 2 - 4$, $n \leq m$) were synthesized, mass-selected, and probed by using the IRMPD technique. Because these clusters are unsaturated and composed of multiple chromium atoms, they are believed to be strongly multiconfigurational. As can be seen above, the TPSS functional can correctly determine the ground and other low-lying states of $\text{Cr}_2\text{O}_2^{-/0}$. Therefore, in this work, the TPSS functional was used to study geometric and electronic structures of Cr_mO_n^+ . However, only the results calculated from the TPSS functional are not reliable enough to ascertain the most stable isomers and ground spin states. To increase the reliability of DFT results, six other density functionals were also utilized to probe these chromium clusters. The seven functionals (B3LYP, B3P86, BP86, BPW91, B3PW91, TPSS, TPSSh) used gave consistent results. All experimentally populated chromium oxide clusters were identified by comparing the simulated IR spectra with the experimental ones. From electronic structures of experimentally populated states, magnetic behaviors and magnetic interaction between magnetic sites within each cluster were revealed. Two main factors control total magnetic moments of these chromium clusters are $3d$ - $3d$ bonding-like formation and $2p$ - $3d$ delocalization. Magnetic evolution of the series Cr_3O_n^+ ($n = 0 - 5$) under the addition of oxygen atoms was drawn. $3d$ - $3d$ bonding-like formation between two closer chromium atoms is dominant, leading to low total magnetic moments when the quantity of chromium atoms in the clusters dominates that of oxygen atoms. If more oxygen atoms are added, $2p$ - $3d$ delocalization becomes dominant, and as a result, total magnetic moments are reduced.

From the previous chapter, three functionals (TPSS, B3P86, and BP86) were found to be good and therefore selected for IR simulations of clusters containing multiple $3d$ -block metallic atoms. In Chapter 8, various bimetallic Cr-Mn oxide clusters ($\text{Cr}_x\text{Mn}_y\text{O}_z^+$, $x + y = 2 - 4$, $z = 4 - 9$) were synthesized and characterized with the IRMPD spectroscopy. Bimetallic oxide clusters with different ratios between chromium and manganese were controlled through mass selection. Geometric and electronic structures of all clusters with well-resolved IRMPD spectra were identified in combination with the simulated spectra. We see that the Cr-Mn ratios and addition of oxygen atoms do not affect geometries and general motifs of all hybrid oxide clusters. Two general trends of magnetic properties could be seen from all series of Cr-Mn oxide clusters. Total magnetic moments of Cr-Mn oxide clusters are usually lower than those of corresponding pure chromium oxide clusters. In all hybrid clusters, averaged absolute local magnetic moments of manganese sites are

larger than those of chromium sites because of the electron transfer from chromium to manganese sites. Further, electrons captured by additional oxygen atoms are believed to cause reduction of total magnetic moments.

Overall, this dissertation comprises a series of studies, starting from small clusters with different levels of multiconfigurational features to larger clusters containing multiple metallic atoms. A summary of all studied clusters and general results in this dissertation are tabulated in Table 9.1. For single-reference systems and study of ground states, single-reference methods such as DFT and CCSD(T) are good enough for the study of geometry and electronic structures, and some other related properties. But for studying excited states and other electronic states characterized with multireference features, multiconfigurational methods are required; even optimization of geometry needs to be done at multiconfigurational levels. In dealing with larger systems, multiconfigurational methods are practically impossible, and DFT is the only choice. So, in this dissertation, we found that there are some specific relevant functionals for study of multiconfigurational systems.

9.2 Outlook

It is clear that if there are more electrons in the $3d$ -subshell of $3d$ -block metals, study of systems doped with these metals is more challenging. In this dissertation, clusters containing transition metals up to manganese were considered. For small cluster systems containing one and two metallic atoms, we can see dozens of experimental works on synthesis and spectroscopic measurements.^{2–11} Similar to small clusters studied in the first part of this dissertation, these clusters are still not fully studied, and therefore, using highly accurate quantum chemical methods to study these systems is of interest. With recent improvements in the development of new methods such as DMRG-CASPT2¹² and DMRG-NEVPT2,^{13,14} a large active space consisting of up to 50 orbitals is possible, and the size of clusters which can be studied by highly accurate methods is increased over the limit of RASSCF/RASPT2. This might open a new door for us to use these methods (DMRG-CASPT2 and DMRG-NEVPT2) to study clusters consisting of three or more transition metal atoms.

Of the several experimentally synthesized and spectroscopically probed species mentioned

Table 9.1: Summary of all studied systems and general results

system	calculation method	experimental data	result ^(α)
ScSi ₂ ^{-/0}	CASSCF/CASPT2, MRCI(Q), B3LYP, BP86, RCCSD(T)	Anion PE spectra	anion: C _{2v} , ³ B ₂ neutral: C _{2v} , ² B ₂ 6, B3LYP, BP86
TiGe ₂ ^{-/0}	CASSCF/CASPT2, NEVPT2, M06L, RCCSD(T)	Anion PE spectra	anion: C _{2v} , ⁴ B ₁ neutral: C _{2v} , ³ B ₁ 9, M06L
VGe ₃ ^{-/0}	CASSCF/CASPT2, MRCI(Q), BP86, RCCSD(T)	Anion PE spectra	anion: C _{3v} , ¹ A ₁ neutral: C _s , ² A', ² A'' 6, BP86
Cr ₂ O ₂ ^{-/0}	RASSCF/RASPT2, DMRG-CASPT2, TPSS, BP86	Anion PE spectra	anion: D _{2h} , ¹⁰ A _g neutral: D _{2h} , ⁹ B _{2g} 30, TPSS
Cr _m O _n ⁺ m = 2 – 4 n ≤ m	B3LYP, B3P86, B3PW91, BP86, TPSS, TPSSh, M06L	IRMPD spectra	Most stable isomers, electronic ground states, magnetic properties
Cr _x Mn _y O _z ⁺ x + y = 2 – 4 z = 4 – 9	TPSS, BP86, B3P86	IRMPD spectra	Most stable isomers, electronic ground states, magnetic properties

^(α) For the first 4 systems, the results include symmetry and electronic states of anionic and neutral clusters, numbers of predicted electronic transitions, and good density functionals used.

above, clusters containing chromium, manganese, and iron are of high priority. To be more detailed, ground and excited states of Cr₂O_n^{-/0} (n = 2 – 6) were experimentally reported⁸ specifying that several ionization processes cause well-resolved bands in the anion photoelectron spectra. With the study on Cr₂O₂^{-/0},¹⁵ we believe that other Cr₂O_n^{-/0} clusters are also featured with strong multireference wave functions. To study these systems, multiconfigurational methods are recommended. The series of transition metal oxide clusters which would be in the list of our future works is Fe₂O_n^{-/0}. Visually, anion photoelectron spectra of Fe₂O_n⁻ seem to be simpler than those of Cr₂O₂^{-/0},^{7,8} but some basic calculations have determined that this series of oxide clusters have even stronger multiconfigurational features than Cr₂O₂^{-/0}. For such inherent multireference systems, we hope that some good density functionals can be identified for the study of Fe₂O_n^{-/0}.

Starting from multiconfigurational results, suitable density functionals are expected to be found for the application to larger systems. This is what we have done so far for the cases of Cr_mO_n^+ and $\text{Cr}_x\text{Mn}_y\text{O}_z^+$ clusters. We would expect that iron oxide, manganese oxide, and cobalt oxide clusters, and their properties are our next consideration. In addition to these single-metal oxide clusters, some other hybrid metal oxide clusters containing two or more transition metals (Cr, Mn, Fe, and Co) are also interesting. On the basis of our experience in the study of $\text{Cr}_x\text{Mn}_y\text{O}_z^+$ clusters, we can see that study of clusters containing multiple transition metals is an enormous challenge. And therefore, more time, computing resources, and experimental techniques are required.

As we can observe that multireference methods cannot be employed for treating large clusters consisting of multiple metallic atoms, and density functional theory is the only current solution. As expected, DFT methods cannot give highly accurate results, and different functionals can lead to different geometrical structures and electronic ground states. Efforts have been made by introducing multiconfigurational pair-density functional theory¹⁶ to overcome the shortcomings of CASPT2 and RASPT2 in terms of computing resource and analytic gradients.¹⁷ However, it is not enough for treatment of large clusters due to this new technique only recovers dynamic correlation on the basis of CASSCF and RASSCF wave functions. Therefore, a new CASSCF and RASSCF algorithm which can handle a larger number of orbitals in the active space is in demand. A newly developed method, the DMRG-CASPT2, can possibly treat larger system with up to 50 orbitals in the active space as mentioned above, but this method requires a huge amount of computing resource and time. Solutions for analytical energy gradients at the DMRG-CASPT2 level are still not available, which blocks this new method from application. Recently, the DMRG-SCF with analytical gradients has been developed,¹⁸ which means this technique can be used for geometrical optimization more efficiently but still the dynamic correlation needs to be incorporated appropriately. A question can, now, be proposed whether dynamic correlation energy recovered from perturbative calculations is important if a larger number of orbitals in the active space is taken into account at the DMRG-SCF step. If it is not important (for specific sizes of systems), the DMRG-SCF with analytic gradients can be applied to large clusters for geometrical optimization without much loss of accuracy and any worry about the bottleneck caused by CASPT2 and NEVPT2.

References

- (1) Varga, Z.; Verma, P.; Truhlar, D. G. *J. Am. Chem. Soc.* **2017**, *139*, 12569–12578.
- (2) Zhang, N.; Kawamata, H.; Nakajima, A.; Kaya, K. *J. Chem. Phys.* **1996**, *104*, 36–41.
- (3) Yang, B.; Xu, X.-L.; Xu, H.-G.; Farooq, U.; Zheng, W. *Phys. Chem. Chem. Phys.* **2019**, *21*, 6207–6215.
- (4) Xu, H.-G.; Zhang, Z.-G.; Feng, Y.; Zheng, W. *Chem. Phys. Lett.* **2010**, *498*, 22–26.
- (5) Yuan, J.-Y.; Xu, H.-G.; Zheng, W.-J. *Phys. Chem. Chem. Phys.* **2014**, *16*, 5434–5439.
- (6) Gutsev, G. L.; Bauschlicher Jr, C. W.; Zhai, H.-J.; Wang, L.-S. *J. Chem. Phys.* **2003**, *119*, 11135–11145.
- (7) Wu, H.; Desai, S. R.; Wang, L.-S. *J. Am. Chem. Soc.* **1996**, *118*, 5296–5301.
- (8) Zhai, H.-J.; Wang, L.-S. *J. Chem. Phys.* **2006**, *125*, 164315.
- (9) Kong, X.; Xu, H.-G.; Zheng, W. *J. chem. Phys.* **2012**, *137*, 064307.
- (10) Zhai, H.-J.; Wang, L.-S. *J. Chem. Phys.* **2002**, *117*, 7882–7888.
- (11) Yuan, J.; Wang, P.; Hou, G.-L.; Feng, G.; Zhang, W.-J.; Xu, X.-L.; Xu, H.-G.; Yang, J.; Zheng, W.-J. *J. Phys. Chem. A* **2016**, *120*, 1520–1528.
- (12) Kurashige, Y.; Yanai, T. *J. Chem. Phys.* **2011**, *135*, 094104.
- (13) Guo, S.; Watson, M. A.; Hu, W.; Sun, Q.; Chan, G. K.-L. *J. Chem. Theory Comput.* **2016**, *12*, 1583–1591.
- (14) Freitag, L.; Knecht, S.; Angeli, C.; Reiher, M. *J. Chem. Theory Comput.* **2017**, *13*, 451–459.
- (15) Pham, L. N.; Nguyen, M. T. *J. Chem. Theory Comput.* **2018**, *14*, 4833–4843.
- (16) Gagliardi, L.; Truhlar, D. G.; Li Manni, G.; Carlson, R. K.; Hoyer, C. E.; Bao, J. L. *Acc. Chem. Res.* **2016**, *50*, 66–73.
- (17) Sand, A. M.; Hoyer, C. E.; Sharkas, K.; Kidder, K. M.; Lindh, R.; Truhlar, D. G.; Gagliardi, L. *J. Chem. Theory Comput.* **2017**, *14*, 126–138.
- (18) Freitag, L.; Ma, Y.; Baiardi, A.; Knecht, S.; Reiher, M. *arXiv preprint arXiv:1905.01558* **2019**.

List of publications

Journal Articles Used in This Dissertation

1. **Pham, L. N.**; Claes, P.; Lievens, P.; Jiang, L.; Wende, T.; Asmis, K. R.; Nguyen, M. T.; Janssens, E. Geometric Structures and Magnetic Interactions in Small Chromium Oxide Clusters. *J. Phys. Chem. C* **2018**, *122*, 27640 – 27647.
2. **Pham, L. N.**; Nguyen, M. T. Another Look at Photoelectron Spectra of the Anion Cr_2O_2^- : Multireference Character and Energetic Degeneracy. *J. Chem. Theory Comput.* **2018**, *14*, 4833 – 4843.
3. **Pham, L. N.**; Nguyen, M. T. Insights into Geometric and Electronic Structures of $\text{VGe}_3^{-/0}$ Clusters from Anion Photoelectron Spectrum Assignment. *J. Phys. Chem. A* **2017**, *121*, 6949 – 6956.
4. **Pham, L. N.**; Nguyen, M. T. Titanium Digermanium: Theoretical Assignment of Electronic Transitions Underlying Its Anion Photoelectron Spectrum. *J. Phys. Chem. A* **2017**, *121*, 1940 – 1949.
5. **Pham, L. N.**; Nguyen, M. T. Electronic Structure of Neutral and Anionic Scandium Disilicon $\text{ScSi}_2^{-/0}$ Clusters and the Related Anion Photoelectron Spectrum. *J. Phys. Chem. A* **2016**, *120*, 9401 – 9410.

Manuscripts Used in This Dissertation

1. **Pham, L. N.**; van Dijk, C. N.; Kirilyuk, A.; Nguyen, M. T.; Janssens, E. et al. Bimetallic Oxide Clusters $\text{Cr}_x\text{Mn}_y\text{O}_z^+$: Geometric structures, structural evolution, and magnetic properties *Manuscript in preparation*

Others during the PhD Program

1. Jia, M.; van der Tol, J.; Li, Y.; Chernyy, V.; Bakker, J. M.; **Pham, L. N.**; Nguyen, M. T.; Janssens, E. Structures and Magnetic Properties of Small Co_n^+ and $\text{Co}_{n-1}\text{Cr}^+$ ($n = 3 - 5$) Clusters. *J. Phys.: Condens. Matter* **2018**, *30*, 474002.
2. Nguyen, T. H. M.; **Pham, L. N.** et al. An Insight into C–H · · · N Hydrogen Bond and Stability of the Complexes Formed by Trihalomethanes with Ammonia and Its Monohalogenated Derivatives. *Int. J. Quantum Chem.* **2016**, *117*, e25338.
3. **Pham, L. N.**; Hendrickx, M. F. A. Contributions of Nearly Degenerate States to the Photoelectron Spectra of the Vanadium Dicarbide Anion. *J. Phys. Chem. A* **2016**, *120*, 9465–9475.

Presentations

1. Electronic Transition in Anion Photoelectron Spectra of VC_2^- and ScSi_2^- Clusters, 2nd Annual Meeting and Conference of the European Joint Doctorate in Theoretical Chemistry and Computational Modelling, EJD-TCCM, Leuven Belgium, Poster presentation 2017.
2. Electronic Structures and Insights into Anion Photoelectron Spectra, WATOC-2017, Munich Germany, Poster presentation 2017.

FACULTY OF SCIENCE
DEPARTMENT OF CHEMISTRY
QUANTUM CHEMISTRY AND PHYSICAL CHEMISTRY

Celestijnenlaan 200F box 2402

B-3001 Leuven

lenhanhoaqn@gmail.com

<https://sites.google.com/prod/view/lenhanpham>

